# Final Report

## AE3200: Design Synthesis

Group 14 – 2021/2022


| | | | |
|---|---|---|---|
| Ekaterina Konopleva | 5025761 | Julius Baas | 4546806 |
| Niels van der Ploeg | 5057833 | Pepijn Hoogervorst | 5025567 |
| Sie Leoi Lee | 5071674 | Tiia Tikkala | 5024439 |
| Ids Oostmeijer | 5098335 | Jasmijn Kipping | 5046211 |
| Nikki Grens | 5034183 | Merlijn Broekers | 5046092 |


Delft University of Technology

TU Delft

This page is intentionally left blank.

# Final Report

by


**Group 14 – 2021/2022**

| | | | |
|---|---|---|---|
| **Ekaterina Konopleva** | **5025761** | **Julius Baas** | **4546806** |
| **Niels van der Ploeg** | **5057833** | **Pepijn Hoogervorst** | **5025567** |
| **Sie Leoi Lee** | **5071674** | **Tiia Tikkala** | **5024439** |
| **Ids Oostmeijer** | **5098335** | **Jasmijn Kipping** | **5046211** |
| **Nikki Grens** | **5034183** | **Merlijn Broekers** | **5046092** |


to complete the AE3200 Design Synthesis Exercise spring 2022.

**Version Control**

| Version | Purpose | Changes | Date |
|---|---|---|---|
| 1 | First draft | - | 15-06-2022 |
| 2 | Final version | Incorporated supervisor feedback, finalised structural analysis and sensitivity analysis | 21-06-2022 |


Supervisor: John-Alan Pascoe
Coaches: Ingeborg de Pater & Vahid Yaghoubi Nasrabadi
Institution: Delft University of Technology
Place: The department of Aerospace Engineering
Course: AE3200 Design Synthesis Exercise


Cover Image: A group of penguins on a mission in Antarctica, Getty Images. Feb 2014.

TU Delft Delft University of Technology

# Preface

This report presents the design of a sustainable aircraft able to perform a medical evacuation between two remote research stations on the Antarctic continent. This report is the final report in a series of reports, finalising the Design Synthesis Exercise (DSE). In the DSE programme, ten aerospace engineering students from the TU Delft perform ten weeks of full time intensive research to produce an aerospace design.

During the DSE, we had the honour of working on a challenging, but extremely interesting design. Numerous design challenges were faced which required us to combine the knowledge we obtained from the Aerospace Engineering bachelor with our creativity. We are proud to present the JAPA-12, an aircraft design to which each of us put our best effort.

We would like to thank our tutor Dr.ir. J.A. Pascoe and our coaches I. de Pater MSc and Dr. V. Yaghoubi Nasrabadi for all their support, excellent advice, and time. Furthermore, we would like to thank Dr. R. de Vries for his expertise on distributed propulsion aircraft, Dr.Ing. S. Castro for his help on the mechanics of a rear loading door and Dr. S.R. Turteltaub for his help with vibration analysis.

**DSE Group 14, ArctEvac**
Tuesday 21st June, 2022, Delft

*'Providing jolly medevac solutions, sustainably'*

# Executive Summary

In this report, the final sizing of an aircraft, designed to operate in harsh Antarctic weather conditions, is presented to the reader. This aircraft, which was named JAPA-12, shall be able to perform rescue missions scheduled for service in 2030. However, implications to design a family of aircraft were considered as well, such that other markets can be served.The JAPA-12 primarily aims to replace the more than 50 year old DHC-6 Twin Otter, which has been used to perform the rescue missions. A team of ten aspiring engineers sized and analysed the aircraft such that it was ready to be presented to investors. The analysis was performed with respect to aerodynamic performance as well as stability & control, payload & range, structural performance and cost.

**Foundation of the design process**

The design process started with the mission need statement (MNS) and project objective statement (POS) which had been established prior to this report and are included below. Three design concepts were selected, worked out and traded off, showing a distributed propulsion aircraft as the clear winner. Accordingly, detailed designing of all subsystems was done. These subsystems have been sized with respect to the requirements leading from the MNS, therefore the team re-analysed all set requirements from the midterm report [1]. These requirements were later analysed for compliance to assess the completeness of the design process. An iterative process influenced the design process significantly. When the outcomes of the detailed analysis differed from assumptions made, the subsystems were resized thereby influencing other subsystems. This iterative process was continued until a maximum of 5% difference was achieved.

**MNS: Design an aircraft that can successfully conduct a medical evacuation under extreme Antarctic weather conditions at the Amundsen-Scott base and, possibly, serve other remote communities and roles.**

**POS: Obtain a better understanding of the full design cycle of a system and gain knowledge on designing an aircraft by producing a design that fulfils the mission need statement together with a group of 10 capable aspiring engineers in 10 weeks.**

**Preliminary sizing**

Preliminary sizing was done following the sizing method of de Vries [2]. The novel design features increased aerodynamic performance as a result of implementing distributed propulsion (DP) at the leading edge of the main wing. An aerodynamic model was implemented to model the effects of DP with respect to lift and drag as a result of coupling effects from DP.

Following this, a powertrain model was used to model the propulsion system due to the design being significantly different compared to conventional designs. It was found that the use of batteries was infeasible for such a long-range with current and prospected technology for delivery in 2030. A partial turbo-electric architecture was therefore selected, in which combustion engines run main propellers and deliver power via generators to electric motors connected to a smaller propeller. A major advantage of distributed propulsion is the easier ability to perform basic manoeuvres in case of one engine inoperative conditions compared to conventional twin-propeller aircraft. The engines were sized for maximum reliability to deliver sufficient power to the propulsors, such that the yawing moment is minimised during OEI conditions, and the mission can be continued nominally. The powertrain model was used to determine the weights of the components of the propulsion system, which were required for range calculations based on operational requirements.

The established weight fractions were used for point performance calculations. Padding factors ensured that underlying technical costs were accounted for, as prediction methods contain uncertainties. These padding factors are crucial to ensure that the aircraft does not under-perform and cause dissatisfied customers. Starting with the take-off distance, challenges occurred as a result of strong winds. Tailwinds influence ground roll, which is also affected by the snowy runway of Amundsen-Scott and cross-winds damage controllability. Similar issues applied for landing distance, where the increase in ground roll is the result of reduced tyre friction and braking. Stall speeds were designed for by analysis of CS-23 requirements prior to Amendment 5. Failure to meet this requirement largely contributes to the number of fatal accidents in Antarctica. For this, the air density was an important parameter as this directly influences the available lift. The maximum design cruise speed was taken as 20% higher than stakeholder requirements for average cruise speed, which is usually calculated at around 80% thrust [3]. Lastly, the service ceiling was based on the location where the maximum achievable rate of climb equals 0.5 m/s.

The actual magnitude of the power required and wing area resulted from generating multiple power loading diagrams per individual power train component. It was concluded that maximum cruise speed and stall speed were the limiting conditions for JAPA-12. These design points in the loading diagram were used to determine the energy required for each flight phase based on aircraft take-off weight. This was determined through Roskam [4] class I sizing methods. Accordingly, relevant masses to be used in further calculations were found for three different missions established by the customer.

**Subsystem design**

Several subsystems were designed in more detail after the preliminary sizing was completed. For the fuselage it was found that the most critical configuration was the 19-passenger configuration. A cross-sectional view was created after which the top-view layout was designed. To make sure the fuselage may be certified the emergency doors were located. Apart from these doors, the rear door was sized. This door will allow for the easy loading of the patient.

The wing planform was designed in combination with selection of the airfoil. In designing the wing planform it was decided to enlarge the surface area, such that the high lift devices and control surfaces may be positioned. These high lift devices are needed to ensure the aircraft can comply with the take-off and landing distance requirements. A difference in the wing design compared to regular aircraft is the anhedral angle of the wing. This angle will aid in the stability of the aircraft, while still maintaining controllability.

The propulsion system and fuel system are interrelated, as the type of fuel used determines the type of propulsion system. The fuel system was sized such that the fuel will be stored in the wing, which will relieve the bending caused by the lift. It was made sure that the fuel in the fuel tanks and piping will not freeze in the air or on the ground in the harsh conditions experienced in Antarctica. The fuel will be supplied to the two combustion engines, which generate the power required for the aircraft's systems and the ten electric engines. These two combustion engines power the two main propellers of the aircraft, which are assisted in the generation of thrust by ten smaller propellers powered by electric motors. The main engines are positioned closest to the fuselage on either wing, the ten electric engines are distributed equally along the wing to have five electric engines on each wing. The Pratt & Whitney Canada PW118 was selected as main engine, which produces a maximum continuous power of about 1340 kW and weigh 390 kg. For the electric motors, the MGM Compro REB30 was selected which produces 30 kW and weighs 8.1 kg. These were selected for cruise conditions such that for one engine inoperative the mission can still be performed.

The horizontal and vertical tail surfaces will ensure the aircraft is controllable and stable in every phase of flight. This started by examining the centre of gravity (cg) location for every loading case. One advantage of the distributed propulsion system chosen for this aircraft is the reduced yawing moment caused by one engine failing. The critical case for this was one combustion engine failing, this will also result in five of the ten electrical engines failing. Because of the way the electric engines are connected to the combustion engines, the electric engines on the opposite wing to the failed combustion engine will fail, resulting in a smaller yawing moment. This reduction in moment was beneficial for the vertical tail, as the tail can be smaller.

The landing gear was sized based on the main failure modes related to Antarctic missions. For this it was found that most failures occur due to the landing gear. This process was started by deciding on the position of the nose and main landing gear. This was largely dictated by the controllability on ground. After which the strut, shock absorbers, and retraction mechanism were sized. This system required blisters to be installed on the aircraft to make sure the landing gear can be stored, including the skis which are required to be able to land on snow and ice. This retraction mechanism will be powered by hydraulics, which will be the main method of controlling other movable surfaces, like the high lift devices and control surfaces.

Hydraulic systems, which are used to move the control surfaces and electric actuators, are also included. These electric actuators will be powered by the generators which are attached to the combustion engines. These generators will in nominal conditions power the aircraft's systems. If one of the engines fails there are backup batteries which can power the essential aircraft equipment and medical equipment. The electric system will also provide the required power for the heating, ventilation and air conditioning (HVAC) system. This system will control the cabin environment in the antarctic, in-flight and other market conditions experienced.

**Operations & logistics**

The Antarctic rescue mission required a thorough analysis of possible subsystems to be designed for the operation of the aircraft in harsh weather conditions. The customer requirements resulted in the selection of synthetic kerosene to have net-zero carbon emissions. As the team opted for refuelling at Amundsen-Scott, fuel storage was therefore required. Currently, the base uses JP-8 aviation fuel to power its electrical components. As a result, the team found it useful to transform the infrastructure to use synthetic kerosene such that the storage tanks can be used to both power the base and refuel the aircraft. However, the compatibility of fuels must still be investigated or the tanks shall be cleaned thoroughly.

JAPA-12 will operate in conditions in which ice may form on the leading edge of the wing. This occurs when supercooled water droplets freeze on impact in temperature ranges of 0°C to -40°C, below this temperature all droplets are frozen and thus do not freeze and attach to the leading edge when they are hit. Therefore, the aircraft features an anti-icing module which heats the leading edge and is incorporated into the main wing, horizontal tail wing and vertical tail wing. This system is powered by excess engine power. The leading edges are split up to feature their own anti-icing system such that not the entire leading edge freezes in case of anti-icing system failure. On ground de-icing works are performed in

the form of de-icing fluids and manual de-icing. In case of short parking times, the engines will be kept on, and in case of longer parking times, the aircraft shall be parked on wooden planks such that it does not freeze fixed into place.

Constant communication is essential to complete a mission successfully. Frequent updates with ground stations regarding the status of both the aircraft and station conditions can benefit the decision-making for example sudden changes in weather conditions. The option of high-frequency data link communication was chosen, where Leonardo SP-2310 and Rockwell Collins CMU-900 were selected as radio module and communication management unit respectively.

Besides communication, a device is required to locate aircraft which is used continuously as strong winds might require a different course to be flown. Normal GPS systems do not allow for sufficient coverage on the south pole. However, as navigation is only required during the cruise which occurs at high altitude, a rough estimation of location was deemed sufficient. This is achieved with a GTN 750 Xi navigation module. In addition, to determine the position at latitudes where GPS coverage is poor, radio navigation is included functioning as a backup system. For this, a BendixKing KN-63 module was selected which uses the non-directional beacon located at both bases.

Both Rothera and Amundsen-Scott experience severe whiteout conditions most of the year. Therefore, visual aids were required to be featured in the design. For the aircraft, this meant that the pilot has to be able to visually inspect the runway. To do this, a synthetic vision system was selected such that the pilot can always identify the runway when at an altitude of 650 ft or below, above the ground. The system however costs about $500k, therefore it will not be included in aircraft that operate in other markets where visibility is not an issue. For both Rothera and Amundsen-Scott base no additional systems were required as it already has an option for an area navigation approach.

**Aircraft performance**

After the system had been designed, an analysis of its performance was performed. This started by analysing the aerodynamic properties of the aircraft. These properties were used in the following performance analyses and were used to check the values used in the design process. Using the aerodynamic coefficients a stability and control analysis was performed. From this analysis, it was concluded that the aircraft is both statically and dynamically stable. However, if the ice would form on the wings the aircraft would become unstable, thus showing the importance of the ant-ice system.

The weights stemming from the sizing of the aircraft were used to generate a payload-range diagram. This diagram shows that the critical loading condition is the 150 NM range with 19 passengers. All other payload-range combinations, which were examined, are not critical. Resulting in the ability to carry additional payload on these ranges in calm weather conditions. To understand the structural limits for which the aircraft's structure had to be designed a loading diagram was constructed. This resulted in a positive maximum load of $n_+ = 6.3$ and a minimum load factor of $n_- = -4.4$.

**Structural analysis**

In the structural analysis it was investigated whether the structure could sustain the (aero)dynamic and static loads on it within the flight envelope. The internal loads corresponding to the minimum and maximum load factor, multiplied by a safety factor of 1.5, were determined for the main structural components: The fuselage, wing and horizontal stabiliser. From the minimum and maximum loads that were determined, the corresponding maximum stresses in the structure were calculated. For respectively the fuselage, wing and empennage, the maximum stresses that were found were 290, 480 and 454 MPa. Following this analysis was the choice of materials for the main components. The choice was made to have each of the three main components made of one material to simplify the structural analysis. The choice for this material was based on numerous parameters such as the Ultimate Yield Strength (UYS), density, Coefficient of Thermal Expansion (CTE), Young's modulus, relative recyclability and relative cost. After comparing the required strength of the component with the UTS of the material, not neglecting the aforementioned material parameters and customer requirements, a choice was made: The main wing and the empennage will be made of aluminium 7075-T6. The fuselage will be made of a combination of aluminium 2024-T3, aluminium 6061-T6 and CFRP.

An attempt was made to make an accurate prediction of the flutter speed of the main wing and empennage. A model simulating the torsional movement of these components was set up. In this model, the engines and wing were approximated as disks. After the equations of motion and the corresponding mass-normalised stiffness matrix were set up, the circular natural frequencies could be computed. These values were then transformed to flutter speed using the reduced frequency equation. The values found using this approach were in the order of at least Mach 113. It was thought an error was present in the logic as a thorough verification process verified the model was mathematically correct. The conclusion of the vibration analysis was that the model shall for sure not suffer from a torsional motion as set up in this model. However, nothing could be said about other modes of failure. Future tests would have to prove what kind and at what velocity flutter behaviour will occur.

**Risk & safety**

A risk analysis was conducted due to the aircraft being designed in a limited time frame, without any physical tests performed. The identified risks were derived from the development and operational phase as well as from a reliability,

availability, maintainability and safety analysis (RAMS). Potential risk categories were established and mitigation strategies were constructed where risks are either removed, reduced, accepted or transferred such that they do not influence the design to a harmful extent. The most unreliable systems were found to be the combustion engines and hydraulic systems as they largely depend on generated electricity. Therefore, frequent maintenance of these subsystems shall be implemented and re-evaluation of design choices shall be performed. Also, the team aims to closely monitor the improvements made in these fields such that high-quality systems are implemented when constructing the aircraft.

**Financial analysis**

Analysis of the JAPA-12 design in an Antarctic configuration, the team noticed the market to be too little to make a profit. Therefore, a family of aircraft shall be designed in the future continuation of the design process. It is believed that manufacturing costs will drastically change, such that fewer aircraft have to be sold to achieve a positive return on investment. Major changes are expected for the landing gear as skis are not required generally, the engine as less harsh weather conditions are generally experienced and adaptation to temperature as less cold environments result in slightly larger wings however for the cabin less insulation and heating is required.

In order to determine what exactly has to be done such that the aircraft can apply to other markets, a market analysis was performed. The analysis also was used to determine the number of aircraft which can be sold. As a start, a SWOT analysis was performed, in which all strengths, weaknesses, opportunities and threats of the aircraft were considered. The main strengths of the JAPA-12 were related to operation in harsh weather conditions, rapid target entry and sustainability. The main markets considered were remote communities, air ambulance services and possible aid to victims of natural disasters, as these markets are expected to grow significantly by over $ 6 billion in total. Across all these markets, a total of 120 aircraft are expected to be sold, which is likely to increase further as concluded from sales data of similar type aircraft.

The total costs of the aircraft were estimated to determine the return on investment. Based on historical data and relations stipulated by Roskam [5], it was estimated that the total design costs of the aircraft would come out at about €119 million. Accordingly, to adhere to a list price of €7.5 million a total of 108 aircraft will have to be sold to achieve a 15% profit margin per aircraft. The total number is however expected to be less when the implications of designing the family of aircraft are known. In the case of 108 aircraft sold, a return on investment of 18% is achieved.

**Sustainability assessment & compliance**

Throughout the design process sustainability was considered. To assess the sustainability a life cycle analysis was conducted. The first life cycle phase evaluated was the production phase. In this assessment not only the production of the aircraft was taken into account, but also the production of the fuel was looked at. As the fuel production process involved the capturing of carbon from the atmosphere, the carbon dioxide emission for the production of the fuel of -5.992 $kgCO_2$ per kg of fuel. After the production of the aircraft, the operations were examined. It was shown that the cruise phase of the flight is the most polluting, with the most belligerent factor being the $NO_x$ emissions. Compared to the Twin Otter the aircraft performs slightly worse, except for carbon dioxide emissions. This is caused by the aircraft being heavier than the Twin Otter, which increases fuel consumption. Since the Twin Otter uses regular kerosene, carbon dioxide is an emission and thus performs worse than the JAPA-12. Lastly, the recyclability of the aircraft was determined to be 90.1% for the end-of-life. The overall sustainability scoring of JAPA-12 compared to DHC-6 Twin Otter is included in Figure 1 from which was concluded that JAPA-12 is superior with respect to customer sustainability requirements.

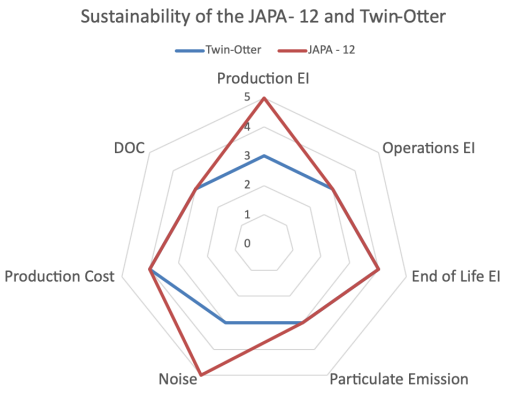


**Figure 1:** *Radar Diagram presenting the sustainability scores of the Twin Otter and JAPA-12.*

To make sure the aircraft complies with ICAO regulations for noise, a noise analysis was performed. This analysis took noise into account generated by the propellers, gas turbines, electric motors and airframe. This resulted in a noise level of the aircraft at the maximum power of 85.2 dBA, which is below the maximum allowed noise level of 88 dBA.

**Final design V&V**

In order to comply with the requirements set, verification and validation are crucial. Verification was done by inspection, demonstration, testing and analysis. Most requirements were verified using mathematical analysis as a result of the current stage design, however, this could only be applied to the technical requirements. A requirement compliance matrix was set up to display if all requirements were verified and which tests were used to do so. Only one requirement

was found to be partially complied with which is **REQ-STA-CUST-02**. Partial compliance has already been shown as the requirement requires the aircraft to be certifiable. This is implemented in the aircraft for example the climb gradient requirement, but to show full compliance with this requirement several subsystems have to be designed in more detail. Apart from the requirements stemming from CS-23 also the requirements from special condition CS E-19 have to be met because the propulsion system is a distributed propulsion system.

Validation of the JAPA-12 was split up into three parts. This was done to evaluate the accuracy of the model with respect to reality, to validate the design based on set requirements and to validate the aircraft based on certification requirements. Model errors were estimated which arose from the use of simplified models. For the sizing method of de Vries, it was shown that the model error regarding point performance is around 1%. As the team deviated slightly from the actual model, a contingency of 15% was implemented in the verification study after which it was deemed the model error in MTOW of JAPA-12 is similar to the original model which was equal to 4%. Therefore, the overall accuracy was deemed sufficient in the preliminary design as the relative errors found were 5% at most.

Design validation was found to be a more user-focused process when related to passenger comfort and safety. For this, a series of steps were implemented related to maintenance, flight crew procedures, training of flight crew and additional staff and finally listing of required flight equipment. Regarding the aircraft, proof of compliance can only be delivered analytically at this point, for which various validation tests were designed based on the relevant category. Structural testing starts from coupons and panels all the way up to full-scale testing, where static and fatigue tests shall be used to demonstrate the validity of calculations. Estimation of aerodynamic interactions require wind tunnel testing to validate obtained results. Initially, the wing and propeller interactions will be investigated and later a scaled aircraft model is manufactured. The obtained results shall be used for the optimisation of the design and models. Validation of flight performance requires flight tests up to dive speed, where items such as manoeuvrability, stability landing and others are evaluated. The noise levels shall be measured for compliance, as well as testing of avionics and flutter. Finally, as JAPA-12 was designed to operate in the Antarctic environment it must be tested in those conditions as well. For the family of aircraft, different temperatures must be tested in hot and elevated test sites. It is recommended to perform the tests for the antarctic missions on sites such as Iqaluit in Canada where the aircraft is subject to authentic conditions.

**Project design & development**

If it is decided to continue with the project, several items are to be designed in more detail. For example, the fuselage and propellers have to be revisited to optimise their performance. Apart from physical structures also the software used in the aircraft has to be written and tested. After the aircraft has been designed several small-scale models can be made to perform small-scale testing after which full-scale aircraft have to be made. These aircraft are used for static testing or flight testing and for certification of the aircraft. After which it can be produced and put into service.

Concluding, the aircraft will be capable of meeting the requirements set out by the customer after the final design, testing and certification phase. The most important aspects are summarized in Table 1 and a render of the aircraft is included in Figure 2. Thus fulfilling its purpose as a medical evacuation aircraft which can operate in antarctic conditions, and in addition fulfil general transportation missions.

**Figure 2:** *Render of JAPA-12.*

**Table 1:** *Summary of the main features of JAPA-12.*

| Parameter | Value and unit |
|---|---|
| MTOM | 6556 kg |
| Ferry range | 6220 km |
| Max payload | 1995 kg (19 pax) |
| Cruise speed | 107 m/s or 208 kts |
| Minimum take-off distance | 255 m |
| Mass percentage recyclable | 90.1% |

# Contents


**Preface** ii

**Executive Summary** iii

**Nomenclature** ix

**1 Introduction** 1

**2 Foundation of the Design Process** 2
- 2.1 Name and Goals . . . 2
- 2.2 Requirements . . . 2
- 2.3 Flying Conditions in Antarctica . . . 4
- 2.4 Sustainability Strategy . . . 5
- 2.5 Summary of Trade-Off . . . 7
- 2.6 Budgeting . . . 8
- 2.7 Technical Performance Measurement . . . 8
- 2.8 The Iterative Process . . . 10

**3 Preliminary Sizing** 11
- 3.1 Aerodynamic Model: Leading Edge Distributed Propulsion . . . 11
- 3.2 Powertrain Model . . . 13
- 3.3 Weight Fractions . . . 14
- 3.4 Point Performance . . . 15
- 3.5 Optimisation . . . 20
- 3.6 Sizing for Energy . . . 20

**4 Subsystem Design** 24
- 4.1 Fuselage Layout . . . 24
- 4.2 Wing Design . . . 29
- 4.3 Fuel System . . . 33
- 4.4 Propulsion . . . 34
- 4.5 Empennage . . . 38
- 4.6 Landing Gear . . . 44
- 4.7 Hydraulics . . . 46
- 4.8 Electrical . . . 47
- 4.9 HVAC and Pressurisation System . . . 48
- 4.10 Class II Weight . . . 51

**5 Operations & Logistics** 54
- 5.1 Refueling . . . 54
- 5.2 Anti-Icing . . . 54
- 5.3 Communication . . . 56
- 5.4 Navigation . . . 56
- 5.5 Visual Aid . . . 57
- 5.6 Software-Hardware Overview . . . 60

**6 Aircraft Performance** 61
- 6.1 Aerodynamic Analysis . . . 61
- 6.2 Stability & Control . . . 65
- 6.3 Payload-Range . . . 71
- 6.4 Flight Envelope . . . 71

**7 Structural Analysis** 75
- 7.1 Stress Analysis . . . 75
- 7.2 Materials . . . 81
- 7.3 Temperature Considerations . . . 84
- 7.4 Fatigue . . . 84
- 7.5 Vibration Analysis . . . 87

**8 Risk & Safety** 90
- 8.1 Risks . . . 90
- 8.2 RAMS . . . 92

**9 Financial Analysis** 96
- 9.1 Family of Aircraft . . . 96
- 9.2 Market Analysis . . . 96
- 9.3 Finances . . . 100

**10 Sustainability Assessment** 102
- 10.1 Life Cycle Analysis . . . 102
- 10.2 Noise . . . 105
- 10.3 Sustainability Assessment . . . 108

**11 Final Design V&V** 111
- 11.1 Design Verification Approach . . . 111
- 11.2 Flight Performance Verification . . . 111
- 11.3 Requirements Compliance Matrix . . . 112
- 11.4 Validation Approach . . . 114
- 11.5 Model Validation . . . 114
- 11.6 Sensitivity Analysis of Performance Parameters . . . 116
- 11.7 Design Validation . . . 117
- 11.8 Aircraft Validation . . . 117

**12 Project Design & Development** 119
- 12.1 Future Planning and Recommendations . . . 119
- 12.2 Project Logic Diagram and Gantt Chart . . . 120

**13 Final Design** 123

**Bibliography** 125

**A Appendix A** 129

# Nomenclature

## Acronyms & Abbreviations

| | | |
|---|---|---|
| AC | Alternating Current | - |
| ACARS | Aircraft Communications Addressing and Reporting System | - |
| ADF | Automatic Direction Finder | - |
| AEO | All Engines Operating | - |
| AMS | Air Mercy Service | - |
| ANS | Analysis | - |
| AR | Aspect ratio | - |
| ATC | Air-traffic control | - |
| c.g. | Center of gravity | |
| CFD | Computational Fluid Dynamics | - |
| CFRP | Carbon Fiber-Reinforced Polymer | - |
| CLmax | Aircraft maximum lift coefficient | - |
| CMU | Communication Management Unit | - |
| CS | Certification Specifications | - |
| CTE | Coefficient of thermal expansion | $K^{-1}$ |
| DC | Direct Current | - |
| DEM | Demonstration | - |
| DEP | Distributed Electric Propulsion | - |
| DME | Distance Measuring Equipment | - |
| DOC | Direct Operating Cost | - |
| DP | Distributed Propulsion | - |
| EAA | European Air Ambulance | - |
| EASA | European Union Aviation Safety Agency | - |
| EI | Environmental Impact | - |
| EM | Electric Motor | - |
| FAC | Factor | - |
| FEM | Finite Element Method | - |
| GA | General Aviation | - |
| GFRP | Glass Fiber-Reinforced Polymer | - |
| GHG | GreenHouse Gas | - |
| GLARE | GLAss REinforced aluminium | - |
| GPS | Global Position System | - |
| GVT | Ground vibration tests | - |
| HEPA | High Efficiency Particulate Air | - |
| HF | High Frequency | - |
| HFDL | High Frequency Data Link | - |
| HVAC | Heating, Ventilation and Air Conditioning | - |
| ICAO | International Civil Aviation Organisation | - |
| INS | Inspection | - |
| IOC | Indirect Operating Cost | - |
| LCA | Life Cycle Assessment | - |
| LE | Leading Edge | |
| LEDP | Leading Edge Distributed Propulsion | - |
| LEMAC | Leading Edge Mean Aerodynamic Chord | |
| LNG | Landing | - |
| LOUT | Lowest Operational Use Temperature | - |
| LTO | Lift and Take-Off | - |
| MAC | Mean Aerodynamic Chord | m |
| Medevac | Medical evacuation | |
| MLG | Main Landing Gear | |
| MMC | Metal Matrix Composite | - |
| MNS | Mission Need Statement | - |
| MSL | Mean Sea Level | - |
| MTOM | Maximum Take-Off Mass | kg |
| MTOW | Maximum Take-Off Weight | N |
| NDB | Non-Directional Beacon | - |
| NLG | Nose Landing Gear | |
| OEI | One Engine Inoperative | - |
| OEW | Operational Empty Weight | N |
| Pax | Passengers | - |
| PKM | Passenger-KiloMeter | - |
| PMAD | Power Management And Distribution | - |
| POH | Pilot Operating Handbook | - |
| POS | Project Objective Statement | - |
| RAMS | Reliability, Availability, Maintenance & Safety | - |
| RASS | Remote Air Services Subsidy | - |
| REQ | Requirement | - |
| RIVM | RijksInstituut voor Volksgezondheid en Milieuhygiëne | - |
| RNAV | aRea NAVigation | - |
| ROC | Rate Of Climb | - |
| ROI | Return On Investment | - |
| SAF | Sustainable Aviation Fuel | - |
| SC | Special Condition | - |
| SCC | Stress Corrosion Cracking | - |

| | | |
|---|---|---|
| SP | Specific Power | - |
| SPL | Sound Pressure Level | dB |
| STOL | Short Take-Off and Landing | - |
| SVS | Synthetic Vision System | - |
| SWOT | Strengths, Weaknesses, Opportunities & Threats | - |
| T-O | Take-Off | - |
| TAB | Technical Advisory Board | - |
| TE | Trailing Edge | |
| TES | Test | - |
| TPM | Technical Performance Management | - |
| TRL | Technology Readiness Level | - |
| TSO | Technical Standard Orders | - |
| TYS | Tensile yield stress | MPa |
| UHF | Ultra High Frequency | - |
| USS | Ultimate Shear Strength | - |
| UTS | Ultimate Tensile Stress | Pa |
| VHF | Very High Frequency | - |
| VOR | VHF omni-directional Range station | - |
| Wcrew | Crew weight | N |
| We | Empty weight | N |
| Wf | Fuel weight | N |
| WIG | Wing In Ground-effect | |
| Wtfo | Trapped fuel and oil weight | N |
| Wto | Take-off weight | N |
| ZVGVS | Zero-Visibility Ground Visual System | - |

## Physics Constants

| | | |
|---|---|---|
| $\rho_0$ | Standard density | 1.225 kg m$^{-3}$ |
| $g_0$ | Gravitational acceleration | 9.80665 m s$^{-1}$ |

| | | |
|---|---|---|
| $\mu_g$ | Aeroplane mass ratio | - |
| $\rho$ | Density | kg m$^{-3}$ |
| $\alpha$ | Angle of attack | ° |
| $\bar{C}$ | Mean geometric chord | m |
| $\beta$ | Sectional lift coefficient | - |
| $\beta$ | Sideslip angle | rad |
| $\chi$ | Thrust delivered by distributed propulsors / thrust delivered by primary propulsors | - |
| $\delta r$ | Rudder deflection angle | rad |
| $\delta_a$ | Aileron deflection | ° |
| $\delta_e$ | Elevator deflection angle | rad |
| $\delta_y$ | Lateral separation factor | - |
| $\epsilon$ | Downwash angle | rad |
| $\eta$ | Efficiency | - |
| $\eta$ | Vertical tail efficiency | - |
| $\frac{d\epsilon}{d\alpha}$ | Downwash gradient | - |
| $\Gamma$ | Dihedral angle | ° |
| $\Lambda$ | Sweep angle | ° |
| $\lambda$ | Taper ratio | - |
| $\mu$ | Ground friction constant | - |
| $\mu$ | Relative density | - |
| $\Omega$ | Rotational speed | rad/s |
| $\omega$ | Circular frequency | Hz |
| $\omega$ | Rotational speed | rad/s |
| $\Phi$ | Supplied power ratio | - |
| $\Psi$ | Tip-over angle | rad |
| $\sigma$ | Bending stress | Pa |
| $\sigma$ | Density ratio | - |
| $\sigma$ | Relative uncertainty | - |
| $\sigma$ | Stress | Pa |
| $\tau$ | Rudder efficiency | - |
| $\tau$ | Shear stress | Pa |
| $\varphi$ | Shaft power ratio | - |
| $\xi$ | Throttle | - |
| $b$ | Wing span | m |
| $C_D$ | Drag coefficient of the 3D wing | - |
| $C_d$ | Drag coefficient of the 2D wing | - |
| $c_f$ | Flap length | $m$ |
| $C_L$ | Lift coefficient of the 3D wing | - |
| $C_l$ | Lift coefficient of the 2D wing | - |
| $C_l$ | Rolling moment coefficient | - |
| $C_m$ | Moment coefficient | - |
| $C_m$ | Pitching moment coefficient | - |
| $C_n$ | Yawing coefficient | - |
| $C_n$ | Yawing moment coefficient | - |
| $C_{L_\alpha}$ | Wing lift curve slope | rad$^{-1}$ |
| $C_{m_\alpha}$ | Change in moment coefficient with respect to the angle of attack | - |
| $C_{N_g}$ | Load factor | - |
| $D$ | Drag force | N |

| | | |
|---|---|---|
| $d$ | Distance | m |
| $D_p$ | Propeller diameter | m |
| $e$ | Oswald efficiency factor | - |
| $h_c$ | convective heat transfer coefficient | - |
| $K_f$ | Fuselage weight configuration factor | - |
| $k_g$ | Gust alleviation factor | - |
| $K_{np}$ | Correction factor for increasing number of blades | - |
| $L$ | Lift force | N |
| $l_h$ | Distance between ac horizontal tail and ac wingm | |
| $M$ | Mach number | - |
| $n_s$ | Number of wheels | - |
| $P_m$ | Load per wheel | N |
| $R_{wf}$ | Wing-fuselage interaction | $m^2$ |
| $S$ | Wing surface area | $m^2$ |
| $T_w$ | Time needed to complete mission | hr |
| $u$ | Gust velocity | $m\ s^{-1}$ |
| $u_{de}$ | Derived gust velocity | $m\ s^{-1}$ |
| $V$ | Velocity | $m\ s^{-1}$ |
| $W$ | Weight | N |
| $W_t$ | Touch down rate | ft/s |
| $x_n$ | Neutral point | m |
| $x_p$ | Upstream distance of actuator disk | m |
| A | Area | $m^2$ |
| a | Axial induction factor | - |
| B | Number of blades | - |
| c | Engine dependant coefficient | - |
| d | Diameter | m |
| E | Energy | J |
| e | Specific energy | J/kg |
| F | Fuel | - |
| f | Frequency | Hz |
| h | Height | m |
| I | Moment of intertia | $m^4$ |
| i | Installation angle | rad |
| K | Non-dimensional radius of gyration | - |
| k | Coefficient of thermal conductivity | - |
| k | Reduced frequency | Hz |
| l | Length | m |
| M | Internal moment | Nm |
| N | Number of distributed propulsors | - |
| n | Load factor | - |
| n | Propeller rotation speed | rad/s |
| P | Power | W |
| p | Pressure | Pa |
| Q | First moment of area | $m^3$ |
| R | Radius | m |
| R | Range | m |
| R | Ratio of the minimum and maximum loads | - |
| r | Radius | m |
| rpm | Rotations per minute | - |
| S | Surface area | $m^2$ |
| s | Distance | m |
| T | Thrust | N |
| t | Thickness | m |
| V | Internal shear force | N |
| w | Width | m |
| y | Distance from neutral axis | m |

## Subscripts

| | |
|---|---|
| $\alpha$ | Derived with respect to the angle of attack |
| 0 | Initial, steady flight |
| 0 | Zero lift |
| a | Amplitude |
| ac | Aerodynamic center |
| b | Asymmetric motions |
| bat | Battery |
| C | Cruise |
| c | Ceiling |
| c | Coefficient |
| c | Symmetric motions |
| cr | Critical |
| D | Dive |
| dp | Distributed propulsion |
| e | Electrical |
| e | Endurance |
| eff | Effective |
| EM | Electrical Machine |
| f | Flutter |
| f | Fuel |

| | |
|---|---|
| fsl | Fuselage |
| GB | GearBox |
| GEN | GENerator |
| GR | Ground Roll |
| GT | Gas Turbine |
| h | Horizontal tail |
| i | Lift induced |
| Inv | Inverters |
| LOF | Lift-OFf |
| m | Mean |
| n | Natural |
| nc | Nosecone |
| OE | Operative Empty |
| p | Derived with respect to the roll rate |
| p | Pressure |
| p | Propeller |
| p | Propulsive |
| p1 | Primary propulsors |
| p2 | Secondary propulsors |
| pax | Passenger amount |
| PL | PayLoad |
| PMAD | Power Management And Distribution |
| q | Derived with respect to the pitch rate |
| r | Derived with respect to the yaw rate |
| r | Wing root |
| Rec | Rectifiers |
| rms | Root mean square |
| s | Shaft |
| s | Shock absorber |
| s | Stall |
| SA | Seats Abreast |
| t | Wing tip |
| t | tire |
| tc | Tailcone |
| TO | Take-off |
| u | Ultimate |
| u | Unblown |
| v | Vertical tail |
| w | Wing |
| X | About the X-axis |
| Y | About the Y-axis |
| y | Vertical |
| Z | About the Z-axis |

# 1 Introduction

”Antarctica is home to a host of research bases, of which the most remote is the Amundsen-Scott South Pole research base. During the polar winter, there are no flights to Amundsen-Scott due to the extreme weather conditions. In the 65 years that the research base has been active, workers have been evacuated in winter due to medical emergencies on three occasions. The preparation time required for these missions with current technology has meant people with serious medical needs had to wait for help for weeks. It is, therefore, important to create a solution with modern technology to facilitate quick medical evacuation of people from the South Pole.” [1]

This report presents the preliminary design of a sustainable medical evacuation aircraft, capable of withstanding the harsh conditions of Antarctic winter. The conceptual design of the previous report was designed into more depth [1]. The subsystems have been sized in more detail, the flight performance has been evaluated and considered more accurately and the operational and logistical challenges have been faced. Furthermore, the design was analysed on sustainability and the risks were identified, to ensure a sustainable and safe medical evacuation aircraft.

The detailed design phase was started with the foundation of the design process, which is laid out in Chapter 2. Secondly, the preliminary sizing process will be explained in Chapter 3. In Chapter 4 the process of sizing internal and external layout of the aircraft is set up. Furthermore, the operations and logistics are covered in Chapter 5 and the aircraft performance is assessed in Chapter 6. Chapter 7 explains the structural analyses performed on the set up design. The risks are identified and analysed, together with an initial safety estimation in Chapter 8. Chapter 9 shows the financial analysis of the preliminary design. Following this, Chapter 10 reflects on the earlier set up sustainability strategy. The verification and validation of the design is presented in Chapter 11. This chapter also shows the compliance of the design with the requirements. Future planning and project development are discussed in Chapter 12. Lastly, the final design is concluded in Chapter 13.

# 2

# Foundation of the Design Process

In this chapter, a description of the mission and the steps taken during the first phases are presented to give the reader an impression of the environment and the mission. First, the name and goals of the design are presented in Section 2.1. The requirements which have driven the design process as well as the top-level subsystem requirements are presented in Section 2.2. Then, general flying conditions in Antarctica are covered in Section 2.3. Next, a sustainability plan is set up in Section 2.4. The summary of the performed trade-off and the description of the final concept are presented in Section 2.5. In Section 2.6 the resources are allocated and a budget breakdown is performed. This is followed by the technical performance measurement strategy in Section 2.7. Finally, in Section 2.8, an overview of the iteration process performed, in the final stages of design up to this point, is provided to the reader.

## 2.1. Name and Goals

The name of the aircraft subject to this report is JAPA-12. JAPA is short for Jolly Antarctic Propeller Aircraft and the 12 follows from the twelve propellers the aircraft has. With this name the most special features of the design are covered: it is mainly designed for the Antarctic environment and uses distributed propulsion.
The main goals and objectives of the project are stated in the form of a mission need statement (MNS) and project objective statement (POS). The MNS and the POS are given below.

**MNS: Design an aircraft that can successfully conduct a medical evacuation under extreme Antarctic weather conditions at the Amundsen-Scott base and, possibly, serve other remote communities and roles.**

**POS: Obtain a better understanding of the full design cycle of a system and gain knowledge on designing an aircraft by producing a design that fulfills the mission need statement together with a group of 10 capable aspiring engineers in 10 weeks.**

## 2.2. Requirements

This section shows the overview of the most important requirements for the design of the JAPA-12. Together with the MNS and POS, the stakeholder requirements and the key and driving requirements, will define the design of the aircraft. The stakeholder requirements are presented in Table 2.1. The key and driving requirements are shown in Table 2.2 and were taken from previous reports in this series [6] [1].

**Table 2.1:** *Stakeholder requirements.*

| Identifier | Description |
|---|---|
| **[REQ-STA-CUST-01]** | The system shall have a list price below 7.5 million euro, while making a profit. |
| **[REQ-STA-CUST-02]** | The system shall be certifiable. |
| **[REQ-STA-CUST-03]** | The system shall perform within Antarctic weather conditions, being able to perform the mission, from notification up until landing again at Rothera, with a 95% probability in a given 7-day window. |
| **[REQ-STA-CUST-04]** | The system shall be brought into service before 2030. |
| **[REQ-STA-CUST-05.1]** | The system shall have a structure of which 90% of the mass is recyclable. |
| **[REQ-STA-CUST-05.2]** | The system shall have a propulsion system with net zero carbon dioxide emissions in the operational phase. |
| **[REQ-STA-CUST-06]** | The system shall have a service ceiling of 25000 ft. |
| **[REQ-STA-CUST-07]** | The system shall have a range of 100 nm with a payload of 4000 lbs. |
| **[REQ-STA-CUST-08]** | The system shall have a range of 400 nm with a payload of 3000 lbs. |
| **[REQ-STA-CUST-09]** | The system shall have a cruise speed of 200 kts. |
| **[REQ-STA-TAP-01.1]** | The system shall land on a snow runway of 6000 ft. |
| **[REQ-STA-TAP-01.2]** | The system shall land on a gravel runway of 2500 ft. |
| **[REQ-STA-TAP-01.4]** | The system shall endure a range of 1350 nm with one medevac payload. |
| **[REQ-STA-PAS-01]** | The system shall allow for easy loading of a patient on a stretcher. |
| **[REQ-STA-MAR-01]** | The structure shall withstand loading from landing with conventional landing gear and skis. |
| **[REQ-STA-MAR-02]** | The system shall accommodate for changing to a configuration which allows for the transport of 19 passengers over a range of 150 nm. |

| Continuation of Table 2.1. | |
|---|---|
| **Identifier** | **Description** |
| **[REQ-STA-MAR-03]** | The system shall accommodate for changing to a configuration which allows for the transport of 3200 lbs of cargo over a range of 150 nm. |
| **[REQ-STA-MAR-04]** | The system shall accommodate for changing to a configuration which allows for performing airdrops. |
| **[REQ-STA-MAR-05]** | The aircraft shall be able to provide sufficient lift in all flight phases in environments with temperatures up to 40°C. |
| **[REQ-STA-MAR-06]** | The aircraft shall be able to provide sufficient thrust to take off on a gravel runway of 2500ft in environments with temperatures up to 40°C. |
| **[REQ-STA-MAR-07]** | The aircraft shall be able to take-off and land at an altitude of 2835 meters. |

**Table 2.2:** *Key and driving requirements.*

| **Identifier** | **Description** | **Key or driving** |
|---|---|---|
| **[REQ-STA-CUST-01]** | The system shall have a list price below 7.5 million euro, while making a profit. | Key |
| **[REQ-STA-CUST-02]** | The system shall be certifiable. | Key |
| **[REQ-STA-CUST-03]** | The system shall perform within Antarctic weather conditions, being able to perform the mission, from notification until landing again at Rothera, with a 95% probability in a given 7-day window. | Key |
| **[REQ-STA-CUST-04]** | The system shall be brought into service before 2030. | Key |
| **[REQ-STA-CUST-05.1]** | The system shall have a structure of which 90% of the mass is recyclable. | Key |
| **[REQ-STA-CUST-05.2]** | The system shall have a carbon neutral propulsion system. | Key |
| **[REQ-STA-TAP-01]** | The system shall comply with target airport constraints. | Driving |
| **[REQ-STA-TAP-01.3]** | The system shall endure a range of 1350 nm with one medevac payload. | Driving |
| **[REQ-STA-MAR-07]** | The aircraft shall be able to take-off and land at an altitude of 2835 meter. | Driving |
| **[REQ-SYS-FUNC-01.1]** | The system shall provide 11 kWh of energy to medical equipment over a mission duration of 24 hours. | Driving |
| **[REQ-SYS-FUNC-08.2]** | The system shall provide 1240 kW of power in take-off/go-around conditions. | Driving |
| **[REQ-SYS-FUNC-10]** | The system shall provide passenger and crew accommodation. | Driving |
| **[REQ-ENV-04]** | The system shall allow for stability at a wind gust velocity of 53.24 kts. | Driving |
| **[REQ-ENV-05]** | The system shall allow for controllability at a wind gust velocity of 53.24 kts. | Driving |
| **[REQ-ENV-07]** | The system shall be operational at -76°C. | Driving |
| **[REQ-ENV-09]** | The system shall land in cross winds of 53.24 kts at an angle of 90°. | Driving |

Subsystem requirements result from the entire aircraft life-cycle. In Chapter 4, the subsystems are designed according to those requirements. The entire life cycle consists out of five general phases: design, manufacturing, certification, operation and end-of-life.

The driving phases consist of manufacturing, operation and end-of-life, as the basic outline for design and certification phases are not aircraft specific. Aircraft in the same class are roughly designed and certified with similar methods, whereas the other phases are determined by the design choices and customer requirements. The design requirements leading from the aircraft functions have been determined in and taken from previous reports in this series [6] [1]. In Table 2.3, the top-level subsystem requirements are included. In Chapter 11, a more detailed requirements list is included where the designed aircraft was checked for compliance with the said requirements.

**Table 2.3:** *Top-level system functional and constraint requirements.*

| **Identifier** | **Description** |
|---|---|
| **[REQ-SYS-FUNC-01]** | The system shall provide power to all subsystems. |
| **[REQ-SYS-FUNC-02]** | The system shall provide communications. |
| **[REQ-SYS-FUNC-03]** | The system shall provide guidance and navigation. |
| **[REQ-SYS-FUNC-04]** | The system shall provide situational awareness in whiteout conditions. |

| Continuation of Table 2.3 | |
|---|---|
| **Identifier** | **Description** |
| **[REQ-SYS-FUNC-05]** | The system shall provide aerodynamic performance. |
| **[REQ-SYS-FUNC-06]** | The system shall provide structural integrity for a load factor of 9. |
| **[REQ-SYS-FUNC-07]** | The system shall provide environmental control. |
| **[REQ-SYS-FUNC-08]** | The system shall provide 6.9 kN of thrust in one engine inoperative conditions. |
| **[REQ-SYS-FUNC-10]** | The system shall provide passenger and crew accommodation. |
| **[REQ-SYS-FUNC-11]** | The system shall be manoeuvrable on the ground. |
| **[REQ-SYS-FUNC-12]** | The system shall take-off safely. |
| **[REQ-SYS-FUNC-13]** | The system shall perform ground operations. |
| **[REQ-SYS-FUNC-14]** | The system shall produce sufficient braking power. |

## 2.3. Flying Conditions in Antarctica

Antarctica's weather is one of the most demanding and challenging on this planet. Such extreme weather conditions are usually not specifically designed for. However, in the development of JAPA-12, they were taken into account as much as possible. For the flights over the Antarctic continent, the most relevant weather conditions are the strength of wind and temperatures.

Antarctica has the most persistent low temperatures throughout the year registered on Earth. An important role in the formation of the Antarctic climate is played by the ice covering the continental mainland which is the greatest source of cold air. On the inland parts of the continent, the weather is mostly clear and sunny, yet, the temperatures are extremely low and reach -87.4°C. At the Amundsen-Scott station, in particular, the average temperature is -49.5 °C and the absolute lowest recorded value was -82.8 °C [7]. The temperature differences encountered by aircraft in polar flights are of the tens degrees Celsius. This introduces problems for aircraft, as follows from polar pilots: "We encountered temperature differences of 40-50 degrees. At the take-off, the aircraft is brand new. Then at landing, due to compression-expansion, everything is loose - cables are loose, elevators are dangling and controllability is very low." [8].

For many Antarctic regions strong and frequent winds are very common. The antarctic wind is called katabatic or downslope wind, which is formed due to low antarctic temperatures and the mountain-like shape of the continent. Due to its downslope nature, recurrent winds and snow storms of extreme destructive nature are especially common near the coastal line. These winds can reach 30-50 m/s and wind gusts can reach 90 m/s. The Rothera station, where the airplane should be able to take-off and land, is located on the coastal line which comes with katabatic winds averaging out at 6.55 m/s with a maximum hourly average of 26 m/s. On the contrary, the Amundsen-Scott station itself is located on the middle of the Antarctic plateau, and experiences relatively mild winds, averaging out at 5.66 m/s in the east-western direction with a maximum wind recorded of 24.69 m/s. Furthermore, a climatology study conducted over the period from 2006 to 2015 suggests that the Antarctic region is a harbour for high vertical wind shear [9]. Vertical shear poses a danger of losing controllability at landing or take-off leading to accidents. In 1979, the Il-14 aircraft, shown in Figure 2.1, was following a route from Molodezhnaya station to station Mirnyi when it suffered a sudden wind shear at low altitude during the take-off and lost controllability leading to a crash [8].

**Figure 2.1:** *Archive photo of Il-14 Antarctic crash at Molodezhnaya station, 1979 [8].*

The majority of polar aircraft incidents can be attributed to weather conditions such as whiteouts and strong winds. Additionally, a large portion of accidents was directly or partially caused by landing gear failure at landing. This could also be perhaps in part connected to the strong cross-winds and hardships to maintain directional control during landings.

Another reason for accidents is the pilot's inability to accurately determine the vertical position of the aircraft due to the Antarctic environment. According to Ignatov, the radar altimeter measurements can be rather inaccurate due to the differences in snow density. In one place the signal is reflected from the surface and in another one from deep ice leading to errors [8]. To summarize, the following factors leading to poor operation and accidents in Antarctica were identified based on research of its air safety profile[1].

- **[FAC.1]** - Difference in temperature could lead to a quick material and subsystem deterioration.
- **[FAC.2]** - Strong winds and gusts could lead to accidents during landing.
- **[FAC.3]** - Unforeseen wind shear could lead to a loss of control and accidents.
- **[FAC.4]** - Incorrect radar altimeter measurements could lead to accidents during landing.

## 2.4. Sustainability Strategy

This section highlights how sustainability is considered throughout the design of the chosen concept. Firstly, the product life cycle is broken-down to reveal all factors relevant towards sustainability in Subsection 2.4.1. Next, the approach and the implications on the requirements are presented in Subsection 2.4.2. Finally, in Subsection 2.4.3 the methodology to assess and monitor sustainability throughout the design process are elucidated.

### 2.4.1. Sustainability Breakdown

For the purpose of this report, sustainability of a product was defined as follows: *a perfectly sustainable product is cradle to cradle certified*. According to Springer Link's Encyclopedia [10] the implications of cradle to cradle certification is that the design and production of the product is such that at the end of life it may be truly recycled. All the components of a product feed another product, become fuel, or biodegrade. Materials stay in a closed loop cycle, continually circulating as valuable nutrients or parts for the industry.

While this is currently unobtainable in the aerospace industry, it serves as idealistic goal to reach towards. In addition, cradle to cradle standards function as the benchmark with which the product was evaluated. To aid the assessment of sustainability, the product life cycle was broken down into all elements relevant for sustainability in Figure 2.2. Three fundamental dimensions were identified: economic, ecological and social. The sustainability was assessed based on the performance with respect to each fundamental dimension.

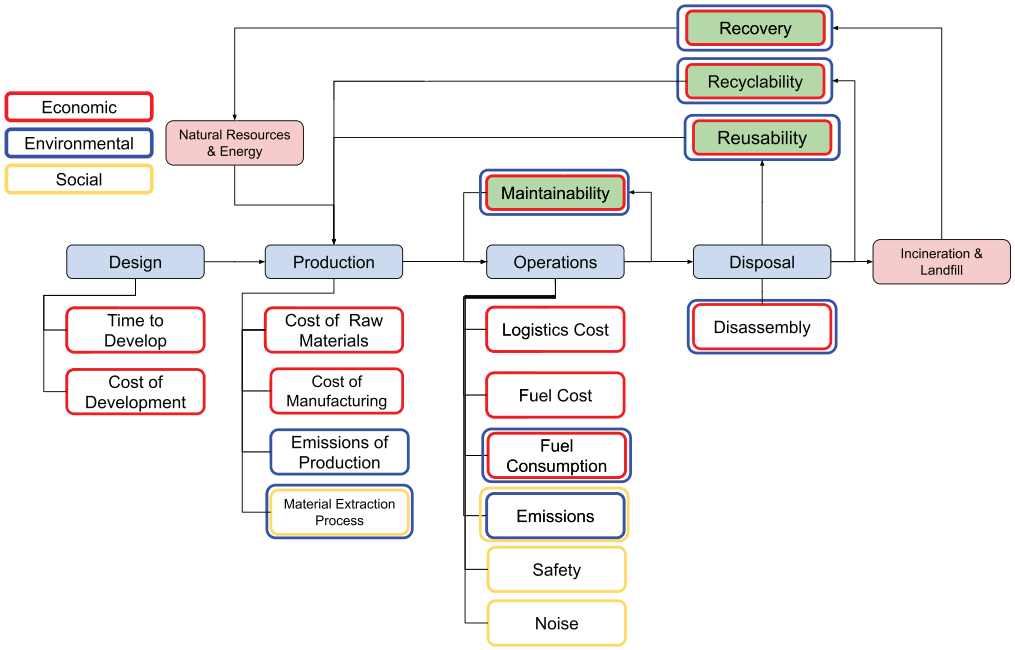


**Figure 2.2:** *Product life cycle broken-down into elements relevant for sustainability.*

[1]Database for aircraft failures on Antarctica, https://aviation-safety.net/database/dblist.php?Country=ant, date accessed = 07-06-2022

### 2.4.2. Green Engineering Approach

This subsection describes the approach to sustainability used throughout the design process. Cornerstone to the approach are the principles of green engineering. The green engineering principles set by the American Chemical Society emphasise creating a product that is benign to human health and the environment, while remaining financially enticing. Through systematically referring to the principles, the design moves beyond baseline quality assurance and safety requirements to satisfy the three sustainability dimensions [11]. The most important principles that are relevant for the design process are summarised below.

**GE-P-1:** Designers need to strive to ensure that all material and energy inputs and outputs are as inherently nonhazardous as possible.
**GE-P-2:** Embedded entropy and complexity must be viewed as an investment when making design choices on recycle, re-use, or beneficial disposition.
**GE-P-3:** Targeted durability, not immortality, should be a design goal.
**GE-P-4:** Products, processes, and systems should be designed for performance in a commercial “afterlife”.
**GE-P-5:** Material and energy inputs should be renewable rather than depleting.

Additional requirements were formulated based on the principles of green engineering to ensure sustainability is considered throughout the product life cycle. The customer specified requirements **REQ-STA-CUST-05.1** and **REQ-STA-CUST-05.2** describing respectively a 90% recyclable system and a system with a climate neutral propulsion system, stem from the need for sustainability. Therefore, one could say that, for this design project, a sustainable status is considered to be obtained when these requirements have been met. These requirements may be satisfied, however, sustainability must be approached holistically. If, for example, in order to satisfy **REQ-STA-CUST-05.1**, a destructive production process is required, the impact on sustainability is shifted to another phase of the product life cycle. The additional requirements and the relevant principles of green engineering used are summarized in Table 2.4.

**Table 2.4:** *Sustainability requirements.*

| **Parent Identifier** | **Description** | **Principle** |
|---|---|---|
| **[REQ-STA-CUST-05.1]** | The system shall have a structure of which 90% of the mass is recyclable. | N/A |
| **[REQ-STA-CUST-05.2]** | The system shall have a propulsion system with net zero carbon dioxide emissions in the operational phase. | N/A |
| **Child Identifier** | **Description** | **Principle** |
| **[REQ-SYS-SUS-1.1]** | The fuselage structure shall be less than 27.1% waste at end of life. | **GE-P-2, 4, & 5** |
| **[REQ-SYS-SUS-1.2]** | The landing gear structure shall be less than 5% waste at end of life. | **GE-P-2, 4, & 5** |
| **[REQ-SYS-SUS-1.3]** | The propulsion system shall be less than 11% waste at end of life. | **GE-P-2, 4, & 5** |
| **[REQ-SYS-SUS-1.4]** | The empennage structure shall be made from 100% recyclable materials | **GE-P-2, 4, & 5** |
| **[REQ-SYS-SUS-1.5]** | The wing structure shall be made from 100% recyclable materials | **GE-P-2, 4, & 5** |
| **[REQ-SYS-SUS-1.6]** | The fixed equipment shall be less than 10% waste at end of life. | **GE-P-2, 4, & 5** |
| **[REQ-SYS-SUS-2.1]** | The production process of the fuel shall have at least 3.15kg$CO_2$ capture per kilo of fuel produced. | **GE-P-1 & 5** |
| **[REQ-SYS-SUS-2.2]** | The emissions of the propulsion system shall be less than 3.15kg $CO_2$ per kilo of fuel burned. | **GE-P-1 & 5** |
| **Miscellaneous sustainability requirements** | | |
| **Identifier** | **Description** | **Principle** |
| **[REQ-SYS-SUS-3.1]** | The system shall be produced from materials that may be disposed or stored without damaging the environment. | **GE-P-1** |
| **[REQ-SYS-SUS-3.2]** | The system shall have an operational life time of at least 20 years. | **GE-P-3** |
| **[REQ-SYS-SUS-3.3]** | The system shall have a method to safely dispose of medical waste. | **GE-P-1, 4** |

### 2.4.3. Assessment

This subsection describes the tools that were used throughout the design process to integrate and evaluate sustainability. The sustainability was carefully monitored to ensure the requirements were met. In addition, new requirements were formulated based on the results of the assessment.

**Life Cycle Assessment:**
A life cycle assessment (LCA) based on the methodology of the Aircraft Design and Systems Group at Hamburg University of Applied Sciences was used [12]. The LCA performed quantified the environmental impact of the design.

Therefore, it verified that the sustainability requirements were met or indicated that the design had to be adjusted. In addition, insight was given to the critical life cycle phases and design parameters.

**Parts Material Breakdown:**
To aid the LCA a parts material breakdown was done for each major sub-system. A percentage mass of a material a sub-system consists of was given. The materials were assessed for their recyclability, price and performance.

**Radar Diagram:**
Finally, to communicate the sustainability performance to the reader a radar diagram is used. Criteria were created to quantify the performance of the product with respect to the three fundamental dimensions of sustainability. A value out of five was assigned to each criterion. If the product scored a five in every category it was said to meet the cradle to cradle certification standards. Firstly, for environmental sustainability, the product was scored based on the environmental impact during production, operations and end of life. For economic sustainability, the product was scored based on production cost and direct operating cost. Finally, for social sustainability, the product was scored based on noise and particulate emissions. The DHC-6 Twin-otter has also been scored and served as a baseline for comparison.

## 2.5. Summary of Trade-Off

During the conceptual phase, three concepts were selected and conceptual sizing was performed. Once all concepts were designed in more detail, they were subjected to a trade-off process. The inputs were a high wing aircraft with a distributed propulsion design, a twin boom aircraft and lastly a wing in ground effect aircraft. The process featured a set of pre-determined trade-off criteria to which weights were allocated. It was determined that the most important criteria for this mission and the ones used during this process were flight performance, adaptability, sustainability and TRL. The according sub-criteria and allocated weights are displayed in Figure 2.3.

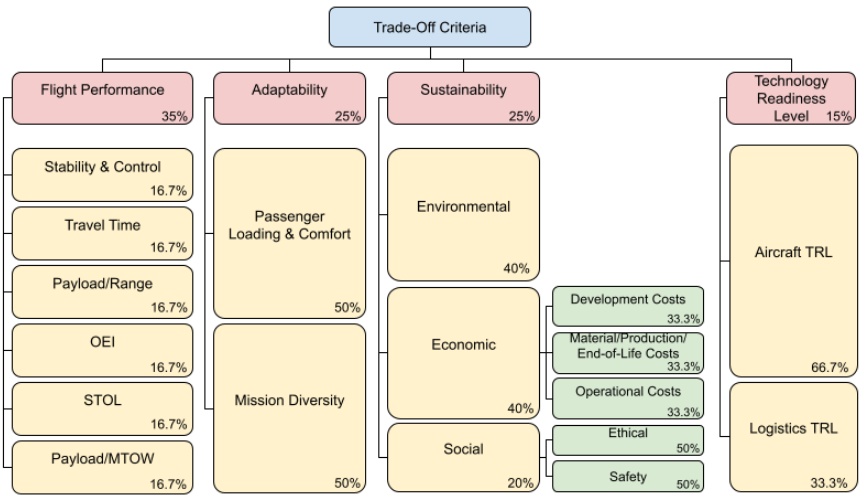


**Figure 2.3:** *Trade-off criteria and sub-criteria [1].*

Flight performance was considered to be the most important criterion as this represents the ability of the design concept to accomplish useful tasks within the harsh operating environment. The adaptability of the design refers to the ability of it being able to perform the mission according to requirements set by the customer and following from the market analysis, as well as it being enticing for potential costumers. Sustainability was also considered in the trade-off as requirements regarding this topic were selected as key requirements to the primary customer. Also, with the current world trend which demands new designs to be more sustainable, this topic was deemed as one making the design more appealing for a wider variety of markets. The last criterion is the TRL which will reflect the feasibility of the design being ready by 2030 both when it comes to subsystems and the ground systems and logistics.

After setting the trade-off criteria, the design options were scored. A score of 1 to 5 was given to each design option for each sub-criterion, with 1 representing a minimum performance and 5 representing excellent performance. The trade-off showed that the distributed propulsion design was the best closely followed by the twin boom. A sensitivity analysis was performed to identify how sensitive the outcome of the trade-off was to changes in scores or weights. It was shown that distributed propulsion wins most of the times and that it might be advantageous to look into the twin boom concept when it comes to sustainability and adaptability.

It turned out the distributed propulsion aircraft is the most suitable design for performing the mission based on the trade-off criteria. It was as first estimate chosen that the aircraft would feature a high wing with conventional tail configuration for improved passenger loading and lower structural weight. The most noticeable design feature is the addition of multiple propellers on the wing, which improves controllability, aerodynamic efficiency and STOL characteristics of the aircraft. It was first determined to include batteries as energy source besides only fuel, however, after careful consideration the team determined to first analyse the possibility of using only a partial turbo-electric propulsion system as this would decrease complexity and thereby associated costs.

## 2.6. Budgeting

A first estimate of the technical and financial budgets was already performed in the baseline report of this series [6]. Below, the team provides the reader with a re-evaluated version to inform the reader to which estimates had been designed regarding financial, mass and electrical parameters.

### 2.6.1. Monetary Budget

According to **[REQ-STA-CUST-01]**, the system shall have a list price of €7.5 million and should still be profitable. It was determined that a profit margin of 15% will be adhered to, such that the total costs before listing the aircraft will not exceed €6.375 million. Out of this total budget, €1.275 million is reserved for the design of the aircraft and €5.1 million is reserved for manufacturing and certification. These budgets are however a rough estimation, if it is determined that resources should be re-allocated it is allowed. Yet, the total costs may not exceed the aforementioned value.

### 2.6.2. Mass Budget

A mass budget had been established in the baseline report [6]. Where, based on the Maximum Take-Off Weight (MTOW) from CS-23 requirements, maximum allowable weights had been set based on statistical data provided by Roskam [13]. Below in Table 2.5, weights of subsystem as percentage of MTOW from CS-23 are displayed for easier analysis of design iterations. The MTOW is set to be 84513 N.

**Table 2.5:** *Mass budget.*

| Component | Mass [%] | Component | Mass [%] |
|---|---|---|---|
| OEW | 63.1 | Nacelle | 3.2 |
| Power plant | 22.0 | Landing gear | 4.9 |
| Wing group | 9.5 | Fixed equipment | 13.3 |
| Empennage | 2.3 | Within fixed equipment: EPS | 20.3 |
| Fuselage | 8.0 | Maximum fuel + payload | 36.9 |

Note that these percentages have not been used as maximum values for the design, but more as indication. The team was convinced that the distributed propulsion aircraft would operate at a lower MTOW, therefore more margin was allocated to subsystems where the DP aircraft differs from conventional designs. Due to design featuring a novel propulsion system, more weight was expected for the power plant group as well as for fixed equipment.

### 2.6.3. Electrical Power Budget

Initially, the onboard energy was estimated to require about 27kWh. About 16kWh was estimated to be required for onboard flight equipment and 11kWh for powering the medical equipment [6]. Engine startup energy was also estimated, but this was estimated to be much lower than 1kWh, based on reference aircraft analysis. A more detailed electrical load analysis is included in Section 4.8.

## 2.7. Technical Performance Measurement

To ensure the final design achieves the required specifications, technical resources must be tracked during the development of the aircraft. To facilitate this in future design phases, Technical Performance Measurement (TPM) was initialised. In TPM, performance parameters are tracked and the developing trends are analysed to ensure the final design meets specification. As an example, the mass of the system can be tracked, and if the specified contingency is exceeded too early in the design cycle, the trend of mass increase must be analysed to see if action needs to be taken to reduce mass in the design. This means that contingencies need to be set for each design phase early on in the design.

An example of this tracking procedure is shown conceptually in Figure 2.4. The procedure should be followed in future design phases with regular checks on all TPM parameters and their contingencies. TPM relies on tracking trends of

parameter development with respect to the target value. As such, it has not been implemented in this design phase, where only the first values for the tracked parameters have been found. As can be seen in Figure 2.4, the idea is to track the current value of a given parameter in relation to the target value. If the tracked parameter exceeds the planned contingencies, such as in the detailed design phase in this figure, action needs to be considered by the systems engineers to reduce the current value of the tracked parameter.

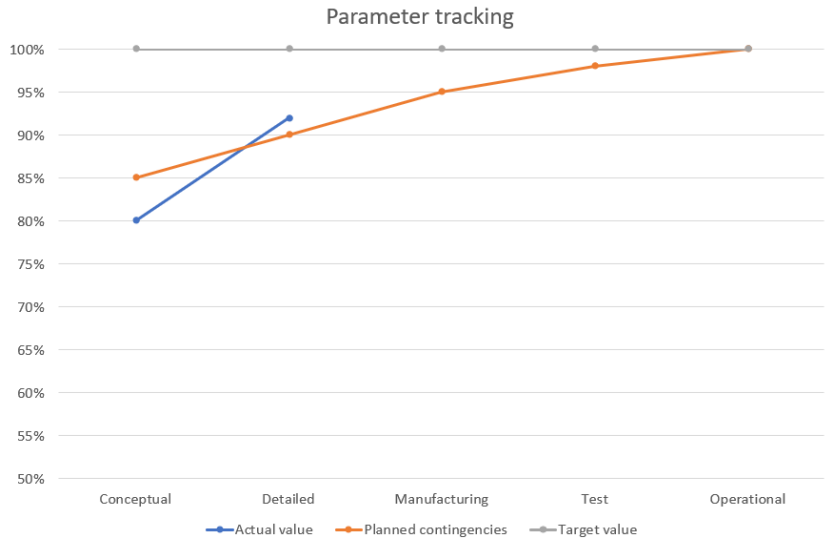


**Figure 2.4:** *TPM tracking procedure.*

A first contingency analysis was performed during the baseline phase [6]. This analysis was expanded upon and revised. The results are shown in Table 2.6. From this table it can be seen that the TPM parameters to be tracked were chosen to be the MTOW, range, power and take-off/landing distance. For example, a contingency of 15% on the MTOW was imposed for the current design phase, which means that the estimate of the MTOW presented later in this report was multiplied by 1.15. The MTOW was chosen as a parameter because of the limitations imposed by CS-23 regulations, as exceeding them would mean adhering to CS-25 regulations, which add numerous additional requirements on the system. In addition, the MTOW influences all subsystems of the aircraft and vice versa, so tracking it is paramount. Range is a parameter of interest as the medical evacuation (medevac) mission range drives the design. The power required by the system is tracked, as it is mission critical, and has uncertainty due to the medical system whose design is still subject to change. Furthermore, the aircraft should be able to take off from a short runway so the take-off and landing distance is tracked.

The values used were based on [14], [15]. They decrease with the maturity of the design and with increasing level of detail. In Table 2.6, the current design phase is referred to as conceptual design, as detailed design would entail designing each aircraft part down to each nut and bolt. The implementation of contingencies is discussed in Chapter 3.

**Table 2.6:** *Contingencies in % of important performance parameters during the maturity of the design and production phases.*

| Design maturity | Description | MTOW | Range | Power | Take-off/ landing runway length |
|---|---|---|---|---|---|
| Conceptual phase | Multiple concepts | 15 | 15 | 20 | 15 |
| Detailed design | Detailed concept & technical drawings | 10 | 10 | 15 | 10 |
| Manufacturing | Manufacture one aircraft | 5 | 5 | 5 | 5 |
| Test phase | Flight and physical tests | 2 | 2 | 2 | 2 |
| Operational phase | Operation of aircraft | 0 | 0 | 2 | 0 |

## 2.8. The Iterative Process

The winning design concept, of which the sizing of all subsystems is covered in the following chapters of this report, was designed by performing an iterative process. This process was a result of the chronological order in which some subsystems were designed as well as the use of assumptions in the initial design stages. The design was performed on online repositories to allow access to all members and easier analysis regarding the effects of changing input and output parameters for the sizing of all subsystems. The iterative cycle was done via the N2 chart presented in Figure 2.5.

| First estimate using Statistical Data |
|---|
| Subsystem Calculation |
| Variables |

| L/D, Range, W/P OEW, $M_{Payload}$, Fuel type, Powertrain | Powertrain, $C_L$, $C_D$, Rate of climb, Performance requirements | $N_{pax}$, Tail size | Drag, Take-off requirements, Propeller configuration | $M_{Payload}$, Wing & Empenage surface area | Maneuver requirements, Take-Off $C_L$ | | Cruise speed, Cruise altitude | Cruise speed, Stall speed | | Material properties | | Power requirements | Altitude, Enviromental conditions |
|---|---|---|---|---|---|---|---|---|---|---|---|---|---|
| Class I Weight Estimation | MTOW | | MTOW, Fuel weight | MTOW, OEW, Fuel weight | | MTOW, OEW, Cg, Propulsion weight | MTOW | MTOW, cg | MTOW, OEW, Propulsion weight, ZFW | Propulsion weight | Cg | | |
| W/P | Wing and Power Loading | | W/P | W/S | | | W/S | W/S | | W/P & W/S | | | |
| | | Fuselage sizing | | Fuselage parameters | | Landing gear constraints | Fuselage parameters | | Fuselage parameters | Fuselage parameters | Fuselage paramteres | | |
| Powertrain | Power available | | Engine sizing | Engine Dimensions | Engine Locations | Engine mass and location | Engine parameters | Engine parameters | Engine weight & geometry | Thrust, Propulsion weight | | Electrical power available | |
| L/D | Wing parameters | Tail Size | | Wing & Empennage sizing | Wing parameters | Wing Parameters | Wing paramters | Wing parameters | Wing & Empennage parameters | Wing parameters | Wing & Empennage parameters | | |
| | Aerodynamic parameters | | | | HLDS & CS | | HLD and CS | | HLD type | | | | |
| | | Landing gear position | | Landing gear placement | | Landing gear | landing gear parameters | | Landing gear type | Landing gear position and forces | | | |
| Aerodynamic parameters | Aerodynamic parameters | | Drag | Aerodynamic parameters | Aerodynamic parameters | | Aero Analysis | Lift coefficients | | Aerodynamic forces | Aerodynamic parameters, Stability derivatives | | |
| Range | Performance, ROC | | | | | | | Flight Performance | Limit loads | Limit loads, Dive speed | | | |
| MTOW, OEW | | Fuselage weight | MTOW, Propulsion wieght | MTOW, OEW, Cg, Wing weight | | Cg, Landing gear weight | MTOW | Cg | Class II Weight Estimation | | Cg | Electrical weight | Internal system weight |
| | | | | | | | | | | Structures | | | |
| | | | | Tail volume | | Cg | | Cg | | | Stability & Control | | |
| | | | Electrical power required | | | | | | Electrical weight | | | Electrical | Electrical power available |
| | | | | | | | | | Internal system weight | | | Electrical power required for internal systems | Internal Systems |

**Figure 2.5:** *N2 chart used for the iterative cycles.*

In Figure 2.5, the most important inputs to the iterative process related to the main wing design, which was the base for the performance parameters such as range, fuel use and lift in all flight phases. With every iterative cycle, a new wing and power loading was established, after which the cycle from Figure 2.5 was repeated. The iterations were carried out until a class II weight difference of less than 5% with respect to the previous iteration was achieved.

# 3
# Preliminary Sizing

The method followed for sizing the aircraft, along with the results of the process are presented in this chapter. An overview of the sizing method is shown in Figure 3.1. In contrast to conventional Class I weight estimation methods, the method followed includes considerations due to the distributed propulsion system to the weights, power-loading performance and aerodynamic performance of the aircraft.

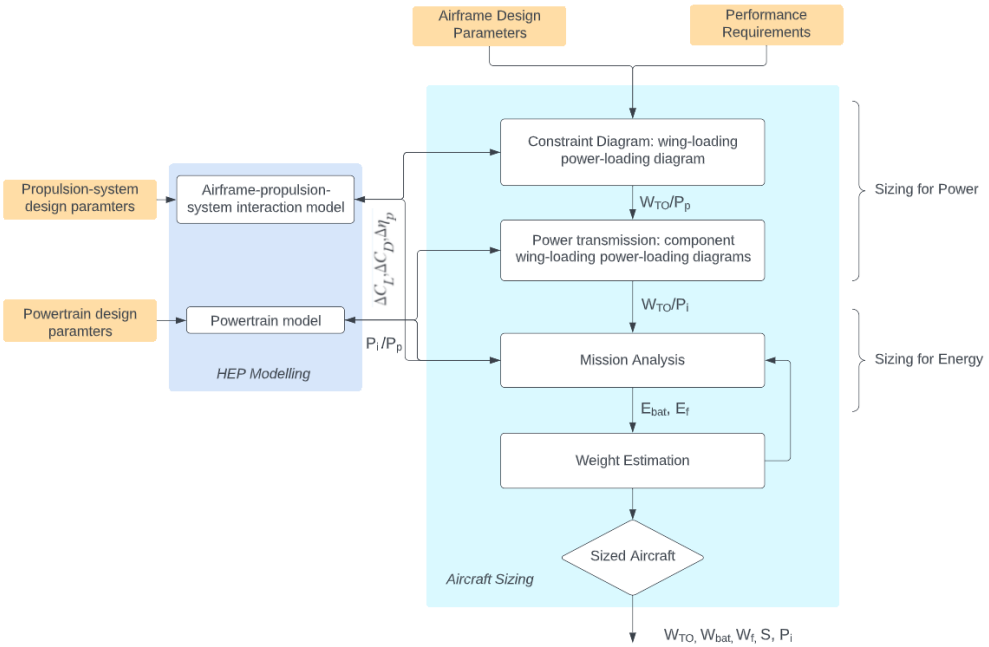


**Figure 3.1:** *Overview of the sizing method used [2].*

The structure of the chapter is as follows: in Section 3.1, the aerodynamic considerations related specifically to distributed propulsion are discussed. In Section 3.2, the powertrain model used to describe the propulsion system is presented. In Section 3.3, the weight fractions of the aircraft are presented. Following this, in Section 3.4 the design point of the aircraft is found. In Section 3.6 the weight determination of the aircraft is discussed, and finally in Section 3.5 the optimised design point of the aircraft based on weight performance is presented.

## 3.1. Aerodynamic Model: Leading Edge Distributed Propulsion

Main characteristics of a distributed electric propulsion system (DEP) include a supposed increase in aerodynamic performance. The main aerodynamic benefits of a DEP described in the literature are attributed to a reduction of installation drag and high lift augmentation. The high lift augmentation is of particular interest to this project as it enhances short take-off and landing (STOL) performance. In order to perform conceptual and preliminary sizing of the aircraft, it was important to take into account the aero-propulsive effects of DEP that are not present in conventional aircraft designs, hence traditional methods had to be modified [16]. The approach adapted was developed by de Vries from Delft University of Technology [16].

One of the modifications that had to be made to traditional methods according to de Vries concerned aerodynamic models used in sizing. As distributed propulsion is a highly integrated system, the aerodynamic interaction between the airframe and the propulsors must be considered during conceptual design due to its direct impact on wing sizing and power requirements. As a consequence of the coupling present, the aerodynamic performance of the system was different from the sum of the aerodynamic performances of individual components.

A general aerodynamic property such as drag can be effectively expressed as a function of two sets of parameters - the ones that affect the system without the coupling and the parameters that exist solely due to the installation of distributed propulsion (DP). Furthermore, the total force can be decomposed into contributions that would exist on isolated airframe

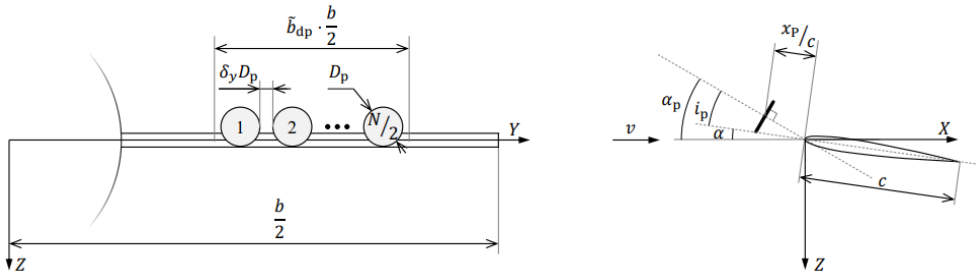


**Figure 3.2:** *Geometric model of leading edge distributed propulsion system, front view (left) and side view (right) [2].*

or propulsors and the change of property due to the installation of DP. This decomposition leads to an expression for lift shown in Equation 3.1.

$$L = L_{\text{u}} + \Delta L(T_{\text{dp}}, L_{\text{airframe}}, S, ...), \tag{3.1}$$

where u stands for unblown - without DP, $T_{dp}$ is the thrust generated by the DP, $L_{\text{airframe}}$ is the lift generated without presence of the DP, S is the surface area of the wing and $\Delta L$ is a lift increase due to thrust generated by propulsors. In the same manner, effects of DP on aircraft drag are included as follows from Equation 3.2.

$$D = D_0 + \Delta D_0(T_{\text{dp}}, S_{\text{w}}, ...) + D_i(L_{\text{airframe}}) + \Delta D_i(T_{\text{dp}}, L_{\text{airframe}}, S_{\text{w}}, ...), \tag{3.2}$$

where $D_0$ is the zero lift drag, $D_i$ is lift induced drag and delta terms are contributions of the DP propulsion. In order to proceed with point performance analysis, a mathematical framework for estimation of these delta terms had to be fixed. Method of choice capitalized primarily on established equations and models from the works of de Vries [16] on preliminary sizing, [2] and the works of Patterson on aerodynamic models of DP [17], [18]. The technique makes use of a number of assumptions, the most important of which are outlined below:

- **AS.1** Velocity increase at the actuator disk equation assumes uniform axial inflow.
- **AS.2** Variations in lift due to swirl are negligible.
- **AS.3** Flow over the wing is attached.
- **AS.4** Symmetric airfoil, hence $C_{L_0}$ = 0.
- **AS.5** Propellers do not affect adjacent propellers.
- **AS.6** Effects of DP on the wing are limited to the portion of wing they occupy.
- **AS.7** In this interval effects of propellers on the wing are uniform in spanwise direction.
- **AS.8** Fully immersed in slipstream wing.

The effect of these assumptions was that this model had limited accuracy; especially when it came to high lift conditions and high angles of incidence of the propellers. Furthermore, it was found that the uncertainty in MTOW due to the aeroydnamic modelling constitutes about $\pm$ 3%. Nevertheless, after conducting verification and validation, de Vries [2] came to the conclusion that this model is suitable for conceptual designs.

### 3.1.1. Geometric Model

A geometric model for distributed propulsion was implemented to assist with the sizing process. The key parameters of DP are outlined on Figure 3.2. $D_p$ is the propeller diameter, $\delta_y D_p$ is the lateral propeller separation and $\frac{\Delta y}{b}$ is the fraction of wingspan occupied by the DP. Propeller installation parameters include $\frac{x_p}{c}$ - upstream distance of the actuator disk as a fraction of chord length, propeller installation angle $i_p$ and propeller effective angle of attack $\alpha_p$ [19]. A formula for propeller diameter normalised with respect to weight is shown in Equation 3.3. In Equation 3.3, N is the number of distributed propulsors and AR is the aspect ratio.

$$\frac{D_p^2}{W} = \frac{(\frac{\Delta y}{b})^2}{N^2(1+\delta_y)^2} \cdot \frac{AR}{\frac{W}{S}}, \tag{3.3}$$

### 3.1.2. Computation of Delta Coefficients

In order to compute the delta terms due to aerodynamic coupling, the axial induction factor $a_p$ at the propeller disc had to be computed first using Equation 3.4 [2].

$$a_p = \frac{1}{2}\left(\sqrt{1+\frac{8}{\pi}T_c} - 1\right) \tag{3.4}$$

The thrust coefficient $T_c$ is the non-dimensional thrust required from a single propulsor and was expressed through Equation 3.5 [2]. In Equation 3.5, $\chi$ is the thrust delivered by distributed propulsors over thrust delivered by primary ones which can be calculated using Equation 3.6.

$$T_c = \frac{1}{N}\frac{\chi\frac{T}{W}}{\rho V^2 \frac{D_p^2}{W}}, \tag{3.5}$$

$$\chi = \frac{1}{1+\frac{\eta_{p1}}{\eta_{p2}}\left(\frac{1-\phi}{\phi}\right)}, \tag{3.6}$$

where $\eta_{p1}$ is the efficiency of primary propulsors and $\eta_{p2}$ is the efficiency of secondary propulsors.

To evaluate the velocity induced by propellers at the leading edge, the upstream position of propellers was expressed as a fraction of propeller radius through $\frac{x_p}{c}$ and $\frac{R_p}{c}$. The radius to chord ratio could then be computed using Equation 3.7 [2].

$$\frac{R_p}{c} = \frac{1}{2}\sqrt{\frac{D_p^2}{W}\frac{W}{S}AR} \tag{3.7}$$

Using the $\frac{x_p}{R_p}$ value, the slipstream contraction ratio $\frac{R_w}{R_p}$ and induction factor at leading edge $a_w$ were calculated using Equation 3.8 [2].

$$\frac{R_w}{R_p} = \sqrt{\frac{1+a_p}{1+a_p\left(1+\frac{\frac{x_p}{R_p}}{\sqrt{(\frac{x_p}{R_p})^2+1}}\right)}} \quad , \quad a_w = \frac{a_p+1}{\left(\frac{R_w}{R_p}\right)^2} - 1 \tag{3.8}$$

Using these relationships and the factor $\beta$, the sectional lift coefficient increase was determined using Equation 3.9. Multiplication factor $\beta$ was implemented to determine effective slipstream velocity. It was estimated using simulation graphs from Patterson [17]. In Equation 3.9, $\alpha_w$ is the main wing angle of attack. The angle of attack of the wing was estimated using Equation 3.10.

$$\Delta c_l = 2\pi\left[(\sin(\alpha_w) - a_w\beta\sin(i_p))\sqrt{(a_w\beta)^2 + 2a_w\beta\cos(\alpha_w+i_p)+1} - \sin(\alpha_w)\right], \tag{3.9}$$

$$\alpha_w \approx \frac{C_{L_{\text{airframe}}}}{2\pi AR}\left[2+\sqrt{AR^2(1-M^2)\left(1+\frac{\tan^2(\Lambda_{c/2})}{1-M^2}\right)+4}\right] \tag{3.10}$$

Ultimately, using assumption **AS.5** that effects of DP are limited to the wing fraction in the wingspan direction DP occupies, three-dimensional delta terms for lift and drag coefficient are computed using Equation 3.11.

$$\Delta C_L = \Delta c_l \frac{\Delta y}{b} \qquad \Delta C_{D_0} = \frac{\Delta y}{b} a_w^2 c_f \qquad \Delta C_{D_i} = \frac{\Delta C_L^2 + 2C_{\text{L, airframe}}\Delta C_L}{\pi ARe} \tag{3.11}$$

## 3.2. Powertrain Model

The propulsion system of a distributed propulsion aircraft differs considerably from a conventional aircraft. Therefore, the powertrain of the design was modelled after the approach of de Vries [2]. The architecture chosen for the powertrain was the partial turbo-electric architecture, as the use of batteries was deemed not feasible with the current technology for the desired range. In the partial turboelectric configuration, two gas turbines drive main propellers, as well as generate electricity for 10 distributed electric motors which run smaller propellers. A schematic of the architecture can be seen in Figure 3.3, in which F stands for fuel, GT for gas turbine, GB for gearbox, P1 for the main propulsor, EM1 for generator, PMAD for power management and distribution, EM2 for electric motor and P2 for secondary propulsor.

The model is a linear-algebraic system of equations, each row describing the flow of power through each component in Figure 3.3, as per Equation 3.12 [2]. Three additional equations were required, representing the power control

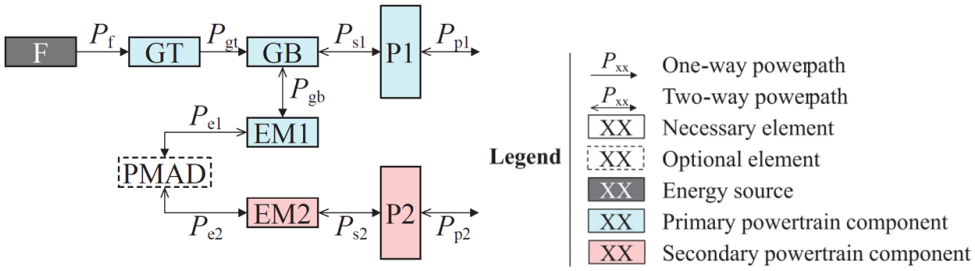


**Figure 3.3:** *Partial turbo-electric powertrain architecture [2].*

parameters $\Phi$, $\varphi$ and $\xi_{GT}$. For the turbo-electric configuration considered, the supplied power ratio, which describes the share of power delivered by the batteries of a hybrid-electric system, is by definition $\Phi = 0$. The shaft power ratio, describing the amount of power delivered by the electric machines, is a design variable. These two parameters are defined by Equations 3.13 and 3.14. The gas-turbine throttle $\xi_{GT}$ can be varied throughout the flight.

$$\sum P_{\text{out}} = \eta \sum P_{\text{in}} \tag{3.12}$$

$$\Phi = \frac{P_{\text{bat}}}{P_{\text{bat}} + P_{\text{fsl}}} \tag{3.13}$$

$$\varphi = \frac{P_{\text{S2}}}{P_{\text{S2}} + P_{\text{S1}}} \tag{3.14}$$

From Equation 3.12, the general powertrain model Equation 3.15 can be found. The model can be modified for changing the throttle setting to find Equation 3.16.

$$\begin{bmatrix} -\eta_{\text{GT}} & 1 & 0 & 0 & 0 & 0 & 0 & 0 & 0 & 0 \\ 0 & -\eta_{\text{GB}} & 1 & 1 & 0 & 0 & 0 & 0 & 0 & 0 \\ 0 & 0 & 0 & -\eta_{\text{P1}} & 0 & 0 & 0 & 0 & 1 & 0 \\ 0 & 0 & -\eta_{\text{EM1}} & 0 & 1 & 0 & 0 & 0 & 0 & 0 \\ 0 & 0 & 0 & 0 & -\eta_{\text{PMAD}} & -\eta_{\text{PMAD}} & 1 & 0 & 0 & 0 \\ 0 & 0 & 0 & 0 & 0 & 0 & -\eta_{\text{EM2}} & 1 & 0 & 0 \\ 0 & 0 & 0 & 0 & 0 & 0 & 0 & -\eta_{\text{P2}} & 0 & 1 \\ \Phi & 0 & 0 & 0 & 0 & (\Phi-1) & 0 & 0 & 0 & 0 \\ 0 & 0 & 0 & \varphi & 0 & 0 & 0 & (\varphi-1) & 0 & 0 \\ 0 & 0 & 0 & 0 & 0 & 0 & 0 & 0 & 1 & 1 \end{bmatrix} \cdot \begin{bmatrix} P_{\text{fsl}} \\ P_{\text{gt}} \\ P_{\text{gb}} \\ P_{\text{s1}} \\ P_{\text{e1}} \\ P_{\text{bat}} \\ P_{\text{e2}} \\ P_{\text{s2}} \\ P_{\text{p1}} \\ P_{\text{p2}} \end{bmatrix} = \begin{bmatrix} 0 \\ 0 \\ 0 \\ 0 \\ 0 \\ 0 \\ 0 \\ 0 \\ 0 \\ P_{\text{p}} \end{bmatrix} \tag{3.15}$$

$$\begin{bmatrix} -\eta_{\text{GT}} & 1 & 0 & 0 & 0 & 0 & 0 & 0 & 0 & 0 \\ 0 & -\eta_{\text{GB}} & 1 & 1 & 0 & 0 & 0 & 0 & 0 & 0 \\ 0 & 0 & 0 & -\eta_{\text{P1}} & 0 & 0 & 0 & 0 & 1 & 0 \\ 0 & 0 & -\eta_{\text{EM1}} & 0 & 1 & 0 & 0 & 0 & 0 & 0 \\ 0 & 0 & 0 & 0 & -\eta_{\text{PMAD}} & -\eta_{\text{PMAD}} & 1 & 0 & 0 & 0 \\ 0 & 0 & 0 & 0 & 0 & 0 & -\eta_{\text{EM2}} & 1 & 0 & 0 \\ 0 & 0 & 0 & 0 & 0 & 0 & 0 & -\eta_{\text{P2}} & 0 & 1 \\ \Phi & 0 & 0 & 0 & 0 & (\Phi-1) & 0 & 0 & 0 & 0 \\ 0 & 0 & 0 & \varphi & 0 & 0 & 0 & (\varphi-1) & 0 & 0 \\ 0 & 1/\xi_{\text{GT}} & 0 & 0 & 0 & 0 & 0 & 0 & 0 & 0 \end{bmatrix} \cdot \begin{bmatrix} P_{\text{fsl}} \\ P_{\text{gt}} \\ P_{\text{gb}} \\ P_{\text{s1}} \\ P_{\text{e1}} \\ P_{\text{bat}} \\ P_{\text{e2}} \\ P_{\text{s2}} \\ P_{\text{p1}} \\ P_{\text{p2}} \end{bmatrix} = \begin{bmatrix} 0 \\ 0 \\ 0 \\ 0 \\ 0 \\ 0 \\ 0 \\ 0 \\ 0 \\ P_{\text{GT,max}} \end{bmatrix} \tag{3.16}$$

## 3.3. Weight Fractions

Performance analysis required the estimation of the aircraft weight fractions during the mission duration. This is typically done using statistical data from similar aircraft for most phases and using range equations for the cruise phase. For the turbo-electric architecture, the range relationship derived by de Vries [16], shown in Equation 3.17, is used.

$$R = \eta_{GT}\eta_{GEN}\eta_{EM}\eta_p \left(\frac{L}{D}\right)_{\text{cruise}} \left(\frac{e_f}{g}\right) \ln\left(\frac{W_{OE} + W_{PL} + \frac{g}{e_f}E_{0,tot}}{W_{OE} + W_{PL}}\right), \tag{3.17}$$

where $e_f$ is the specific energy of the fuel, g is gravitational acceleration and $E_{0,tot}$ is the total fuel energy carried on board at the beginning of the mission

The weight fractions were estimated based on statistical data presented by Roskam for the twin engine props [4] and de Vries' values from leading edge distributed propulsion study [16]. The results for most important flight phases of Rothera - Amundsen-Scott mission are summarised in Table 3.1, where $W_i$ is the weight at a the indicated moment in the mission.

**Table 3.1:** *Weight fractions derived for the Rothera - Amundsen-Scott mission.*

| HDEP | Take-off | Climb/OEI | Cruise | Landing |
|---|---|---|---|---|
| $W_i/W_{TO}$ | 1 | 0.974 | 0.853 | 0.831 |

These fuel fractions were applied in the point performance analysis when constructing the power loading diagrams. Due to the fact that different constraints have to be satisfied at different points of the mission and the diagrams make use of $W_{TO}$, the weights had to be expressed in terms of the take-off weight.

## 3.4. Point Performance

In order to size the aircraft in compliance with set requirements, the allowable design space had to be determined by means of power and wing loading diagrams. Taking into account the unconventional propulsion system design, the point sizing was performed for the entire propulsion system as well as its components using the method proposed by de Vries [16]. This section examines the requirements specified by the stakeholders and performs design space exploration for JAPA-12.

### 3.4.1. Padding Policy

Information on aircraft performance can be very sensitive when it comes to marketing and meeting the stakeholder requirements. There is a difference between predicted and real performance values. Due to the shortcomings of the prediction methods used to estimate values of relevant parameters, the values resulting from analysis have a certain uncertainty and result in an outcome that presents a range of values the real parameter falls under. While it is tempting to say that according to the calculations the aircraft can fly at 250 knots and it is tempting to market it as capable of achieving this value, there could be underlying costs in doing so. If the actual airplane turns out to be under-performing the customers and stakeholders will be left unhappy and the manufacturer will lose revenue. Furthermore, there is also a cost in terms of effort - the manufacturer would have to please the unhappy customers.

In order to prevent such things from happening there was a need to introduce a padding policy which could be integrated with the performance analysis. The factors taken were estimated based on recommendation of Gudmundsson for high performance GA aircraft and are summarized in Table 3.2 [20].

**Table 3.2:** *Padding factors used in performance analysis.*

| Performance phase | Parameter | Multiplication factor |
|---|---|---|
| Take-off | Take-off ground run length [ft] | 1.1 |
| Climb | Rate of climb [fpm] | 0.97 |
| Cruise | Cruise speed, KTAS | $V_{\text{TAS}}$ - 6 |
| Cruise | Absolute ceiling [kft] | 0.99 |
| Landing | Landing ground run length [ft] | 1.1 |
| Cruise | $L/D_{\text{max}}$ | 0.95 |
| Landing | Stall speed, KTAS | 1.03 |
| Range | Total range [nm] | 0.98 |

In the following subsections, the requirements are presented in the following way VAL1 / VAL2 where VAL1 is the original requirement value that should be achieved and VAL2 is the value that includes the padding factor.

### 3.4.2. Take-off Distance

**[REQ-STA-TAP-01.5]** The system shall take-off from a snow runway of 6000 / 5455 ft.
**[REQ-STA-TAP-01.6]** The system shall take-off from a gravel runway of 2500 / 2273 ft.

Special considerations had to be taken when designing JAPA-12 for the take-off distance requirement. At Rothera airport and Amundsen-Scott station, challenges arise due to relatively strong winds that could potentially be detrimental for take-off performance. Tailwinds are adverse specifically to the take-off ground roll while cross-winds are mostly damaging for aircraft's controllability. Although it should be noted that if in cross-wind conditions the brakes are applied to keep aircraft straight, the ground roll will increase. Slight tailwinds can lead to a substantial increase in required runway length, which was taken into account. Furthermore, snowy runway conditions at the South Pole also create unfavorable take-off environment. Per se, snow has an effect of increasing rolling resistance, thereby increasing the ground run. In order to account for these contextual constraints, safety factors were introduced and applied during sizing for performance requirements. As per safety leaflet issued by civil aviation authority [21] and Flight Safety Foundation briefing notes [22], recommended safety factors of 1.2 for general take-off distance and 1.6 for snowy runway were applied in this design. In conditions where both factors are relevant such as at Amundsen-Scott, the factors are multiplied. This effectively reduces required landing distance from 1829 m of snow runway to 952 m and 899 m of gravel runway to 749 m. Equation 3.18, used for sizing, is derived using approach described by Gudmundsson and adapted by using propulsive effects described by de Vries. [20] [16]

$$s_{GR} = V_{\text{LOF}} + \frac{V_{\text{LOF}}^2}{2g\left(\frac{P}{W}\frac{\sqrt{2}}{V_{\text{LOF}}} + 0.5\rho\frac{V_{\text{LOF}}^2}{2}\frac{S}{W}\left(\mu\left(C_{L_{TO,u}} + \Delta C_{L_{TO}}\right) - \left(C_{D_{TO,u}} + \Delta C_{D_{TO}}\right)\right) - \mu\right)}, \tag{3.18}$$

where $\mu$ is the ground friction constant, $s_{GR}$ is the ground roll distance, g is gravitational acceleration, $\rho$ is the air density at take-off and $V_{LOF}$ is the liftoff speed which is equal to 1.1 times stall speed

### 3.4.3. Landing Distance

**[REQ-STA-TAP-01.1]** The system shall land on a snow runway of 6000 / 5455 ft.
**[REQ-STA-TAP-01.2]** The system shall land on a gravel runway of 2500 / 2273 ft.

Landing distance constraint is designed for, in a manner similar to the take-off distance. Despite the fact that snow increases the ground friction coefficient which intuitively should decrease the ground roll, the snow can also significantly increase the ground roll. This increase is a result of decreased tyre friction and hence the braking. While it is unclear which effect will dominate the aircraft, the design assumed that the effect is to increase the landing distance for a more conservative design. The same safety factors were applied as for the take-off distance - 1.2 for gravel runway and 1.2·1.6 for the snow runway [22] [21]. The equation used to estimate the ground roll distance is taken from Raymer [23] and adapted to Equation 3.19.

$$s_{GR} = 80 \cdot \left(\frac{W}{S}\right)\left(\frac{1}{\sigma\left(C_{Lmax_u} + \Delta C_{Lmax}\right)}\right), \tag{3.19}$$

where $\sigma$ is the density ratio

It is important to note that Equation 3.19 uses imperial units: ft for distance, slugs/cubic ft for density and lb/square ft for wing loading.

### 3.4.4. Stall Speed Requirement

**[REQ-PER-01.1]** The aircraft shall have a stall speed of 63 / 61 kts.

Stall speed requirement is not explicitly stipulated by the CS-23 Amendment 5 regulations for a twin engine commuter aircraft. Therefore, the requirement was established using the old CS-23 regulations for a different category of aircraft - light normal, utility and aerobatic. The stall requirement is usually one of the most limiting ones for the design space. A pilot stalling the aircraft is a considerable contributor to the number of fatal accidents, requiring thorough stall speed analysis. The air density is an important parameter in the maximum stall speed calculations and is also indirectly regulated by **[REQ-STA-MAR-05]**. The critical sizing condition was found to be at the Amundsen-Scott station due to its high elevation with an average air density of 1.1 kg/m$^3$. Stall condition was then calculated for the air density of 1.0

kg/m³, which is around average minimum. Equation 3.20 presents wing loading relationship for which the airplane was sized.

$$\frac{W}{S} = \frac{1}{2}\rho V_s^2 (C_{Lmax_u} + \Delta C_{Lmax}) \tag{3.20}$$

### 3.4.5. Maximum Cruise Speed

**[REQ-STA-CUST-09]** The aircraft shall have a cruise speed of 200 / 203.1 kts.

When sizing for the cruise speed requirement, it is also important to consider the maximum speed that the aircraft is able to achieve in cruise. Since the requirement for maximum cruise speed is the more limiting one, it was selected for the the preliminary sizing. Furthermore, the maximum cruise speed is taken to be 20% higher than the average cruise speed stipulated by the stakeholder requirements. This assumption is a consequence of the fact that cruise speed for propeller aircraft is typically calculated at around 80% thrust [3]. The baseline equation for the maximum cruise speed achieved by a propeller-driven airplane at a given altitude is retrieved from Sadraey and augmented into Equation 3.21 [3]. This equation assumes maximum available engine power that is equal to the maximum required engine power. The estimates of $C_{D0_u}$ for different mission phases were taken from de Vries' analysis of leading edge distributed propulsion systems (LEDP)[16].

$$\frac{W}{S}\frac{\rho_{cr}}{\rho_0} = \frac{W}{P}\frac{1}{2}\rho_{cr} V_{cr_{max}}^3 (C_{D0_u} + \Delta C_{D0}) + \left(\frac{W}{S}\right)^2 \left(\frac{W}{P}\right) \frac{2}{\rho_{cr} V_{cr_{max}} \pi A R e} \tag{3.21}$$

### 3.4.6. Rate of Climb

**[REQ-PER-01.2]** The aircraft shall be able to achieve AEO maximum rate of climb of 8 / 8.25 m/s.
**[REQ-PER-01.3]** The aircraft shall be able to achieve OEI maximum rate of climb of 2 / 2.06 m/s.

Rate of climb is not explicitly specified by stakeholder requitements, henceforth it was derived based on similar aircraft such as DHC-6 twin otter and DO-228. Similarly to the maximum cruise speed requirement, the design space was constrained by the maximum rate of climb achievable in the second mission segment. The baseline method was taken from Roskam and adapted to Equation 3.22 [4].

$$\frac{W}{P} = \frac{1}{ROC + \frac{\left(\frac{W}{S}\right)^{\frac{1}{2}} \cdot 0.95017}{\left(\frac{\rho_1}{\rho_0}\right)} \frac{(ARe)^{\frac{3}{4}}}{C_{D0_u} + \Delta C_{D0}}}, \tag{3.22}$$

where $\rho_1$ is the density at climb altitude

For the one engine inoperative (OEI) climb requirement, the Equation 3.22 is modified by multiplying the $\frac{W}{P}$ fractions by a factor corresponding to the redundancy of the component failed, as described in Subsection 3.4.8.

### 3.4.7. Service Ceiling

**[REQ-STA-CUST-06]** The system shall have a service ceiling of 25000 / 25253 ft.

The service ceiling is the altitude at which maximum achievable rate of climb of the aircraft is 0.5 m/s. Given that it is essentially a rate of climb requirement, the Equation 3.22 is modified by multiplying the right hand side with $\frac{\rho_c}{\rho_0}$ and replacing $\rho_1$ with $\rho_c$ which is air density at the service ceiling. In contrast with the rate of climb requirement, the service ceiling implies the best rate of climb speed $V_y$ which results in maximum achievable rate of climb. The best rate-of-climb speed is obtained when the difference between power required and power available is the greatest. For the preliminary sizing it was estimated using Equation 3.23 for propeller aircraft which was taken from Gudmundsson [20].

$$V_y = \sqrt{\frac{2}{\rho_c}\left(\frac{W}{S}\right)\sqrt{\frac{1}{3(C_{Dmin_u} + \Delta C_{Dmin})\pi A R e}}} \tag{3.23}$$

### 3.4.8. Designing for Component Failure

According to the EASA regulations any multi-engine aircraft has to be able to perform basic maneuvers in one engine inoperative (OEI) condition to be certifiable. Usually, this requirement is reflected and embedded in the climb rate or gradient condition. Since this design mainly focuses on the most constraining requirements, the design for OEI was incorporated in the rate of climb requirement.

Traditional preliminary sizing for component failure focuses on engines only. However, for the hybrid-electric propulsion systems the one engine inoperative condition was redefined to one powertrain component inoperative while keeping the same terminology - OEI. During the preliminary design, many different OEI conditions and combinations of such were considered for the turbo-electric architecture. This limited the design for component failure to examination of impact of failure of individual components treated as black boxes. Furthermore, the powertrain is divided into a primary and secondary branch connected by PMAD. The primary branch contains primary propulsors, gas turbine, gearbox and generators, while the secondary powertrain branch houses electric motors and secondary propulsors. Components sized for failure were the gas turbine, gearbox, generator and electric motor. The power management and distribution unit (PMAD) was assumed to contain enough redundant buses to not be sized for failure. This also means that failure of components in the primary branch does not affect the components of the secondary branch. Figure 3.4 shows the simplified powertrain representation with primary and secondary branch as well as failure factors N for each branch.

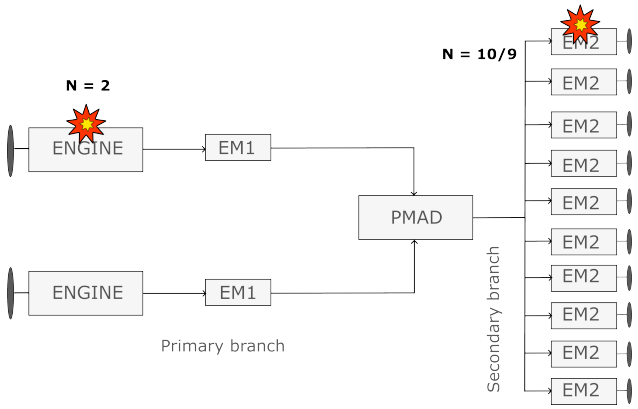


**Figure 3.4:** *Simplified powertrain representation with failure factors for primary and secondary branches.*

The failure of engine, gearbox or generator in either sub-branch of the primary branch requires oversizing components in the other sub-branch by the factor of $\frac{N_1}{N_1-1}$. For the JAPA-12 the $N_1$ factor is equal to 2. Similarly, for the secondary branch in case of component the components have to be oversized by a factor of $\frac{N_2}{N_2-1}$. The $N_2$ has a value of 10/9 for the JAPA-12.

### 3.4.9. Loading Diagrams

Contrary to the conventional fuel and gas turbine propulsion systems, the partial turbo-electric architecture required analysis of multiple power loading diagrams generated per individual component of the power train. These are presented in Figure 3.5 and Figure 3.6. For simplicity, this design differentiates between main components such as the gas turbine, gearbox, electric motor, generator and PMAD, and secondary components. The secondary powertrain components were grouped with the main ones - inverters and rectifiers with the EM1, cables and switches with the PMAD block. For each component the power-loading diagram was sized using power ratios obtained from the powertrain model per constraint. Consequently, the design space exploration was performed and evaluated.

Upon iterations, it was determined that the effect of distributed propulsion on aerodynamic efficiency in cruise is marginal. With an average cruise speed of 115 m/s the increase in $C_L$ due to DP was calculated to be $+1.3\%$. It was then decided that since DP does not have a significant impact on cruise performance the distributed propellers will not be actively used in cruise hence $\phi_{cr} = 0$. Furthermore, iterations on the design space showed that the take-off constraints do not actively limit the gas turbine, which is the main contributor to the the powertrain weight. Similarly, the aerodynamic benefits during take-off do not outweigh the power dissipated in the electrical powertrain leading to a somewhat conservative value of shaft power ratio, $\phi_{to}$. As could be seen from the subfigure a in Figure 3.5 and Figure 3.6, the cruise condition in this case did not constrain the electrical components of the system.

For the gas turbine specifically, the power displayed on the diagram after applying the powertrain power fractions had

to be normalised to the maximum sea level gas turbine power. The change due to the application of gas turbine throttle to constraints active during different mission phases is illustrated by subfigures b and c on Figure 3.5.

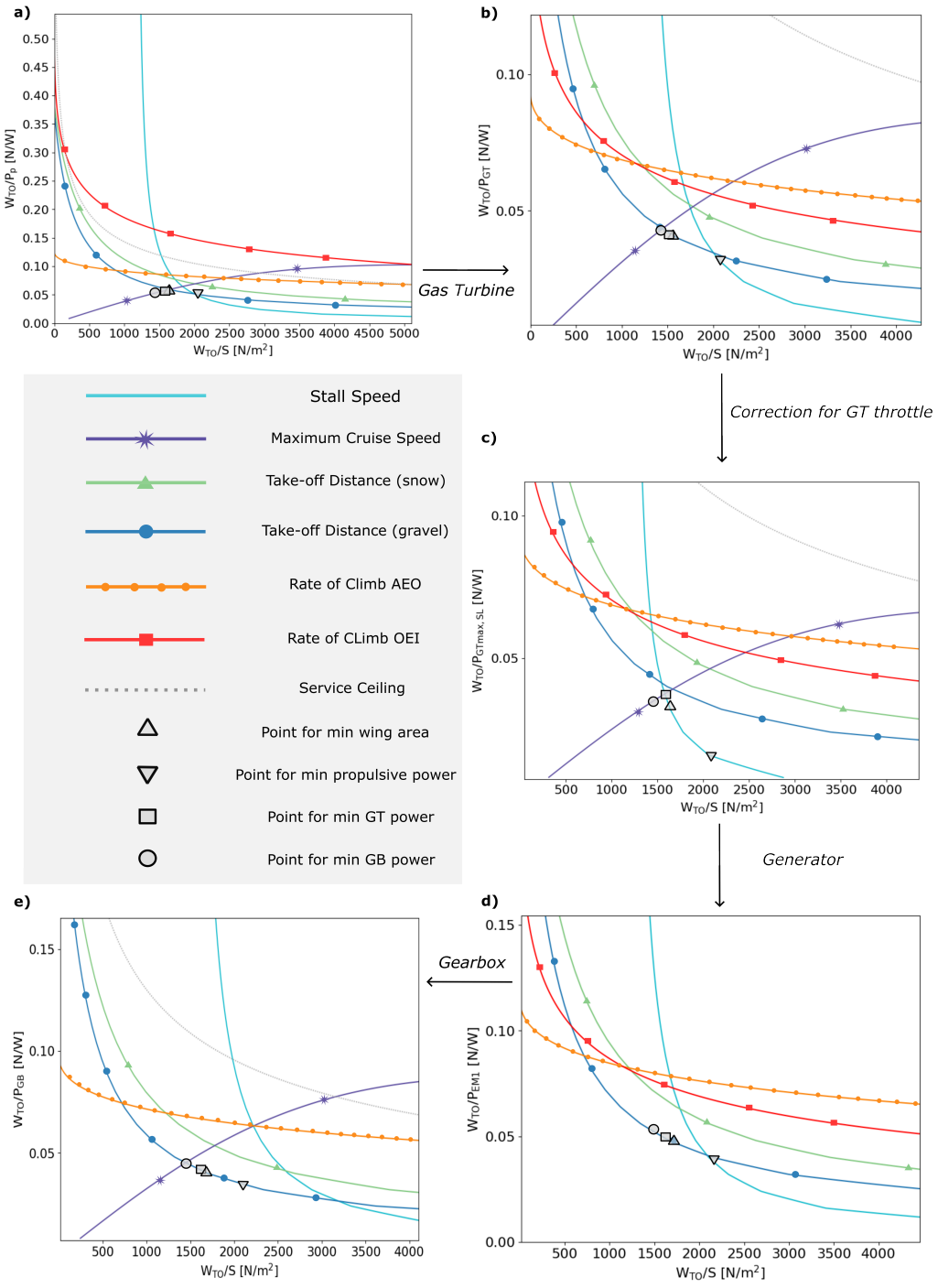


**Figure 3.5:** *Propulsive and component power-loading diagrams.*

The results revealed that the limiting conditions for JAPA-12 are the maximum cruise speed and stall speed requirement. The one engine inoperative and service ceiling requirements do not actively constrain the design space. It was also observed from the diagrams that distributed propulsion significantly increases the range of possible wing loadings. With a conventional propulsion system the maximum wing loading at air density of 1.05 kg/m$^3$ is 1185 N/m$^2$ and with distributed propulsion this value increases to 2900 N/m$^2$, which equates to an increase of +250%. Although 2900 N/m$^2$ is not a

realistic value as it occurs at an extremely low power loading, the general pattern showed that the design space becomes more flexible with the introduction of distributed propellers.

The point performance model was verified by replicating results provided by Matrone and de Vries in their verification studies [16] [24]. No significant incoherence was found in the implementation of the method which lead to the conclusion that the implementation was consistent. With respect to the resulting uncertainties in the design points, similar results to the aforementioned studies are expected. The verification study of de Vries determined uncertainty in the design point of $\pm$ 1% whereas Matrone came to a value of $\pm$ 1.5%.

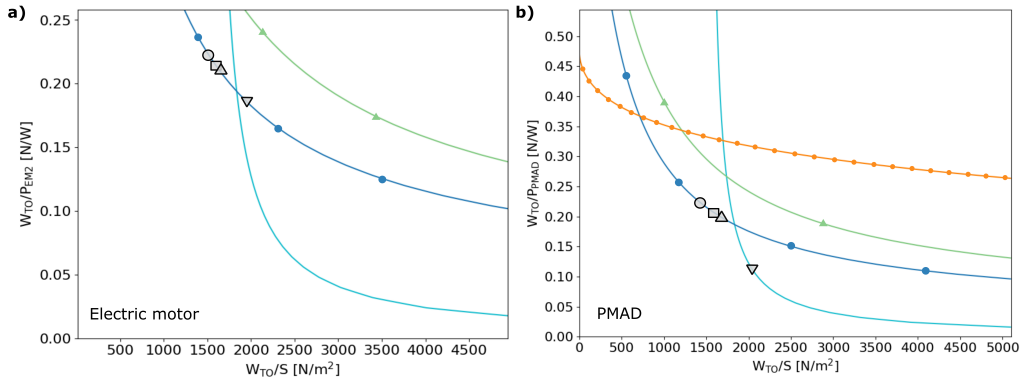


**Figure 3.6:** *Electric motor and PMAD power loading diagrams obtained.*

## 3.5. Optimisation

In order to properly optimize the design point beyond propulsive power loading diagram, multiple combinations of wing loading and component loading ratios were considered. As could be seen from Figure 3.5, various points were selected for this process - for minimum propulsive power, minimum wing area, minimum gas turbine power and minimum generator power. Wing loading values corresponding to minimum power loading of other components were located close to the chosen point and hence were omitted from the analysis. For each selected W/S value, corresponding power fractions for other components were determined from Figure 3.5 and Figure 3.6. Finally, the mission analysis was performed in order to calculate take-off weights corresponding to different design points.

The summary of design points, power fractions and corresponding take-off weights is shown in Table 3.3.

**Table 3.3:** *Optimisation inputs and outputs.*

| **Design Point** | **1 (□)** | **2 (○)** | **3 (△)** | **4 (▽ )** |
|---|---|---|---|---|
| $W_{TO}/S$ [N/m$^2$] | 1446 | 1580 | 1643 | 2147 |
| $W_{TO}/P_p$ [N/W] | 0.053 | 0.057 | 0.059 | 0.049 |
| $W_{TO}/P_{GT}$ [N/W] | 0.035 | 0.038 | 0.032 | 0.015 |
| $W_{TO}/P_{EM1}$ [N/W] | 0.053 | 0.050 | 0.049 | 0.038 |
| $W_{TO}/P_{EM2}$ [N/W] | 0.23 | 0.22 | 0.21 | 0.10 |
| $W_{TO}/P_{PMAD}$ [N/W] | 0.22 | 0.21 | 0.20 | 0.10 |
| $W_{TO}/P_{GB}$ [N/W] | 0.045 | 0.042 | 0.041 | 0.034 |
| $W_{fuel}$ [N] | 16480 | 16480 | 17070 | 24130 |
| $W_{TO}$ [N] | 60630 | 60530 | 62590 | 88580 |

Based on the results of the optimisation the optimum design point corresponding to wing loading of 1581 N/m$^2$ and propulsive power loading of 0.05 N/W was determined. This point corresponds to the minimum gas turbine power loading as could be seen on Figure 3.5.

## 3.6. Sizing for Energy

After a design point was chosen, the energy sizing of the mission was performed. This consisted of finding the energy required for each flight mission phase, from which the fuel weight required was found, allowing for estimation of a new

take-off weight. Two methods for energy sizing were considered: a relatively simple method and a more complicated method, both following de Vries [2].

To start both methods, an initial estimate of the empty weight was necessary. This empty weight could then be used in Equation 3.24 to find the take-off weight of the aircraft. The operating empty weight was found through class I weight estimation methods from Roskam [4]. The main differences to traditional class I weight estimations for hybrid electric distributed propulsion aircraft came from the weight of the wing and the weight of the propulsion system. For this aircraft, the weight of the wing was considered similar to traditional aircraft: The increased airflow over the wing increases the lift distribution, but the weights of the distributed propellers counteract the bending moment caused by the additional lift. This was considered a reasonable estimate for this design phase after a discussion with de Vries. The weight of the propulsion system was removed from the estimate to find $W_{\mathrm{OE}'}$ of Equation 3.25, so that it could be updated using the distributed propulsion powertrain model of Section 3.2.

$$W_{\mathrm{TO}} = W_{\mathrm{OE}} + W_{\mathrm{PL}} + W_{\mathrm{fsl}} \tag{3.24}$$

$$W_{\mathrm{OE}} = W_{\mathrm{OE}'} + W_{\mathrm{PT}} \tag{3.25}$$

Following this, the weight of the powertrain was estimated, using Equation 3.15 with the power-loading required for take-off $W_{TO}/P_P$, as well as the specific powers (SP) of each powertrain component. The values for SP used during sizing are shown in Table 3.4. Here Inv and Rec stand for the inverters and rectifiers, respectively, which make up the power converter system. To account for cables and additional elements, a 30% penalty was added to the powertrain weight [2]. As the powertrain component weights depend on the take-off weight and vice versa, they were both iterated upon until convergence.

**Table 3.4:** *Specific powers for components of the powertrain.*

| Parameter | Value |
|---|---|
| $SP_{GT}$ [kW/kg] | 3.6 |
| $SP_{GB}$ [kW/kg] | 12.7 |
| $SP_{EM1}$ [kW/kg] | 12.7 |
| $SP_{EM2}$ [kW/kg] | 7.7 |
| $SP_{Inv}$ [kW/kg] | 19 |
| $SP_{Rec}$ [kW/kg] | 19 |

The first method considered for energy sizing was simpler, relying on the range equation of Equation 3.17. Through this simplified equation, the energy required for cruise could be found, from which the fuel weight could be calculated. In this equation, $e_f$ is the specific energy of kerosene, taken to be 42.8 MJ/kg. Equation 3.17 only estimates the energy required for the cruise phase of the mission. This means that it is best for estimating the fuel weights of long-haul flights where cruise is the longest mission phase.

The second method considered relied on sizing the energy requirements of each mission phase separately. First, the duration of each flight phase was estimated. The flight was divided into four main phases: take-off, climb, cruise and landing. Take-off was estimated to last 30 seconds based on the average take-off time of a twin-engine jet[2]. The time for the climb phase was estimated from a rate of climb of 8 m/s based on similar aircraft, as mentioned in Subsection 3.4.6, and the cruise altitude with $T_{climb} = h_{cr}/ROC$. The cruise time was estimated from the cruise speed and range with $T_{cr} = R/V_{cr}$. The landing time included both the descent and landing times, and was estimated from a rate of descent of 3% from CS-23 requirements using the same procedure as for the climb time. To this time, 10 seconds were added to account for the landing itself.

Following this, the energy required for each phase was calculated using Equation 3.26. The required power of fuel was found for cruise through solving the linear-algebraic powertrain model of Equation 3.15, using the previously calculated power-loading for the total propulsive power $W_{TO}/P_P$. For other flight phases, Equation 3.16 was used with the installed gas turbine power $P_{GT,max}$.

$$E_{\mathrm{fsl},i} = P_{\mathrm{fsl},i} \cdot \Delta t_i \tag{3.26}$$

From this, the fuel weight required could be calculated and the weight of the aircraft updated as per Equation 3.27. Following this procedure for each flight phase, the final weight of the aircraft was found. As the fuel weight depends on the take-off weight and vice versa, iteration was required until convergence was reached.

[2]Article about take-off time, https://eu.usatoday.com/story/travel/columnist/cox/2013/01/13/ask-the-captain-takeoff-take-same-amount-of-time/1831525/, date accessed = 31-05-2022

$$W_{i+1} = W_i - \frac{gE_{\text{fsl},i}}{e_{\text{fsl}}} \tag{3.27}$$

Next, the powertrain weight could be iterated on again, after which a new fuel weight could be found and so on. This allowed for converging on a final estimate for an initial estimation of the take-off weight of the aircraft. For this phase, the iterative process was performed until the difference between the MTOW estimated before calculating the new powertrain weight & fuel weight, and after, was less than 0.1 N.

To verify the results of the weight estimation, a case study by de Vries was reproduced [2]. The top-level requirements and mission information were used and implemented in the iterative process [2]. For these values, the MTOW and the mass breakdown for the fuel weight, the OEW and the payload weight were calculated and compared to the given results from the case study. The results from the process can be seen in Table 3.5 for which the values for the OEW, the fuel weight and the payload weight are given as percentages of the MTOW.

**Table 3.5:** *Results from the case study.*

| Parameter | Value case study [2] | Value simple method | Value complex method |
|---|---|---|---|
| MTOW [kg] | 22400 | 25767 | 28281 |
| OEW [% MTOW] | 57 | 59 | 55 |
| Fuel weight [% MTOW] | 10 | 12 | 19 |
| Payload [% MTOW] | 33 | 29 | 27 |

From Table 3.5 it can be seen that the results of the two methods differed significantly, with the more complex method overestimating the MTOW by 33%, while the simpler method overestimated the MTOW by 15%. The more complex method was found to not converge to results close to the original work, and due to time constraints it was decided to follow the simpler method while accepting a loss in accuracy. It can be seen that for the simpler method, the difference in mass percentage of both the OEW and the fuel weight is below the 2% and for the payload approximately 4%. The values for the OEW and the fuel weight have been overestimated which lead to a smaller mass percentage for payload since this was a given constant value. In general, it was noted that the method implemented had an uncertainty of 15% with respect to the value obtained for the MTOW. Since the mass percentages were approximately the same, the way the method was implemented was considered correct, while taking the uncertainty into account. The first method was preferred over the second as it gives relatively accurate results and implementing the method was feasible within the time frame the group had. In addition, this was a first estimate which was used as a starting point for the rest of the sizing after which iterations could be performed.

Before being able to size for energy, the different mission profiles including critical flight conditions, namely headwind, diversion and OEI, were assessed. Regarding the direction of the wind, for weight sizing, headwind was considered the most critical wind direction as it increases the effective range, $R_{eff}$, the aircraft must fly. Wind coming from other directions will influence both stability & controllability and fuel weight, but the component that influences weight will be smaller than purely headwind. When an aircraft is subjected to headwind the time needed to complete the mission, $T_w$, increases, as shown in Equation 3.28. This is because the resultant ground speed is lower than the cruise speed at which the aircraft would fly at without wind, $V_{cr}$, since the wind speed, $V_w$ is subtracted from the cruise speed to acquire the ground speed. As the ground speed decreases and the mission range, $R_m$, stays the same, the flight time increases. Given this, the effective range also increases as the aircraft is still flying at the same airspeed as before. The TOW was then calculated based on the effective range given by Equation 3.29. Diversion and loiter were assumed to add 30 minutes to operation, added similarly to the effective range.

$$T_w = \frac{R_m}{V_{cr} - V_w} \tag{3.28}$$

$$R_{eff} = V_{cr} \cdot T_w \tag{3.29}$$

For OEI conditions, the L/D decreases since part of the propellers stop, causing more drag. The power the gas turbines provide was oversized by a factor of 2 so that in case of failure of one gas turbine, there is enough power to continue the mission nominally. For the electric motors the power they need to provide was oversized by 10/9 in cause of failure of one of the motors.

The different mission profiles checked for weight sizing are summarised in Table 3.6. The mission profile set in **REQ-STA-CUST-07** was not included in the Table as both range and payload were higher for mission A. For mission A and B, a headwind of 15 kts was used as for 3500 flights of the Cessna 182S Skylanes the average headwind speed was of

7.5 kts[3]. For mission C, the ArctEvac mission, a headwind of 53.24 kts was used based on **REQ-STA-CUST-03** and the previously performed environmental analysis [6]. The effect of diversion was also analysed. For this it was assumed that in OEI conditions ATC would allow priority landing to the aircraft, so diversion was only considered for nominal operation. It was found that headwind and OEI were the critical case in comparison to diversion, so the aircraft was sized based on increased effective range due to headwind and OEI conditions.

**Table 3.6:** *Mission profiles.*

| Mission | Range [nm] | Payload [lbs] | Conditions |
|---|---|---|---|
| A | 150 | 4400 | Headwind of 15 kts |
| | | | OEI halfway |
| | | | Headwind of 15 kts + OEI 2/3 of range |
| B | 400 | 3000 | Headwind of 15 kts |
| | | | OEI halfway |
| | | | Headwind of 15 kts + OEI 2/3 of range |
| C | 1350 | 426 | Headwind of 53.24 kts |
| | | | OEI halfway |
| | | | Headwind of 53.24 kts + OEI 2/3 of range |

After verifying the method and analysing the different mission profiles, the distributed propulsion concept was sized. The critical mission profile, or the one that resulted in the highest MTOW, was found to be mission A, with a range of 150 nm and payload mass of 1995 kg accounting for 19 passengers, with a headwind of 15 kts throughout the mission, and OEI at 2/3 of the mission. The weights of the different components are shown in Table 3.7. The fuel weight for mission C, which is the medevac mission, shown in the table is the amount of fuel needed taking into account the OEW of the mission A. The values in the table correspond to the weights for the optimum design point presented in Section 3.5. A contingency of 15% should be added to the MTOW. However, as the verification study shows that the method oversized the weight by 15%, the effect of the sizing method uncertainty and design contingency cancel each other out.

**Table 3.7:** *Weights of different components based on energy sizing.*

| Parameter | Value |
|---|---|
| MTOW [N] | 64322.23 |
| OEW [N] | 42826.88 |
| Empty weight [N] | 28246.01 |
| Propulsion system weight [N] | 11975.44 |
| Fuel weight mission A [N] | 1924.40 |
| Fuel weight mission C [N] | 16714.08 |

[3]Wind analyses on the Cessna 182S Skylanes, https://www.aopa.org/news-and-media/all-news/2017/january/pilot/savvy-maintenance-big-data, date accessed = 08-06-2022

# 4

# Subsystem Design

As the foundation of the aircraft performance was established, the JAPA-12 was sized. The sizing procedure of the aircraft configuration is covered in this chapter. The sizing started off with the layout of the fuselage, which is covered in Section 4.1. After that, the wing was designed together with its high lift devices and control surfaces. The wing sizing is presented in Section 4.2. The wing sizing is followed by the fuel system in Section 4.3 as the fuel is stored inside the wings. The sizing of the propulsive group is discussed in Section 4.4. This is followed by the sizing of the horizontal and vertical tail in Section 4.5. To be able to safely land on snow and ice, an unconventional landing gear was incorporated. The sizing of the uncommon landing gear is explained in Section 4.6. To allow for translation and rotation of all on-board movables, hydraulics were included. The hydraulics are covered in Section 4.7. To power the aircraft, on-board electricity was required. The electrical components are presented in Section 4.8. Additionally, due to the harsh environmental conditions, heating, ventilation and air conditioning was included, which is covered in Section 4.9. Finally, the weight of the aircraft was estimated via the class II estimation method, which is presented in Section 4.10.

## 4.1. Fuselage Layout

In this section the layout of the fuselage is presented and justified. A configuration with two or three seats abreast was considered feasible. The two configurations were sized based on **REQ-STA-MAR-02**, the requirement that 19 passengers shall be seated. Firstly, the cross section is presented in Subsection 4.1.1. Based on the diameters of the fuselages and the seating configurations, the lengths of the fuselages were determined. The lengths are presented in Subsection 4.1.2. A trade-off was performed. The methodology of which is highlighted in Subsection 4.1.3. The doors required and the pressurisation of the aircraft is discussed in Subsection 4.1.4. Finally, an adapted fuselage interior with all the medical equipment is shown in Subsection 4.1.5.

### 4.1.1. Set Up Cross Section

This section elucidates how the cross section of the fuselage was determined. Firstly, all the interior was placed and sized depending on the minimum dimensions set for comfort and safety as determined by Roskam in Airplane Design Part III [25]. For both design options the choice was made to lower the aisle floor. This was done to provide enough space such that passengers can stand in the aircraft and reduce the diameter of the fuselage. In addition, in the case of a medical evacuation mission it is necessary for the doctor to be able to stand such that they may comfortably operate. The cross-sections are shown in Figure 4.1 and the dimensions are summarised in Table 4.1.

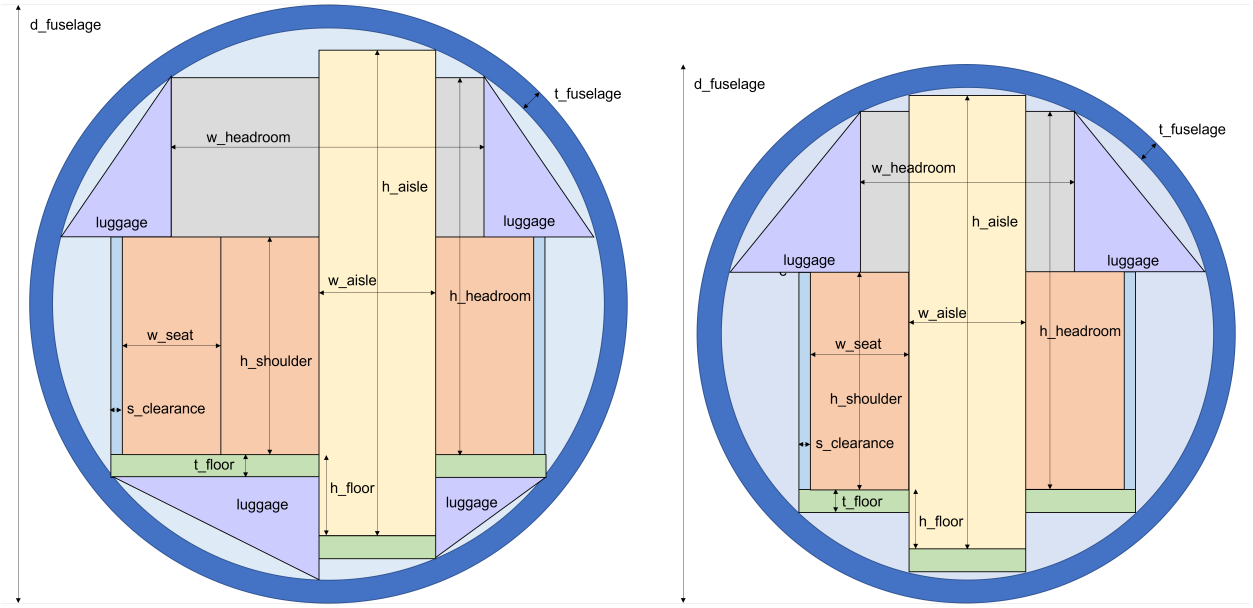


**Figure 4.1:** *Fuselage cross section. Design option with three seats abreast on the left and two seats abreast on the right.*

Note, the choice was made to use a circular fuselage cross-section. The CS-23 regulations dictate that the fuselage must be pressurized such that an equivalent pressure of 8000ft is maintained within the cabin. As **REQ-STA-CUST-06** specified the service ceiling to be at least 25000ft, pressurisation is required. The cyclic loading due to the pressurisation of the fuselage during each flight makes the fuselage prone to fatigue failure. Fatigue failure may be accelerated through stress concentrations. A pressurised non-circular vessel suffers from stress concentrations. To prevent failure and ensure longevity, a non-circular fuselage requires additional reinforcement, therefore increasing weight [26]. To make the fuselage as light as possible, the option of a non-circular cross-section was discarded

**Table 4.1:** *Fuselage cross section dimensions.*

| Seats abreast | 3 | 2 |
|---|---|---|
| $d_{fuselage}$ [m] | 2.61 | 2.35 |
| $w_{seat}$ [m] | 0.43 | 0.43 |
| $h_{shoulder}$ [m] | 0.95 | 0.95 |
| $w_{headroom}$ [m] | 1.37 | 0.94 |
| $h_{headroom}$ [m] | 1.65 | 1.65 |
| $w_{aisle}$ [m] | 0.51 | 0.51 |
| $h_{aisle}$ [m] | 2.12 | 1.98 |
| $t_{floor}$ [m] | 0.10 | 0.10 |
| $h_{floor}$ [m] | 0.35 | 0.26 |
| $s_{clearance}$ [m] | 0.05 | 0.05 |
| $t_{fuselage}$ [m] | 0.10 | 0.10 |
| $A_{luggage}$ [$m^2$] | 0.62 | 0.40 |

### 4.1.2. Fuselage Length

Following from the fuselage cross-section dimensions, the fuselage length was determined. The approach taken was to first determine the minimum length of the fuselage with all required interior, then check with statistical data and aerodynamic effects if the fuselage design is reasonable. Again the minimum dimensions for comfort and safety determined by Roskam in Airplane Design Part III [25] are used.

The nose and tail lengths are dictated by the fineness ratios set. The nose fineness ratio was not considered a driving factor for the performance of the fuselage. Due to the low cruise mach number, drag divergence at the nose is not an issue. The nose fineness ratio is therefore dictated through the minimal space required to facilitate the cockpit and frontal pressure bulkhead. The tail cone fineness ratio dictates the aerodynamic characteristics and the amount of extra storage volume [25]. The implications of having a longer fuselage is that the empennage may be smaller, however the skin friction also increases. An analysis was done to assess whether the total weight of the aircraft may be optimised through increasing the length of the fuselage and decreasing the size of the empennage. This analysis is presented in Subsection 4.5.7. The conclusion of this analysis was that the fuselage should be as short as possible. Therefore the tail cone fineness ratio was set to be as small as possible. All parameters for the length of the fuselage are summarized in Table 4.2.

### 4.1.3. Fuselage Design Selection

The two different fuselage designs were compared based on the weight, drag, and cargo storage volume. The methods used to quantify these parameters are described below. Based on these parameters a trade-off was performed.

#### Weight

To estimate the weight of the fuselage the method of Torenbeek was used [25]. Equation 4.1 uses statistical data of commercial transport aircraft with a dive speed higher than 250 kts.

$$W_{fsl} = 0.021 K_f \left( \frac{V_D l_h}{w_f + h_f} \right)^{\frac{1}{2}} (s_{fsl})^{1.2} \tag{4.1}$$

The value of $K_f$ is set depending on the configuration of the aircraft. The fuselage was pressurised as will be explained in Subsection 4.1.4 and the landing gear was attached to the fuselage as a high wing configuration was used, therefore a value of 1.155 was used [25]. The dive speed followed from the flight envelope which is presented in Section 6.4. The $w_f$ and $h_f$ are the width and height of the fuselage respectively. The value of $l_h$ depends on the location of the

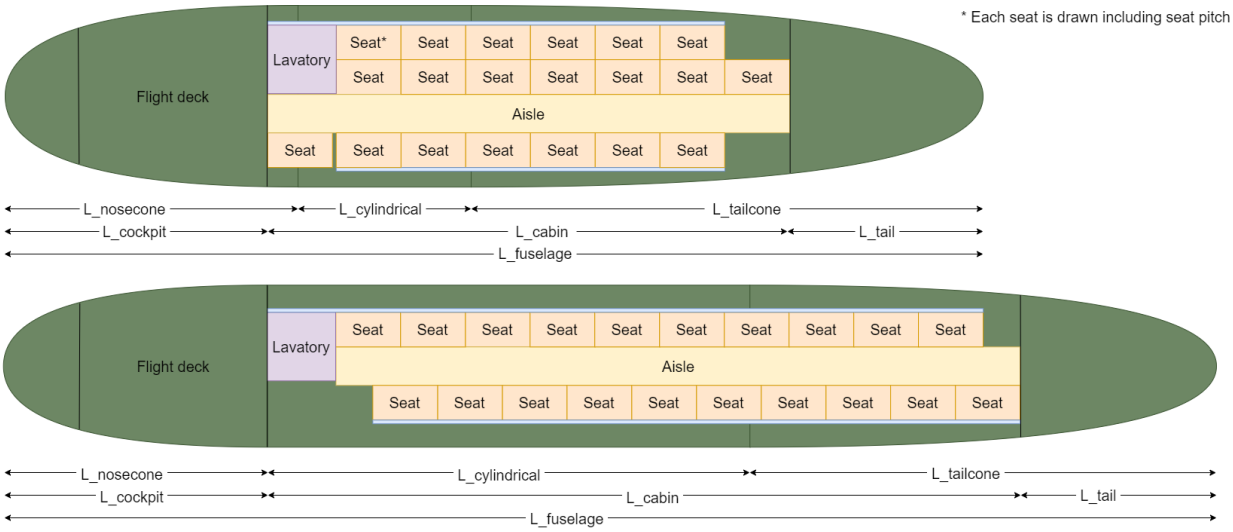


**Figure 4.2:** *Fuselage top view options with three and two seats abreast.*

**Table 4.2:** *Fuselage top view dimensions.*

| Seats abreast | 3 | 2 |
|---|---|---|
| $l_{fuselage}$ [m] | 13.0 | 16.1 |
| $l_{cockpit}$ [m] | 3.5 | 3.5 |
| $l_{cabin}$ [m] | 6.9 | 10.0 |
| $l_{tail}$ [m] | 2.6 | 2.6 |
| $l_{nc}/d_{fsl}$ | 1.5 | 1.5 |
| $l_{tc}/d_{fsl}$ | 2.6 | 2.6 |
| $l_{nosecone}$ [m] | 3.9 | 3.5 |
| $l_{cylindrical}$ [m] | 2.3 | 6.4 |
| $l_{tailcone}$ [m] | 6.8 | 6.2 |
| $w_{lavatory}$ [m] | 0.91 | 0.91 |
| #pax | 19 | 19 |
| #flight attendants | 1 | 1 |

empennage and follows from the analysis presented in Section 4.5. Finally $S_{fsl}$ denotes the surface area of the fuselage gross shell area. This is calculated through assuming the fuselage is cylindrical and has spherical ends.

**Drag**

To estimate the drag of the fuselage the statistical formulas of Roskam are used. The drag of the fuselage consists of two components, the zero-lift drag and drag due to lift. The zero-lift drag coefficient follows from Equation 4.2 and the lift due to drag coefficient is calculated through Equation 4.3.

$$C_{D_{0_{fsl}}} = R_{wf} C_{f_{fsl}} (1 + \frac{60}{(l_f/d_f)^3} + 0.0025(l_f/d_f)) \frac{S_{fsl}}{S} \tag{4.2}$$

$$C_{D_{L_{\text{fsl}}}} = 2a^2 S_{b_{\text{fsl}}}/S + \eta c_{d_c} |\alpha|^3 S_{plf_{\text{fsl}}}/S \tag{4.3}$$

The parameter $R_{wf}$ dictates whether there is significant fuselage-wing interaction. As only the fuselage drag was considered, a value of 1 was assigned. For both fuselages the relevant dimensions were input and the drag was calculated.

**Cargo Storage Volume**

More cargo storage volume was a desirable quality as it allowed for transportation of more and different types of goods. In Subsection 4.1.1 the area of the cross section where cargo may be stored was estimated. As the aircraft has a high wing configuration, the cargo compartments are interrupted by the root chord of the wing propagating through the fuselage. The storage of the landing gear also interrupts the cargo compartment. Taking this into account and using

the lengths of the fuselages defined in Subsection 4.1.2 the cargo volume was calculated. The allocation of the cargo compartment is shown in Figure 4.3.

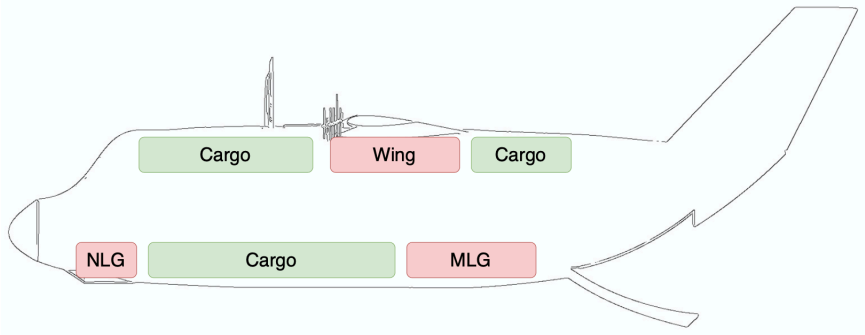


**Figure 4.3:** *Cargo compartments of the JAPA-12.*

**Aisle Height**
Finally, the aisle height was also taken into account. The reason why this was considered an important parameter was that for the medevac mission the doctor must be able to comfortably stand. If the aisle height was too small this may hinder the doctor from operating.

**Design Selected**
All the relevant parameters discussed are summarized in Table 4.3. The three seats abreast option was chosen for the final design. The main reason for the selection of the three seats abreast configuration was due to the weight. The three seats abreast option was more than 650 kilos lighter, which is a colossal difference. The two seats abreast fuselage was only advantageous with regards to drag. Nevertheless the reduction in drag did not justify the large increase in weight. With respect to the other parameters the three seats abreast option was also slightly better.

**Table 4.3:** *Fuselage parameters comparison.*

| Seats abreast | 3 | 2 |
|---|---|---|
| Mass [kg] | 2452.12 | 3129.69 |
| Drag coefficient | 0.01199 | 0.00996 |
| Cargo volume [$m^3$] | 3.6252 | 3.184 |
| Aisle height [m] | 2.12 | 1.98 |

### 4.1.4. Fuselage Doors
In this subsection the layout of the doors are explained. Firstly, as per CS-23 regulations, emergency exit doors must be placed. Next, the inclusion of a rear door is explained and the effects on the weight of the aircraft are assessed.

**Emergency Exits**
The CS-23 regulations require the fuselage to have at least three emergency exits, besides the bigger passenger entry door. Two of those exits should be on the opposite side of the passenger entry door, the other should be on the same side [27]. The emergency exits should have a minimum size of 61 cm wide and 122 cm high. The passenger entry door was located at the left side of the fuselage and at the back of the cabin. The three emergency exits were the minimum width of 61 cm and are located around windows. Besides, the aircraft had a rear loading door which could be used for loading a patient or could be used as main loading door.

**Rear Door**
Having a loading door in the rear facilitates easy patient loading. The patient could be carried directly into the fuselage without needing to perform a difficult rotation when entering the fuselage. However, installing a back door implied that additional thought was required for the tail cone design. Furthermore, the connection between the door and the tail cone needed to be made airtight to not lose pressure during flight. This then lead to the problem of replacing a spherical bulkhead with a non-optimal pressure resisting shape, which resulted in additional weight.

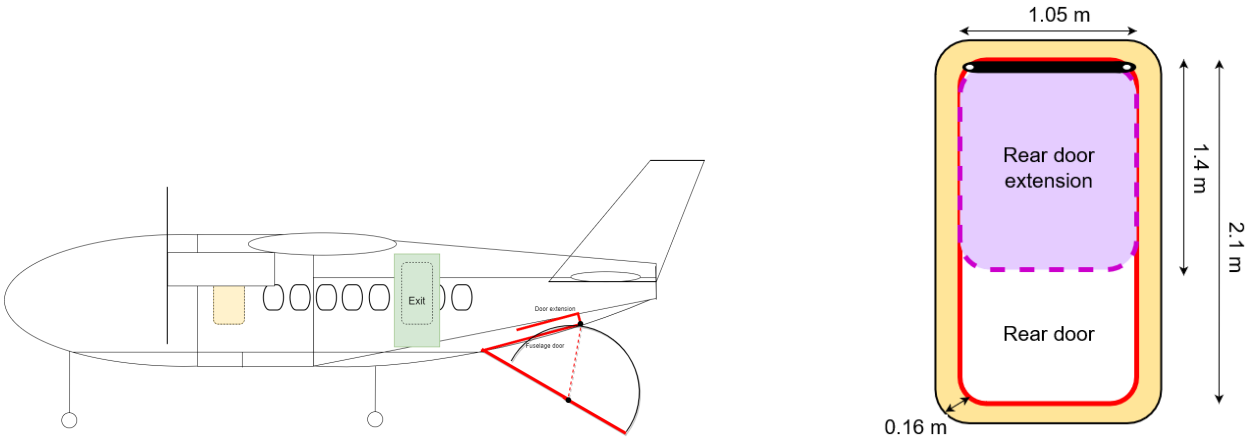


**(a)** *Fuselage side view used for rear door sizing.*

**(b)** *Illustration of the rear door as seen from inside the fuselage.*

**Figure 4.4:** *Fuselage illustrations used for rear door sizing.*

To determine the required size of the rear door, a sketch was made of the side view of the fuselage. The door size was made such that it was connected to the cabin floor, and allowed for a $30^{\circ}$ slope to ease the loading of payload. The sketch is provided in Figure 4.4a.

Looking at Figure 4.4a, where the rear door is indicated in red, a $30^{\circ}$ slope was created when a folded door was present. The folded door was required as a long single door did not fit inside the tail cone due to the empennage. Additionally, the door extension was shorter than the fuselage part of the door, as it had to be able to rotate to be able to reach the ground. This length was determined via the black half-circle, indicating the radius required to rotate the door extension in Figure 4.4a. This resulted in a loading door, with a fuselage door length of 2.1 m, and a door extension length of 1.4 m. Additionally a door width of 1.05 m was set, as this was the maximum width which fitted between the two most aft seats, where the door was located. Therefore, the pressure bulkhead had to be extra reinforced for the 2.1 m long door, with a width of 1.05 m at the tail cone. The door needs to be air tight using the same closing mechanism as a standard airliner door.

The end of a pressure vessel, such as a fuselage, is usually spherical to minimise the pressure stresses in the fuselage. When this shape is altered, calculations are needed to prove this design is feasible. The fuselage was thought of as a pressure vessel with a semi-spherical bulkhead in the cockpit area and a bullet tip type bulkhead in the tail cone. The door is designed to withstand the pressure difference between the 8000 ft minimum pressurisation altitude and the 25000 ft surface ceiling pressure. The pressure difference was calculated to be 37.67 kPa using the ISA equations.

The minimum thickness was calculated using standard formulas for specifically shaped pressure vessels [28]. Furthermore, the thin walled structure assumption was used, which resulted in simplified formulas being used. This assumption was considered valid as the radius of the fuselage was more than 10 times larger than the wall thickness [28]. This minimum thickness came from the connection between the bullet-shaped tail cone and the cylindrical fuselage. Comparing this minimum thickness with the minimum required thickness to cope with the structural stresses imposed by aerodynamic loading

Now, as a rear door (or cut-out) was being used, an additional stress concentration was expected. For large cut-outs, the stress concentration was determined via approximating the door as an elliptical shape. For this, the general approach of the Introduction to Aerospace Engineering II was used to determine the stress concentrations in close proximity of the cut-out [29]. This resulted in a stress concentration factor of 5 in close proximity of the rear door due to the large dimension of the door. The minimum required fuselage thickness when the material properties of respectively Al 7075-T6, Al 2024-T3 and unidirectional CFRP were implemented were 0.049, 0.079 and 0.016 mm. More details regarding the properties and choice of these materials will be presented in Section 7.2. For the door, a reinforced band around the door frame with a width of 16cm was necessary to cope with the peak stress. This band was estimated using images of fuselage frames from other pressurised aircraft. Using these images, it was estimated that the reinforcement bandwidth is approximately 10% of the door width, with an error margin of 5%. The minimum thickness for the door area plus reinforcement band must then be, for the aforementioned materials respectively, 0.245, 0.395 and 0.08 mm. This resulted in a rear door sized as depicted in Figure 4.4b, where the orange area represents the additional door reinforcements, and the black cylinder represents the hinge connecting the rear door extension to the rear door. The

minimum required thickness due to applied loads was analysed as well. The results shall be presented in Section 7.1.

### 4.1.5. Medical Configuration

For the medical evacuation at Amundsen-Scott and possibly other airports, the aircraft configuration was altered to a medical one. The configuration is shown for the X seats abreast fuselage in Figure 4.5. The last four rows of chairs are removed. Instead, a standard ambulance stretcher of 2 m long and 60 cm wide is put in, as depicted in Table A.1. [4] The medical equipment is divided over ICU carts, which are 62.5 cm long, 47.5 cm wide and 92 cm high[5]. The total volume of medical equipment resulted in five carts. The stretcher is placed directly next to the aisle and at the rear of the fuselage to ensure easy loading via the rear door. In addition, to the medical equipment and the stretcher there are seats for two doctors or nurses and nine passengers (or eight passengers and a flight attendant). Note, that for the Amundsen Scott medical evacuation mission these seats may only be filled with the required medical personnel. The list of medical equipment considered can be found in Table A.1.

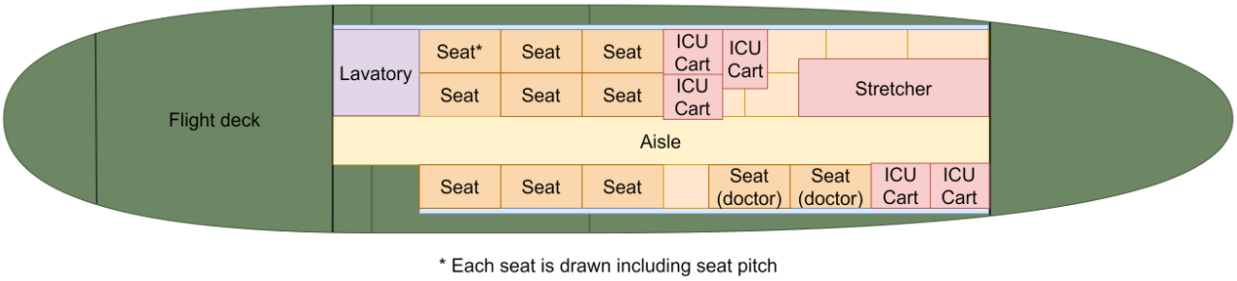


**Figure 4.5:** *Top view of fuselage in medical configuration.*

## 4.2. Wing Design

Sizing the aircraft wing was done according to the constructed wing-loading diagram. Initially, the wing dimensions were determined based on methods established by Torenbeek [30], which is covered in Subsection 4.2.1. Accordingly, an airfoil was selected as result of a trade-off process, which is covered in Subsection 4.2.2. Finally, the sizing of the high lift devices and control surfaces is covered in Subsection 4.2.3.

### 4.2.1. Wing Planform

This subsection presents and justifies the dimensions of the wing planform. The wing surface area was set to be 42.23 $m^2$. The loading diagrams and the design point determined in Section 3.5 were used to determine the initial surface area of the wing. However from the analysis conducted in Subsection 4.2.3 the surface area had to be increased to provide sufficient space to house the high lift devices and control surfaces.

The quarter chord sweep angle of the wing was set to zero degrees. Wing sweep is used to prevent drag divergence. The cruise mach speed of the aircraft was below the mach at which drag divergence occurred, therefore no wing sweep was required. On top of that, sweeping the wing also adds weight, which is undesired.

The taper ratio of the wing was set to 0.4. The reason for this was to achieve an elliptical lift distribution, reducing the effects of induced drag. The value set was also in line with the sizing methods described by Torenbeek [30].

The aspect ratio was set to 10. The value was slightly higher than reference aircraft [25] due to the effects of distributed propulsion. The distributed propulsion system provided additional bending relief over the span of the wing. This was due to the weight of the engines being more spread out compared to a conventional aircraft. Therefore the aspect ratio could be increased without having to reinforce the structure.

Finally, the dihedral angle was set to be -1°. Conventional aircraft have a dihedral angle of approximately 5° [31]. Higher dihedral provides more roll instability during side-slipping flight. This may be desired to make the aircraft controllable. The high wing configuration tends to cause roll instability in side slipping flight [32]. During the stability analysis, it was

[4] Universal Medical, Ambulance stretcher, https://www.universalmedicalinc.com/ferno-model-35-a-mobile-transporter-x-frame-ambulance-cot-with-burgundy-460-mattress-and-black-restraints.html#:~:text=SPECIFICATIONS%3A,Min%209%22%20%2D%20Max%2040%22, date accessed = 21-06-2022

[5] Medical emergency trolley for ICU, https://www.medical-hospitalbed.com/sale-1979516-adjustable-ambulance-cart-medical-emergency-trolley-for-icu.html, date accessed = 25-05-2022

found that the dutch roll eigenmotion was damped exceptionally slow. To speed up the dutch roll damping, an anhedral angle of 1° (or dihedral of $-1°$) was set. The extreme anhedral angle was found as $-4.5°$, as at that point rolling became unstable. Therefore, to meet both the roll and dutch roll stability, and allow for roll control, a dihedral angle of $-1°$ was set. This justified the significantly lower value for dihedral compared to conventional aircraft. The major wing dimensions are summarized in Table 4.4

**Table 4.4:** *Wing planform parameters.*

| Parameter | Value |
|---|---|
| Dihedral [°] | -1 |
| Aspect ratio | 10 |
| Surface area [m$^2$] | 42.23 |
| Taper ratio | 0.4 |
| Span [m] | 20.55 |
| Chord root [m] | 2.94 |
| Chord tip [m] | 1.18 |
| MAC [m] | 2 |
| Quarter chord sweep [°] | 0 |

### 4.2.2. Main Wing Airfoil Selection

The first step of designing a wing was the selection of the airfoil. Selecting the airfoil for the main wing was done based on a set of pre-determined criteria established by the team. With these criteria, a trade-off was made to find the most suitable airfoil type for the main wing. The trade-off criteria are first covered below, together with their rationale. Note that the trade-off does not include the effects of the distributed propulsion configuration on the wing performance. This was intentionally left out due to the fact that sizing methods from de Vries [2] assumed the wing to be fully immersed in the propeller slipstream, and therefore the effect would be the same.

- The lift to drag ratio at $5°$ angle of attack: Airfoil lift to drag ratios were compared at $\alpha = 5°$ in order to determine basic performance characteristics in a configuration similar to cruise conditions. The largest score was favourable as this directly results in increased performance benefits.
- The thickness to chord ratio t/c: A higher t/c results in more fuel storage and a larger moment of inertia of the wing. Therefore, a higher t/c ratio was desired.
- Maximum lift coefficient ($C_{l_{max}}$): Maximum airfoil lift coefficients were compared to determine which airfoil allowed for the least complex high lift devices. Less complexity results in a lighter design, with a lower probability of component failure for the high lift devices. Therefore, a high $C_{L_{max}}$ was favourable.
- Stall angle of attack $\alpha_{stall}$: The stall angle of attack allows for angle of attack margins during flight. For example, when a wind gust is experienced in cruise, a pitch up moment could be generated, increasing the angle of attack, which could lead to stall. Therefore, a high stall angle of attack was desired.
- Trailing Edge (TE) devices: As it was expected that the wing would have to feature trailing edge devices to achieve the required $C_{L_{max}}$ for take-off and landing. The TE of an airfoil was scored between 1 (worst) and 5 (best) for allowing TE devices to be placed. Airfoils with little thickness at the TE were scored lower for this requirement. Leading edge devices were not considered as criteria, as the distributed propulsion would not allow for sufficient available space.

The found values[6] are tabulated in Table 4.5, where the TE devices scoring was found qualitatively by investigating the airfoil shape. The TE scoring was done between 1 and 10, where 1 was horrible for TE device inclusion, and 10 was perfect.
As the necessary values for the airfoil trade-off were found, the actual trade-off was carried out. For the actual trade-off, the weights of each criteria had to be determined. The weight, together with their rationale is listed below, where the assigned weights could range from 1 to 5. Here, a weight of 1 was considered nice to have, but not really important; and a weight of 5 was considered as a driving criteria and thereby very important.

- L/D at $\alpha = 5°$: The aerodynamic efficiency of an aircraft was considered very important (5). As one of the design missions requires a flight distance of 1350 nautical miles, it was desired to prioritise efficient flight. On top of that, a high efficiency made it easier to meet the sustainability requirements. Therefore, a weight of 5 was assigned to aerodynamic efficiency.

[6]Website containing simulation data for various airfoil types, http://airfoiltools.com/, date accessed = 30-05-2022

**Table 4.5:** *Airfoil values based required for the trade-off.*

| Airfoil | L/D$_{\alpha=5^\circ}$ | t/c [%] | $C_{l_{max}}$ | $\alpha_{stall}$ | TE friendly |
|---|---|---|---|---|---|
| NACA 0018 | 65 | 18 | 1.4 | 17.5 | 6 |
| NACA 63(2)-215 | 72 | 15 | 1.65 | 18 | 6 |
| NACA 2415 | 100 | 15 | 1.55 | 16 | 6 |
| NACA 24112 | 84 | 12 | 1.5 | 15 | 4 |
| NACA 64-209 | 68 | 9 | 1.15 | 10.5 | 4 |
| NACA 23012 | 82 | 12 | 1.55 | 18 | 9 |
| NACA 23015 | 80 | 15 | 1.56 | 19 | 9 |
| NACA 642-015A | 62 | 15 | 1.2 | 16 | 6 |

- The thickness to chord ratio t/c: The t/c ratio was assigned an above average importance (4). As a high t/c allowed for fuel storage and a lighter structure, this translated back to the cruising capabilities of the aircraft. Storing more fuel in the same wingspan meant either allowing a smaller wing, which reduces drag, or fly further distances as more fuel could be included. Therefore, a weight of 4 was assigned to the thickness to chord ratio of the airfoil.
- $C_{L_{max}}$: The maximum lift coefficient of the airfoil was considered an above average importance (4). This idea resulted from the fact that not all aircraft lift has to be generated by the wing solely. Additional high lift devices were allowed to be used to obtain a certain take-off and landing lift coefficient. However, due to the required STOL characteristics of the aircraft, it was also desired to generate high lift with the wing. This resulted in considering $C_{L_{max}}$ as important, with a weight of 4.
- $\alpha_{stall}$: The stall angle of attack of the airfoil was considered to be of average importance (3). As a high stall angle of attack resulted in some contingency with respect to the cruise angle of attack. For instance, when cruising at $\alpha = 8^\circ$, with a stall angle of $\alpha_{stall} = 10^\circ$, little room for disturbances was present. However, it was also possible to make a stable aircraft, which was very disturbance-resistant. Therefore, a high stall angle is desired, but when this criteria was not met, the design was still feasible. Hence, a weight of 3 was assigned.
- TE devices: The ability to include trailing edge devices was considered to be of above average importance (4). The main reason for this resulted from the idea that high lift devices were likely to be used at the trailing edge to achieve the required lift coefficient for take-off and landing. It was assumed to be slightly less important with respect to the first criterion, as additional lift would also be generated as a result of the distributed propulsion configuration. Therefore, less complex trailing edge devices were expected to be used.

Once all criteria and related airfoil parameters had been established, the airfoil trade-off was carried out. An overview of the scoring per criterion is included in Table 4.6 below. The airfoil performance was scored via the performance indicator $\eta$, which ranged from 0 to 10. The performance indicator stated how well the airfoil scored on a certain criterion. Thereby, the cumulative score of each airfoil was established by summing up all the multiplications of the criterion weight with the performance indicator. Or in mathematical terms: $\sum w_i \cdot \eta_t$, where $w$ indicates the criterion weight, and $\eta$ indicates the airfoil performance indicator for that criterion.

**Table 4.6:** *Trade-off table for the airfoil of the wing.*

| Criterion / Airfoil | L/D$_{\alpha=5^\circ}$ | t/c [%] | $C_{l_{max}}$ | $\alpha_{stall}$ | TE devices | $\Sigma w_i \cdot \eta_t$ |
|---|---|---|---|---|---|---|
| NACA 0018 | 25 yellow | 32 green | 28 yellow | 24 yellow | 24 yellow | 133 |
| NACA 63(2)-215 | 30 green | 28 yellow | 36 green | 24 yellow | 24 yellow | 142 |
| NACA 2415 | 45 bright green | 28 yellow | 32 green | 21 yellow | 24 yellow | 150 |
| NACA 24112 | 35 green | 24 yellow | 32 green | 18 red | 16 red | 125 |
| NACA 64-209 | 30 green | 20 yellow | 16 red | 12 red | 16 red | 94 |
| NACA 23012 | 35 green | 24 yellow | 36 green | 24 yellow | 36 green | 155 |
| NACA 23015 | 35 green | 28 yellow | 36 green | 27 yellow | 36 green | 162 |
| NACA 642-015A | 25 yellow | 28 yellow | 20 red | 21 yellow | 24 yellow | 118 |

From the trade-off presented in Table 4.6, it was concluded that the NACA 23015 airfoil was superior as the cumulative score was the highest based on the pre-determined criteria. As a result, the NACA 23015 airfoil was used for the main wing.

### 4.2.3. High Lift Devices & Control Surfaces

As the main wing planform had been designed, the sizing of the high lift devices and control surfaces was carried out. The location of both the high lift devices and control surfaces were mainly focused on the trailing edge of the wing, as the leading edge was mainly filled up with engines and propulsors. The sizing of the high lift devices and control surfaces was done via the Torenbeek method [30].

#### High Lift Devices Sizing

To size for the high lift devices, the maximum required difference in lift coefficient, $\Delta C_L$, was established. From the wing- and power loading, a maximum lift coefficient for landing of $C_{L_{landing}} = 3.2$ was required to allow for a maximum landing distance of 2500 ft. Additionally, from the aerodynamic analysis of the aircraft, a maximum clean configuration lift coefficient of $C_{L,max_{clean}} = 1.38$ was found. Meaning that the flaps had to generate an additional 1.74 of lift coefficient, as the remaining 0.08 of lift coefficient was generated via the $\Delta C_L$ terms of distributed propulsion.

As a significant increase of lift coefficient was required, the team had chosen to use Fowler flaps as high lift device type. The main reason for this was that Fowler flaps were the simplest flap type possible to achieve the required increase in lift. Simpler flap types, like the plain flap or the split flaps, did not provide the required lift increase without using the majority of the wing. The reason the simplest flap type was picked was to minimise structural complexity, chance of failure, and maintenance cost. Now, due to the inclusion of Fowler flaps, additional flap tracks were added to the wing. The flap tracks were not sized in detail, but the weight and drag of the tracks were taken into account during the design process. The inboard flap location was dominated by the fuselage, as the high lift devices were not to be placed inside the fuselage. Additionally, as the flaps are movables, a clearance of 18 cm was introduced. This resulted in an inboard flap location of 1.5 m along the wing span. Carrying out the high lift devices sizing method of Torenbeek [30] resulted in a flap width of 5.9 m for the wing planform established in Subsection 4.2.1. The major high lift device parameters are presented in Table 4.7.

#### Aileron Sizing

The sizing of the ailerons was dominated by regulations. The CS-23 regulations state that an aircraft weighing more than 2722 kg should be able to roll 60° within 7 seconds [33]. Therefore, the ailerons were sized such that a minimum roll rate of $8.57°/s$ was achieved.

The aileron sizing was mainly dependent on the airfoil type selected in Subsection 4.2.2. However, as the airfoil type had already been selected, the only possible way to manipulate the roll rate was via selecting proper aileron dimensions. To allow for excellent roll control, to counter the harsh weather environments from the requirements, a large aileron was desired. Therefore, the inner aileron location was set to be at 7.5 m along the wing to provide clearance with respect to the Fowler flap. Additionally, an outer aileron location of 10 m was selected, to allow some clearance with the wing tip. Working out the sizing method from Torenbeek [30] resulted in a maximum roll rate of $26.8°/s$. Note that this was very over-designed regarding the CS-23 requirements. However, as it is generally desired that an aircraft can still be operational when a single point of failure is experienced, the team decided to keep the sized aileron size, as the required roll rate could still be met when one aileron fails. The aileron parameters are presented in Table 4.8.

**Table 4.7:** *High lift devices parameters.*

| Parameter | Value |
|---|---|
| Flap type | Fowler flap |
| Maximum flap deflection [°] | 40 |
| Inboard flap location [m] | 1.5 |
| Outboard flap location [m] | 7.4 |
| Flap width [m] | 5.9 |
| Chord-wise flap length, $c_f/c$ | 0.2 |

**Table 4.8:** *Aileron parameters.*

| Parameter | Value |
|---|---|
| Maximum roll rate [$°/s$] | 26.8 |
| Maximum aileron deflection [°] | 10 |
| Inboard aileron location [m] | 7.5 |
| Outboard aileron location [m] | 10 |
| Aileron width [m] | 2.5 |
| Chord-wise aileron length, $c_f/c$ | 0.25 |

Finally, the wing planform is presented in Figure 4.6. What is important to note is that the flaps and aileron structures restricted the placement of the spars. This effected the sizing of the fuel tanks and the wingbox, as will be discussed in Subsection 4.3.1 and Subsection 7.1.2 respectively.

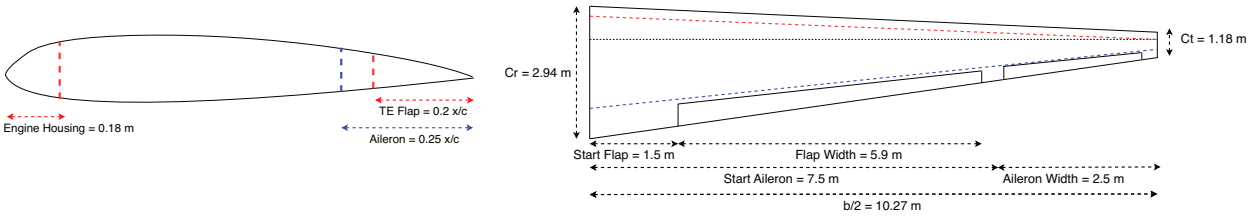


**Figure 4.6:** *Wing planform. The front spar must be placed behind the red line and the rear spar must be place in front of the blue line.*

## 4.3. Fuel System

This section presents the design of the fuel system. Firstly, the procedure used to size the fuel tanks is highlighted in Subsection 4.3.1. The integration of the fuel tanks in the wing is also discussed. Then in Subsection 4.3.2 the system used to control the fuel flow is presented.

### 4.3.1. Fuel Tank

To facilitate bending relief it is desirable to store the fuel in the wings of the aircraft. The weight of the fuel opposes the load due to lift and therefore allows for a leaner wingbox design. Therefore the fuel tanks were integrated inside the wingbox. The final dimensions of the wingbox and fuel tank are set in Subsection 7.1.2. Based on the analysis presented in Section 3.5, the fuel tanks must had to be able to store 1144.1 kg of synthetic kerosene. This translated to a volume of 1.43 $m^3$.

As will be justified in Subsection 7.1.2 the front and rear spar are placed at 17% and 70% of the chord, respectively. The chord and thickness of the wing change along the span. The chord length is calculated through Equation 4.4. The cross sectional area available for storing fuel at each span-wise location was derived using the contour of the airfoil. To facilitate the storage of 1.43 $m^3$ of synthetic kerosene the fuel tanks were set to span from the root of the wing 2.83 m outwards.

$$C_{\left(\frac{y}{b/2}\right)} = C_r - C_r(1-\lambda)\left(\frac{y}{b/2}\right) \tag{4.4}$$

In addition, due to the extremely cold temperatures at Amundsen-Scott a system is installed to stop the fuel from freezing. Synthetic kerosene has a freezing point of -47°C[7]. As was analysed in the Baseline Report, the temperature at cruise altitude is around -32°C. However at the surface of Amundsen-Scott the temperatures may reach -82.2°C [6].

During the ground operations at Amundsen-Scott there is a special heating system to ensure the fuel doesn't freeze, this is discussed in Section 5.2. However when approaching or taking off from Amundsen-Scott the extremely low temperatures may potentially freeze the fuel. To determine whether the temperature of the fuel drops below the freezing point, Newton's law of cooling is applied. Equation 4.5 represents the temperature of the fuel dependant on time. The parameter $h$ represents the heat transfer coefficient. A conservative value of 5 W/$m^2$K is set. This value is typical for the transfer of heat of a liquid to a gas[8]. For the heat capacity $C_p$, the value is set for the smallest amount of fuel. Taking an external temperature of -82.2°C and an initial fuel temperature of -32°C the time for the fuel to reach its freezing point is 50.2 minutes.

$$T(t) = T_{\text{env}} + (T(0) - T_{\text{env}})\, e^{-\frac{h \cdot SA}{Cp} t} \tag{4.5}$$

No additional insulation or heating system is required. The value set for the heat transfer coefficient assumes that the kerosene is in direct contract with the outside air. This is not the case and the transfer of thermal energy is limited by the fuel tank and wing structure. To add, the assumption was made that the temperature is -82.2°C throughout the approach and take off phase. In reality the temperature decreases gradually with altitude. Therefore the actual time for the fuel to freeze is much higher than 50.2 minutes. Nevertheless, the decent and take-off flight phases will take less than 50.2 minutes and no insulation or heating is required for nominal flight. However, when the aircraft has to perform a go-around, this period might be longer than 50.2 minutes, after which the fuel is completely frozen. Therefore, for future development, the go-around and loiter situations have to be further investigated.

[7] JP-8 Characteristics, https://www.repsol.com/en/products-and-services/aviation/jp-8/index.cshtml, date accessed = 02-06-2022

[8] Heat transfer coefficient, https://www.engineeringtoolbox.com/overall-heat-transfer-coefficient-d_434.html, date accessed = 15-06-2022

### 4.3.2. Fuel Flow Control

This subsection shows the system used to control the fuel flow. An overview of the design is given in Figure 4.7. Firstly, the two fuel tanks are connected through a pump system. The pump system ensures that fuel may be transferred in the case a tank is leaking or clogged. The transfer pipes do not need pressurised flow, therefore a weak electrical pump is sufficient. The vents on each fuel tank ensure that atmospheric pressure is maintained, otherwise a vacuum will be drawn as fuel is used. Two selector valves dictate from which fuel tank the respective engine receives fuel. This yields the ability to cross-feed fuel and adds redundancy[9]. Next, the fuel is filtered through a strainer to remove sediment and water. The system is pressurised through the fuel-pump built in the turbo-electric engines, however for certification and redundancy an auxiliary fuel pump is required[10]. For this reason an additional electrically driven fuel pump is placed before the fuel injection unit. In the case that the engine driven pump fails, the electrical pump should be able to produce the required pressure. Finally, the fuel passes through the injection unit where the set mixture ratio and throttle setting are applied.

The most important aspect is that there is no single point of failure, the aircraft should still be able to operate when any component breaks. The implications of a component breaking may be divided into two different categories. Either the propulsion system is not affected, or the aircraft experiences one-engine inoperative conditions. The only elements that fall into the latter class are the strainer, selector valve, and fuel injection unit. As the strainer is a static component the probability of failure is very low. The risk of the fuel injection and selector valve unit failing may be mitigated by pre-flight checks and frequent maintenance.

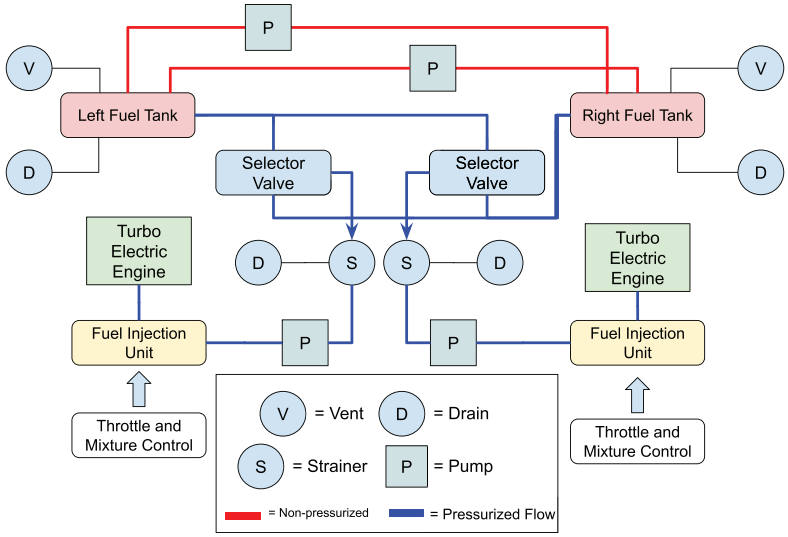


**Figure 4.7:** *Fuel flow control system.*

## 4.4. Propulsion

The hybrid-electric propulsion system was chosen to have a partial turbo-electric configuration. The implications of this is that the power required to propel the aircraft forward is provided by internal combustion engines. The power is divided with a gearbox between two large main propellers, and a generator driving electric motors, as shown in Figure 3.3. For JAPA-12 the configuration was chosen to consist of two gas turbines driving 10 electric motors.

### 4.4.1. Engine Choice

From the power-loading diagram and powertrain model presented in Sections 3.2 and 3.4.9, the required power for the main components of the propulsion system could be found. The required power for the gas turbines was found through Equation 3.15 using the MTOW of the aircraft and a shaft power ratio of 0.2 as determined for take-off, and was found to be around 1237 kW.

[9] Aircraft fuel systems, https://www.aircraftsystemstech.com/p/eachmanufacturer-designs-its-own-fuel.html, date accessed = 07-06-2022

[10] Fuel pump systems, https://www.eaa.org/eaa/aircraft-building/builderresources/while-youre-building/building-articles/fuel-systems/basic-fuel-pump-system, date accessed = 07-06-2022

In addition to take-off power, the propellers need to deliver the thrust required to overcome drag. The total clean configuration aircraft drag in cruise was found to be around 4.90 kN, as explained in Subsection 6.1.2. The thrust delivered by the gas turbines was found from $P = TV$. The power was first adjusted to cruise altitude, as air-breathing engines lose performance at lower air densities. Equation 4.6 taken from Sadraey's book "Aircraft Design: A Systems Engineering Approach" [3] describes the loss of performance of air-breathing engines at increasing altitudes. In this equation m is a parameter dependant on engine type, which for turboprops was assumed to be 1.2 [3]. It was found that the cruise altitude power is reduced to 782 kW for an engine exactly meeting the take-off power requirement of 1237 kW. To overcome drag at OEI conditions, 6.9 kN of thrust, or 820 kW of power, is needed. This means that the engines need to be oversized enough to account for loss of performance at cruise altitude and overcome the additional drag from stopped engines. On the other hand, for the electric motors, the limiting flight condition was found to be landing, as the shaft power ratio is much higher at 0.8, even though the aircraft weight is lower. The power required for the electric motors was found to be 330 kW, so 33 kW per motor.

$$P_{\max} = P_{\max_{\mathrm{SL}}} \left( \frac{\rho}{\rho_{\mathrm{o}}} \right)^{m} \tag{4.6}$$

To limit design complexity, existing off-the-shelf engines were analysed to find a suitable option. For the gas turbines, the engine chosen was the Pratt & Whitney PW118, which is a 1342 kW turboprop engine[11], used in propeller aircraft such as the Embraer EMB 120. This engine can deliver 849 kW of power at cruise altitude, which means that it can overcome drag in OEI conditions, with around 29 kW of power leftover to run aircraft systems and power the medical equipment on board. As the power required to overcome OEI drag at the cruise altitude is 820 kW, the engines could be downsized from the current design choice in the next design phase. Due to time constraints the current gas turbines were chosen while keeping in mind that the final engine choice would be lighter than this one. The dry mass of one engine is 390 kg, and the additional integration mass, including, among others, the propellers and engine mounts, was found from Roskam [4] through Equation 4.7. This gave a total installed mass of around 927.8 kg for the two gas turbines.

$$m_{ICE,\,\text{integ}} = 0.25 \cdot m_{ICE,\text{dry}} \cdot n_{ICE}^{0.6} \tag{4.7}$$

For the electric motors, public data on engine performance and parameters is extremely scarce. The MGM Compro REB30, a 30 kW continuous power aviation motor[12], was taken as the base for the design. The weight of one motor is 8.1 kg, and the integration weight was again found through Equation 4.7. As this equation is based on statistical data of combustion engines its accuracy for estimating electric motor weights was debatable, but as stated, data of electric motors was not readily available, so it was used as a first estimate of the installed mass. The total mass of the 10 electric motors was found to be around 89.1 kg.

As the main mission of the aircraft is under extreme weather conditions, the operating temperature of the engines was an important consideration in the design. For the gas turbines, it was assumed that they can perform the mission, as the Twin Otter, which has previously flown to the South Pole in the winter, has as its engines the PT6A-34 which is a turboprop engine produced by the same company as the PW118. For the electric motors, however, the temperature performance is more difficult to acquire information on. The electric aircraft motors produced by Magnix can operate up to altitudes of 35000 ft[13]. This means that they can operate in ambient temperatures down to -54°C. If similar temperature performance can be expected of smaller electric motors, the electric motors used for the aircraft may need additional heating to operate in Antarctic conditions, where temperatures can reach -76°C. Table 4.9 presents the main characteristics of the chosen engines.

**Table 4.9:** *Main characteristics of the PW118 and REB30 motors.*

| Engine parameter | PW118 | REB30 |
|---|---|---|
| Dry mass [kg] | 390 | 8.1 |
| Max. continuous power [kW] | 1342 | 30 |
| Take-off power [kW] | 1775 | 40 |
| Diameter [mm] | 660 | 267 |
| Length [mm] | 2130 | 101 |

[11] EASA PW100 Series type certificate data sheet, https://www.easa.europa.eu/downloads/7725/en, date accessed = 10-06-2022

[12] MGM Compro REB30 technical parameters, https://www.mgm-compro.com/electric-motor/40-kw-electric-motor/, date accessed = 09-06-2022

[13] Magnix electric aircraft motor technical information, https://www.magnix.aero/services, date accessed = 02-06-2022

### 4.4.2. Propeller Sizing

Following the choice of the engine, the propellers were sized. The detailed performance characteristics of the propellers, such as twist angle and blade airfoil selection, were considered outside of the scope of this design phase, but to select engine locations along the wing, first estimates of propeller diameters were needed. For this, the approach of [3] was used.

Equation 4.8 presents the relation used for finding a ballpark estimate for the diameter of the propellers. Here $K_{np}$ is a correction factor for increasing number of blades. It has a value of 1 for two-blade propellers, 0.72 for propellers with six or more blades, and for other numbers of blades linear interpolation is used. $P$ is the shaft power of the engine and $\eta_p$ is the propeller efficiency, with typical values between 0.75 and 0.85 [3]. $AR_p$ is the aspect ratio of the blade, typically between 7 and 15, $\rho$ is the air density at cruise altitude and $V_{\text{tip cruise}}$ is the limit speed of the propeller tip, which is dependant on the material of the blades. For example, composite blades have a limiting tip speed of 250 m/s [3]. The limiting tip speeds are in place to ensure the tips of the blades do not cross into the supersonic regime. For example, the limiting speed of high-performance metal blades, 310 m/s, is 0.95 Mach at the cruise altitude of the aircraft. Furthermore, $C_{L_p}$ is the lift coefficient of the propeller, and $V_C$ is the cruise speed.

$$D_{\mathrm{P}} = K_{\mathrm{np}} \sqrt{\frac{2P\eta_{\mathrm{P}}\mathrm{AR}_{\mathrm{P}}}{\rho \left(0.7V_{\text{tip cruise}}\right)^2 C_{L_{\mathrm{P}}} V_{\mathrm{C}}}} \tag{4.8}$$

To check that the chosen engines could deliver the required performance, the rotational speeds of the propellers were calculated. The tip of a propeller blade moves through the air in a helical pattern due to the forward motion of the aircraft. The tip speed can then be divided into the cruise tip speed and static tip speed, where the static tip speed describes the rotation of the tip around the axis of the propeller, as shown in Figure 4.8. The static tip speed can be found through Pythagoras with $V_{\text{tip static}} = \sqrt{V_{\text{tip cruise}}^2 - V_C^2}$. The rotational speed of the propeller can be then found through $\omega = 2V_{\text{tip static}}/D_P$.

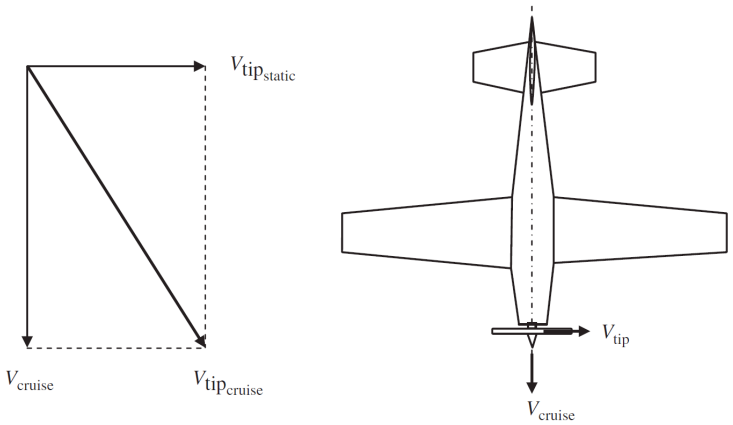


**Figure 4.8:** *Propeller tip speeds [3].*

For the main propellers, the following parameters were chosen to ensure the propellers fit on the wing and matched the rated propeller shaft speed of the engine of 1313 rotations per minute (rpm): first, the propeller was chosen to have six blades made of composites to save weight. The aspect ratio of the blades was chosen to be seven, with a $C_{L_p}$ of 0.3. This gave a propeller diameter of 3.1 m, with a propeller rotational speed of 1350 rpm. This rotational speed is slightly higher than the rated speed of the engine, but the method used for propeller sizing is a very rough first estimate, so it was assumed that the rotational speed would be finalised when doing detailed propeller design, such as optimising the shape and airfoil of the blades.

For the electric propellers, a configuration with three composite blades was chosen, with an aspect ratio of 10 and a $C_{L_p}$ of 0.3. This gave a propeller diameter of 0.95 m, and a rotational speed of 4400 rpm. This rotational speed was considered very high, but it was deemed reasonable for a first estimate as the NASA X-57 propellers have a rotational speed above 4500 rpm [34].

Table 4.10 presents the results of the propeller sizing calculations. From Table 4.10, it can be seen that a propeller diameter of 3.1 m and 0.95 m is required for the main and distributed propellers, respectively. If the propeller diameter is larger, the engine can be run at lower speeds to acquire the same thrust, increasing the lifetime of the engine. Therefore, the diameter determined here is the minimum diameter required for the given blade characteristics.

**Table 4.10:** *Propeller dimensions.*

| Parameter | Main propellers | Distributed propellers |
|---|---|---|
| Number of blades | 6 | 3 |
| Continuous engine shaft power [kW] | 1604 | 40 |
| Propeller efficiency | 0.75 | 0.85 |
| Aspect ratio | 7 | 14 |
| Material | Composite | Composite |
| Propeller lift coefficient | 0.3 | 0.3 |
| Required propeller diameter [m] | 3.1 | 0.95 |

The propellers were chosen to have a constant speed, variable-pitch configuration. This means that the propeller blades can rotate spanwise around their base, improving efficiency at a range of speeds. A propeller moves an aircraft forward by generating a lift force via rotating blades. Varying the pitch of the propellers means that the engine can be run at its rated rotational speed across a range of aircraft speeds, as the varying pitch varies the torque required to move the blades through the air. A propeller governor, or constant speed unit, controls the pitch of the propellers through a hydraulic mechanism. The governor uses oil pressure to decrease the blade pitch as needed. This means that when the governor fails the propellers will feather, or turn in the direction of incoming air, so that drag is reduced while the aircraft flies on the functioning engines. A variable-pitch configuration also allows for reversible thrust, as blades can be turned to generate thrust in the opposite direction. This is common for turboprop aircraft, and was chosen to be included in the design to allow for better STOL performance on landing.

### 4.4.3. Weight

The calculation of the weight of the propulsion system was the next step in the sizing process. The weight was calculated for the different components of the powertrain. The weight of the generators, inverters, rectifiers and Power Management And Distribution (PMAD) was calculated. This was done using the specific powers and the power required since little information was found about off-the-shelf components. The maximum power the generators needed to provide was 855 kW which lead to a total mass of 67.3 kg using the specific power presented in Section 3.6. For the inverters and rectifiers the power used was the power for the electric motors and the total mass was estimated to be 17.2 kg for each. For the PMAD the mass is 57.2 kg and this value was calculated by taking 30% of the total mass of the generators, inverters, rectifiers and electric motors together. This is a weight penalty to account for elements of thermal management system and additional elements of the power distribution system. The mass of the gearboxes was set to 45 kg each based on the only aircraft gearbox that was found.[14] For the next phase in the design, engine manufacturers will be contacted to get more information about the specifications of the different components of the powertrain. All the masses can be found in Table 4.11. For some components only the total mass is given as there is no clear division of the mass per component. For example, the integration mass does not increase linearly with the dry mass as can be seen by the number of engines to the power of 0.6 as some components are present only once. The total mass of the powertrain is 1265.7 kg or 12412.3 N.

**Table 4.11:** *Mass per powertrain component.*

| Component | Mass per component [kg] | Number of parts | Total mass [kg] |
|---|---|---|---|
| Gas turbine (GT) | 390 | 2 | 780 |
| Integration mass GT | - | - | 147.8 |
| Electric motor (EM) | 8.1 | 10 | 81 |
| Integration mass EM | - | - | 8.1 |
| Gearbox | 45 | 2 | 90 |
| Generator | 33.65 | 2 | 67.3 |
| Inverter | 8.6 | 2 | 17.2 |
| Rectifier | 8.6 | 2 | 17.2 |
| PMAD | - | - | 57.2 |

[14] PBS aircraft gearboxes, https://www.pbs.cz/en/Aerospace/Aviation-devices-andgine-components/Aircraft-gearboxes, date accessed = 03-06-2022

### 4.4.4. Propulsion System Configuration

After having the dimensions for the different components of the power train, the wiring configuration could be analysed and the positioning of the different components could be defined. For the wiring, it was decided that the left engine provides power to the right electric motors and the right engine provides power to the left electric motors. This configuration was chosen based on the OEI condition. If a powertrain component fails the difference in moments about the centre of the fuselage will be minimum with this configuration as only the main propeller will be producing thrust on one side and only the electric propellers will be producing thrust on the other side. This will make sure that the required additional control forces from the vertical tail can be as small as possible.

For the positioning of the components , the clearance between the main propeller and the fuselage has to be between 0.5 and 1 m [35]. For the electrical propellers, the lateral propeller separation is given by $\delta_y D_p$ for which $\delta_y$ is the fraction of the diameter of the propellers that determines the separation distance and it was set to 0.1 as defined in [1]. The spacing between the main propeller and electrical propellers was defined by using the same equation as before and the diameter of the main propeller. The last propeller was set to have the midpoint at 0.22 m from the end of the wing tip. Keeping everything into account and the propeller diameters and fuselage diameter, the final clearance between the main propeller and fuselage is 0.5 m. Figure 4.9 shows the final configuration of the propulsion system. The dashed line represents the center line of the fuselage and the dimensions given are for the space between the two vertical lines. The final dimension adds up to half the wing span.

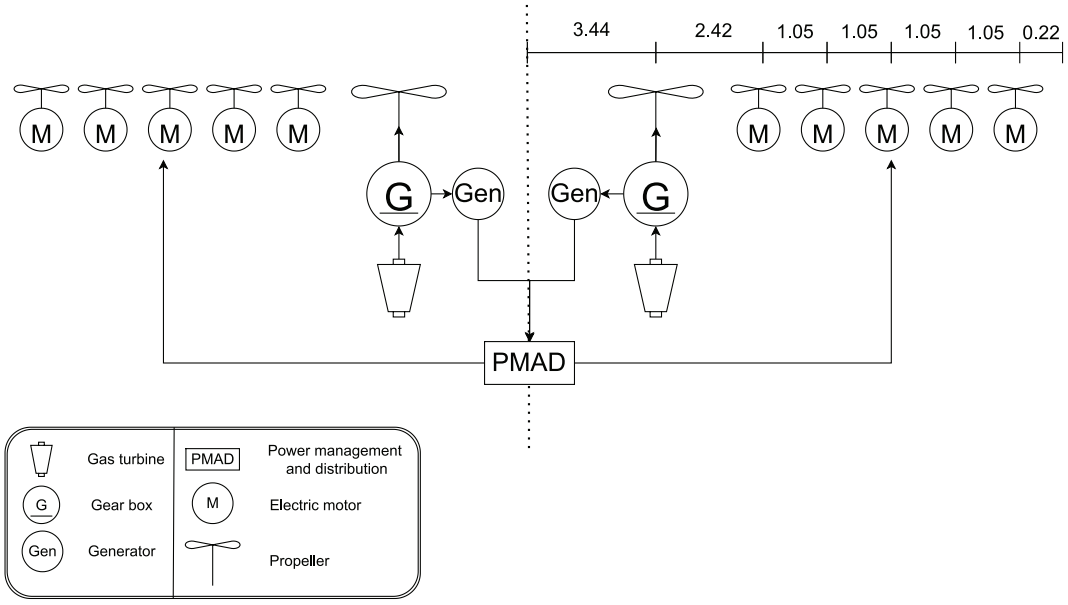


**Figure 4.9:** *Configuration of the propulsion system.*

## 4.5. Empennage

In this section the horizontal and vertical tail sizing is presented. The empennage subsystem is an indispensable component of the aircraft as it allows for stable and controllable flight. Firstly, an airfoil was picked for the horizontal and vertical tail. This selection process is discussed in Subsection 4.5.1. The sizing of the empennage started with the determination of the center of gravity range. For this, a loading diagram was constructed, which is treated Subsection 4.5.2. With the found center of gravity range, an initial stability range could be established, which was treated in Subsection 4.5.3. To allow for controllable flight, a similar range was constructed for in-flight trimming. This is presented in Subsection 4.5.4. Using both the stability and controllability ranges the scissor plot was constructed after which, with the loading diagram, the minimum required tail size was found. The horizontal tail sizing is concluded in Subsection 4.5.5. The vertical tail sizing is covered in Subsection 4.5.6. Finally, a fuselage-empennage weight optimization proposal is presented in Subsection 4.5.7, where it was investigated if an optimum of fuselage length and horizontal tail combination was present to minimise weight.

### 4.5.1. Empennage Airfoil Selection

The airfoil of the horizontal and vertical tails were determined by the desired function of both tail types. The methodology of determining the most appropriate airfoil types are covered below.

First, it was established that both airfoils should comprise of a symmetric airfoil. For the vertical tail, this was desired as one generally does not want lift generation on either sides of the airfoil when in equilibrium state. For example, when a cambered airfoil was used, the aircraft would introduce a yawing moment at a 0° angle of attack of the vertical tail, which is undesired. Additionally, in some flight conditions e.g. take-off, the horizontal tail should generate negative lift for a pitch up moment. This meant that the horizontal tail had to generate positive and negative lift in an easy manner. Therefore, a symmetric airfoil was picked for both the horizontal and vertical tail.

To allow for controllability and stability, it is generally desired to have a horizontal tail that has a high lift gradient, as this results in a smaller horizontal tail area and thereby a smaller drag [36]. A short trade-off was made based on symmetrical airfoils with a high lift gradient. The trade-off had shown that generally symmetric airfoils with a high t/c ratio perform well due to the high lift gradient. However, to limit the parasite drag of the stabilizer, which also imposes a pitching moment on the aircraft, the team decided that the NACA 0012 airfoil was most suitable for the horizontal tail. Therefore, the NACA 0012 airfoil was used for further horizontal tail sizing.

The vertical tail is generally used for the directional stability of the aircraft, allowing the aircraft to fly in crosswind conditions [32]. As there was a strict crosswind landing requirement, as stated in **REQ-ENV-09**, where the system had to land in 90° crosswind conditions, excellent stall characteristics for the vertical tail were desired. After a trade-off between symmetrical airfoils with good stall characteristics, the NACA 0015 airfoil was selected, which has attached flow up to $\alpha = 17.5°$[15]. Note that although the airfoil was picked for excellent stall characteristics, the stall behaviour of the vertical tail was also manipulated via the vertical tail planform. The planform layout is covered in Subsection 4.5.6.

### 4.5.2. Loading Diagram

The loading diagram is a useful way of displaying the center of gravity range of the aircraft for various loading cases. This should be done as, when the center of gravity shifts behind the neutral point, the aircraft becomes unstable. On top of that, when the center of gravity shifts too much forward, the aircraft becomes uncontrollable. Therefore, to size the horizontal tail such that the aircraft is both controllable and stable, the loading diagram was constructed.

The loading diagram was constructed by adding the considered weights together, and constructing the resulting moment arm to find the shared c.g. locations. This was done for the OEW, the cargo, the passenger weight, and the fuel. Additionally, the loading procedure was done in this order, as this is a commonly used loading order when constructing the loading diagram [37]. On top of that, it made more sense that, for the medevac mission, the cargo was loaded before the patient such that the cabin interior was already set; which improves patient comfort.

#### Operational Empty Weight

The contribution of the operational empty weight to the loading diagram was straight forward. From the weight estimation as done in Section 3.6, an operational empty weight of 42810 N was found. On top of that, the cg location of the OEW was estimated. This was done via the class II estimation of Torenbeek [30]. Here, weight estimations of each subsystem together with their cg location were found, based on found parameters and statistical data. This resulted in an operational empty weight location of 5.7 m from the nose, or 0.365 x/c. The combination of the OEW and the OEW cg location constructed the starting point of the loading diagram.

#### Cargo

The cargo of the aircraft was considered mission specific, as for example less cargo as payload was expected for the medevac mission than for a 19 pax flight. The considered cargo weight are presented in Table 4.12 for each mission. This was determined by first including the required fuel weight for the mission after which the passenger weight was added. Then, the cargo weight was computed to fill the aircraft until MTOW was reached. Additionally, as the cargo is stored in 3 cargo compartments of the aircraft, a fixed center of gravity location was used for the 3 cargo holds. These locations were set during the fuselage design in Subsection 4.1.3. Finally, the cargo weight was distributed over the 3 cargo compartments, whose locations can be found in Table 4.12. The combination of the cargo weights and cg locations provided the next points in the loading diagram.

#### Fuel

Just like the cargo contribution to the loading diagram, the fuel contribution was simply set up via a mission specific fuel weight. The fuel cg was assumed to be constant during flight, as little detail was known about fuel shifts inside the

[15] Database displaying simulation data of the NACA 0015 airfoil, http://airfoiltools.com/airfoil/details?airfoil=naca0015-il, date accessed = 31-05-2022

fuel tanks. However, as the loading diagram was used in a rather robust manner of tail sizing, it was expected that, when adding margins at the extreme cg locations, this simplification was not posing an issue. The mission specific fuel weights are presented in Table 4.12. The cg location considered was to be at 50% of the mean aerodynamic chord, as the fuel was stored at the center of the wingbox.

**Table 4.12:** *Cargo & fuel weights data used for the loading diagram.*

| Mission | Cargo weight [N] | Cargo cg [x / $\overline{c}$] | Fuel weight [N] | Fuel cg [x / $\overline{c}$] |
|---|---|---|---|---|
| 19 passengers | 3x 1195 | -1, 0.38, 1.6 | 1923 | 0.5 |
| Medevac | 3x 97 | -1, 0.38, 1.6 | 16708 | 0.5 |

**Passengers**

The final contribution to the loading diagram were the passengers on board of the aircraft. As loading procedure, the window seating rule was adopted [37], meaning that the passengers were loaded step-wise from the window seats to the aisle seats. Using the chosen fuselage configuration as presented in Figure 4.2, the loading method is done by first adding 2 rows of passengers (window seats), and then the final aisle row. On top of that, the passenger loading was one-by-one, and done loading front to back and back to front, with a passenger weight of 85.7 kg as set by regulations [38]. This generated a potato-like shape in the loading diagram of which the cg locations at a certain number of passengers could be read of. The seating of the passengers was done in accordance to the passenger placements in Figure 4.2 for the 3 seats abreast configuration, as this fuselage configuration also allowed for the medical evacuation mission.

The medical passenger loading was done in a different manner. When looking at Figure 4.5, it can be seen that some seats are replaced by a stretcher and ICU carts, which in turn impacted the loading diagram. The seats were loaded in a similar manner to the 19 pax loading method, but now only for 3 passengers as that was the maximum number of passengers available to reach the MTOW. Additionally, the medical equipment, the patient, and the stretcher were treated as a single weight with its own dedicated cg location. Via the incorporated medical equipment determined in Table A.1, and patient weight, a point load of 200 kg was used. By constructing the loading diagram in this way, an unconventional loading diagram was established. The doctor was included in the OEW, where the weight of the doctor was swapped with the weight of the flight attendant.

**Loading Diagrams**

By executing the method explained above, a loading diagram for the 19 pax mission and a loading diagram for the medevac mission was established. Additionally, to account for the fuel shift ambiguity, a commonly used safety margin of 2% was used [37]. This resulted in the loading diagrams as shown in Figure 4.10 and Figure 4.11.

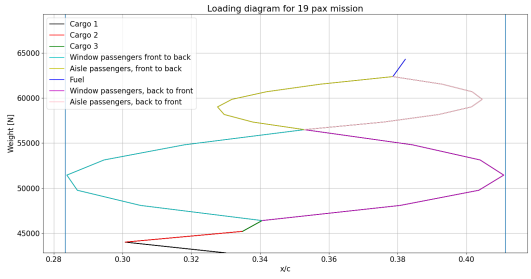


**Figure 4.10:** *Constructed loading diagram for the 19 pax transportation mission profile.*

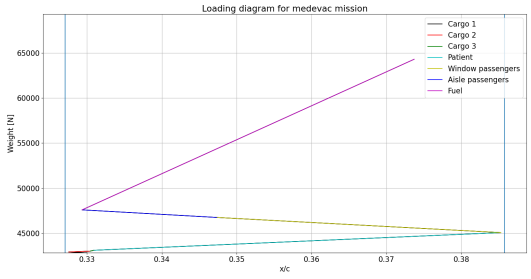


**Figure 4.11:** *Constructed loading diagram for the medevac mission profile.*

The most extreme cg locations of Figure 4.10 and Figure 4.11 were combined such that the maximum cg range was found. The most extreme cg range was found to be between 0.283 x/c and 0.411 x/c along the mean aerodynamic chord. Therefore, the tail sizing was done with this center of gravity range, as the tail would allow for both controllability and stability when any loading configuration was used.

### 4.5.3. Stability Range

To have a static longitudinally stable aircraft, it is required to have a negative moment coefficient slope with respect to $\alpha$. Or in other words, $C_{m_\alpha} < 0$ is required for stability. This ensures that the aircraft automatically returns to its equilibrium attitude, as set by the pilot, when a disturbance is encountered.

To find the slope of the $C_m - \alpha$ curve, the force and moment equilibrium of the aircraft was set up. This equilibrium was set up via the free body diagram as presented in Figure 4.12. Finding the equilibrium state was done via a set of simplifications and assumptions made to the model presented in Figure 4.12. The simplifications and assumptions are listed below, together with their rationale. Note that the forces and moments of the aircraft in Figure 4.12 are solely for illustration purposes, as the distributed propulsion has engines under the wing rather than at the fuselage and the JAPA-12 uses a high wing configuration.

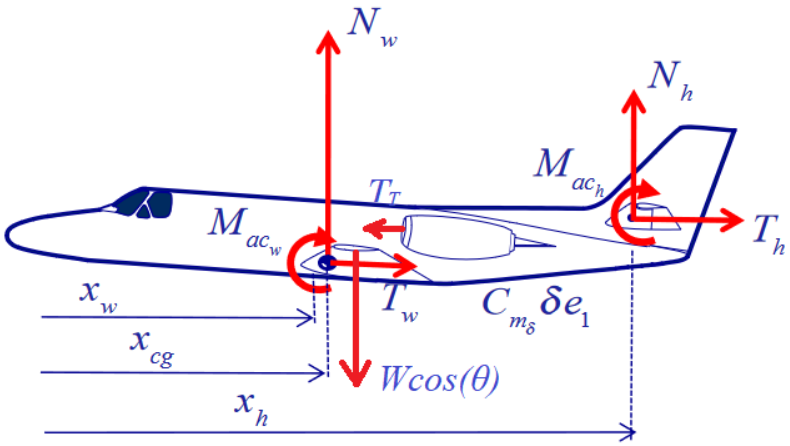


**Figure 4.12:** *Aircraft free body diagram used for stability analysis [39].*

- **The horizontal tail experiences no moment around the aerodynamic center (ASMP-1):** As the horizontal tail uses the symmetric NACA 0012 airfoil, the pressure distribution at $\alpha_h = 0$ is equal for both the top and bottom side of the airfoil. Therefore, during $\alpha_h = 0$, no moment around the aerodynamic center is present. Now, as the moment around the aerodynamic center is constant for varying angles of attack, the momenent around the aerodynamic center can be omitted. Or simply: $M_{ac_h} = 0$.
- **The tangential component of the horizontal stabilizer, $T_h$, was omitted (ASMP-2):** The tangential component of the horizontal stabilizer was computed by shifting from the aerodynamic reference frame to the body reference frame. This was done via the coefficient transformation $C_{T_h} = \cos\alpha_h \cdot C_{D_h} - \sin\alpha_h \cdot C_{L_h}$. By assuming a small angle of attack during flight, the sin component vanished. Additionally, due to the relative small drag expected by the horizontal tail, $C_{D_h}$ became negligible. Thus, $T_h = 0$ and was thereby omitted from the equilibrium equation.
- **The aerodynamic center of the wing lies in close proximity of the aircraft center of gravity (ASMP-3):** As the aircraft had a significant number of engines attached to the wing, the weight component of the wing group was relatively large. Therefore, it was expected that the vertical distance in Figure 4.12 between the cg of the aircraft and the aerodynamic center of the wing was small. Because of the small z-arm, both the moments of the thrust component and the tangential wing component were small. Therefore, both the thrust component $T_T$ and the tangential wing component $T_w$ were omitted. Now, ignoring the thrust in the moment equilibrium of the aircraft might have had implications regarding stability and controllability. However, as stability was derived via the derivative of angle of attack, the thrust component fell off. On the other hand, as controllability was not angle of attack dependent, some issues might have arisen. However, as controllability is dominant during landing [36], when lower thrust settings are present, neglecting the thrust for controllability was deemed reasonable during this stage in the design as both the z-component and the thrust component were small.

After the assumptions were made, the moment equilibrium was worked out. Then, by expressing the moment coefficient in angle of attack, the slope of the $C_m - \alpha$ curve could be expressed in ratios of $S_h/S$, where a commonly used 5% safety margin was included [36]. This resulted in Equation 4.9, where $\bar{x}_{cg}$ indicates the preliminary neutral point location for stability.

$$\frac{S_h}{S} = \frac{\bar{x}_{cg}}{\frac{C_{L\alpha_h}}{C_{L\alpha_w}}\left(1 - \frac{d\epsilon}{d\alpha}\right)\frac{l_h}{\bar{c}}\frac{V_h}{V}^2} - \frac{\bar{x}_{ac} - 0.05}{\frac{C_{L\alpha_h}}{C_{L\alpha_w}}\left(1 - \frac{d\epsilon}{d\alpha}\right)\frac{l_h}{\bar{c}}\frac{V_h}{V}^2} \tag{4.9}$$

By expressing the $S_h/S$ ratio versus the cg location of the entire aircraft, a stability line was plotted, which is depicted in Figure 4.13. As $C_{m_\alpha} < 0$ was required for stability, a region of design feasibility is generated left of the stability line, as the cg was required to be in front of the neutral point. This means that, when the cg location of the aircraft was left of the stability line, the horizontal tail was sized such that the aircraft would become static longitudinally stable.

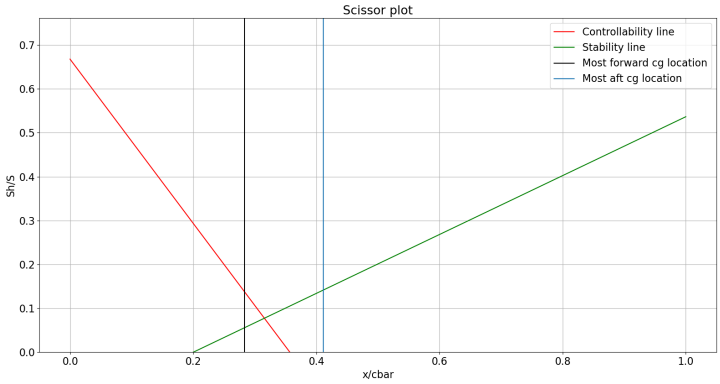


**Figure 4.13:** *Scissor plot used for empennage sizing.*

### 4.5.4. Controllability Range

To have a controllable aircraft, it is required to be able to trim the aircraft. This means that there has to be a condition in flight where there is no moment acting on the aircraft. Or in other words, $C_m = 0$.

Just like stability, the moment coefficient was to be computed. This was done for a free body diagram similar to Figure 4.12, again with a high wing configuration and wing-mounted engines. Then, by isolating $S_h/S$ in the $C_m$ expression, Equation 4.10 was found.

$$\frac{S_h}{S} = \frac{\overline{x}_{cg}}{\frac{C_{L_h}}{C_{L_w}} \frac{l_h}{\overline{c}} \frac{V_h}{V}^2} + \frac{\frac{C_{m_{ac}}}{C_{L_w}} - \overline{x}_{ac}}{\frac{C_{L_h}}{C_{L_w}} \frac{l_h}{\overline{c}} \frac{V_h}{V}^2} \tag{4.10}$$

Subsequently, the controllability line was plotted for $S_h/S$ versus the cg location of the entire aircraft. From this line, the most forward cg location was found, as the cg location was constrained to the right of this line.

### 4.5.5. Horizontal Tail Sizing

Now that the loading diagram, stability range and controllability range were determined, they could be combined into a scissor plot. The scissor plot is generally used to find the minimal horizontal tail size for a given cg range. The scissor plot for this design is presented in Figure 4.13.

To find the minimal horizontal tail size, the most aft and forward cg lines needed to be between the controllability and stability line. Therefore, an optimum was found when the forward cg line crossed the controllabiltiy line at the same $S_h/S$ ratio at which the most aft cg line crossed the stability line. As this ensured the aircraft to be both controllable and stable for all cg locations experienced once operational.

Unfortunately, in first instance, the cg range did not fit perfectly as it does in Figure 4.13. To force the most extreme cg locations to fit perfectly between the allowable range, the wing was shifted along the fuselage. By shifting the wing, both the most extreme cg values and the stability & controllability lines were adjusted. Through iterating the scissor plot with varying wing positions, the optimum wing location was found to be for $X_{lemac} = 5.84$ m, and resulted in Figure 4.13. Additionally, the minimum $S_h/S$ ratio was read off from the scissor plot, which was found as $S_h/S = 0.1417$. Then, by multiplying this ratio with the surface area of the wing, the horizontal tail surface area was found to be $S_h = 5.98$ m$^2$. Note that shifting the wing along the fuselage imposed a number of changes in the design. Therefore, to carry out a single shift, the entire aircraft was iterated.

The horizontal tail planform was, just like the main wing, more accurately sized via the Torenbeek method [30]. However, the surface area of the horizontal stabilizer was dependent on the stability and controllability rather than the wing loading. For this, the scissor plot provided a surface area of $S_h = 5.98$ m$^2$. Additionally, an aspect ratio was chosen to be 6, as the aspect ratio had to be smaller than the main wing as this delays stall of the tail [40]. Finally, the 3-quarter chord sweep was set to $0°$. This was done for two reasons. First, to allow sweep in the leading edge of the horizontal tail, extending the moment arm with respect to the cg of the aircraft. And secondly, because sweep postpones adverse compressibility effects [40], making the tail 'less worse' at high angles of attack to allow for stall recovery. The major horizontal tail dimensions are presented in Table 4.13.

**Table 4.13:** *Horizontal tail planform parameters.*

| Parameter | Value |
|---|---|
| Surface area [$m^2$] | 5.98 |
| Aspect ratio | 6 |
| Span [m] | 5.99 |
| Taper ratio | 0.45 |
| Root chord [m] | 1.38 |
| Tip chord [m] | 0.62 |
| Quarter chord sweep [°] | 7.21 |
| Distance between wing and horizontal tail [m] | 6.16 |

### 4.5.6. Vertical Tail Sizing

The distributed propulsion system of the aircraft allowed for better controllability and, therefore, a smaller vertical tail. To calculate the required vertical tail surface, two situations were considered. First, the required vertical tail surface area was calculated for the OEI condition. The engine that had the most impact when it failed was one of the gas turbines. In case one of the gas turbines failed, the propellers on the other wing also failed. As a result, a yawing moment arises from the non-uniform thrust that remains and the drag of the inoperative engine and propellers [41]. For this aircraft, the moment due to drag on the inoperable engines was bigger from the five propellers, than from the inoperable gas turbine. As the thrust moment acted in an opposite direction of the drag due to the inoperative engines, the moment of the still operable gas turbine was bigger than the thrust moment of the five functioning propellers. The yawing moment that must be counteracted was 9.36 kN. The vertical tail, and especially the rudder, had to counteract this yawing moment. The maximum rudder deflection was set to 30°[16]. Using Equation 4.11 and Equation 4.12, the required $C_{n_{\delta r}}$ and the corresponding vertical tail surface area of 1.17 m² was found. The efficiency of the vertical tail was estimated to be 0.9 and the efficiency of the rudder 0.6 [42] [43]. The vertical tail area required is small compared to other aircraft, however, this is as expected, since the drag and thrust moment already counteract each other.

$$N_{propulsion} + N_{rudder} = (T_e + D_e) \cdot l_e + C_{n_r} \delta r \cdot \frac{1}{2} \rho V^2 S b \tag{4.11}$$

$$C_{n_{\delta} r} = -\eta S_{VT} l_{VT} \tau C_{L_{\alpha}, VT} / (S b) \tag{4.12}$$

The second case considered was for stability in crosswind which is very important for aircraft performance in Antarctica **[FAC.2]**. The vertical tail was sized for a high sideslip angle, $\beta$, of 25°[44]. Equation 4.13, Equation 4.14 and Equation 4.15 were used and $\frac{d\sigma}{d\beta}$ was set to $\frac{1}{5}$ and the stability derivatives were taken from the stability and control calculations [42]. The vertical tail surface area was found to be 2.56 m² [41].

$$C_{n_\beta} \beta + C_{n_{\delta r}} \delta r = 0 \tag{4.13}$$

$$C_{n_\beta} = C_{n_{\beta, wing}} + C_{n_{\beta, fuselage}} + C_{n_{\beta, VT}} \tag{4.14}$$

$$C_{n_{\beta, VT}} = \eta (1 + \frac{d\sigma}{d\beta} S_{VT} l_{VT} / (S b) \tag{4.15}$$

The critical condition was the crosswind and the minimal tail surface area required was 2.56 m². Since this was small compared to other aircraft and multiple inputs for the calculations are rough estimates, a margin of 50% was applied. This lead to a vertical tail surface area of 3.84 m². The aspect ratio was set to 1.5, the quarter chord sweep angle was 40°and the taper ratio was 0.5 [44]. This resulted in the vertical tail geometry presented in Table 4.14.

### 4.5.7. Fuselage Length and Empennage Size

The effect of the length of the fuselage and required size of the empennage was assessed. Increasing the length of the fuselage improved the stability and controlability characteristics as the moment arm of the empennage was increased, provided that the wing was constrained to the same location. Potentially the decrease in weight through decreasing the size of the empennage outweighed the increase in weight of the longer fuselage. Therefore, the procedure described in Subsection 4.5.5 was repeated for a range of feasible fuselage lengths. From this analysis it was revealed that there was indeed a decrease in empennage size as the fuselage length was increased. This relationship is presented in Figure 4.14. Unfortunately, the weight increase of the fuselage when the length was increased overpowered the decrease in weight

[16] Use of rudders on transport category airplanes, A310/A300-600 FCOM Bulletin, https://www.smartcockpit.com/docs/Use_Of_Rudder_On_Airbus_Aircraft.pdf, date accessed = 10-06-2022

**Table 4.14:** *Vertical tail planform parameters.*

| Parameter | Value |
|---|---|
| Surface area [$m^2$] | 3.84 |
| Aspect ratio | 1.5 |
| Height [m] | 2.40 |
| Taper ratio | 0.5 |
| Root chord [m] | 2.13 |
| Tip chord [m] | 1.07 |
| Quarter chord sweep [°] | 40 |

of the smaller empennage, as shown in Figure 4.15. The fuselage length was therefore the critical design point for the sizing of the fuselage. The smallest possible fuselage was therefore set as described in Subsection 4.1.2.

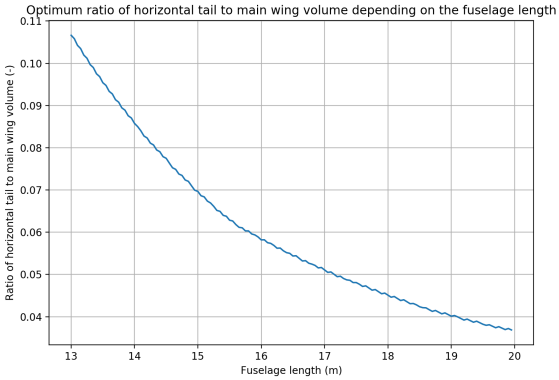


**Figure 4.14:** *Ratio of horizontal tail volume to wing volume depending on fuselage length.*

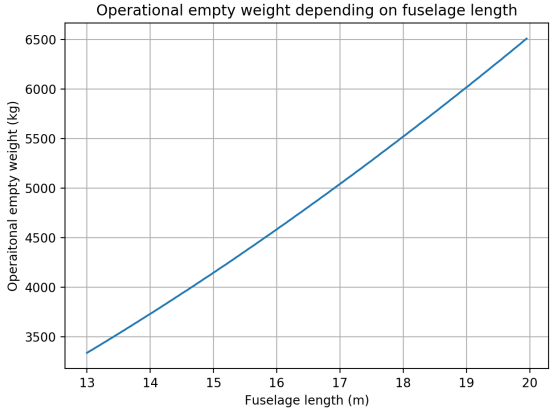


**Figure 4.15:** *Operational empty weight of the aircraft depending on fuselage length.*

## 4.6. Landing Gear

The aircraft landing gear is crucial for safe landing and take-off from different kinds of runways. Landing gears provide static stability and absorb shocks upon landing and taxiing. Shock absorption is achieved by both the wheels and struts which attach them to the fuselage. The following subsections describe the positioning and sizing of the landing gear. For design, the most extreme loading cases were taken into account, as landing gear failure is one of the most common failure modes on Antarctic flights, which is also outlined as one of the factors in flight performance in Antarctica **[FAC.2]** [17]. Finally, the landing gear was chosen to be stored, as the drag penalty in cruise was deemed too large for fixed landing gear.

### 4.6.1. Positioning of Landing Gear

Positioning of the landing gear began with selecting a configuration. The triangle configuration was chosen over others because of visibility, ground loop stability and steering performance reasons. The positioning of the nose (NLG) and main landing gear (MLG) within this configuration was based on the static stability of the aircraft. First, the position along the longitudinal axis of the aircraft was determined based on the distribution of the total aircraft weight. The NLG was selected to carry 12% of the MTOW, where a minimum of 8% is generally required for sufficient steering capability [45]. The larger allocation of load to the nose landing gear was favourable for increased steering capability as Amundsen-Scott's runway is made of compacted snow.

Accordingly, the landing gear height with respect to the lowest location of the fuselage was determined by applying a $15^{\circ}$ scrape angle, in combination with the MLG positioning with respect to the most aft c.g. for longitudinal static stability. A height of 1.2 m resulted in a position of the MLG at 7.41 m with respect to the nose and 1.82 m for the NLG. The NLG is

[17] Database for aircraft failures on Antarctica, https://aviation-safety.net/database/dblist.php?Country=ant, date accessed = 07-06-2022

located on the centerline of the aircraft, while the MLG is at a distance of 0.97m as a result of Equation 4.16, ensuring that there is no lateral tip-over. Here $l_n$ and $l_m$ indicate landing gear positions with respect to the most aft c.g. and $\Psi$ the tip-over angle of $\Psi < 55°$. Tip and propeller clearance with respect to the ground where considered to not form a problem as the aircraft features a high wing configuration.

$$y_{mlg} = \frac{l_n + l_m}{\sqrt{\frac{l_n^2 \tan \Psi^2}{z^2} - 1}} \tag{4.16}$$

## 4.6.2. Selection of Wheels

The maximum static design load was determined based on aircraft touchdown conditions in order to select wheels for both the NLG and MLG. All struts were selected to have two wheels, as this was optimal for storage inside the fuselage. The load on the NLG was determined to be 780 kg per wheel. As it was expected that the aircraft weight might increase, and including an additional safety margin of 1.25 as suggested by Roskam [46], the tyres were selected for a maximum load of 1000 kg. The MLG tyres were found to be subject to a static load of 1440 kg, for which tyres with a maximum load of 2200 kg were selected for the same reasons as the NLG tyres. An overview of the tyre properties is shown in Table 4.15. Tyre clearance was also taken into account, as tyres can grow up to 4% in width and 10% in diameter during their service life [46].

**Table 4.15:** *Tyre parameters.*

| Parameter | NLG | MLG |
|---|---|---|
| Diameter [cm] | 40.6 | 45.7 |
| Width [cm] | 11.2 | 14.0 |
| Height clearance [cm] | 4.2 | 4.7 |
| Width clearance [cm] | 0.5 | 0.7 |
| Weight [kg] | 3.63 | 6.35 |
| Max load [kg] | 1000 | 2200 |
| Manufacturer | Goodrich | Goodrich |

## 4.6.3. Shock Absorber Design

Shock absorbers are used, in combination with wheels, to absorb the shocks experienced by the aircraft during landing and taxi. The kinetic energy upon landing was calculated in order to size the shock absorbers. A maximum touchdown rate of 10 fps at MTOW was taken as the critical case, which was obtained from CS-23 regulations. The entirety of the kinetic energy was assumed to be absorbed by the MLG as this is the first point of contact with the ground. Shock stroke and diameter were determined with Equation 4.17[46] and Equation 4.18[46], where the touchdown rate was $W_t = 10$ feet per second, $n_s$ the number of wheels, $P_m$ the load per wheel in lbs in which the 1.25 safety factor was also included, the load factor $N_g$ was 3 as required by CS-23 regulations, and $\eta_t$ and $\eta_s$ are the tyre efficiency and shock absorber efficiency, respectively.

$$s_s = \left( \frac{0.5 \frac{MTOW}{g} (W_t)^2}{n_s P_m N_g} - \eta_t s_t \right) / \eta_s \tag{4.17}$$

$$d_s = 0.041 + 0.0025 (P_m)^{0.5} \tag{4.18}$$

The type of shock absorber was selected based on the harsh environmental conditions, as extreme cold may not interfere with the damping properties of the shock absorber. Therefore, a metal spring in combination with synthetic fluid for improved temperature properties was selected, for which $\eta_s$ was equal to 0.7. However, the shock absorbers shall still be investigated to determine if any additional insulation or heating is required. Further sizing resulted in a shock stroke of 23.5 cm and 14.0 cm for the MLG and NLG, respectively, as well as a strut diameter of 7.4 cm and 5.2 cm.

## 4.6.4. Braking System

Aircraft brakes are used to decelerate the aircraft, aid in steering and hold the aircraft stationary. Regular disc brakes were selected to slow down the aircraft on various types of runways, apart from Amundsen-Scott, where skis are used instead of the wheels. To also be able to decelerate at Amundsen-Scott, the propellers provide reverse thrust, which provide sufficient braking force to slow down the aircraft on all runway types.

### 4.6.5. Integration of Skis

In order to land safely at the Amundsen-Scott base, skis were added to the landing gear as the runway consists of snow. It was determined that skis were essential to distribute landing loads such that the aircraft would not tip over on impact. There are no standard sizing methods for aircraft skis, and therefore it was decided to implement ski dimensions based on specifications of aircraft ski manufacturers. Airglass, Inc. manufactures skis with a technical standard orders (TSO) rating of 4300 lbs[18], which is slightly larger than the experienced landing loads. The dimensions of the skis are 1.86x0.34x0.19 m. In addition, they feature a cutout based on the clearance requirements for the wheels where one ski is used per strut. The skis have a hydraulic system such that they can be placed underneath the tyre when landing on snow and the tyre can be used when landing on gravel at Rothera.

### 4.6.6. Storage of Landing Gear

In order to achieve optimal aerodynamic efficiency in cruise, the landing gear was designed to be stored. A challenge arose, as retractable skis are not common. It was found that skis can be partially retracted and extended with the help of hydraulics, which is currently already applied to, among others, skis for the Twin Otter[19]. As there is limited space in the fuselage, fairings were designed around the skis, in which the ski wheel combination can fully retract. For this, the additional drag was also analysed as presented in Subsection 6.1.2. The fairing was designed such that it is closed off by the ski to limit drag. Figure 4.16 shows the landing gear in its extended and retracted configuration to indicate the position of all items.

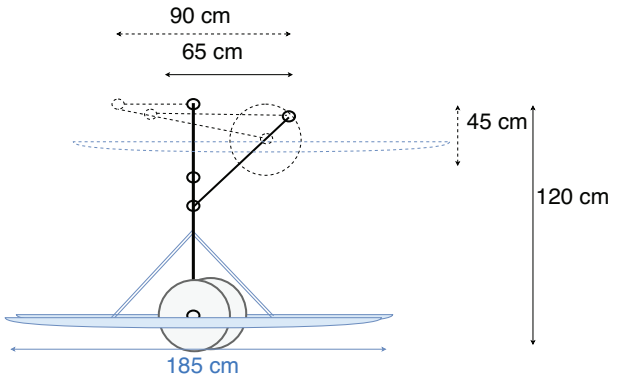


**Figure 4.16:** *Landing gear when deployed and when stored, shown as the solid and dotted lines respectively. The implications of the ski landing gear are shown in blue.*

## 4.7. Hydraulics

Hydraulics were chosen as the main method to operate various aircraft mechanical devices, this decision was made as the hydraulics were already required for skis to be extended or retracted. Flaps, trim tabs, the rudder, wheel brakes, the landing gear, doors and propeller pitch are operated by using highly pressurised fluid to provide mechanical energy. For this, the aircraft features hydraulic pumps, reservoirs, control valves and various safety systems in case of emergencies. The pumps are powered by the generators connected to the combustion engines, however in case of engine failure the additional power can be supplied by the batteries.

The hydraulic system was designed such that single point failure does not occur. This is done by having one main system which can operate all subsystems on both the left and right side of the aircraft centerline, as well as a hydraulics system for both sides individually. In order to switch between the systems, control valves are used as well as pipes which connect the reservoir to the relevant subsystem. During regular operations, when there is no failure, only the individual systems will be used such that the pressure that needs to be provided by the hydraulic motors remains limited.

The downside of hydraulics is that current hydraulic fluids for aircraft only operate as low as -45°C[20]. Therefore, the hydraulic tanks are heated and the pipes are insulated. When parked at Amundsen-Scott, where the lowest temperatures

[18] Airglass, Inc. ski specification overview, http://www.airglas.com/Portals/6/NWDS_StcFiles/6/GENERAL%20AVIATION%20SKI%20SPECIFICATIONS%20(TSO%20INCLUDED.pdf, date accessed = 08-06-2022

[19] Hydraulic aircraft skis, http://www.genaireltd.com/manufacturing, date accessed = 08-06-2022

[20] Datasheet for aircraft hydraulic fluid, https://productcatalog.eastman.com/tds/ProdDatasheet.aspx?product=71093410&pn=Skydrol+PE-5#_ga=2.247792263.1824798051.1654760386-1140799185.1654760386, date accessed = 09-06-2022

occur, heat blowers are used as contingency. Next to this, different failure modes that might occur were considered. Contamination of the hydraulic fluid is mitigated by careful maintenance procedures. Overheating and pressure loss might also occur, for which electrical actuators were included as contingencies up to the point where the hydraulic system is restored.

## 4.8. Electrical

The following subsections provide the reader with the details of the electrical system in the aircraft. The full system is described in combination with an electrical block diagram and the batteries were sized accordingly.

### 4.8.1. Block Diagram

The electrical block diagram was constructed as visual representation of the interconnected electrical subsystems and is presented in Figure 4.17. For this, the system was designed in such a way that single point failure would not be catastrophic for aircraft operations. The main source of power in all flight phases are the generators connected to the engines, from which the available power gets distributed to various busses. These busses, featuring circuit breakers, were implemented to protect other electrical circuits in the system.

Each combustion engine is connected to a starter/generator. The generators produce an alternating current (AC) as is required by the electric motors. Also, AC generators are generally considered to produce more power, have lower maintenance costs and are more efficient at low rpm. The generated power is distributed to the generator bus for the left and right engine separately, from which the power gets directed to the main propulsion bus, the avionics bus and the battery bus. The primary bus distributes power from the batteries, main propulsion bus and auxiliary power supply towards all other aircraft subsystems besides the cockpit and propulsors. Most of these other subsystems, as well as batteries, require direct current (DC) input which is achieved by the addition of rectifiers and voltage regulators. The conversion from AC to DC occurs in the relevant busses, such that most of the circuit experiences AC power distribution to limit energy losses by transporting higher voltage electricity compared to DC.

The setup of the electrical systems makes sure that all main busses, namely avionics, battery, propulsion and primary, have multiple power inputs. In this way, if failure were to occur in one of the electric components, the subsystems that are crucial to perform the mission can still be operated without the need for direct repair works. For example, if battery 1 were to fail, the medical systems in the primary bus would still be powered by the connection to the main propulsion bus and battery 2. Also, letting the busses have multiple power inputs limits the required battery size as in that case not all power needs to be supplied by the batteries. In case of failure in the left generator bus, the auxiliary power supply and right avionics bus can still be used to power other subsystems. The auxiliary power supply however is only available when the aircraft is on the ground and parked.

In the cockpit, ammeters are used to monitor generator performance and other monitoring devices are included as well. The propulsion system however is drawn as if all propulsors can still be operated in case of engine failure. It was decided that that the propulsors on the opposing side to engine failure would be turned off as explained in Section 4.4. The electrical block diagram has only been included to visualise the path of electricity throughout the aircraft. The cockpit also contains master switches, which are used to switch the electrical circuits on or off. This might be required in the case of engine startup, as power demand is high the other subsystems may be turned off such that the batteries are not fully depleted.

### 4.8.2. Estimation of Battery Size

In order to allow crucial subsystems to operate, two batteries were included in the design. However, since detailed data regarding the power required for general aircraft subsystems was lacking, the batteries were sized by analysis of similar twin-propeller aircraft with respect to MTOM. Table 4.16 contains the reference aircraft and parameters[21].

**Table 4.16:** *Reference aircraft for power estimation.*

| Aircraft | DHC-6 Twin Otter | Dornier 228 | NAL Saras | Beechcraft king air 350 |
|---|---|---|---|---|
| MTOM [kg] | 5670 | 6500 | 6100 | 7484 |
| Total battery capacity [Ah] | 43.6 | 50 | 43 | 42 |

By averaging battery capacity over MTOM and multiplying this value with MTOM of JAPA-12 and adding the contingency as established, a battery capacity of 52.3 Ah was found. However, as the engines are much larger compared to the

[21] Database for reference aircraft, https://customer.janes.com/janes/home, date accessed = 08-06-2022

reference aircraft the team analysed the capacity required for the starter. The EMB-120 uses the same engine as the JAPA-12 and the battery, which is used for engine startup and emergencies, has 40 Ah capacity running on 28 V[22]. This meant that the required battery capacity did not need to be altered accordingly.

It was decided that the DC required for the batteries runs on 28 V which is generally used for aircraft [47], this resulted in batteries of about 1.5 kWh. From the overview of the power required for medical systems, which is included in Appendix A, it was estimated that 1.5kWh is required if all systems are constantly operative. However, the medical systems might also need to be operative when engines are out. Therefore, it was assumed that the medical systems require two hours of power with engines inoperative, resulting in a total of 3kWh. Operation of the medical systems in flight was not taken into account as the current engines selected can still provide 30 kWh to the electrical system in case of one engine inoperative as concluded in Subsection 4.4.2.

Based on the battery trade-off in [1], lithium-ion batteries were selected with a specific energy of 320 Wh/kg. This resulted in selection of two batteries of 7.1 kg each to be used in design, providing 4.5kWh.

### 4.8.3. Power Budget

The power budgets for nominal cruise and OEI cruise conditions were determined. The results are presented below in Tables 4.17 and 4.18. For OEI conditions, it was assumed that one gas turbine remains operational and is outputting its maximum continuous power, taking into account the altitude effects described in Subsection 4.4.2. To ensure all five electric motors can be run at full power to reduce yawing moment, the aircraft cruise speed in OEI conditions was lowered slightly, from 107 m/s to 100 m/s. In addition to overcoming drag, the gas turbine needs to power 5 electric motors, medical equipment, HVAC systems, anti-icing systems and navigation and communications systems. From Table 4.17 it can be seen that 28 kW of power is left over, which can then be used for miscellaneous aircraft systems such as avionics and anti-collision lights on the wings. The largest power demand in the miscellaneous category is expected to come from the hydraulic pumps. The Twin Otter requires about 100 bar of pressure. However, as the exact required capacity for hydraulic pressure is currently unknown, electrically powered hydraulic pumps were analysed with a much larger capacity to find a maximum amount of power required. For a pump that provides about 690 bar, a total of 0.75 kW is required as input power. As the aircraft features three separate hydraulic systems, a maximum of 2.25 kW is required for operating all hydraulic pumps. This leaves about 26.45 kW for other systems which includes items such as lights, additional avionics and power outlets for passengers to charge devices. It was concluded that the remainder is more than sufficient for the other items to be powered.

For nominal operations, it was assumed that both gas turbines are fully functioning, and are producing their maximum continuous power at the cruise altitude. From the results it can be seen that 45% of total available power is unused after powering the necessary aircraft systems. This highlights the fact that the engines were sized for OEI conditions.

**Table 4.17:** *Power budget for OEI operations.*

| Parameter | Power [kW] | Share of available power |
|---|---|---|
| Power available from GT, OEI cruise | 848.5 | 100% |
| Overcome drag | 651.3 | 76.76% |
| Electric motors | 150 | 17.68% |
| Medical | 1.5 | 0.18% |
| HVAC | 3.65 | 0.43% |
| Anti-ice | 13 | 1.53% |
| Navigation & communication | 1 | 0.12% |
| Misc | 28.0 | 3.30% |
| Power left over | 0 | 0% |

## 4.9. HVAC and Pressurisation System

In this section the heating, ventilation, air conditioning (HVAC), and pressurisation of the cabin is discussed. For the ArtEvac mission these were important factors to ensure the survival and comfort of the patient due to the rough Antarctic environment.

[22]EMB-120 specifications, https://customer.janes.com/Janes/Display/JAU_9151-JAU_ date accessed = 13-06-2022

**Table 4.18:** *Power budget for nominal operations.*

| Parameter | Power [kW] | Share of available power |
|---|---|---|
| Power available from GT, cruise alt | 1696.9 | 100% |
| Overcome drag | 583.1 | 34.36% |
| Electric motors | 300 | 17.68% |
| Medical | 1.5 | 0.09% |
| HVAC | 3.65 | 0.22% |
| Anti-ice | 13 | 0.77% |
| Navigation & communication | 1 | 0.06% |
| Misc | 28.0 | 1.65% |
| Power left over | 766.7 | 45.18% |

### 4.9.1. Heating

Firstly, the thermal control system is presented. Insulation and heating is required to maintain a comfortable temperature. To size such a system an initial calculation was done to determine how much heat is lost from the fuselage. Two cases were considered, standing still at Amundsen-Scott and cruise. At Amundsen-Scott the highest temperature difference between the cabin and the environment was experienced. For cruise the temperature difference was smaller but due to the speed of the aircraft convection effects came into play.

For both calculations the assumption was made that the fuselage is a cylinder. For insulated cylinders, Equation 4.19 dictates the flow of heat from the body [48]. The $r$ values represent the different radii of the pipe. The $k$ values represent the coefficient of thermal conductivity of the materials. The value of $L$ represents the length of the of the fuselage that needs thermal control, this includes the cabin and cockpit. An electrical heating system was used, as these systems convert all power input to heat[23]. The efficiency of the heating system is represented through $\eta$ and was set to 1. Finally, the value of $h_c$ represents the convective heat transfer coefficient. The variables are visualised in Figure 4.18.

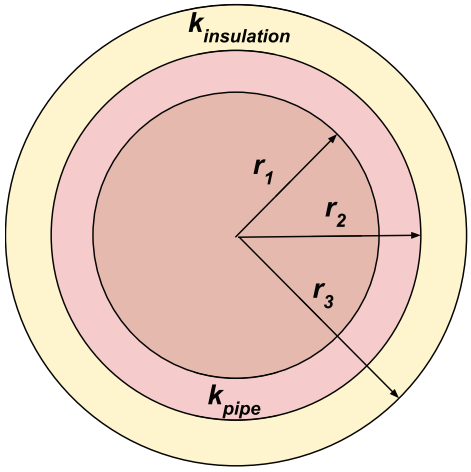


**Figure 4.18:** *Pipe nomenclature.*

$$Q = \frac{2 \cdot \pi \cdot L \cdot (\Delta T)}{\left(\frac{\ln\left(\frac{r_2}{r_1}\right)}{k_{\text{pipe}}}\right) + \left(\frac{\ln\left(\frac{r_3}{r_2}\right)}{k_{\text{insulation}}}\right) + \left(\frac{1}{r_3 \cdot h_c}\right)} \cdot \eta \tag{4.19}$$

At Amundsen-Scott an environmental temperature of -82.2°C was found as an extreme through the investigation conducted in the Baseline Report [6]. Australian and US guidelines specify that an ICU should have a temperature of 21°C [49]. This resulted in a temperature difference of 97°C. Additionally, by making use of fibreglass insulation, a thermal

[23] Room heaters, https://www.cse.org.uk/advice/advice-and-support/room-heaters#:~:text=Electric%20heaters%20are%20all%20considered,shown%20in%20kilowatts%20(kW), date accessed = 08-06-2022

conductivity of 0.04 W/mk was found[24]. Finally, the heat conduction case at Amundsen-Scott was executed for a stand still situation, where the aircraft was not moving. This resulted in no convective heat transfer, which dropped the $\frac{1}{r_3 \cdot h_c}$ from Equation 4.19. Working Equation 4.19 out for a non-moving aircraft at Amundsen-Scott, a conductive heat loss of 3420W was found.

During cruise, the environmental temperature was significantly different, as the cruise temperature was computed as $-32°$C. This resulted in a temperature difference between the cabin temperature and the environment temperature of $30.76°$C. Now, as during cruise convective heat transfer was present, the convective heat transfer coefficient was to be found. This was simply done via Equation 4.20[25].

$$h_c = 12.12 - 1.16V + 11.6\sqrt{V} \tag{4.20}$$

The convective heat transfer coefficient during cruise was computed as $h_c = 0.648$ W/m$^2$K. Then, by computing the conductive heat loss of the aircraft during cruise via Equation 4.19, a conductive heat loss of 1347W was found.

Comparing the aircraft in cruise with the stationary aircraft on ground, it was concluded that the stand-still aircraft at Amundsen-Scott lost significantly more heat than the aircraft during cruise. Therefore, the power required for the thermal control of the aircraft was determined to be 3420 W.

It was investigated whether increasing the thickness of the insulation has a critical effect on the decrease in the heat per second lost from the fuselage. Fibre glass insulation will be used as this is the industry standard. Differentiating Equation 4.19 with respect to the thickness of the insulation revealed that increasing the insulation thickness has less effect on the power saved the thicker the insulation becomes. At first, the amount of power saved through increasing the insulation thickness was significant. However, this effect quickly diminished as the thickness increased. The weight of the insulation was dependant on the volume of the insulating layer. The insulation volume had a quadratic proportional relationship with the thickness. Therefore the weight of the insulating material increased rapidly with the thickness of the insulation. Because of this it was opted to not increase the thickness of the fuselage beyond what was set in Subsection 4.1.1. The thickness of the insulation was set as 9.4 cm and had a mass of 88.06 kg.

### 4.9.2. Ventilation

The air ventilation is vital to ensure the health of the patient during the medical evacuation. The main reason for this is that proper ventilation is required to prevent the spread of bacterial and viral infections, and to prevent molds and chemicals movement through the air [50].

To prevent the spread of these infection sources, general control measures are to be implemented in air ventilation systems. These control measure categories are: filtering (basic and HEPA), temperature, humidity, UV-light, and fresh air [50]. To meet these requirements, a medical ventilation system was set up. A sketch of such a ventilation system is provided in Figure 4.19, where each ventilation component is placed in the required order [51].

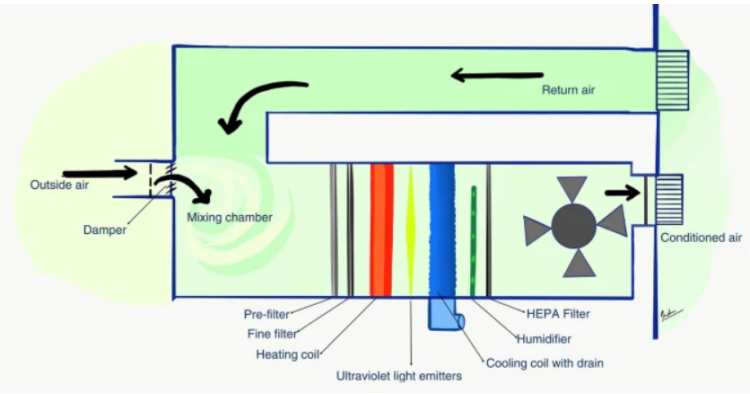


**Figure 4.19:** *Illustration of the aircraft ventilation mechanism required for medical purposes [51].*

Looking at Figure 4.19, one can note that an outside air inlet was required. Therefore, to allow for a ventilation system, a passage from the outside air to inside the cabin was required. Now, as the engines have a combustion chamber, which

[24] Website containing basic thermal conductivities of various materials, https://www.engineeringtoolbox.com/thermal-conductivity-d_429.html, date accessed = 07-06-2022

[25] Website containing basic engineering formulas, https://www.engineeringtoolbox.com/convective-heat-transfer-d_430.html, date accessed = 08-06-2022

requires oxygen to function, an air inlet is already present at the main engines of the aircraft. Therefore, to allow for fresh air intake, an air duct was designed, to transfer fresh outside air to the ventilation system inside the cabin.

As there was little information to be found on the required power of medical ventilation systems, the power usage was estimated. For this, the ventilation system of the aircraft was compared to one of a general household. A basic household ventilation system consists of fans and basic filters[26]. Thus, when comparing a basic household ventilation system to the one used on the aircraft, the main difference was the temperature and humidification control and the additional HEPA filter. Now, as the cabin heating was already covered in Subsection 4.9.1, the heating power was dropped from the ventilation system. To account for the humidifier, the maximum power for a portable humidifier was used, simply to have a first estimate. The humidification power required was found as 50 W[27]. The HEPA filter did not require additional power. Finally, taking the required power for a simple household ventilation system, without heating, humidification and an HEPA filter, a required power of 50 W[28] was found. This means that the estimated ventilation power required came down to 100 W.

### 4.9.3. Air Conditioning

Apart from a heating system, the outside temperature can also be higher than inside the cabin. In such cases, an air conditioning system is required to cool the cabin temperature down to the desired 21°C [49]. Now, as the temperature on Antarctica ranged from -76°C to 7.7°C [6], there is generally no cooling required as the outside temperature is lower than the cabin temperature. However, from the market analysis, it was established that the aircraft should fly to remote communities in Canada [6]. At the mainland of Canada, summer temperatures of 30°C are not uncommon[29]. Therefore, as 30°C exceeds the cabin temperature of 21°C, an air conditioning system is required.

As during cruise, the temperature was computed as $-9.76$°C, only operations close to the ground require a cooling system. Therefore, for aircraft cooling, only static ground operations at $30$°C was analyzed. With a desired $21$°C cabin temperature, the temperature difference considered was $\Delta T = 9$°C. Then, by having the same aircraft fuselage as in Subsection 4.9.1, Equation 4.19 resulted in a conductive heat loss of 298 W. To size the power required for the air conditioning unit a coefficient of performance of 2.3 is assumed [30]. The coefficient of performance quantifies the ratio of heat an air conditioner moves out of a system to the energy input. Therefore an air conditioning system was assigned with at least a required wattage of 130 W.

### 4.9.4. Pressurisation

As discussed in Subsection 4.1.1 the fuselage of the aircraft should be pressurised. The pressure was set to 75237 Pa as that was the minimum required by regulations [27]. In order to maintain a comfortable pressure throughout the flight a pressurisation system was designed. Lightweight electrical air compressors pump fresh air from the outside into the fuselage. Stale air leaves the fuselage through an outflow valve. This valve is automatically controlled to prevent the fuselage from over-pressurising. Two pressure relief valves were also implemented for safety and redundancy as required by regulations [27]. The pressure relief valve releases air when the cabin pressure and atmospheric pressure differ by more than 40 kPa. This pressure difference is slightly higher than the difference that is obtained when flying at the service ceiling altitude. The fuselage structure is sized for this value as discussed in Subsection 7.1.1.

To add, aircraft structures are not designed for the case where the outside pressure is greater than inside the fuselage. To avoid this, two negative pressure release doors are used. These doors work similarly to the pressure relief valve. However, the pressure release doors are much more sensitive to pressure differences. If the outside pressure is more than 0.01 MPa larger than the inside pressure the negative pressure release door will open and the pressure will equalise.

## 4.10. Class II Weight

After sizing the JAPA-12, class II weight estimation was performed. For this, the method of Torenbeek for commercial transport airplanes presented in Roskam was used [13]. This method was chosen in order to be consistent with the estimation methods used for the different sub-systems. The dimensions of different sub-systems were input along with

[26] Website describing household ventilation systems, https://www.energy.gov/energysaver/whole-house-ventilation, date accessed = 08-06-2022

[27] Website covering various types of humidifier power usage, https://theozonehole.com/do-humidifiers-use-a-lot-of-electricity.htm, date accessed = 08-06-2022

[28] Website covering basic ventilation power required and cost, https://www.pluggit.com/portal/en/how-much-power-do-the-ventilation-fans-use--2748, date accessed = 08-06-2022

[29] General Canadian weather and climate data, https://weather-and-climate.com/average-monthly-Rainfall-Temperature-Sunshine-in-Canada, date accessed = 08-06-2022

[30] Typical coefficient of performance values, https://www.nuclear-power.com/nuclear-engineering/thermodynamics/thermodynamic-cycles/heating-and-air- conditioning/coefficient-of-performance-cop-refrigerator-air-conditioner/, date accessed = 17-06-2022

the mission profile to yield a better estimation of the weights. The weights of each aircraft component are presented in Table 4.19.

**Table 4.19:** *Overview of class II sub-system weights.*

| Subsystem | Torenbeek [kg] |
|---|---|
| Wing | 931.55 |
| Empennage | 110.33 |
| Fuselage | 691.87 |
| Landing gear | 370.74 |
| Powerplant | 1210.03 |
| Fixed equipment | 1384.90 |
| OEM | 4699.42 |

Adding the payload and fuel weight for the critical mission to the OEW gave a MTOM of 6891.0 kg. This value was 4.9 % higher than the estimated mass obtained from energy sizing presented in Section 3.6. Due to time constraint it was decided to stop the iterative process at a difference in MTOM lower than 5%. Iterating until a difference of 1%, which is desirable [52], will be done in the next phase of the design process.

With the purpose of comparing the results obtained from the class II estimation, two different methods were looked into, namely the Torenbeek method and the Raymer method. Table 4.20 shows the percentage breakdown of the OEW for the different sub-systems. From the table, it can be concluded that both methods have a similar percentage breakdown for the empennage, fuselage and powerplant. Since the landing gear is being over-designed for the JAPA-12, the percentage of the weight of this sub-system should be analysed in the next phase of the design process as for the second method the percentage breakdown is higher. For the powerplant, the weight should also be analysed as for a distributed propulsion aircraft this sub-system is more complex which leads to an increase in weight. When comparing the weight calculated in Section 4.4 to the weight estimated with class II, it can be seen that class II is underestimating this value by 4.6%. The weight estimated for the wing can for example be reduced, as for the Torenbeek method this is higher than for the Raymer method, and can be added to the powerplant weight in order to keep the same OEW and compensate for the complexity of the distributed propulsion with respect to the powertrain.

**Table 4.20:** *% of OEM for the different sub-systems.*

| Sub-System | Torenbeek | Raymer |
|---|---|---|
| Wing | 19.8 | 11.7 |
| Empennage | 2.4 | 1.9 |
| Fuselage | 14.7 | 12.7 |
| Landing gear | 7.9 | 12.2 |
| Powerplant | 25.8 | 27.8 |
| Fixed equipment | 29.5 | 33.7 |

The weight of the aircraft is an important parameter, therefore, the iterative process should, in future phases, be carried out until a 1 % difference is achieved. Afterwards, a class III weight estimation followed by a class IV weight estimation should be performed to have an accurate weight breakdown since the design uses a novel propulsion configuration which cannot accurately be captured by statistical equations used in class II weight estimation.

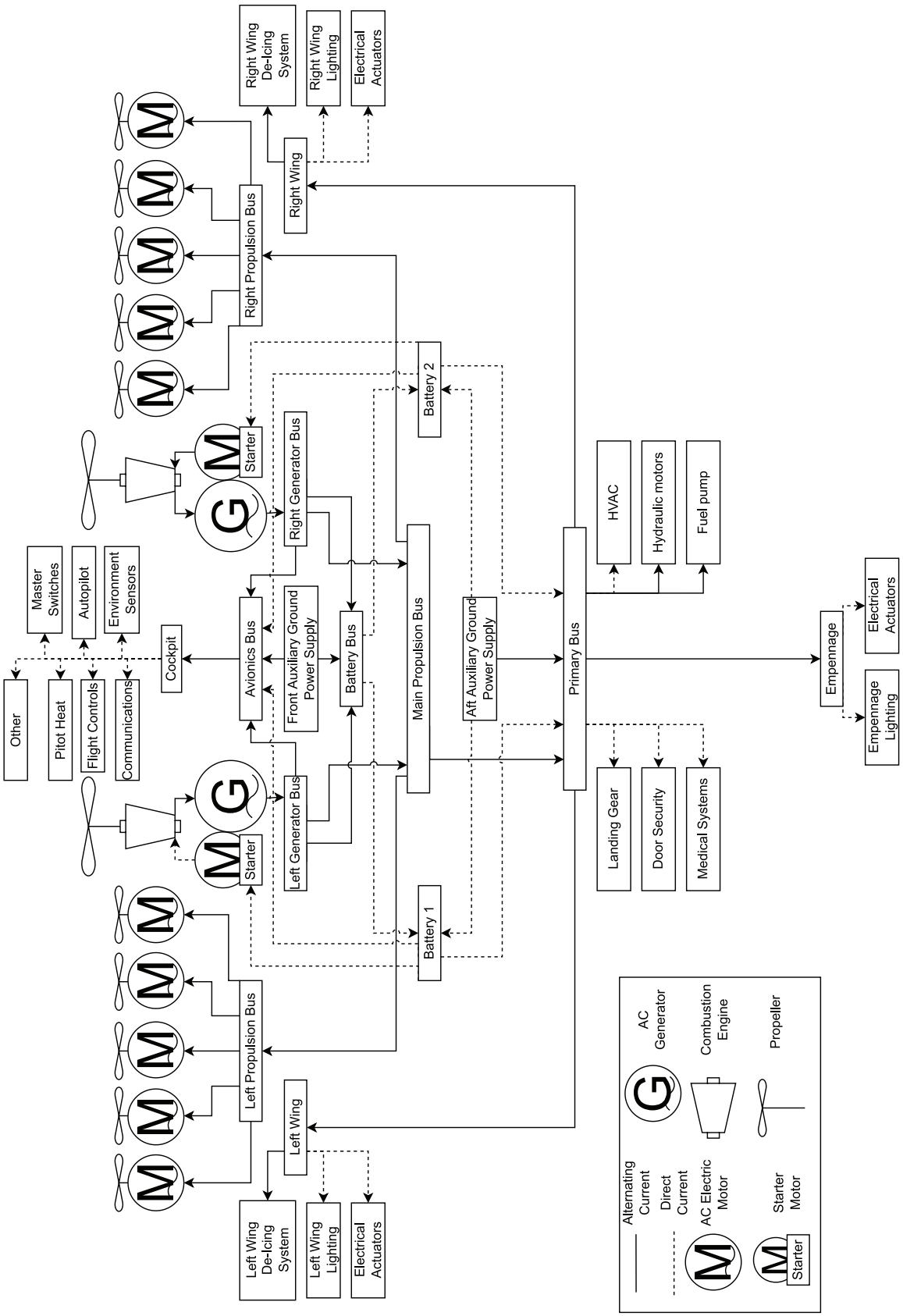


**Figure 4.17:** *Electrical block diagram for JAPA-12.*

# 5
# Operations & Logistics

As the JAPA-12 aircraft is operational in rough environmental conditions, the operations and logistics attached to the mission differ significantly from common flight profiles. Therefore, an operations & logistics strategy was established to tackle possible issues that arise due to this ambitious mission. This chapter covers the strategy in the following way: first, adaptations to the on-ground fuel system are presented in Section 5.1, as the JAPA-12 makes use of an uncommon fuel type. Next, due to the cold temperatures experienced, the anti-icing system is discussed in Section 5.2. How to facilitate constant communication in challenging conditions is covered in Section 5.3. This is followed by discussing the navigation system in Section 5.4. As the aircraft has to operate with very limited vision, additional measures were required. Therefore, the approach, take-off, and ground operations visual strategy is discussed in Section 5.5. Finally, the software-hardware overview is presented in Section 5.6, showing all subsystem connections.

## 5.1. Refueling

The Amundsen-Scott research station uses JP-8, which is a commonly used military aircraft fuel, as their main power source. As the design flies on synthetic kerosene, it would be convenient to transform the JP-8 fuel infrastructure to using synthetic kerosene, such that Sustainable Aviation Fuel (SAF) can both power the generator at Amundsen-Scott, and refuel the aircraft.

The composition of jet fuels can differ, depending on the refinement method used. This difference can cause incompatibilities in storage if the fuels are mixed [53]. This means that before the synthetic kerosene can be stored in the tanks used for the JP-8 at Amundsen-Scott, the compatibility of fuels has to be examined or the tanks have to be cleaned.

One advantage of storing synthetic fuels over conventional JP-8 is that many of the deposit forming reactions are not present in hydro-treated synthetic kerosene [53]. This is caused by the reduced solubility of water in synthetic jet fuel, which contains no aromatic content. However, a possible disadvantage is the possibility of microorganisms metabolising the fuel. This is not a problem with conventional jet fuel as these fuels contain aromatic and sulfur-containing compounds, which are toxic to most microorganisms. The growth of the microorganisms can be reduced by regularly removing water from the fuel tank as these microorganisms require the presence of water to grow.

In long-term storage, fuels tend to form peroxides and gums, which contaminate the fuel. Petroleum-derived fuels are less susceptible to contamination. This is caused by the natural anti-oxidants present in these fuels [54]. The anti-oxidants may be added to the synthetic fuel to reduce contamination as these anti-oxidants are not naturally included in synthetic kerosene.

Since synthetic kerosene is similar to the already used JP-8, it can be supplied by the conventional, currently used method. Currently, the station is supplied with fuel in one of two ways. Fuel is flown in by the United States Antarctic Program (UNAP) LC-130 aircraft[31]. In addition to these flights, three times per year the South Pole Traverse arrives at Amundsen-Scott. This is a fleet of tractors hauling fuel bladders, which are unloaded at Amundsen-Scott. This fuel is used to power the station during winter and supply aircraft departing Amundsen-Scott[32].

The fuel required to fly to Amundsen-Scott is available from Rothera airport. The Rothera research base uses the same infrastructure as Amundsen-Scott to generate power for its facilities. Currently, it uses JP-8 as fuel, which could be changed to synthetic kerosene as explained above. The fuel is supplied to the research station every summer by ship[33].

## 5.2. Anti-Icing

Icing of an aircraft occurs when an aircraft flies into a supercooled water droplet, which freezes on impact. This occurs at an ambient air temperature between $0$ °C and $-40$ °C of which $0$ °C to $-15$ °C has the highest threat of icing to occur[34]. Below a temperature $-40$ °C all droplets are frozen, and thus do not freeze and attach to the surface of the wing or propeller once they are hit. This ice build-up will thus happen at the edges of the airframe and the propeller which can

[31] The antarctic sun on fuel used on the south pole https://antarcticsun.usap.gov/features/4405/, date accessed = 25-05-2022

[32] The antarctic sun on the south pole traverse, https://antarcticsun.usap.gov/features/4397/, date accessed = 25-05-2022

[33] Information on the Rothera airfield, https://www.bas.ac.uk/polar-operations/sites-and-facilities/facility/rothera/rothera-air-facility/runway/, date accessed = 25-05-2022

[34] Icing conditions, https://www.weather.gov/source/zhu/ZHU_Training_Page/icing_stuff/icing/icing.htm, date accessed = 18-05-2022

strike water droplets, such as the leading edge of the wing and horizontal stabiliser. This affects the performance of the aircraft in two ways: Firstly, the weight of the aircraft is slightly increased. Secondly, the main disadvantage is the reduction in lift and the increase in drag as the airfoil shape is altered.

There are two solutions for icing conditions; firstly anti-ice. Anti-ice is used to stop ice from forming on the wings by heating the leading edges of the wing. The other solution is de-icing. De-icing works by removing the formed ice on the wing by for example temporarily expanding the leading edge of a wing, by inflatable de-icing boots, breaking the ice which is subsequently blown away.

It was decided to use heated surfaces on the leading edge of the wing, vertical and horizontal stabiliser and propeller. These leading edges will be split up into several parts which can be turned on or off independently of each other. This ensures that if one part fails not the whole wing surface, empennage surface or propeller will experience icing. It will also enable the aircraft to cyclically heat the leading edges and propellers, by heating up one element after the other. This will reduce the power required for the anti-ice system. To make sure the future design is capable of performing the anti-icing it was made sure that the excess power of the engines in one engine inoperative conditions is sufficient to power the system. To comply with this it was assumed that the leading edges will be heated in a cyclic manner. The power required estimation took into account the effect of sensible heating, convective cooling, evaporate cooling, kinetic heating, aerodynamic heating and dynamic heating. The difference in heating required for the leading edge to have a temperature of 6 °C and the cooling and heating effects will have to be supplied by the power of the aircraft. The power required was calculated using a method that first calculates the power required to remove ice per square meter of ice. This was then multiplied by the area of the anti-ice to result in the power required for the anti-icing subsystem, which is 13 kW [55]. The area of the aircraft which has anti-ice was estimated by multiplying the area required for the 787 by a correction factor, which is based on the size of the wing surface area. This resulted in a surface area of 2.35 $m^2$. In the calculations, the most power-intensive estimates had been used for every part of the heating. This will make sure the power required will not increase once the subsystem will be sized in more detail.
For the de-icing of the windshield, it was decided to use electric heating elements included in between the several window plys of which a windshield is built[35].

To prepare the aircraft for departure, possible built up of ice on the aircraft has to be removed. This can be done by either using a de-icing fluid or by manual de-icing. De-icing fluid is done by spraying a fluid on the aircraft which consists of a mixture of glycol and water. Manual de-icing is performed by mechanically removing ice from the aircraft with the use of brooms, brushes or air blowers[36]. It was decided to use manual de-icing by using hot air blowers, which are already present at Amundsen Scott. Apart from this, the use of glycol-based de-icing fluids is not possible at Amundsen-Scott, because the lowest freezing temperature of a water-glycol mixture is approximately -50 °C[37]. According to regulations, the lowest operational use temperature (LOUT) is determined based on the freezing point of the de-icing fluid. For a type I fluid the freezing point of the fluid is 10 °C lower than the LOUT for a type II or IV fluid this is 7 °C lower[38]. This thus makes the use of fluid de-icing impossible at Amundsen-Scott as the outside air temperature can reach -76 °C, thus requiring a freezing temperature of -86 °C for type I and -83 °C for type III and IV. It was deemed not necessary to be able to de-ice the aircraft at Rothera research station as the aircraft can be stored in a heated hangar[39].

Apart from icing conditions, the extreme cold experienced at Amundsen-Scott will have several other consequences. If it is required to leave the aircraft parked at Amundsen-Scott for a period requiring the engines to be shut down, it is required to keep the aircraft hot. If this is not done properly the fuel, oil and lubricants can freeze and thus not be able to start the engines or operate the aircraft. This can be done by storing the aircraft in a heated hangar or, as done on an earlier rescue mission, by using hot air blowers[40]. Since these hot air blowers are available at Amundsen-Scott it was decided to use this method of keeping the aircraft hot on the ground. The Rothera research station has a heated hangar, which is used for aircraft storage, thus this hangar will be used to store the aircraft for prolonged periods.

The last on-ground problem stemming from the extreme cold is the possibility of an aircraft getting stuck. This happens if the skis or ski/wheel combination freezes to the ground. At Amundsen-Scott there are wooden platforms available to

[35] Windshield anti-ice, https://www.aircraftsystemstech.com/2017/05/aircraft-windshield-frost-fog-and-ice.html, date accessed = 25-05-2022
[36] Aircraft de-icing, https://www.naa.edu/aircraft-deicing/, date accessed = 25-05-2022
[37] Ethylene glycol freezing point chart, https://corecheminc.com/wp-content/uploads/2020/06/Freeze-Point-Chart-GlycoChill-Ethylene-Glycol-Heat-Transfer-Fluid.pdf, date accessed = 30-05-2022
[38] Deicing/Anti-icing Fluids, https://tc.canada.ca/en/aviation/publications/when-doubtsmall-large-aircraft-aircraft-critical-surface-contamination-training-tp-10643/chapter-3-deicing-anti-icing-fluids-14, date accessed = 30-05-2022
[39] Information on the facilities at Rothera airfield, https://www.bas.ac.uk/polar-operations/sites-and-facilities/facility/rothera/rothera-air-facility/runway/, date accessed = 25-05-2022
[40] Antarctic rescue mission, https://www.nationalgeographic.com/adventure/article/Antarctic-winter-risks-for-pilots-and-planes, date accessed = 25-05-2022

park the aircraft on. This removes the problem of the aircraft freezing to the ground.

## 5.3. Communication

Constant communication with the ground was deemed essential for a successful mission. With efficient communication, ground stations can continuously be updated regarding the status of the aircraft, the crew and the patient. For communication, several methods are commonly used by aircraft. VHF/HF radio modules are generally used for aircraft to aircraft and aircraft to ground communication. On top of that, satellite communication is also a frequently used means on communication, to provide fast and reliable communication with the outside world. Both options are investigated below.

Very High Frequency (VHF) radio was not possible, as this requires a line-of-sight connection. However, High Frequency (HF) was possible, but the quality of information is low and transferred slowly. Another radio communication option was using High Frequency Data Link (HFDL) communication. HFDL is an Aircraft Communications Addressing and Reporting System (ACARS) to exchange data between aircraft and ground based HFDL systems. The advantage of using HFDL over standard HF is that it uses less bandwidth due to its digital nature[41].

Satellite communication is done over broadband or narrowband. As it is unknown what frequencies are desired to use during this stage of the design, a broadband connection is desired as this covers a wide variety of frequencies. Currently, the only broadband communication system Amundsen-Scott uses, is the Iridium Multi-Channel system for communication[42]. Therefore, communication via satellites is possible at Antarctica.

After careful consideration, it was decided that the JAPA-12 will use both radio and satellite communication. The reason for this was that communication was vital to provide the best medical assistance to the patient. The radio communication module consists of a Communication Management Unit (CMU), a radio module and a satellite communication system. The radio module was required to be both capable of HF voice and HFDL communication so both for the shorter range and longer range communication can be established. The Rockwell Collins CMU-900[43] and Leonardo SP-2310[44] were chosen as CMU and radio respectively. For satellite communication, a Blue Sky Network Hawkeye-7200A[45] was chosen for the radio module.

**Table 5.1:** *Communication module requirements.*

| Component | Average power consumption [W] | Max. power consumption [W] | Required voltage | Weight [kg] |
|---|---|---|---|---|
| SP-2310 | 125 | 400 | 115 V AC, 400 Hz | 20 |
| CMU-900 | 17.5 | 35 | Primary 115 V AC; 400 Hz (28 V DC) | 5.5 |
| Hawkeye-7200A | 12 | 15 | 10-32 V DC | 0.45 |

## 5.4. Navigation

As the route from Rothera to Amundsen-Scott is roughly 2500km, it cannot simply be flown by flying in a straight line. For example, if the aircraft experiences crosswind during cruise, the aircraft may be having an offset and needs to fly a different course. Therefore, a device was needed to locate the aircraft, such that the pilot can alter the heading of the aircraft to compensate for the flight path deviation.

[41] ACARS information, https://skybrary.aero/articles/aircraft-communications-addressing-and-reporting-system, date accessed = 19-05-2022

[42] Website describing the means of communications at Amundsen-Scott, https://www.usap.gov/technology/sctnsouthpolesats.cfm, date accessed = 17-06-2022

[43] CMU-900 brochure, https://www.collinsaerospace.com/-/media/project/collinsaerospace/collinsaerospace-website/product-assets/files/public/products/product-brochures/communication-and-networks/data-links/cmu-900/cmu-900.pdf?rev=d045ea2eadd5431fa64d107fada2f52b, date accessed = 19-05-2022

[44] SP-2310 brochure, https://www.yumpu.com/en/document/view/39363977/hf-data-link-hfdl-sp-2310-selex-es, date accessed = 19-05-2022

[45] Blue Sky Network Hawkeye-7200A, https://shop.blueskynetwork.com/products/hawkeye-7200-aviation-he7200a/, date accessed = 17-06-2022

In general aviation, apart from radio beacons, GPS is often used to show the pilot the position of the aircraft[46]. A reason for this is that only three basic components are required to notify the user on their location: an antenna, a receiver-processor unit, and a display unit[47]. On top of that, GPS satellites provide global coverage, meaning that GPS can show the pilot the position of the aircraft across the globe. Unfortunately, general GPS coverage is lacking accuracy at the north and south pole [56]. This meant that the location of the aircraft is less accurately provided to the pilot near the south pole, which was inconvenient. However, as navigation was mainly desired at high altitudes during cruise, a rough location estimation was deemed sufficient. Meaning that GPS was used to navigate the aircraft during cruise. A GTN 750 Xi was chosen as navigation module. This module also provided a back-up option for satellite communication and provided helpful assistance and advice in case of emergencies. The GTN 750 Xi module is priced at $18245.

In addition to the GPS system, specifically for the latitudes where GPS coverage is extremely poor, a radio navigation system will be used. This would also function as a back-up system to facilitate non-precision approaches when insufficient visuals are present. The radio navigation system works as follows: either a VOR or NDB sends out a signal, after which DME equipment in the aircraft determines the relative bearing to the transmitter. This allows the aircraft to determine its position relative to the beacon. Both the station of departure and station of arrival have an NDB or similar signal transmitter. Amundsen-Scott however has a system that transmits signals in the VHF, or Ultra High Frequency (UHF) using military equipment, while Rothera has a standard NDB transmitting in the HF range. This was not considered a problem for the DME. A BendixKing KN-63 module was chosen, which costs approximately €15000. Looking at a map of active Antarctic bases it was expected that NDBs or similar radio transmitters exist at bases along the route such that signals from at least one beacon could always be received[48].

**Table 5.2:** *Navigation modules requirements.*

| Component | Average power consumption [W] | Max. power consumption [W] | Required voltage | Weight [kg] |
|---|---|---|---|---|
| GTN 750Xi | - | - | 11-33 V DC | 3.22 |
| KN-63 | 100 | 117 | 11-33 V DC | 1.598 |

Now, to define the heading of the aircraft, generally a compass is used inside the cockpit. However, at close proximity of the magnetic south pole (or Amundsen-Scott research station), a compass does not function accurately [57]. This meant that when approaching at and departing from Amundsen-Scott, the heading of the aircraft could not be accurately determined. A solution to this problem would be to design a system which takes the two most recent GPS location points from the aircraft, after which the heading could be determined by assuming flight in a straight line between the two points. Hence, by taking a straight line between the two most recent locations, the heading could be computed rather than measured with a compass. For this, new software had to be created. For a medium sized project from scratch, a cost estimation of $75000[49] was established.

## 5.5. Visual Aid

As presented in the baseline report, both Rothera and Amundsen-Scott research stations experience severe whiteout conditions [6]. These whiteout conditions are described as ”An atmospheric optical phenomenon of the polar regions in which the observer appears to be engulfed in a uniformly white glow. Neither shadows, horizon, nor clouds are discernible; sense of depth and orientation is lost; only very dark, nearby objects can be seen.”[50]. As found from the weather analysis in [6], to comply with **REQ-STA-CUST-03**, the aircraft must be able to land during these whiteout conditions [6]. Therefore, one has to ensure the pilot is able to land without sight. In other words, the system must allow for a landing solely based on instrumental flight. The zero-visibility ground visual system (ZVGVS) makes use of systems carried both on the aircraft and on the ground at target airports. Therefore, the ground visual aid is treated for the 3 critical cases: on-board the aircraft, at Rothera research station and at Amundsen-Scott research station.

[46] Article about tracking planes, BBC, https://www.bbc.com/news/world-asia-pacific-26544554, date accessed = 19-05-2022

[47] Introduction to GPS, National Academy Press, https://nap.nationalacademies.org/read/9254/chapter/5#7, date accessed = 19-05-2022

[48] Map of active Antarctic bases https://blogs.egu.eu/divisions/cr/2016/08/19/image-of-the-week-where-do-people-stay-in-the-coolest-place-on-earth/, date accessed = 17-06-2022

[49] Software development cost estimation, https://www.spheregen.com/cost-of-software-development/, date accessed = 19-05-2022

[50] Aeronautical information manual, instructing pilots on flight actions and hazards https://www.google.com/url?sa=t&rct=j&q=&esrc=s&source=web&cd=&ved=2ahUKEwjV06Ttyuj3AhWHC-wKHYmyDF8QFnoECCsQAQ&url=https%3A%2F%2Ftc.canada.ca%2Fsites%2Fdefault%2Ffiles%2F2020-10%2Faim-2020-2_air-e.pdf&usg=AOvVaw0RJz_EYVWoEV16Vec0gZdl, date accessed = 18-05-2022

### 5.5.1. Aircraft Visual Aid

During approach, the aircraft has to be able to descend from cruise altitude to a set altitude after which the aircraft can be guided for final approach and landing. For this, the aircraft can make use of two main means of guidance: air-traffic control (ATC) and GPS. Both Rothera and Amundsen-Scott have an office for ATC. Combining both, the ATC can guide the aircraft towards the runway, as the aircraft can be tracked via GPS. Vice versa, the aircraft can descend towards the rough location of the runway via GPS. However, this mean of approach is far from sufficient to accurately land the aircraft during rough weather conditions.

To be able to land, the pilot has to have visual of the runway. To ensure the pilot has visual of the runway both during approach and on the ground, a synthetic vision system (SVS) was chosen. SVS generates a synthetic visual of the environment, which is shown to the pilot via a heads-up display as illustrated in Figure 5.1 [58].

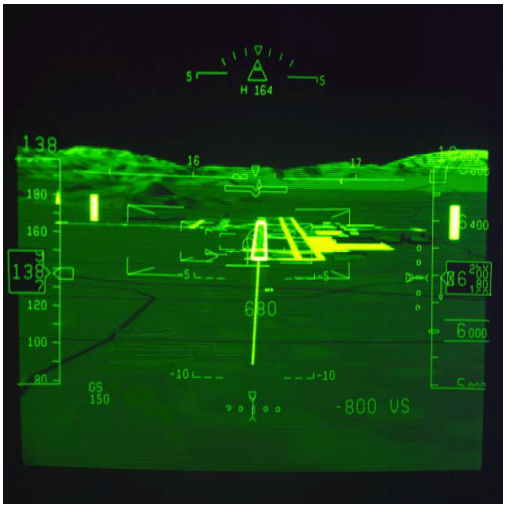


**Figure 5.1:** *Illustration of SVS head-up display [58].*

The SVS aids the pilot by providing vision through rough atmospheric conditions like darkness, fog, haze, rain and snow [58]. This makes the system interesting as the pilot can practically always identify the runway within an altitude of 650ft above the ground [59]. Additionally, these systems are widely used in military applications, and are slowly being introduced to commercial flights [58]. This means that SVS can be initialised during approach at or below an altitude of 650ft, during ground operations such as taxiing, and during take-off.

As the SVS allows for a constant runway visual to the pilot during all weather conditions experienced at both the Rothera and Amundsen-Scott research stations, the SVS was chosen to be implemented in the cockpit. This meant that additional systems were included on-board the aircraft, as they are required to make the SVS system functional. This list is provided in Table A.2. The estimated costs of SVS for a commercial aviation aircraft are $500k[51]. Therefore, the SVS system is an investment into the aircraft, and due to the high cost should only be applied to the aircraft series which expect to land with very poor vision. However, inclusion of the SVS system also provides further market opportunities, as it is convenient for, for example, search and rescue missions.

### 5.5.2. Rothera Ground Aid

As the synthetic vision system can only be initialised at an altitude of 650 ft, additional measures are required to guide the pilot towards the runway. This guidance has to be done both for heading and altitude of the aircraft, as there is limited room for flight path adjustments at a height of 650 ft.

Currently, the Rothera runway has an option for so-called area navigation (RNAV) approach[52]. The RNAV approach makes use of a series of way points, speeds and altitudes which are stored in the on-board database of the aircraft[53]. This means that at the runway of Rothera, there are already RNAV existing waypoints. In fact, the waypoints can guide an aircraft towards the runway up to a decision height of 630ft, provided that the aircraft has a climb gradient of 4% to provide sufficient ground clearance in case of a missed approach[54]. This means that Rothera airport does not need additional ground instruments to guide the aircraft towards an altitude of 650ft where the SVS can be turned on. This makes ground operations at Rothera feasible during all weather conditions vision-wise. An illustration of approach at Rothera is presented in Figure 5.2.

[51] Purchase of private synthetic vision system, https://www.astronics.com/enhanced-vision-systems, date accessed = 18-05-2022

[52] Rothera runway approach procedures, https://www.bas.ac.uk/wp-content/uploads/2018/09/Rothera-Approach-Departures-and-Airfield_Skiway-Information.pdf, date accessed = 18-05-2022

[53] General description of the RNAV system, provided by Eurocontrol, https://www.icao.int/EURNAT/Other%20Meetings%20Seminars%20and%20Workshops/PBN%20TF/PBN%20TF8/PBNTF8%20IP08_RNAV%20approaches.pdf, date accessed = 18-05-2022

[54] Rothera runway approach procedures, https://www.bas.ac.uk/wp-content/uploads/2018/09/Rothera-Approach-Departures-and-Airfield_Skiway-Information.pdf, date accessed = 18-05-2022

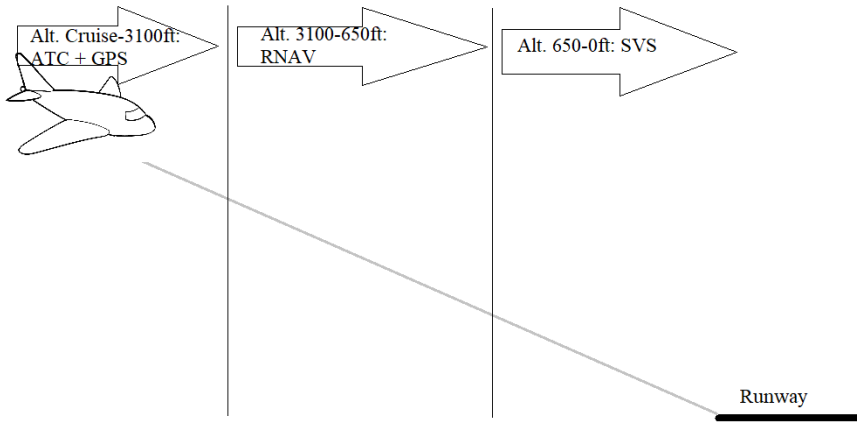


**Figure 5.2:** *Illustration of visual aid series during approach at Rothera.*

### 5.5.3. Amundsen-Scott Ground Aid

The ground aid system at Amundsen-Scott research station is similar to the one at Rothera, as Amundsen-Scott also contains an RNAV system [60]. This means that at Amundsen-Scott the same approach procedure can be adopted as at Rothera. The RNAV system at Amundsen-Scott initiates at an altitude of 10500 ft above sea-level[55]. As Amundsen-Scott is located at an elevation of 9300 ft, this means that the RNAV initiates at an altitude of 1200 ft above the runway. The runway approach procedure for Amundsen-Scott is illustrated in Figure 5.3.

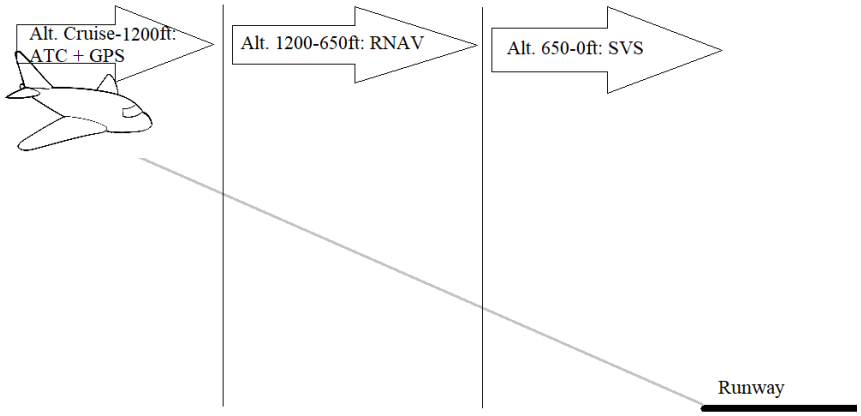


**Figure 5.3:** *Illustration of visual aid series during approach at Amundsen-Scott.*

To comply with constraints from the market analysis, it was assumed that not every remote community has an RNAV system for approach. Even though it is expected that remote communities provide a better visual of the runway, due to the absence of whiteouts, proper vision can still be lacking due to e.g. mist. In such cases, one can make use of non-directional-beacons (NDB). An NDB system consists of a radio beacon, which sends omni-directional signals to the aircraft, which are translated via an automatic direction finder (ADF) to determine the bearing and position of the aircraft[56]. This means that the NDB system can accurately pinpoint the location and bearing of the aircraft. Therefore, to decouple the GPS locations of the RNAV, it was decided to make use of the NDB system during approach at remote communities to pinpoint the location and heading of the aircraft.

[55] Approach information Jack Paulus Skiway, https://www.southpolestation.com/trivia/history/paulus.html, date accessed = 25-05-2022

[56] Article about an NDB system, https://www.systemsinterface.com/products/navaids/ndb/, date accessed = 25-05-2022

## 5.6. Software-Hardware Overview

To get an overview of the interactions between software and hardware of the aircraft, a hardware-software diagram was constructed. This diagram is shown in Figure 5.4. It shows the path of interactions in the system of both the aircraft internal systems, as well as the medical system. For example, navigation data is received, which is then interpreted by the data handling system, after which it is displayed on the navigation display. The autopilot and/or pilot then acts upon this by changing the control inputs, which the flight control system will pass on to the flight control actuators.

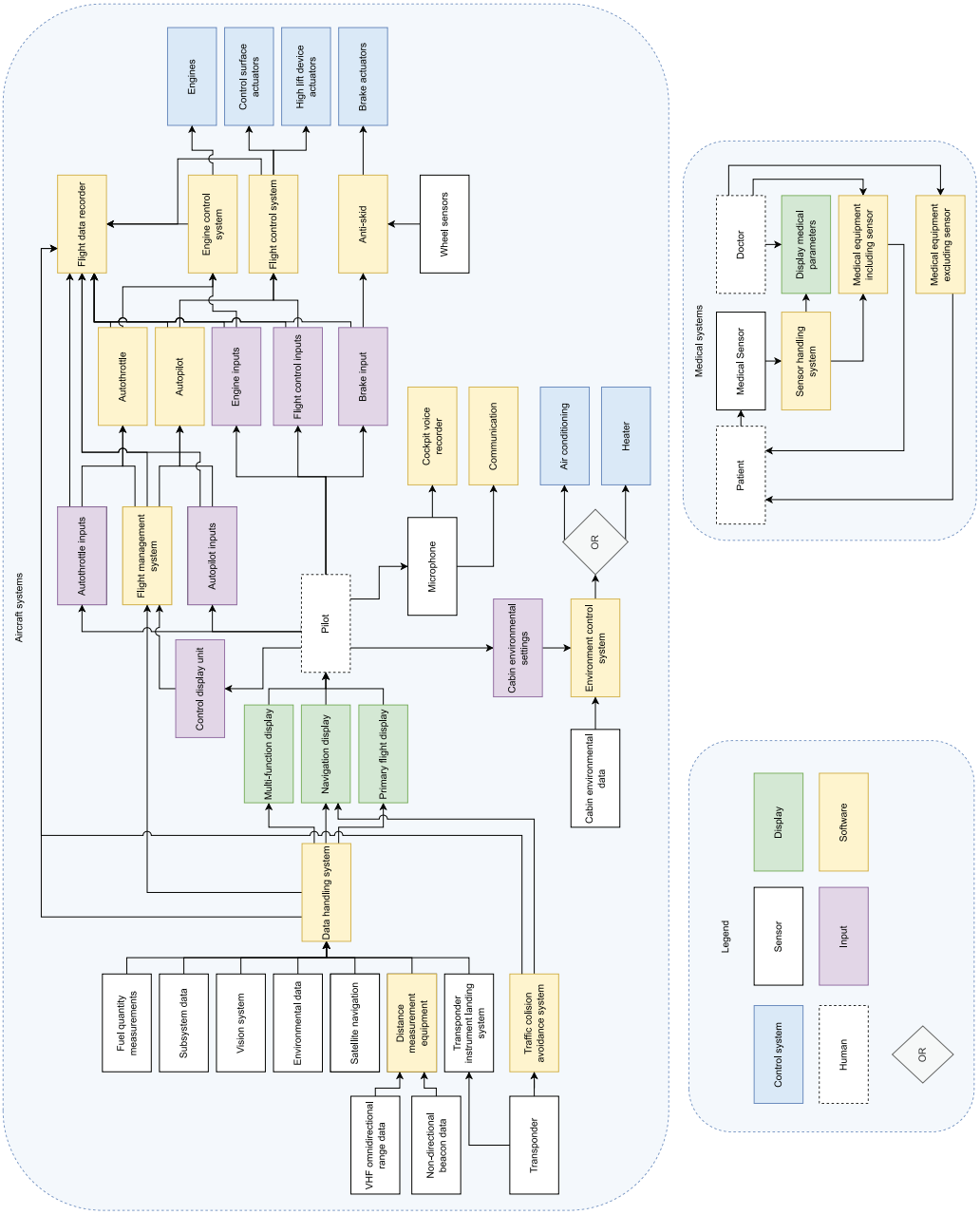


**Figure 5.4:** *The aircraft and medical systems hardware-software interaction diagram.*

# 6 Aircraft Performance

After sizing the JAPA-12, the performance of the aircraft was analysed. This allowed the team to come to conclusions about the safety and market opportunities of the aircraft as well as to verify the compliance with established requirements. The performance of the aircraft is covered in this chapter. The performance analysis begins with an aerodynamics analysis, determining the aerodynamic properties of the aircraft, which is covered in Section 6.1. This is followed by a stability & control analysis to determine whether the aircraft is stable and controllable in-flight, presented in Section 6.2. The payload-range limits are covered in Section 6.3. Finally, a flight envelope of the aircraft is shown in Section 6.4, where the extreme load factors during operation are found.

## 6.1. Aerodynamic Analysis

The aircraft aerodynamic analysis was performed as part of the iterative process to obtain a more detailed understanding of the aircraft lift, drag and moment coefficients. The parameters were acquired through methods from Roskam [61], and used to review the correctness of assumptions made when designing for range and STOL.

### 6.1.1. Aircraft Lift

The main goal of the aircraft aerodynamic lift analysis was to construct $C_L - \alpha$ curves, which show all combinations of lift coefficient values with respect to angle-of-attack in cruise and take-off/landing configurations. The curves provided the team with relevant information to assess the correctness of previously estimated values of lift-coefficient required for the stated flight configurations.

First, the $C_L - \alpha$ curves were constructed for the airfoils selected in Subsection 4.2.2 for the main wing and in Subsection 4.5.1 for the horizontal tail surface. The airfoil data used to construct the curves, and to perform the moment analysis, is shown in Table 6.1 below.

**Table 6.1:** *Airfoil data for main wing and horizontal tail [61].*

| Airfoil | $\alpha_{0_l}$ [°] | $c_{m_0}$ | $c_{l_\alpha}$ [1/°] | a.c. [tenths c] | $\alpha_{c_{l_{MAX}}}$ [°] | $c_{l_{MAX}}$ | $\alpha^*$ [°] |
|---|---|---|---|---|---|---|---|
| NACA23015 | -1.0 | -0.007 | 0.107 | 0.243 | 18.0 | 1.72 | 10.0 |
| NACA0012 | 0.0 | 0.0 | 0.110 | 0.25 | 15.5 | 1.39 | 12.0 |

The curve constructed with the values from the aforementioned table is shown in Figure 6.1, where the dotted lines indicate the non-linear part of the curve. These non-linear parts had to be guesstimated, however as only the maximum lift coefficient was of interest it was determined not to construct the non-linear part. Furthermore, the graph contains information regarding the shifting of data points as a result of selecting a Fowler flap for the flaps down configuration. It was found that a higher maximum lift coefficient was required for take-off and landing configurations, which is achieved by deploying the Fowler flaps.

Accordingly, the curves were altered based on the sizing of the wing and the entire aircraft. The wing $C_L - \alpha$ curve was constructed by first determining the point where the aircraft does not create lift by multiplying this point for the airfoil with a Mach correction factor based on the cruise conditions and airfoil thickness. As the aircraft operates at a Mach number of about 0.37, this correction factor was calculated to equal 1 and therefore the wing will produce lift at $\alpha = -1°$. The wing lift slope was determined from Equation 6.1, where AR is the wing aspect ratio, $\beta = (1-M_{cr}^2)^{0.5}$ where $M_{cr}$ is cruise Mach number, $\Lambda_{c/2}$ is half chord sweep and $k = \frac{C_{l_\alpha @ M_{cr}}}{2\pi\beta}$. All these parameters take into account the wing dimensions and cruise conditions.

$$C_{L_{\alpha_w}} = \frac{2\pi AR}{(2 + ((\frac{AR^2\beta^2}{k^2})(1 + \frac{\tan^2 \Lambda_{c/2}}{\beta^2}) + 4))^{0.5}} \tag{6.1}$$

The final step was to determine the maximum wing lift coefficient and the associated stall angle of attack. For higher accuracy, this could have been done by simulating the spanwise lift distribution over the wing by means of a computer model. However, as the design was subject to change and time was limited it was decided to follow the DATCOM method to determine $C_{L_{MAX_W}}$ and $\alpha_{stall_W}$ within a 2-4% error margin [62]. This was deemed sufficiently accurate for this stage of the design. $C_{L_{MAX}}$ was calculated by taking the ratio of $\frac{C_{L_{MAX}}}{C_{l_{MAX}}}$, based on airfoil thickness and wing leading edge sweep, multiplying this by the airfoil maximum lift coefficient and adding a delta term based on cruise conditions and

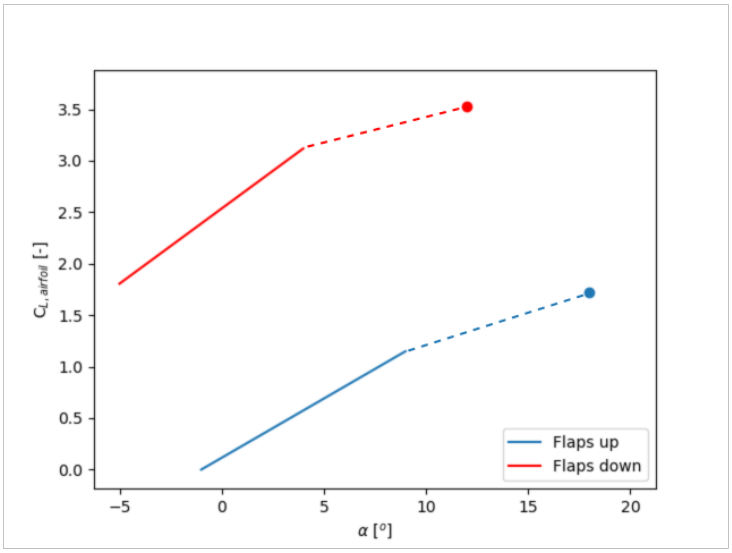


**Figure 6.1:** *$C_l - \alpha$ curve for NACA 23015.*

leading edge sweep. The wing $C_{L_{MAX}}$ was found to be 1.25. When comparing this to the airfoil, a major reduction can be seen as a result of considering the finite wing. The wing stall angle was determined in a similar way to equal 12.11°.

The influence of high lift devices on the wing in the form of Fowler flaps was also determined by first calculating the increase in lift coefficient and later the new maximum lift coefficient as well as the lift curve slope which is shown in Figure 6.2a. Similar steps were taken for the final stage of the aerodynamic analysis, where contributions of the horizontal tail, as well as wing fuselage interactions are added. The aircraft $C_{L_{MAX}}$ was computed using Equation 6.2, where $C_{L_{\alpha_h}}$ was computed by substituting relevant parameters in Equation 6.1, $S_h$ is the horizontal tail surface area, $\alpha_{CL_{MAX}}$ is the aircraft stall angle, downwash gradient $\frac{d\epsilon}{d\alpha}$ was computed using Equation 6.3 and downwash angle $\epsilon_{o_h}$ and horizontal tail incidence angle $i_h$ were set to zero as it was determined that the horizontal tail does not produce lift at $\alpha = 0$.

$$C_{L_{MAX}} = C_{L_{MAX_W}} + C_{L_{\alpha_h}} \left(\frac{S_h}{S}\right) (\alpha_{CL_{MAX}} \left(1 - \frac{d\epsilon}{d\alpha}\right) - \epsilon_{o_h} + i_h) \tag{6.2}$$

$$\frac{d\epsilon}{d\alpha} = 4.44 \left(\frac{1}{A} - \frac{1}{1 + A^{1.7}}\right) \left(\frac{10 - 3\lambda}{7}\right) \left(\frac{1 - \frac{h_h}{b}}{\frac{2l_h}{b}}\right)^{\frac{1}{3}} \tag{6.3}$$

The contributions of the high lift devices with respect to the aircraft lift were computed as well in a similar manner. The final aircraft $C_L - \alpha$ curves are displayed in Figure 6.2b for the flaps up and flaps down configurations. These curves were then used to compute delta terms as a result of the distributed propulsion configuration, which is further explained in Subsection 6.1.4.

### 6.1.2. Aircraft Drag

The aircraft drag was analysed in order to acquire information regarding aerodynamic efficiency. This was of special interest with respect to the cruise phase, where low drag is crucial for achieving maximum range, and landing where high drag is required to limit the landing distance. Analysis was based on both zero-lift drag and drag due to lift, where zero-lift drag is the result of both skin friction and pressure drag. This was predicted for each subsystem by relating the subsystem wetted area to the wing area, in combination with correction factors for different types of subsystem interactions based on detailed statistical data. Skin friction drag originates from the shear forces within the boundary layer due to the viscous properties of air. Pressure drag depends on the ability of the boundary layer to remain attached to the aircraft surface. In case the flow separates and becomes turbulent, a significant increase in drag occurs. Drag due to lift comes in the form of induced and viscous drag. This was for most components predicted with the help of the $C_L - \alpha$ curves which were constructed in Subsection 6.1.1. Induced drag is the result of vortices at the trailing edge and the viscous drag occurs due to influence of lift on the boundary layer.

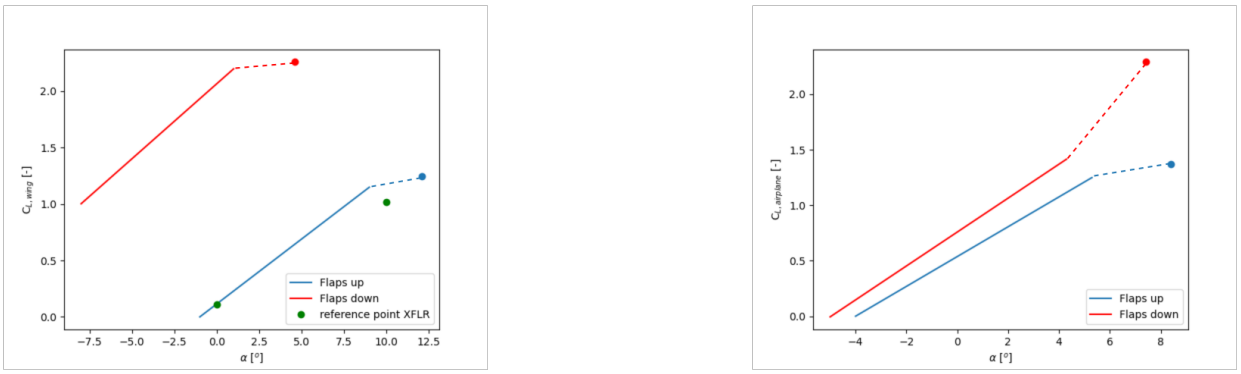


**(a)** *Wing $C_L$-$\alpha$ curve.*

**(b)** *Aircraft $C_L$-$\alpha$ curve.*

**Figure 6.2:** *Lift curves of the wing and aircraft.*

**Wing**
Since the aircraft operates in the subsonic range, defined as $M_{cruise} < 0.6$, the main contribution to wing drag is zero-lift drag. This comes from skin friction as the selected airfoil only contains gradual thickness changes and a smooth leading edge, therefore the vortices at the trailing edge are limited compared to transsonic operative conditions. Also, the drag properties of the wing were largely determined when the airfoil was selected. Therefore, the share of drag due to lift was already expected to be smaller.

**Fuselage**
The fuselage is a subsystem which was designed for low drag due to lift. This can be seen from the smooth transitions at the nose and tail, as non-gradual changes in circular diameter result in significant vortices. The large frontal and wetted areas result in a large skin friction drag.

**Empennage**
The empennage consists of the horizontal and vertical tail surfaces. As these systems are required to provide stability to the aircraft the main contributor to drag is skin friction. Both surfaces have been designed to have a smooth leading and trailing edge, such that the drag contribution due to vortices is greatly reduced. Also, these systems do not produce lift in straight, horizontal flight.

**Propulsion System**
The propellers are located on the leading edge of the main wing. Because of this design choice, no additional drag due to pylons was introduced. Overall, the downside of distributed propulsion is the additional drag of the propulsors. Each propulsor affects the laminar flow of air over the wing and creates vortices in its wake, thereby increasing drag in addition to the drag due to the large wetted area of all propeller/engine combinations. As a result, the propulsion system is the largest contributor of drag in cruise conditions.

For the propulsion system, one engine inoperative and windmilling conditions were also considered as the increased drag influences the maximum range of the aircraft. These were however not included in general cruise analysis, as they were considered to only occur very rarely. Both conditions result in increased pressure drag, as the flow is not energised by the propeller wake.

**Landing Gear**
The landing gear is only deployed for a short amount of time to limit its drag contribution, especially at high cruise speeds. The main contributor to drag was found to be pressure drag at zero-lift conditions, which is influenced by the aircraft speed. As the speed in cruise is much higher than in take-off or landing conditions, the team deemed it necessary to design a fairing for gear storage to have less drag impact in cruise.

**Flaps**
Flaps were seen as the main contributor to drag in both landing and take-off configurations. The selected Fowler flaps both increase the effective chord and are deflected which results in significant vortices introduced at the trailing edge. It was however determined that redesign of the flaps was not required, as the high drag is only experienced for a short amount of time in the mission. Flaps are essential for take-off and landing so the drag penalty was accepted.

**Trim**
Trimming the aircraft is done by tabs located on the horizontal tail. As the horizontal tail was designed to not generate lift in straight horizontal flight, deflection of flaps increases the pressure drag significantly. Trimming the aircraft is a frequently occurring process in cruise, therefore the drag was considered to occur constantly.

**Windshield**
The windshield is essential for visual inspection of the surroundings by the pilot. However, windshields increase drag as they are usually not fully streamlined with the fuselage. In order to limit complexity of design, and thereby limit costs, it was decided to use flat windows that are flush with the surface. This mainly increased the skin friction, but the increase was low enough to be acceptable.

**External Storage**
The final drag contribution on the list originates from external storage. As the landing gear was designed to be retractable, but there was not sufficient space in the fuselage to fully do so, fairings were designed. These were approached as small fuselages underneath the actual fuselage. Therefore the drag contribution is similar but with much smaller contributions to total aircraft diameter, such that drag is mostly caused by skin friction.

The final results of the drag analysis are displayed in Figure 6.3a for cruise conditions where $C_D = 0.0384$ equal to 4900 N of drag and in Figure 6.3b for take-off/landing conditions where $C_D = 0.0965$ equal to 4200 N of drag. The drag increments due to one engine inoperative and windmilling conditions are $C_D = 0.0156$ and $C_D = 0.0160$ respectively, which both resulted in about 6900 N of total drag force in cruise.

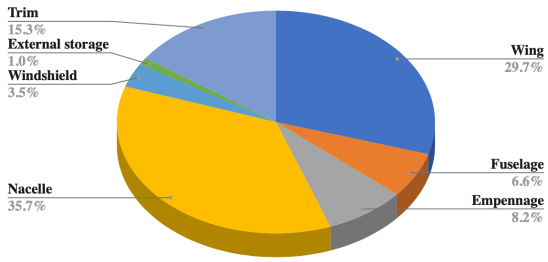


**(a)** *Drag contribution per subsystem in cruise configuration.*

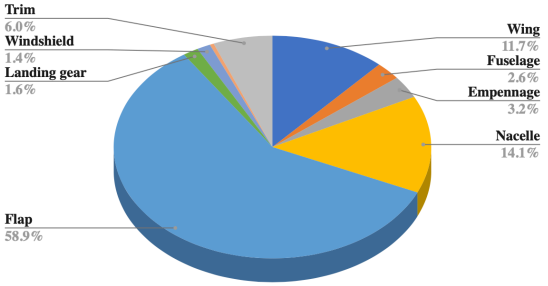


**(b)** *Drag contribution per subsystem in take-off/landing configuration.*

### 6.1.3. Aircraft Pitching Moments
The aircraft pitching moment coefficients were computed using Roskam [61]. First, the $(C_L, C_m)$-curves for the airfoil were set up, then for the wing and lastly for the whole aircraft. The approach for creating each graph was the same and is explained below. The only difference is that for the airfoil $(C_l, C_m)$-curve, the lift coefficient has a lower case l instead of an upper case L.

For the airfoil, wing and aircraft, the flaps up and flaps down configuration was considered. For the flaps up configuration, the $C_{m_0}$, the slope of the straight part of the graph, $\frac{dC_m}{dC_L}$, the $C_L$ at which the straight part ends, $C_L*$ and the maximum lift coefficient, $C_{L_{max}}$, were determined or calculated. Then the graph was converted to the flaps down configuration by calculating the effect of the flaps to the moment and lift coefficient. The $\Delta C_m$ and $\Delta C_{L_{max}}$ were added to the points of the flaps up curve. It was assumed that the slope of the straight part of the flaps down curve is the same as for the flaps up configuration. This results in the graphs shown in Figure 6.4.

### 6.1.4. Influence of Distributed Propulsion
The effects of the distributed propulsion were not taken into account in the analysis performed above. This was due to the fact that this analysis was required to construct the delta terms associated with leading edge distributed propulsion. The implications of the distributed propulsion configuration are covered in Section 3.4. The analysis of the delta terms showed an achievable $C_{L_{max}}$ in flaps up configuration of 1.382 and in flaps down configuration of 2.74.

### 6.1.5. Verification
The analysis of lift and drag was performed by using methods included in Roskam. The constructed $C_L - \alpha$ looked different than expected for the aircraft, the main reason being that the method applied correction factors for canard

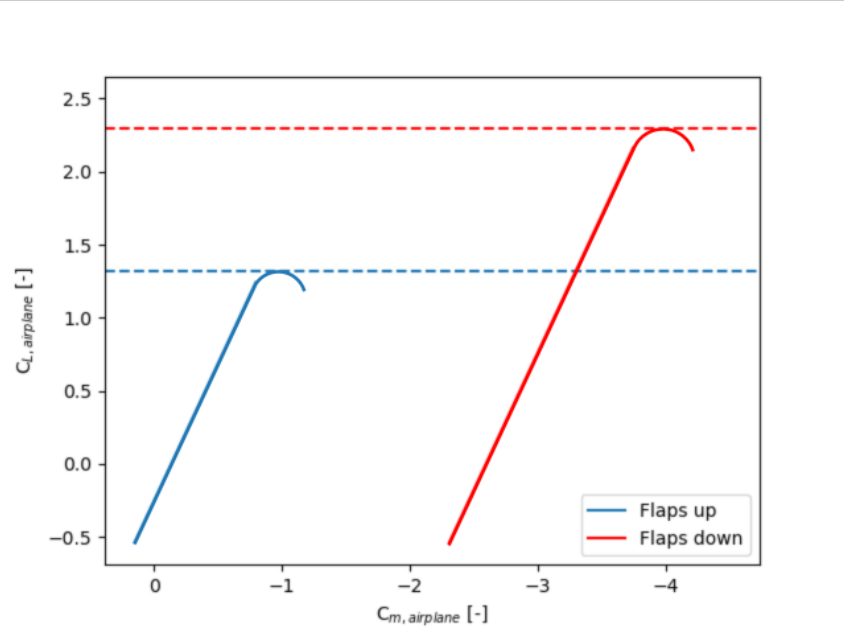


**Figure 6.4:** $(C_L, C_m)$*-curve for the whole airplane.*

aircraft. As the JAPA-12 does not feature a canard configuration these correction terms were left out. Also, as the method included parameters that had to either be ”guesstimated” or read from graphs, it was determined that the error was a combination of all aforementioned items. Due to time constraints, the team was not able to correct the curve for the aircraft. These curve corrections should be re-evaluated in future design phases. The wing curve was evaluated by comparing the graph to points extracted from XFLR, for which a curve with a slope 21% lower was found compared to Roskam's method. This deviation was found to be the result of reading off graphs and assumptions made by XFLR. The only way to verify the results of XFLR is to construct a detailed model for wind-tunnel testing which is outside the scope of the DSE. The critical flight phase with respect to the required $C_L$ was found to be for landing. As $C_{L_{max}}$ was determined by DATCOM with an error margin up to 4%, the accuracy was deemed sufficient to be used in this stage of design. In addition, a standard NACA airfoil was selected such that the accuracy from DATCOM was leading. The implications of the error in the slope were that the aircraft would have to fly at a slightly higher angle of attack to achieve $C_L$ required for cruise to achieve the same lift to drag ratio required for the mission range.

For the analysis of pitching moments it was assumed the method of estimating the moment coefficients by Roskam is valid. The correct implementation of Roskam in the code to create the graphs was verified by comparing the graphs for the airfoil and wing with some points on the $(C_L, C_m)$-curve extracted from the analysis of the wing in XFLR. These results can be seen in Figure 6.5. The calculated $\frac{dC_m}{dC_L}$ was found to be -0.25, but when drawing a straight line through the reference points, the slope is -0.33. This is a difference of 32%. However, the points themselves are not far from the graph, the straight part is relatively short, with a $C_L$ range of 1.14, and the slope is small, so a small change results in a large percentage change. In conclusion, the result is considered valid, but it is necessary to calculate the coefficients in more detail at the next stage of the design.

## 6.2. Stability & Control

To determine the operational limits of the aircraft in flight, a stability & control analysis was performed. Via this analysis, the most extreme cg locations were found, to be able to notify the customer of its constraints and allow for safe operations. Additionally, the response of the system to disturbances was investigated to see how the aircraft responded. This stability analysis was performed in two categories. First, the neutral points of the aircraft were determined, of which the results are presented in Subsection 6.2.1. The S&C analysis was finalised with the dynamic stability analysis in Subsection 6.2.2, where the response of the aircraft to disturbances was covered, in both the longitudinal and lateral directions.

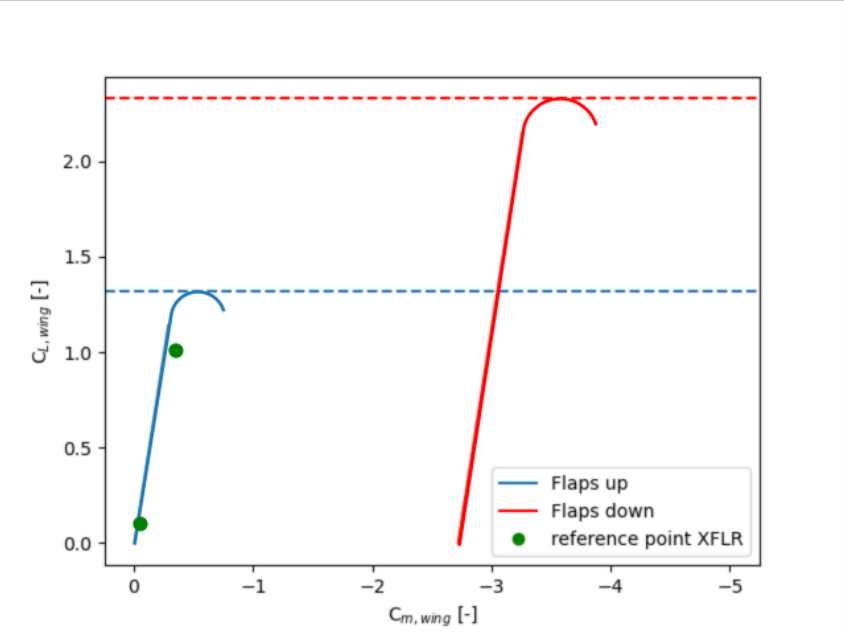


**Figure 6.5:** $(C_L, C_m)$*-curve for the wing, with reference points from XFLR.*

### 6.2.1. Neutral Points

The neutral points of an aircraft are vital for aircraft operations, as they indicate the most aft cg location allowable of the aircraft. There are two neutral points: a stick free neutral point, allowing for free elevator movement, and a stick fixed neutral point, setting the cg limit at a certain elevator angle. Once the cg of the aircraft moves behind either the stick free or stick fixed neutral point, it becomes statically longitudinally unstable and very unpleasant to fly. In general, when the cg of the aircraft is in front of both neutral points, it is statically longitudinally stable. Therefore, it was vital to determine the two neutral points.

#### Stick Fixed Neutral Point

The stick fixed neutral point was established via the free body diagram presented in Figure 4.12. The neutral point indicates the cg location at which $C_{m_\alpha} = 0$. This means that for a cg at the neutral point, there is neutral response to a disturbance, and for a cg behind the neutral point $C_{m_\alpha} > 0$ and thereby the aircraft is unstable. The 'fixed' term corresponds to a set elevator angle, meaning that the elevator is constrained from movement when a disturbance is encountered. This resulted in $\delta_e$ =constant, where $\delta_e$ was the elevator deflection angle.

Rewriting the moment coefficient equation from Figure 4.12, and re-expressing it in terms of angle of attack, an expression for the stick fixed neutral point was found by setting $C_{m_\alpha} = 0$. This expression is given in Equation 6.4.

$$\frac{x_{n_{fix}} - x_w}{\overline{c}} = \frac{C_{N_{h_\alpha}}}{C_{N_\alpha}}\left(1 - \frac{d\epsilon}{d\alpha}\right)\left(\frac{V_h}{V}\right)^2 \frac{S_h l_h}{S\overline{c}} \tag{6.4}$$

The coefficients with subscript N were expressed in the body-frame of the aircraft. As the general lift coefficients were expressed in L, which were in the aerodynamic frame, the coefficients had to be rewritten. However, in accordance to **ASMP-2** in Subsection 4.5.3, a small angle of attack could be assumed during flight. This meant that the aerodynamic frame was considered to coincide with the body frame. Therefore, the lift coefficients in Equation 6.4, $C_{N_\alpha}$ and $C_{N_{h_\alpha}}$, were expressed in the aerodynamic frame as $C_{L_\alpha}$ and $C_{L_{h_\alpha}}$ respectively. And thereby the aerodynamic coefficients from Subsection 6.1.1 could be used for neutral point analysis.

Filling in all the coefficients in Equation 6.4, a neutral point location of 0.454 x/c was found. As the most aft cg location computed in Subsection 4.5.2 was found to be 0.411 x/c, the aircraft was stable for stick fixed conditions.

#### Stick Free Neutral Point

The stick free neutral point was determined in a slightly different way than the stick fixed neutral point. Where the stick fixed neutral point was constrained to a fixed elevator deflection, the elevator deflection was dropped out of the stability analysis as it was independent of angle of attack. However, by allowing movement of the elevator, the elevator

deflection could no longer be treated as a constant. Hence, for the stick free stability analysis, the elevator deflection was not constrained, nor did $\delta_e$ remain constant.

Now, as the elevator deflection was no longer constrained, the hinge, which is the structural part keeping the elevator at its deflection, no longer experienced a moment as it was free to rotate. This resulted in a hinge moment coefficient of 0. Working out the equilibrium state of the horizontal elevator, Equation 6.5 was found to express the elevator deflection in horizontal tail angle of attack $\alpha_h$.

$$\delta_{e_{free}} = -\frac{C_{h_\alpha}}{C_{h_\delta}}\alpha_h \tag{6.5}$$

As the horizontal tail angle of attack was dependent on the main angle of attack of the aircraft, the elevator deflection was returning in the neutral point expression. This resulted in the stick free neutral point expression, which is presented in Equation 6.6.

$$\frac{x_{n_{free}} - x_w}{\overline{c}} = \frac{(C_{N_{h_\alpha}} - C_{N_{h_\delta}}\frac{C_{h_\alpha}}{C_{h_\delta}})}{C_{N_\alpha}}(1 - \frac{d\epsilon}{d\alpha})(\frac{V_h}{V})^2\frac{S_h l_h}{S\overline{c}} \tag{6.6}$$

To find the stick free neutral point, the hinge moment coefficients $C_{h_\alpha}$ and $C_{h_\delta}$, and the additional lift generated by the elevator $C_{N_{h_\delta}}$ were to be found. To find these, the horizontal tail was reconstructed in XFOIL[57]. For this, the chosen NACA 0012 airfoil was used, with a constructed flap at $0.8x/\overline{c}$. The flap was added to represent the elevator of the horizontal stabilizer. To find the elevator deflection dependent hinge moment coefficient, $C_{h_\delta}$, the cruise angle of attack was used, after which the flap deflection was adjusted between $-5°$ and $5°$, to allow for accurate simulation measurements. The measurements were plotted, after which a regression line was drawn. This regression line, with an $R^2$ value of 0.98, resulted in $C_{h_\delta} = -0.464$ rad$^{-1}$.

Additionally, the angle of attack dependent hinge moment coefficient, $C_{h_\alpha}$, was found by setting a fixed elevator deflection as $\delta_e = 5°$, and plotting the hinge moments versus the angles of attack. The elevator deflection $\delta_e$ was set as $5°$ as simulation data loses accuracy when larger angles of attack are used. The angle of attack range used was between $-10°$ and $10°$. Again, the measurements were plotted in a regression line. This regression line, with an $R^2$ value of 0.684, resulted in $C_{h_\alpha} = 5.37 \cdot 10^{-5}$ rad$^{-1}$. Note that the $R^2$ value is not particularly convincing. However, XFOIL struggled to compute accurate data at the boundaries of the $\alpha$ range, and due to a fixed elevator deflection, the data around $\alpha = 0°$ was mirrored. Therefore, the $R^2$ value was still accepted as there was a clear pattern at smaller values of angle of attack.

Finally, the additional lift generated by the elevator, $C_{N_{h_\delta}}$, was found in a similar manner as $C_{h_\delta}$ regarding the simulation. However, in this case, the regression line was set up for the lift coefficient versus the elevator deflection, at a constant angle of attack of $\alpha_{cruise}$. This regression line, with an $R^2$ value of 0.98, resulted in $C_{N_{h_\delta}} = 3.37$ rad$^{-1}$.

Then, by filling in Equation 6.6, the stick free neutral point was found as 0.4543 x/c. Comparing this to the stick fixed neutral point, which was located at 0.454 x/c, it was concluded that the stick fixed neutral point was most constraining, as this was the most forward neutral point, even though the difference was small. Comparing this to the most aft cg location computed in Subsection 4.5.2, where a most aft location of 0.411 x/c was computed, it was concluded that the aircraft would be statically longitudinally stable as all possible cg positions were in front of the constraining neutral point.

Comparing the constraining neutral point with the most aft cg location, a difference of 9.47% over the mean aerodynamic chord was found. However, the sizing procedure should have lead to both points in close proximity of one another. This difference is mainly explained by the safety margins that were used during the loading diagram and scissor plot. For the loading diagram, a 2% margin was taken due to fuel uncertainties. Additionally, in the scissor plot, a 5% safety margin was established to ensure safe flight. Combining these 2 margins, a 7% safety margin was found. The team suspects the final 2.47% difference is due to errors in determination of statistical data used, and rounding errors. This justified the relatively large margin between the most aft cg and the constraining neutral point.

### 6.2.2. Dynamic Stability

Apart from static stability, it is generally desired to have an aircraft that is dynamically stable as well. Therefore, a dynamic stability analysis was conducted. The dynamic stability of an aircraft is generally characterized via five eigenmotions. The first two in the longitudinal direction, i.e. short period and phugoid motion. And the final three, i.e. aperiodic roll, dutch roll and spiral motion in the lateral direction. To determine the dynamic stability of the aircraft, the behaviour of the eigenmotions was included. The general approach as taught by the TU Delft course Aerospace Flight Dynamics &

[57] XFOIL 6.99 download, https://www.softpedia.com/get/Science-CAD/XFOIL.shtml, date accessed = 07-06-2022

Simulation [63] was followed to determine the simplified aircraft response to disturbances. Note that the analysis was simplified, mainly due to the limited time available.

To perform the dynamic stability analysis, the stability derivatives of the aircraft were to be found. As the aircraft was still being designed, the stability derivatives were estimated via various methods. For this, a combination of the TU Delft course Aerospace Flight Dynamics & Simulation [64], Roskam [61] and the Cornell University masters course Introduction to Aircraft Stability and Control [65] was used. This resulted in the coefficients required for analysis in Table 6.2. Additionally, the effectiveness of the aileron and the rudder were estimated via Roskam [61], and are presented in Table 6.3.

**Table 6.2:** *Stability derivatives & inertial coefficients estimations used for dynamic stability analysis.*

| Parameter | Value | Parameter | Value | Parameter | Value |
|---|---|---|---|---|---|
| $C_{Z_\alpha}$ | -0.29 | $C_{m_\alpha}$ | -1.14 | $K_X^2$ | 0.005 |
| $C_{Z_{\dot{\alpha}}}$ | -0.08 | $C_{m_{\dot{\alpha}}}$ | -2.93 | $K_Y^2$ | 0.372 |
| $C_{Z_q}$ | -0.19 | $C_{m_q}$ | -0.59 | $K_Z^2$ | 0.006 |
| $C_{Z_0}$ | -0.39 | $C_{X_u}$ | -0.052 | $\mu_b$ | 12.25 |
| $C_{Z_u}$ | -0.21 | $C_{Y_\beta}$ | -1.8 | $\mu_c$ | 141 |
| $C_{l_\beta}$ | -0.15 | $C_{n_\beta}$ | 0.104 | | |
| $C_{l_p}$ | -0.61 | $C_{n_p}$ | -0.1 | | |
| $C_{l_r}$ | -0.23 | $C_{n_r}$ | -0.09 | | |

**Table 6.3:** *Control surface effectivenesses used for dynamic stability analysis.*

| Parameter | Value | Parameter | Value |
|---|---|---|---|
| $C_{Y_{\delta_a}}$ | 0 | $C_{X_{\delta_e}}$ | -0.0373 |
| $C_{l_{\delta_a}}$ | -0.22 | $C_{Z_{\delta_e}}$ | -0.69612 |
| $C_{n_{\delta_a}}$ | -0.014 | $C_{m_{\delta_e}}$ | -0.5443 |
| $C_{Y_{\delta_r}}$ | 0.11 | | |
| $C_{l_{\delta_r}}$ | 0.008 | | |
| $C_{n_{\delta_r}}$ | -0.031 | | |

With all the stability derivatives, intertial coefficients and control surface effectivenesses, the aircraft response to a disturbance could be plotted. The longitudinal response to a simulated gust (or a sudden pitching motion) is illustrated in Figure 6.6.

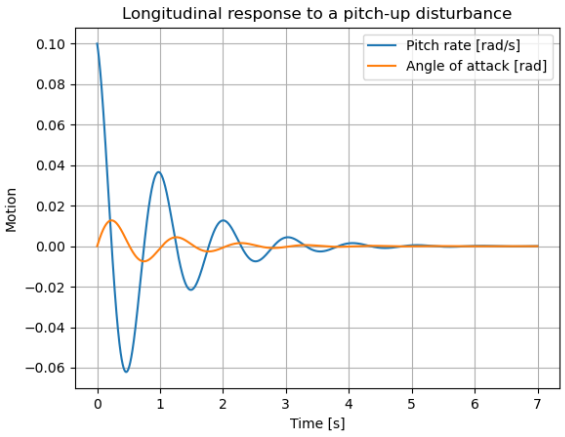


**Figure 6.6:** *Aircraft longitudinal response to a pitch-up disturbance.*

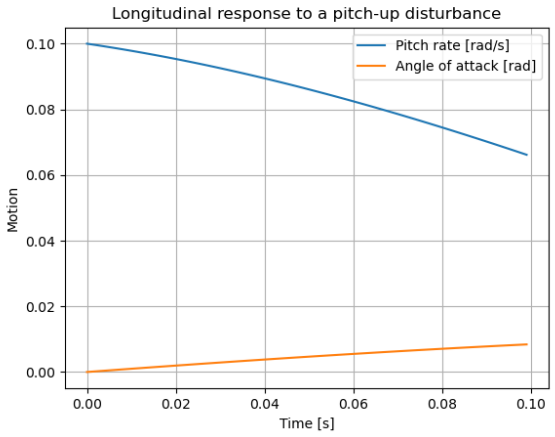


**Figure 6.7:** *Zoomed in longitudinal response to a pitch-up disturbance.*

Looking at Figure 6.6, one can note that when a disturbance is implemented, the aircraft returns to its equilibrium state. This was as expected, as the most aft cg location computed in Subsection 4.5.2 was in front of the neutral points computed in Subsection 6.2.1. Therefore, by definition, the response was expected to be stable. Additionally, an oscillation was seen. This oscillation was due to the phugoid eigenmotion of the aircraft, which slowly damped out. Finally, the short period motion was somewhat returning in the response. When looking at Figure 6.7, little initial response was seen, which indicated the lack of the short period eigenmotion. The team suspected the relative small value of $C_{z_\alpha}$ to be the cause of this behaviour, as now the vertical motion of the aircraft was little damped for a change in angle of attack. For example, for a shift in angle of attack, the vertical velocity of the aircraft changed very slowly.

Additionally, the lateral response of the aircraft was generated. This was done for steady, no pilot input flight, for sideslipping flight and banking flight. This is presented in Figure 6.8 and Figure 6.9 respectively.

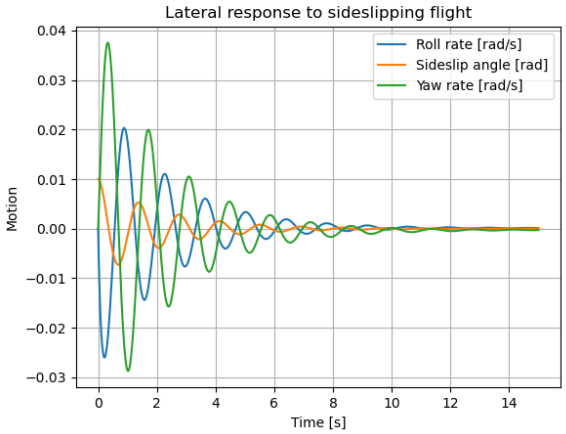


**Figure 6.8:** *Aircraft lateral response to a sideslip angle.*

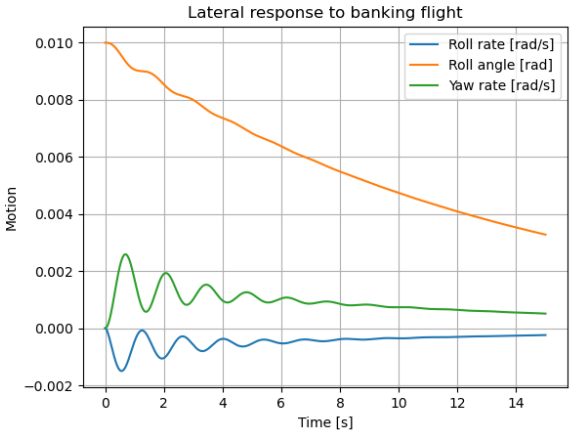


**Figure 6.9:** *Aircraft lateral response to banking flight.*

As the aircraft had to be able to land with sideslipping conditions it was desired to have a stable lateral response to sideslip. Looking at Figure 6.8, the sideslip angle returned to equilibrium state when a sideslip angle was introduced. Therefore, the aircraft was stable regarding sideslipping flight. Now, one can also note that the recovery of sideslip was a rather bumpy flight due to the oscillations. The oscillations are due to the roll and yaw rate interacting with one another, representing the dutch roll eigenmotion. As the oscillations also damp, the aircraft has a stable dutch roll eigenmotion.

Now, as sideslipping flight could impose a roll angle on the aircraft, it was desired to look into the aircraft response to a banking flight. Looking at Figure 6.9, one can see that, when a roll angle was introduced, the aircraft slowly recovers back to equilibrium state. Therefore, no spiral eigenmotion was developed when no pilot input was given. Hence, the spiral eigenmotion was concluded as stable. Again, the dutch roll eigenmotion was seen, as oscillations were experienced during recovery. Thus, the response of the aircraft to a roll angle was stable.

Note that the aircraft response to any disturbance was rather unpleasant due to the oscillations experienced. This was the case due the fact that during the simulation, no additional (auto)pilot inputs were implemented. Therefore, the simulations have shown that the aircraft has a stable response in case no (auto)pilot was present. And thereby, it was expected that when a (auto)pilot was present, the (auto)pilot could damp the oscillations by his or her expertise or programming; making the flight more pleasant. Unfortunately, due to time constraints, the required (auto)pilot inputs for pleasant flight were not determined.

To finalize the stability analysis, the team was interested in the aircraft response when ice developed on the wing, empennage, and control surfaces due to anti-icing failure. For this, the stability derivatives and the control surface effectivenesses were corrected via a correcting term established by research [66]. The correcting terms are summarized in Table 6.4. To simulate the icing conditions, the correcting term had to be added to the original coefficients presented in Table 6.2 and Table 6.3.

With the icing conditions, the aircraft response of the same pitch disturbance, sideslipping flight, and banking flight were simulated. The responses to these conditions are presented in Figure 6.10 for icing conditions.

**Table 6.4:** *Correctional terms for icing conditions of light airplanes [66].*

| Parameter | Correcting term | Parameter | Correcting term |
|---|---|---|---|
| $C_{m_\alpha}$ | -0.099 | $C_{l_p}$ | -0.1 |
| $C_{m_q}$ | -0.035 | $C_{l_{\delta_a}}$ | -0.1 |
| $C_{m_{\delta_e}}$ | -0.1 | $C_{l_{\delta_r}}$ | -0.08 |
| $C_{Y_\beta}$ | -0.2 | $C_{n_\beta}$ | -0.2 |
| $C_{Y_{\delta_r}}$ | -0.08 | $C_{n_r}$ | -0.061 |
| $C_{l_\beta}$ | -0.1 | $C_{n_{\delta_a}}$ | -0.083 |

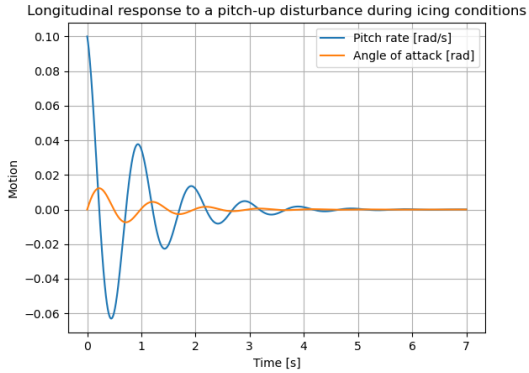


**(a)** *Aircraft longitudinal response to a pitch-up disturbance during icing conditions.*

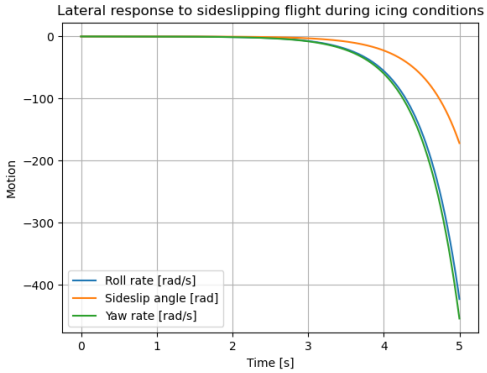


**(b)** *Aircraft lateral response to a sideslip angle during icing conditions.*

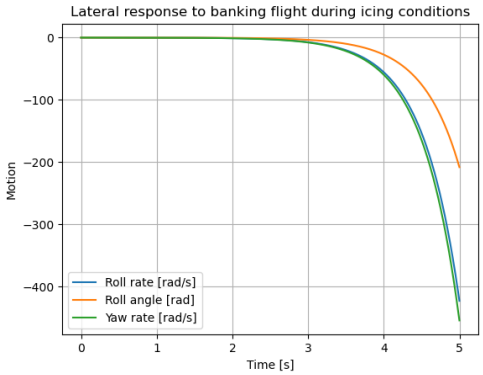


**(c)** *Aircraft lateral response to banking flight during icing conditions.*

**Figure 6.10:** *Aircraft dynamic stability revised for icing conditions.*

As expected, when icing occurs, the aircraft would have been unstable. Looking at Figure 6.10, the lateral components immediately diverged when a disturbance was present. Meaning that the aircraft would simply crash when the anti-icing system would fail. Apart from the lateral response, even though the magnitude of the longitudinal response increased and the phugoid eigenmotion was damped a little slower, the longitudinal response was still stable. The team suspects that this was due to the simplicity of the icing conditions applied. In practice, when ice develops on the wing and other lifting surfaces, the lift decreases approximately 30% and the drag doubles[58]. As these aerodynamic effects were not taken into account, the horizontal tail was still capable of producing enough lift to provide stability. Therefore, by simply decreasing the elevator effectiveness, the icing conditions of the aircraft were underestimated; making Figure 6.10a unreliable. However, the team investigated the stability to determine whether the aircraft was capable of flying during icing conditions, which was determined unfeasible due to the lateral instability. Concluding, the JAPA-12 aircraft will

[58]NASA in-flight icing aerodynamics training, https://aircrafticing.grc.nasa.gov/1_1_3_2.html, date accessed = 09-06-2022

crash if the anti-icing system fails while flying in icing conditions. This was the main reason for the high redundancy design of the anti-ice system in Section 5.2.

### 6.2.3. Model Verification

To check whether the results of the stability models were reliable, the model was verified. The verification process was done in a systematic manner. First, unit, subsystem, and system tests were performed. This was done by manually changing model inputs, and see whether the aircraft response made sense. An error was found regarding the horizontal tail volume due to a computational error, and an error was found in the contribution of the wing-fuselage combination due to unit inconsistencies.

To verify the short period behaviour of the aircraft, the phugoid motion was damped out for the initial response. This was done by diminishing the main contributor to the eigenvalue of the response matrix, by setting $\mu_c = 1$. This way, the phugoid motion was accelerated slowly, and thereby the initial seconds were solely manipulated via the short period. By cancelling out the initial phugoid contribution, the short period was clearly visible. When looking at Figure 6.11, the initially sharp but quickly damped response (which indicates the short period) can be seen at the red circle, as the oscillation is disturbed in a rapid manner. Therefore, it was concluded that the simplified model used was still appropriate to determine the short period response, and the phugoid motion was clearly dominating over the short period for this system.

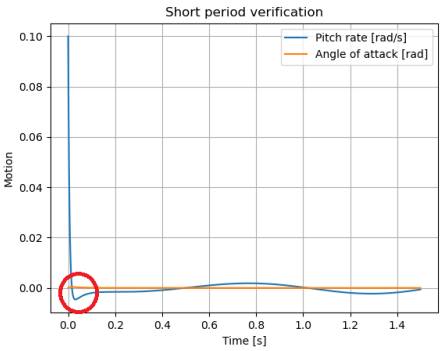


**Figure 6.11:** *System response used for short period verification with manually damped phugoid motion.*

## 6.3. Payload-Range

Based on the design point selected in Section 3.5, the maximum take-off weight was determined by calculating aircraft take-off weights for different missions. Aside from the Rothera - Amundsen-Scott mission the aircraft has to be able to perform 100 nm mission with 4000 lbs payload, 150 nm mission with 3200 lbs of payload and 400 nm mission with 3000 lbs. Calculated take-off masses for these missions are summarised in Table 6.5

**Table 6.5:** *Aircraft's take-off masses for different missions.*

| Mission Range | 100 nm | 150 nm, 19 passengers | 150 nm | 400 nm | 1350 nm |
|---|---|---|---|---|---|
| Payload [kg] | 1814.3 | 1995.8 | 1451.5 | 1361 | 459 |
| TOM [kg] | 6117.1 | 6848.0 | 5757.2 | 5940.5 | 5458.7 |

From Table 6.5 it could be seen that maximum take-off mass determined is 6848.0 kg, which corresponds to designs' MTOW of 67.2 kN.

To identify the possible range which can be flown in calm weather with a certain payload a payload-range diagram was constructed. This diagram is shown in Figure 6.12. As can be seen from this graph, the short-range with 19 passengers requirement (**[REQ-STA-MAR-02]**) was limiting. The other payload-range requirements are satisfied with the possibility to take more payload, for example, the medevac mission can be performed with approximately three times the payload weight. These payload-range requirements are indicated in the diagram as a point (the identifier is abbreviated as follows; **REQ-STA-MAR-02** becomes RSM-02). The graph also indicates that the design is over-designed for calm weather conditions because the critical payload-range requirement is not critical for the range on the graph. This is caused by the calculations for the fuel required as discussed in Section 3.6 take into account headwind, while the payload-range diagram was created for calm weather conditions where no wind is taken into account.

## 6.4. Flight Envelope

It is important that the engineers and pilots understand the structural limitations of the aircraft. The V-n diagram shows the limits of the aircraft in terms of airspeeds and load factors. The diagram was produced in accordance with the CS-23

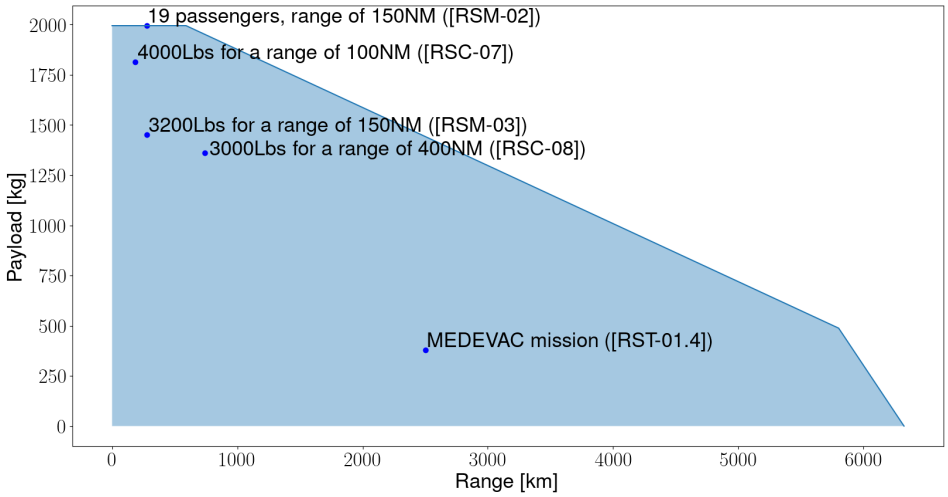


**Figure 6.12:** *Payload-Range diagram.*

requirements for commuter category aircraft. The configurations analysed are the clean aircraft at cruise altitude and high lift devices deployed aircraft at low altitudes. The requirements concerning Maneuvering loads are stated below.

**[.CON-1.32]** The positive limit manoeuvring load factor shall be 3.08 in clean configuration.
**[.CON-1.33]** The negative limit manoeuvring load factor shall be -1.23 in clean configuration.
**[.CON-1.34]** The positive limit manoeuvring load factor shall be 2 in flapped configuration.
**[.CON-1.35]** The negative limit manoeuvring load factor shall be 0 in flapped configuration.

In addition to that, the loads introduced by vertical gusts were analysed and integrated with the manoeuvring load diagram. The CS-23 regulations for the gust performance are summarised in the following requirements.

**[.CON-1.36]** Positive and negative gusts of 50 fps at $V_c$ shall be considered
**[.CON-1.37]** Positive and negative gusts of 25 fps at $V_D$ shall be considered
**[.CON-1.38]** Positive and negative rough air gusts of 66 fps at $V_B$ shall be considered

### 6.4.1. Design Speeds

The design speeds are also regulated by the CS-23 certification requirements. The following paragraphs analyse the limits and compatibility of speeds with respect to each other.

The minimum cruise speed $V_{c,min}$ is set by the regulation to be 113 m/s. The average cruise speed was calculated to be 115 m/s TAS using the minimum value calculated according to CS-23 requirements and the maximum speed determined in Subsection 3.4.5. Upon iterations these values slightly decreased as described in Section 11.2, however, the effect on the flight envelope was negligible. Next, the design dive speed was determined. The dive speed is important as it is the maximum airspeed that aircraft can resist. Furthermore, the dive speed is used as an indication for minimum flutter speed which shall not be less than $1.2V_D$. As per the CS-23 regulations the dive speed must satisfy $V_D > 1.4 \cdot V_{cr,min}$. Design manoeuvring speed $V_A$ is determined based on the following requirements. $V_A$ cannot be less than $Vs\sqrt{n_+}$ and need not be more than $V_c$. The negative manoeuvring speed $V_D$ lower limit was determined to be 50 EAS based on CS-23 requirements. Next, the design speed for maximum gust intensity $V_B$ is also limited by the regulations with the lower limit given by the speed at which the stall curve intersects the rough air gust velocity line. Furthermore, the $V_B$ need not be higher than $V_c$

### 6.4.2. V-n Diagrams

Consequently, the manoeuvring load diagrams are established using the aforementioned speeds, positive and negative stall limits and lift coefficients. The manoeuvring loads were evaluated at sea level as it presents the most critical conditions with the highest load factors. A differentiation is made between flapped and clean configurations with the flapped condition having different regulation limits, stall speeds and maximum speed $V_F$. The difference between configurations can be seen on Figure 6.13 where the flapped condition poses much lower load factors than the clean configuration. Further analysis was then conducted to evaluate specifically the limits of the clean aircraft under different conditions.

Gust loads were also evaluated per instructions of the CS-23 regulations. Due to the fact that gust loads vary with air density and aircraft weight, the gust envelope was constructed for 6 different cases. By varying altitude from mean sea level (MSL) to the average cruise altitude FL100 and aircraft weight from minimum to average to maximum, it was possible to identify the most critical condition which turned out to be clean configuration, FL100 at minimum aircraft weight. The diagrams produced during this process are shown on Figure 6.14, where all speeds are in m/s. General patterns show that load factors decrease with an increase in weight and increase with altitude due to the fact that the gust alleviation factor also increases with altitude. Furthermore, it can be seen that the limiting requirement in terms of load by a margin is the gust speed. The maximum vertical gust speed which should be sustained is 20 m/s. Although no exact information could be found on vertical gust intensity in Antarctica JAPA-12 will most likely be within the limits due to the fact that vertical winds are small compared to the horizontal ones the maximum sustainable gust speed of which is around 26 m/s. The final maximum design load factors were determined to be $n_+$ = 6.3 and $n_-$ = -4.4.

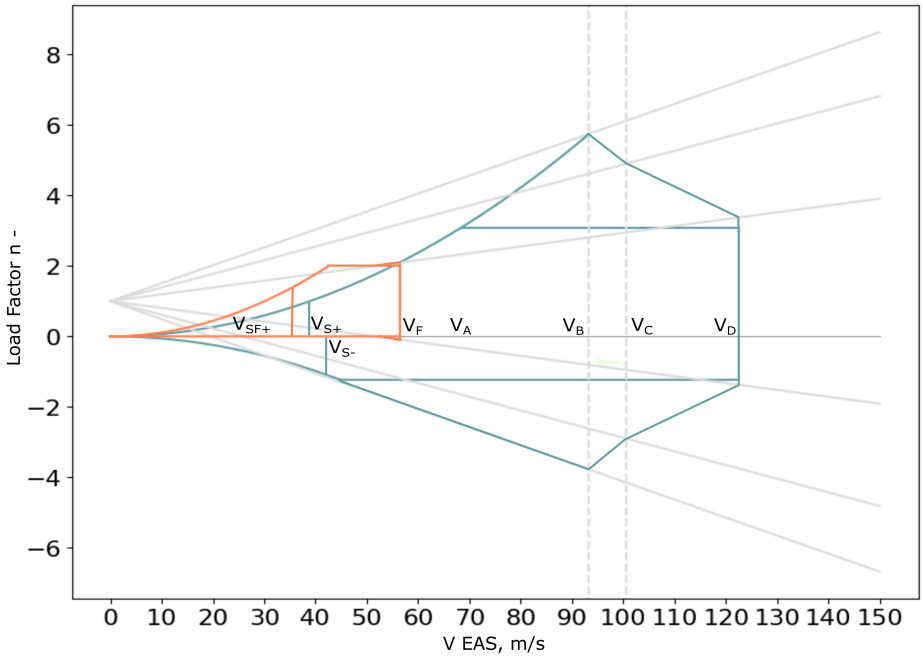


**Figure 6.13:** *V-n diagram for the most critical configuration - clean, cruise altitude at minimum weight.*

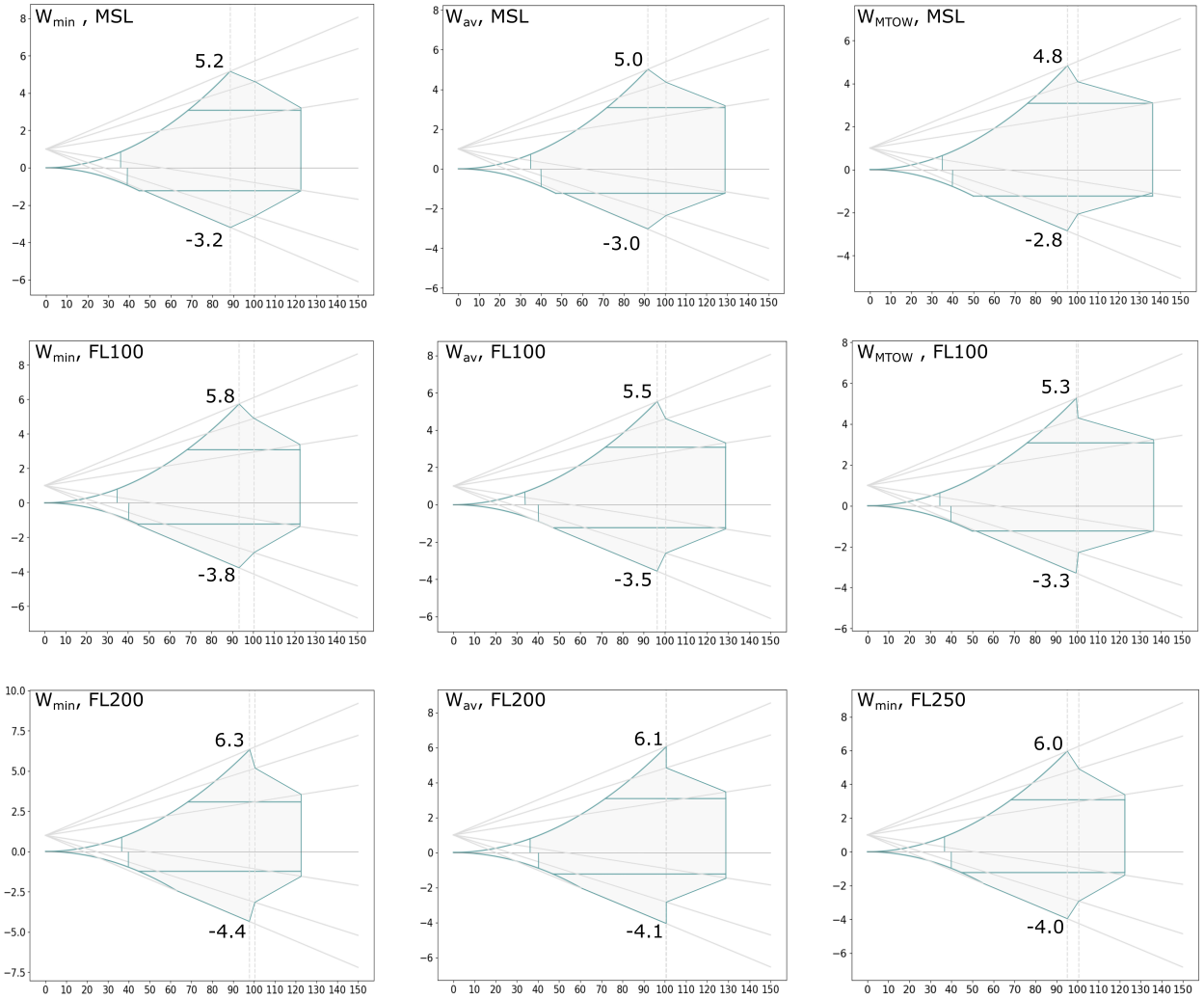


**Figure 6.14:** *V-n diagrams for cases with varying flight levels and aircraft weights.*

# 7

# Structural Analysis

The structure of the aircraft will experience high aerodynamic loads during operation. These loads induce stresses throughout the aircraft structure. If these stresses become too high, the material, component or even entire aircraft may fail. It was therefore necessary to determine the locations in the aircraft where the structural stress will be the highest and determine if the structure will be stiff and strong enough to withstand these loads. If it was found that the local structure were too strong, less reinforcement could then be used and a lighter structural weight obtained. In this chapter the results of the structural investigation of the aircraft are presented.

## 7.1. Stress Analysis

In this section, the effect of different loading cases on the structure of the aircraft is analysed. For this, the loading on the aircraft on the ground was considered, as well as in flight. The design load factors of n = 6.3 and n =-4.4, found in Subsection 6.4.2, were multiplied with a safety factor of 1.5, to obtain the ultimate load factor according to certification requirements [27]. These ultimate loads, of 9.48 and -6.6, were then used in the calculations for the loads in the structure, together with the flight conditions corresponding to the load factors. On-ground, the weight and reaction forces from the landing gear were considered. The most critical loading case was then determined, and the maximum stresses in different structural parts of the aircraft were designed to remain below the ultimate tensile and shear stress of the materials used.

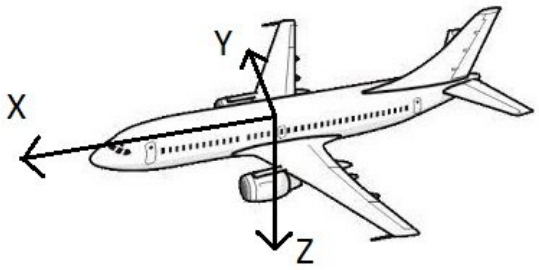


**Figure 7.1:** *Aircraft body reference frame [67].*

The coordinate system used to analyse the loading was the body reference frame depicted in Figure 7.1.

To obtain the loads acting on the aircraft, caused by the ultimate load factors, two main assumptions were made. Firstly, it was assumed that the aircraft did not experience any acceleration due to the load factor. In reality, the aircraft would accelerate upwards due to a positive load factor, as from the definition of the load factor, n, as stated in Equation 7.1, it can be seen that the lift force, L, would have to become n times larger than the weight, W, resulting in a force upwards. This would cause problems for the static structural analysis, and therefore it was decided that the weight was also to be multiplied by the load factor, such that the aircraft would remain in equilibrium for the analysis. This assumption could be justified by the fact that the initial response of the aircraft to a varying load factor, would be to remain in its initial position.

$$n = \frac{L}{W} \tag{7.1}$$

Furthermore, assumptions had to be made on the forces acting on the aircraft. Thus, the weight of the aircraft was modelled as a linearly distributed force over the whole fuselage, and the lift force was spread over the horizontal tail and the wing. The distribution of the lift over the wing and the horizontal tail was established by assuming moment equilibrium around the y-axis, which yielded a specific amount of lift required to be generated by the wing and horizontal tail, as the locations of the wing and horizontal tail on the fuselage were already known.

### 7.1.1. Fuselage

The fuselage was analysed in the longitudinal direction, which is the x-axis shown in Figure 7.1. For the on-ground case, the weight of the aircraft was modelled as a distributed force over the whole length of the fuselage. The reaction moments through the nose and main landing gear were considered to be point loads. For the in-flight cases, the lift of the wing was approximated as a point load applied at $x_{LEMAC}$, and the lift of the horizontal tail was applied at 12 m measured from the nose. The free body diagram (FBD) of the two loading cases can be seen in Figure 7.2, where the left free body diagram is the in-flight case, and the right diagram is for the on-ground loading case. In Figure 7.2, the force due to the weight of the aircraft is labelled as Fweight, the lift force on the wing as Flift, and the lift force on the horizontal tail as Fhor. As can be seen in Table 7.1, the maximum load factor was the loading condition which gave the highest loads in all structural components. Therefore, it was decided that only the loading condition for the maximum positive load factor was to be analysed for the stress analysis. The internal shear and moment diagram for the maximum load factor for the fuselage can be seen in Figure 7.3.

$$\tau = \frac{VQ}{It} \quad (7.2) \qquad \sigma = \frac{My}{I} \quad (7.3)$$

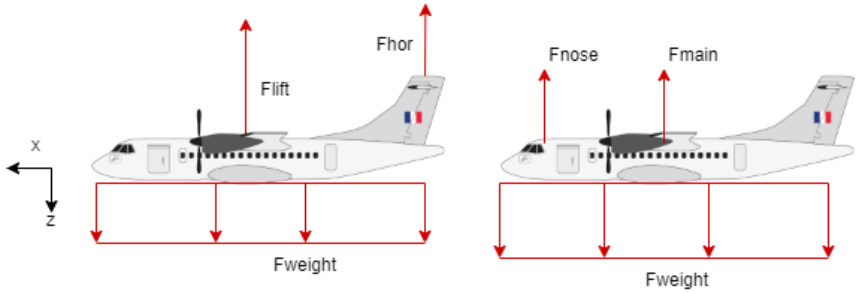


**Figure 7.2:** *Free body diagram of fuselage structure. Left FBD is for the in-flight condition, and the right FBD is for the on-ground loading condition.*

Equation 7.2 and Equation 7.3 from [68] were thereafter used to convert the loads in the structure to stresses. Equation 7.2 was used to calculate the shear stress $\tau$. In Equation 7.2, V is the internal shear force, Q the first moment of area, I the moment of inertia of the cross section, and lastly the material thickness perpendicular to the shear is t. Equation 7.3 was used to calculate the bending stress, $\sigma$. In this equation, M is the internal moment at that location of the fuselage, y is the maximum distance from the neutral axis, and I is again the moment of inertia of the cross section.

**Table 7.1:** *Maximum internal shear force and moment for different loading cases and structural components.*

| | **Max. shear force [kN]** | **Max. moment [kNm]** |
|---|---|---|
| Fuselage | | |
| Max. load factor | ±190 | -490 |
| Min. load factor | ±130 | 330 |
| On-ground | ±27 | -80 |
| Wing | | |
| Max. load factor | -192 | 665 |
| Min. load factor | 140 | -470 |
| On-ground | 9 | -40 |
| Horizontal stabiliser | | |
| Max. load factor | -50 | -75 |
| Min. load factor | 34 | 52 |

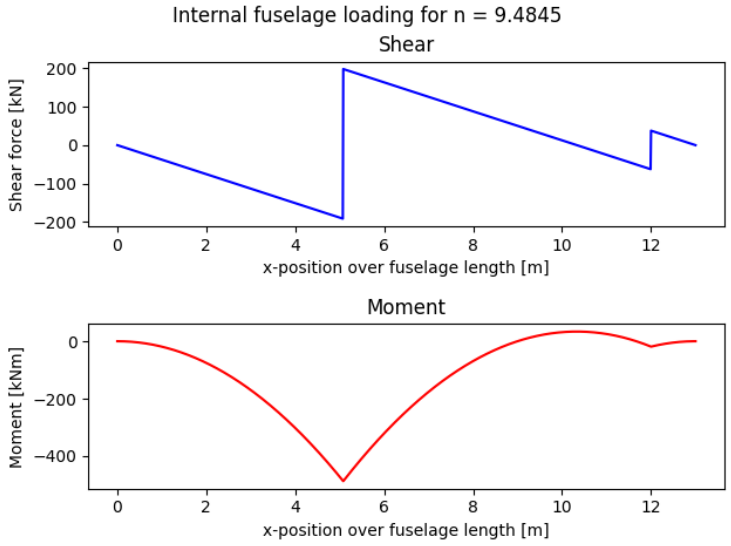


**Figure 7.3:** *Internal load diagrams of fuselage for maximum positive load factor.*

For the fuselage, the stresses in the structure due to the pressurisation of the cabin were also taken into account. For

the highest pressure difference, the pressure at the surface ceiling of 25 000 ft was taken [6], and the pressure at 8000 ft was subtracted from this pressure, as this was the pressure altitude specified in regulations [27]. This lead to a pressure difference, $\Delta p$, of 37661.5 Pa, which could be inserted in Equation 7.5 and Equation 7.6 [68], together with the radius of the fuselage, R, and the thickness of the fuselage skin, t. For this analysis, the fuselage structure was assumed to be a hollow cylinder, with a constant radius and a constant thickness of 0.4 mm. The axial stress due to pressurisation was superimposed on the bending stress. Furthermore, the torque introduced by the vertical tail was also taken into account, as this torque would introduce a shear stress when wind would hit the tail, which could be superimposed to the shear stress due to the shear force. The torque was assumed to be present throughout the whole length of the fuselage, and was calculated by assuming a 53 kts constant wind, at a 90 degrees angle. The dynamic pressure, $p = \frac{1}{2}\rho V^2$, in which $\rho$ was the density, and V the wind speed, was then multiplied by the total vertical tail area to obtain the total wind force on the tail. It was considered that the wind force could be modelled as a uniformly distributed force over the length of the vertical tail, and using this assumption, the torque introduced in the fuselage due to the wind force was calculated to be 2098 Nm. This was converted to a shear stress in the fuselage by using Equation 7.4, in which T is the internal torque, t, is the fuselage thickness and $A_m$ is the mean area enclosed by the fuselage [69]. The maximum value for the shear stress was then found to be 250 MPa, and the maximum value for the bending stress was found to be 290 MPa, at the point where the lift force of the wing was applied, so $x_{LEMAC}$. All the different stresses are depicted in Figure 7.4.

$$\tau = \frac{T}{2tA_m} \quad (7.4) \qquad \sigma_{hoop} = \frac{\Delta p \cdot R}{t} \quad (7.5) \qquad \sigma_{axial} = \frac{\Delta p \cdot R}{2t} \quad (7.6)$$

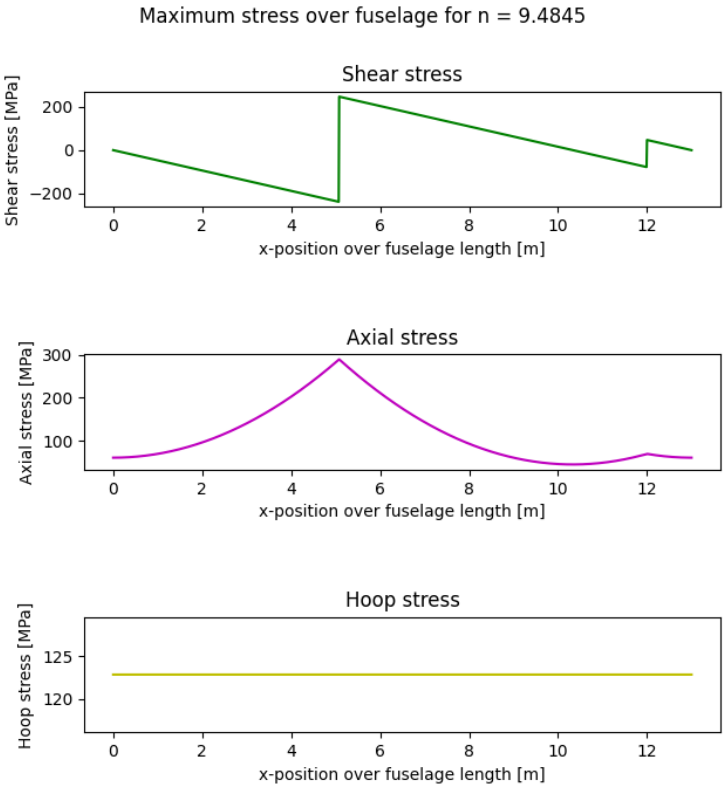


**Figure 7.4:** *Maximum stresses in the fuselage skin over the fuselage length.*

## 7.1.2. Wing

For the on-ground loading case, the weight of the wing, engines and propellers were used to analyse the internal loading of the wing. For the in-flight loading case, the total lift force was modelled as a triangular load over the wing span, with the largest load at the root chord, and the gas turbine weight and all propellers with electric motors were considered to be a point load. In flight, the weight of the wing itself was neglected, which led to a more conservative analysis. Again, the positive load factor was found to yield the highest internal loads, and thus this loading case was used to perform the stress analysis. The FBD of the wing structure in-flight is shown in Figure 7.5. In Figure 7.5, Flift is the lift force on the wing, Fengine and Felectric are the weights of the gas turbine and electric motors respectively, and lastly, Mx and Rz

are the reaction moment and force in the z-direction at the root respectively.

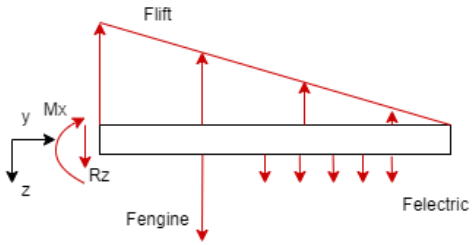


**Figure 7.5:** *Free body diagram of wing structure for the in-flight condition.*

To convert the internal shear and moment to a structural stress, a load-bearing structure was designed. A preliminary wingbox was developed, which was assumed to carry all the loads in the wing. First, the positions of the front and rear spar were determined, as these form the sides of the wingbox. As the front spar is usually between 15 and 30 percent of the chordline, and the rear spar is normally positioned between 65 and 75 percent of the chord [25], it was decided that the front spar would be placed at 17% of the chord, and the rear spar at 70% of the chord. These locations for the spars also accommodated sufficient height for the spars, which was estimated to be 0.13 times the chord length. The spars were then connected on the top and bottom with two horizontal panels, resulting in a rectangular cross section for the wingbox with a height of 375 mm and a width of 1560 mm at the root chord. The spars and both the horizontal panels had a thickness of 20 mm. Furthermore, to increase the stiffness of the wingbox, 24 stringers in total were added and distributed equally over the top and bottom of the wing box. The dimensions of the used stringer can be found in Figure 7.6. These stringers increased the cross sectional area resisting the bending, and thus increased the moment of inertia of the wingbox. Lastly, since the wing taper was decided to be 0.4, the wingbox width and height had to decrease over the wingspan, in order for the wingbox to fit into the wing. This caused the moment of inertia to decrease over the wingspan, as can be seen in Figure 7.7.

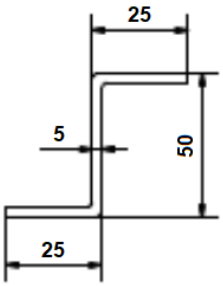


**Figure 7.6:** *Dimensions of used stringer.*


**Figure 7.7:** *Moment of inertia around the x-axis over half the wing span.*

Using Equation 7.2 and Equation 7.3, the stresses over the wingspan could be calculated, and are shown in Figure 7.8. The maximum stress was found to be the bending stress at the root chord, and had a value of 480 MPa. The shear stress was expected not to be limiting, even though the shear stress in the wing structure arises from both the shear force and the torsion on the wing. The reason for this was that the maximum shear stress due to the shear force is only 20 MPa, and the torsion from the thrust in the wing structure would be limited, due to the propellers being located at the same height as the leading edge. This would result in only the weight of the propellers and engine and the lift force causing a torque, as both forces were assumed to have an offset from the centroid. However, these forces would act in opposing directions during the limiting load case, which would limit the maximum internal torque in the wing structure, and hence, the bending stress was expected to be limiting.

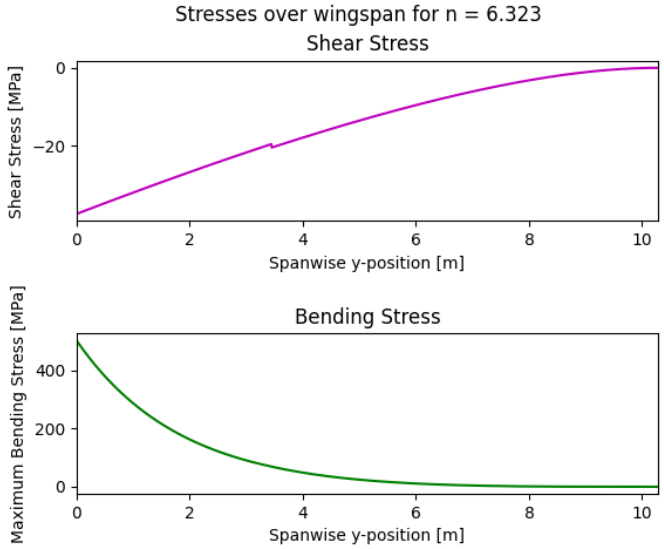


**Figure 7.8:** *Shear and maximum bending stress over the half wingspan for the maximum load factor.*

### 7.1.3. Horizontal Stabiliser

For the tail, the lift force required for the critical condition, which was the maximum load factor, was calculated to be 100 kN. This force was modelled as a uniformly varying load over the span of the horizontal stabiliser, in the same manner as the wing was loaded in Subsection 7.1.2. Again, the weight of the horizontal tail was neglected for a more conservative analysis. The wingbox of the horizontail stabiliser also had its spars located at 17% and 70% of the chord, and also had a height of 0.13 times the chord. The spars and the horizontal panels of the wingbox of the horizontal stabiliser both were considered to have a thickness of 7 mm. Furthermore, the wingbox also decreased in size due to the taper of 0.45 of the horizontal stabiliser. This resulted in a shear stress and bending stress over the span of the horizontal tail shown in Figure 7.9.

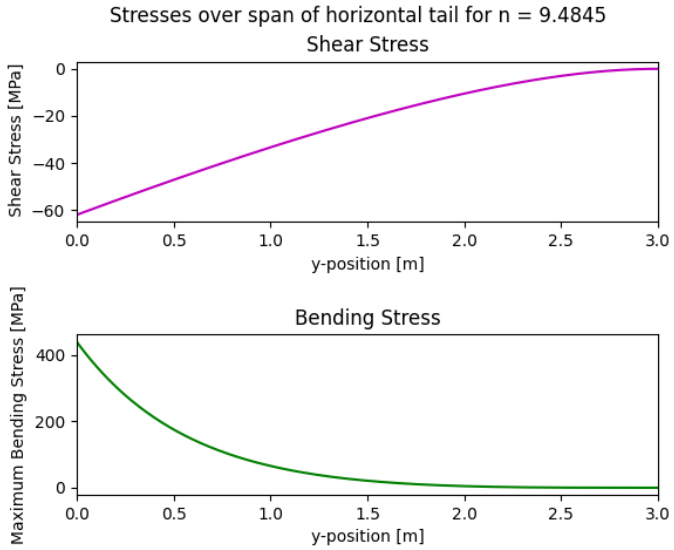


**Figure 7.9:** *Shear and maximum bending stress over the horizontal tail.*

The maximum bending stress of the horizontal tail was found to be 435 MPa, and the location of this maximum stress was at the root chord of the horizontal tail.

### 7.1.4. Exploration of Wing Strut

As the wingbox structure had components with a relatively large thickness, a wing strut, placed between the engine fairing and the fuselage was considered to save wing weight. This strut would be able to carry tensile and compressive normal forces, which would decrease the total internal moment at the root chord of the wing. This would allow for a decrease of the wingbox weight. The wing strut would add a new component and thus drag and weight, but the correct sizing of a wing strut could also decrease the wing structural weight significantly, to the point where the aircraft becomes more efficient overall [70]. Therefore, the option of a strut-braced wing was investigated, and mainly the influence of such a strut on the wing structure was considered. The altered free body diagram is shown in Figure 7.10, and includes the new forces introduced by the wing strut, which are Fstruty and Fstrutz, the horizontal and vertical force carried by the strut, and Ry, the reaction force in the y-direction at the root.

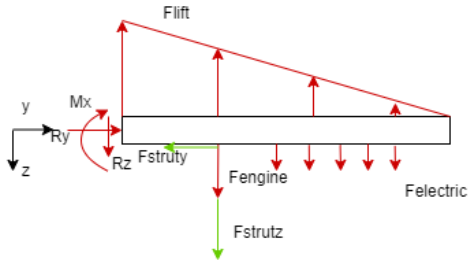


**Figure 7.10:** *Free body diagram of wing structure including wing strut.*

Despite all efforts made to solve the statically indeterminate wing structure, it was assumed that for the first analysis on the influence of a wing-strut, the strut would carry 30% of the total vertical load introduced into the structure due to the lift force. This meant that only 70% of the total lift force, instead of 100% was to be transferred into the structure as a shear force at the root chord of the wing. This led to a change in the internal loading diagrams. This change can be seen in Figure 7.11, in which the red line indicates the load in the wing structure without the strut, and the blue line shows the internal load for the structure including the strut.

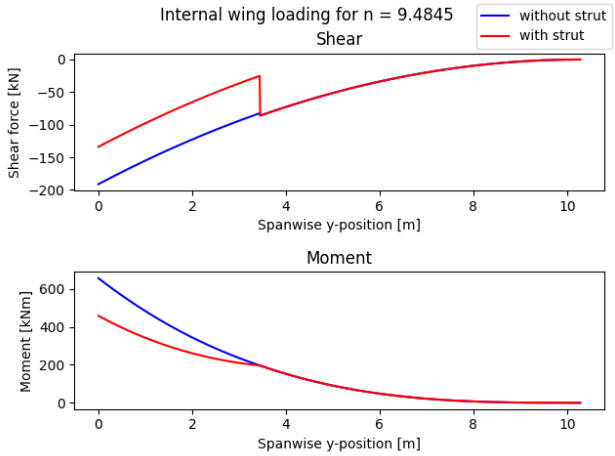


**Figure 7.11:** *Internal shear and moment diagram of the wing structure for the maximum load factor. The red line indicates the internal load in the structure without the strut, the blue line is for the structure with the strut.*

As can be seen from Figure 7.11, the maximum value for the internal shear force and moment were lowered by introducing a strut. Therefore, the maximum bending stress at the root would also be lowered due to the strut. Usually, a lower bending stress would also allow for a lighter structure, as the moment of inertia of the cross section could be decreased, whilst obtaining the same maximum stress. However, in this case, a compressive normal force, of 43 kN was also introduced into the structure by the strut for the maximum load case. The introduction of this normal force could decrease the buckling or crippling stress, as a compressive force should be superimposed on the bending stress, on the side which is in compression. These stresses have not been analysed in this preliminary analysis yet, and thus, even though the addition of a wing-strut looked promising in decreasing the weight of the wing structure, more analysis is required to be able to properly design the wing structure in detail.

### 7.1.5. Verification

To ensure that the programme functioned as expected, several verification tests were performed. The first test included the generation of internal shear and moment diagrams of simple loading cases, which were then compared to diagrams made by hand. Furthermore, the programme was also verified by inputting practice problems from Hibbeler's Mechanics of Materials [69], and comparing the outputted diagrams with the solution manual.

## 7.2. Materials

Due to the high emphasis on sustainability, as specified by requirements **REQ-STA-CUST-05.1**, **REQ-SUS-PROD-01** up and until **REQ-SUS-PROD-07**, **REQ-SUS-OPR-03** and **REQ-SUS-END-3.1.1**, a thorough investigation of materials was carried out. Each material type has its advantages and disadvantages, but when used for a specific purpose usually one material type exceeds over others. The airframe requires lightweight materials which are sufficiently stiff to withstand the loads applied to it. Materials with a lower density to performance ratio allow for greater range and velocity and could reduce operational cost [71]. For aforementioned reasons, in Subsection 7.2.1, the most prominent materials of each material type which could be useful for (a part of) the aircraft are listed. In Subsection 7.2.2 the materials that were selected are presented.

### 7.2.1. Material Options

For the material selection process the engines were not considered as they would be bought from a manufacture. Thus, for this selection process, only the aircraft structure and interior were considered. Using literature and the material database of MatWeb[59], the material options were assessed.

#### Materials Introduction

The material selection process was started by investigating the properties of the main material groups considered: metals, polymers, ceramics, natural materials and composites. Considering the importance of strong but lightweight materials it was relevant to look at the density vs strength of materials chart in Figure 7.12. The strength in Figure 7.12 describes yield strength for metals and polymers, tear strength for elastomers, compressive strength for ceramics and tensile strength for composites. For load-bearing aerospace structures it is desired to be able to carry as much load as possible with the least structural weight. From Figure 7.12 it can be seen that composites are desired where tensile stresses are expected. Another advantage of composites is that they can be tailored to more efficiently handle specific loads. Of composite matrix options, only metallic and epoxy matrices were considered as ceramic matrices have limited tensile strength and low resistance to mechanical impact and thermal shock [72].

Metals are relatively well-performing in all loading cases due to their isotropic properties. Steel is cheap but dense and not significantly better performing than aluminium, thus aluminium is preferred over steel. However, high performance steel is generally used in engines. Titanium alloys are denser than aluminium alloys, but outperform all other metals in terms of tensile strength. However, it is more expensive compared to other metals. In addition, titanium is difficult to machine or weld, making tooling costs higher for this material.
Ceramics have a high compressive strength and heat and corrosion resistance, and are therefore used in engines. However, due to their high brittleness, low tensile strength and weak resistance to bending and torsion this material is not considered for the aircraft structure.

Natural materials such as wood and rubber have a low density and are therefore desired in aircraft when applied correctly. Wood is a low density material with a relatively high stiffness and does not suffer from corrosion. However, wood was not considered for the external structure due to its vulnerability to weather and unpredictable failure behaviour due to its irregular grains. Rubber is an extremely flexible natural polymer which is commonly used in combination with high pressure for tires. Rubber however does not have the required properties to be used for a main structural component such as the airframe or wing.

Synthetic polymers cannot be used on their own as structural materials due to their low stiffness and strength, creep properties and working temperatures [74]. Therefore, polymers were chosen to be used in the interior of the aircraft due to their low density, or used in combination with other materials in composites. Polymers usually act as fibre reinforcement for a matrix made of a metal, plastic or ceramic material.

#### Materials Assessment

Of each material type, a variety of commonly used materials were assessed. For the candidate materials the Ultimate Tensile Strength (UTS), Ultimate Shear Strength (USS), Coefficient of Thermal Expansion (CTE), Young's modulus, relative recyclability and relative cost were tabulated. For aluminium, one alloy of each of the main aluminium series used in the aerospace industry, 2000, 6000 and 7000, was selected and investigated. For titanium, the commonly used

[59] Material Property Data, https://matweb.com/, date accessed = 03-06-2022

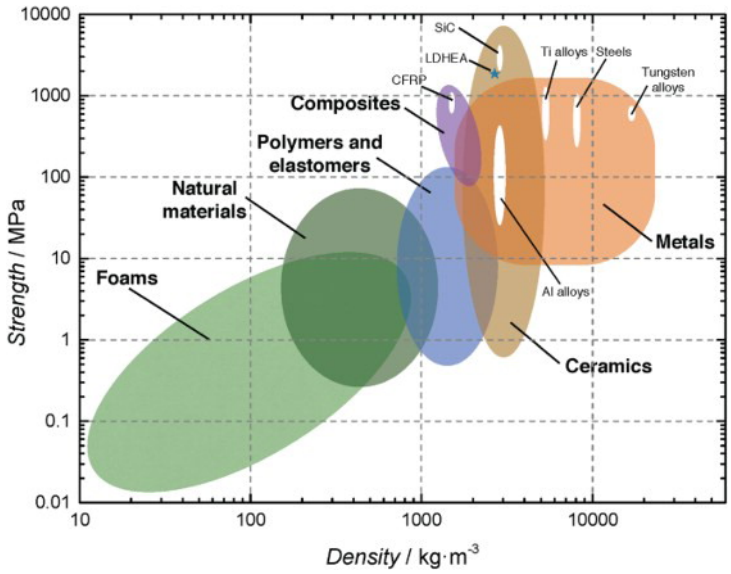


**Figure 7.12:** *Chart showing the density vs strength for each material type [73].*

alloy Ti-6Al-4V was assessed. Regarding composites, Carbon fibre-Reinforced Polymer (CFRP), Glass fibre-Reinforced Polymer (GFRP), GLAss REinforced aluminium (GLARE) and Metal Matrix Composites (MMC) were considered. For composites, the ultimate tensile strength was taken for a unidirectional lay-up in the fibre direction. For CFRP and GFRP, the UTS was determined for a 60% fibre volume with thermoplastic resin. Regarding GLARE it was assumed it has three layers of Al 2024-T6 and two prepreg layers. Each prepreg has a 50% fibre volume and consists of E-glass fibres with an epoxy resin. For the MMC option it was assumed that an Al 6061-T6 alloy would be reinforced with siliciumcarbide particles. The volume fraction of the silicumcarbide was taken as 30%.

The candidates and their parameter values for aforementioned assessment criteria can be found in Table 7.2. The relative recyclability and cost were assessed with a score ranging between: --, -, 0, +, ++. For recyclability, a score of -- signifies that it is expensive, or not yet commercially possible, to recycle. A ++ score signifies that recycling of the material is a simple and cheap process. Regarding relative cost, a score of -- means the material is expensive to produce, a score of ++ means the material is cheap to produce. It should be noted that the CTE for GLARE could not be found, but was estimated to be less than MMC and more than GFRP due to their respective components. Furthermore, for aluminium 2024 the Alclad version is taken to cope with the corrosive nature of the pure Al 2024 alloy. Finally, for GLARE, Al 7075 was chosen as this would form the strongest GLARE component.

**Table 7.2:** *Candidate materials for fuselage, empennage and wing.*

| Material | UTS [MPa] | USS [MPa] | Density [kg/m$^3$] | CTE [$10^{-6}K^{-1}$] | Young's modulus [MPa] | Relative recycla-bility | Relative cost |
|---|---|---|---|---|---|---|---|
| **Metals** | | | | | | | |
| Al 2024-T3 | 448 | 276 | 2780 | 22.9 | 73.1 | ++ | ++ |
| Al 6061-T6 | 310 | 207 | 2700 | 23.6 | 68.9 | ++ | ++ |
| Al 7075-T6 | 572 | 331 | 2810 | 23.4 | 71.7 | ++ | + |
| Ti-6Al-4V | 950 | 550 | 4430 | 8.6 | 114 | + | 0 |
| **Composites** | | | | | | | |
| CFRP | 1500 | 70.0 | 1600 | 0.113 | 135 | - | -- |
| GFRP | 1000 | 40.0 | 1900 | 0.216 | 65 | -- | - |
| GLARE | 365 | 40.2 | 2480 | / | 55 | - | -- |
| MMC | 420 | 274 | 2790 | 22 | 400 | 0 | -- |

### 7.2.2. Material Selection

This subsection describes the material selection and the relevant reasons why a specific material is preferred over others. During the selection process, the recyclability, density and thermal expansion coefficient were both kept as main parameters to decide on what material should be used where. Furthermore, to simplify the stress analysis, it was assumed that the wing, empennage and fuselage were made from one material. In a future design phase, a more detailed analysis regarding combinations of materials and internal layout should be investigated to optimise the weight to performance ratio.

In Table 7.3 the ultimate tensile strength and ultimate shear strength of the selected materials is compared to respectively the required tensile strength and required shear strength of the wing, empennage and fuselage. The left three columns repeat the ultimate strengths of the material. The columns on the right present whether or not the material complies to the calculated required strength of the wing, empennage and fuselage as calculated in Section 7.1. When a material was found to have a sufficiently high ultimate strength, the box of that combination between material and component was made green. The ultimate strength was analysed instead of the yield strength, as the loads that were considered were the ultimate loads the structure experiences. After experiencing this load the aircraft would need severe inspection, reparations or even be decommissioned. Thus the aircraft needs to withstand this force only once, and it is enough to analyse these loads. Nominal operation loads are considered in the fatigue analysis. Combining the compliance to the ultimate stress criteria with the criteria for low density, high recyclability and low relative cost, a choice was made on the material for aforementioned three components.

**Table 7.3:** *Material compliance table.*

| **Materials** | **UTS [MPa]** | **USS [MPa]** | **Wing [MPa]** | | **Empennage [MPa]** | | **Fuselage [MPa]** | |
|---|---|---|---|---|---|---|---|---|
| | | | Tensile | Shear | Tensile | Shear | Tensile | Shear |
| Al 2024-T3 | 448 | 276 | 480 | 37 | 435 | 62 | 290 | 250 |
| Al 6061-T6 | 310 | 207 | 480 | 37 | 435 | 62 | 290 | 250 |
| Al 7075-T6 | 572 | 331 | 480 | 37 | 435 | 62 | 290 | 250 |
| Ti-6Al-4V | 950 | 550 | 480 | 37 | 435 | 62 | 290 | 250 |
| CFRP | 1500 | 70 | 480 | 37 | 435 | 62 | 290 | 250 |
| GFRP | 1000 | 40 | 480 | 37 | 435 | 62 | 290 | 250 |
| GLARE | 365 | 40.2 | 480 | 37 | 435 | 62 | 290 | 250 |
| MMC | 420 | 274 | 480 | 37 | 435 | 62 | 290 | 250 |

It was chosen to have the main wing made of aluminium 7075-T6. Composites are great in tensile loading, but significantly worse in compressive, bending and torsional loading. Of the mentioned metals, titanium is the best performing. However, it is heavy compared to aluminium, less recyclable and more expensive. It is therefore preferred to use aluminium. Of the aluminium alloys 7075-T6 was chosen as it is thought the strength of this alloy compared to a slight increase of density was thought to justify the choice for this aluminium alloy.

The material that was chosen for the empennage was Al 7075-T6. This material was chosen as the empennage and its control surfaces will undergo, apart from tensile stresses, non-negligible compressive, bending and torsional stresses as discussed in Section 7.1. Therefore, the empennage may not be made of composites. From the metals, the titanium alloy would be undesired, as its high strength is simply unnecessary. Initially, Al 2024-T3 was chosen as it was expected its strength would be sufficient and weight could be saved using this alloy over the 7075. This metal would also be preferred over Al 6061-T6 as the CTE was lower, thus it would suffer less from thermal stresses. However, as can be seen in Table 7.3, its strength was sufficiently strong, but only barely. As this design was not iterated over, the margin was considered too close and thus the next best metal was taken.

For the fuselage it was initially chosen to use CFRP. The tail would be the only place where torsion could be introduced into the fuselage. As the tail would be made of Al 7075-T6, which has a high torsional resistance, it was expected that the fuselage carries negligible torsional loads. Therefore, a more weight saving and less torsional resistant material could be chosen for the fuselage. Of the composites, CFRP has the lowest density yet still has the highest performance regarding tension. However, it was found that the relatively poor recyclability of CFRP caused the requirement of needing to be 90% recyclable by mass, **REQ-STA-CUST-05.1**, to not be complied to. For this reason, it was chosen to have the fuselage made of aluminium for 73.1% of the fuselage mass. Interior elements of the fuselage, such as the stringers, shall be made of Al 6061-T6 as it is slightly less dense than the 2024-T3 alloy. It was thought that the UTS of Al 6061-T6 was too close the required stress level of 290 MPa, therefore it would only function as interior strengthening element. As both are deemed equally recyclable, the exact mass percentages of each alloy were deemed irrelevant for this section. It was chosen to use CFRP to still benefit from a weight advantage due to the low density of the material.

CFRP would be used in the fuselage and would make up for 13.1 % of the fuselage mass. To be more specific, CFRP shall be used in the skin of the roof of the fuselage as the most intense tensile stresses of the fuselage are expected there [75]. Furthermore, this choice was made to limit the interference with fuselage cutouts.

The optimal decision regarding the connection between the aluminium and composite material shall be determined in the next design phase based on a more advanced structural analysis. Methods that shall be considered are include adhesion, welding and mechanically connecting [76], [77].

For a more detailed future stress analysis, wing design options using multiple materials and varying internal geometry with corresponding varying moment of inertia should be considered. For this analysis it would be advantageous to consider the use of carbon fibre based composites at places where high tensile stresses are expected, such as for the skin on the bottom side of the wings. Carbon fibre based composites could also be used for components for which it is critical that the thermal expansion and shrinkage is minimised. Lastly, composites could also be used to replace components which do not require the performance of metals and thus could be replaced to reduce weight. Titanium could be used to reinforce the wing root and engine attachment points to reduce the stress and therefore the required aluminium mass. For the interior design, lightweight materials such as plastics and wood will be used to save weight.

In Table 7.4, the material choices for the subsystems and the total recyclability of the aircraft are displayed. Although a material is never 100% or 0% recyclable, it was assumed metals are 100% and composites are not recyclable to simplify the compliance assessment with relation to the 90% recyclability requirement, **REQ-STA-CUST-05.1**. Fixed equipment entails flight controls, hydraulics, electrical equipment, instrumentation, air conditioning and oxygen systems. It was unsure which exact materials would be used for the fixed equipment and to what extent these materials would be used. However, it was assumed most of the fixed equipment material mass would come from metal as it would be required that the materials either have high strength, high manufacturability, high conductivity or a combination of these parameters. With the uncertainty in mind, a recyclability value of 90% was assumed for fixed equipment. It can be seen that with a mass recyclability percentage of 90.2%, requirement **REQ-STA-CUST-05.1** is complied to. The margin was considered safe with respect to the requirement as composites can (partially) be recycled. However, the recycling of composites is a complex, relatively expensive and relatively new process.

## 7.3. Temperature Considerations

Extreme temperature differences were identified as one of the key factors in aircraft performance in Antarctica - **[FAC.1]**. Hence, the effect of the temperature change during operations was considered in material choice. The temperature difference flying up and down to and from the service ceiling can be 50°C. This value was calculated using International Standard Atmosphere (ISA) relations relating altitude and temperature. Using the formula for linear thermal expansion, the assumption the aircraft starts at the higher temperature and the assumption Al 7075 is used, a half-span shrinkage of 1.17 cm is to be expected. If a wing were to be made of solely one material, this shrinkage would not be a problem as all components would shrink at the same rate. However, as discussed in Section 7.2, the wing may be made of multiple materials to optimise the performance to weight ratio. For CFRP, in the fibre direction for a unidirectional sheet, the shrinkage is only 5.65E-3 cm, which results in complementary stresses at locations where the materials are joined. However, this would be solved by having sufficient clearance between the critical parts. For example, after a more detailed structural analysis, it could be decided to have the control surfaces made of CFRP if it is proven to be feasible and have a clear advantage compared to aluminium control surfaces. Clearances shall then be incorporated to allow the aluminium wing to shrink or expand without restricting the movement of the control surfaces.

## 7.4. Fatigue

To analyse the behaviour of the materials used in the aircraft over its lifespan, the fatigue characteristics of the materials were also to be taken into account, as many aircraft components are inevitably subjected to fluctuating stresses, which causes many of the components to fail by fatigue fracture [78]. Since homogeneous and monolithic materials with isotropic material properties have dissimilar fatigue characteristics from composite materials [79], a different approach for metals and composites is required to evaluate the fatigue life of the structure. However, as only 27% of the weight of the fuselage structure was decided to be composite, only the fatigue behaviour of the utilised metals were analysed for this first analysis.

### 7.4.1. Fatigue in Metals

For metals, it was decided to analyse the fatigue life using S-N curves. A S-N curve gives a logarithmic relation between the stress amplitude and the number of cycles to failure [80]. To be able to generate S-N curves, a value for the ultimate stress of the material and fatigue limit of a metal has to be found. For fully-reversed loading, it is then assumed that below $10^2$ cycles, the material fails at a stress amplitude equal to its ultimate stress. A second assumption is that after a million cycles, infinite life is reached at the fatigue limit. This yields two points on a graph, and these two points can

**Table 7.4:** *Aircraft subsystems, their components and the respective recyclability of the components.*

| Subsystem | Weight [kg] | Material | Material make up | Percentage of weight | Recyclable | Mass recycled |
|---|---|---|---|---|---|---|
| Wing | 682.76 | Al 7075-T6 | Aluminium | 90.0 | Yes | 614.483 |
| | | | Zinc | 5.6 | Yes | 38.235 |
| | | | Etc. | 4.4 | Yes | 30.041 |
| Empennage | 102.33 | Al 7075-T6 | Aluminium | 94.6 | Yes | 96.805 |
| | | | Copper | 5.4 | Yes | 5.526 |
| Landing gear | 491.84 | S53 steel | Steel | 100.0 | Yes | 491.835 |
| Attachment points | 75.86 | Ti-6Al-4V | Titanium | 89.9 | Yes | 68.200 |
| | | | Aluminium | 6.1 | Yes | 4.628 |
| | | | Vanadium | 4.0 | Yes | 3.034 |
| Fuselage | 665.15 | CFRP | Carbon fibres | 4.1 | No | 0.000 |
| | | | Thermoplastic matrix | 9.5 | No | 0.000 |
| | | Al 2024-T3/Al 6061-T6 | Aluminium | 73.1 | Yes | 486.425 |
| | | Insulation | Glass fibres | 13.2 | No | 0.000 |
| Propulsion | 1303.13 | - | Aluminium | 5.0 | Yes | 65.157 |
| | | | Steel | 38.0 | Yes | 495.190 |
| | | | Composites | 11.0 | No | 0.000 |
| | | | Titanium | 21.0 | Yes | 273.657 |
| | | | Nickel | 16.0 | Yes | 208.501 |
| | | | Miscellaneous | 9.0 | Yes | 117.282 |
| Fixed eq. | 1538.15 | Metals/PEEK | - | 100.0 | 90% | 1384.331 |
| **Total** | **4859.22** | | | | | **4381.515** |
| **Percentage recycled** | | | | | | 90.2 % |

be connected with a straight line on a logarithmic graph, which yields a way to observe the number of cycles to failure for stress amplitudes between the ultimate stress and the fatigue limit [81].

However, this approach is only true for fully-reversed loading, but if the absolute value of the minimum stress does not equal the maximum stress, the fatigue life of a material changes. The parameter linking the minimum and maximum stress is called the R-value, which is the ratio of the minimum and maximum loads during the fatigue loading, as stated in Equation 7.7. This ratio is important in fatigue loading, as the fatigue threshold tends to decrease with increasing R [82].

$$R = \frac{\sigma_{min}}{\sigma_{max}} \tag{7.7}$$

For values other than R = -1, Goodman's relation was applied. The formula for this relation is stated in Equation 7.8, and using this relation, different failure stress amplitudes at a specific number of load cycles can be calculated for different R-values [83]. In Equation 7.8, $\sigma_{N,R}$, is the failure stress at a specified number of loads, N, and a specific R-value. Logically, $\sigma_{N,R=-1}$ is the failure stress at a specified number of loads, N, for R = -1. Furthermore, $\sigma_{m,R}$ is the mean stress for the specified R, and $\sigma_{ult}$ is the ultimate tensile stress of the material used. The mean stress of a specific cyclic loading case can be found using Equation 7.9, and the stress amplitude of a cyclic loading case can be calculated using Equation 7.10.

$$\frac{\sigma_{N,R}}{\sigma_{N,R=-1}} = 1 - \frac{\sigma_{m,R}}{\sigma_{ult}} \tag{7.8}$$

$$\sigma_m = \frac{\sigma_{max} + \sigma_{min}}{2} \tag{7.9}$$

$$\sigma_a = \frac{\sigma_{max} - \sigma_{min}}{2} \tag{7.10}$$

### 7.4.2. Fatigue Analysis

As described in Subsection 7.4.1, a stress amplitude and a mean stress had to be found, in order to analyse the fatigue behaviour of the structural components of the aircraft. For this, load factors were taken from the manoeuvring diagram, at cruise conditions, shown in Subsection 6.4.2, as these loads are the loads that the aircraft would frequently encounter. The positive load factor was thus chosen at n = 3.08, and the negative load factor at n = -1.23. Forces on the structure under the load factors needed to be obtained and could then be converted to stresses, as described in Section 7.1. For the wing, a lift distribution was obtained from XFLR5 [60], which was then applied to the wingbox structure, which is described in Subsection 7.1.2. For the stresses in the fuselage, the same method as described in Section 7.1, was applied to obtain the internal loads and stresses. For the pressurization loads of the fuselage, difference between the pressure at the cruise altitude and 8000 ft were taken, to obtain the pressure differential. The maximum stresses in both the wing and fuselage structure due to the load factors are tabulated in Table 7.5.

**Table 7.5:** *Fatigue stress parameters for the cyclic loading during manoeuvring.*

| | Max stress for n = 3.08 [MPa] | Max stress for n = -1.23 [MPa] | Stress amplitude [MPa] | Mean stress [MPa] |
|---|---|---|---|---|
| Fuselage | 92 | -10 | 51 | 41 |
| Wing | 225 | -125 | 175 | 50 |

For the first evaluation of the fatigue life of the structure, it was decided that the structure would be loaded cyclically between the positive and negative load factor. This led to a R-value of -0.56 for the wing, and a R-value of -0.11 for the fuselage. It was assumed that the fatigue limit of aluminium was 161 MPa, which was one third of its ultimate tensile strength, for a value of R of -1 [80]. The value for the fatigue limit for fully reversed loading was then inserted as $\sigma_{N=10^6,R=-1}$ in Equation 7.8, and $\sigma_{N=10^6,R=-0.11}$ and $\sigma_{N=10^6,R=-0.56}$ could be found for using the mean stress for the fuselage and wing respectively, which are tabulated in Table 7.5. Taking an ultimate tensile stress of 448 MPa for the fuselage, and 572 MPa for the wing structure, yielded fatigue limits for both the fuselage and wing structure. With these parameters, S-N curves for both structures could be generated, and are shown in Figure 7.13 for the fuselage, and Figure 7.14 for the wing.

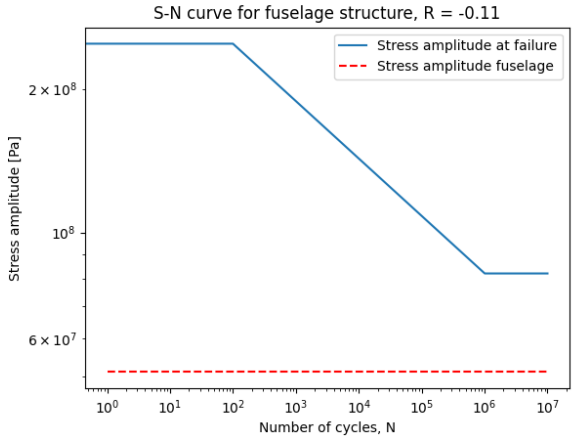


**Figure 7.13:** *S-N curve for the fuselage structure, with R = -0.11.*

As can be seen in Figure 7.13, the stress amplitude under nominal manoeuvring loads is well below the fatigue limit. This means that for the fuselage, fatigue was not expected to be critical under normal operating procedures.

From Figure 7.14, it was noted for that the stress amplitude in nominal manoeuvring conditions would could cause the structure to fail, around $10^5$ load cycles. Since this was still considered a relatively high number of cycles, it was believed that with proper and frequent maintenance procedures, with a specific focus on the root of the wingbox, failure of the wing structure could be prevented.

[60] XFLR5 download, http://www.xflr5.tech/xflr5.htm, date accessed = 02-06-2022

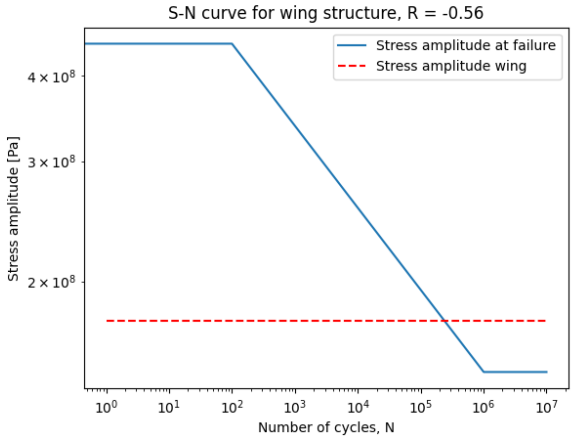


**Figure 7.14:** *S-N curve for the wing structure, with R = -0.56.*

# 7.5. Vibration Analysis

A vibration analysis was performed to assess whether a component of the aircraft could experience damage due to vibrations during standard operations. This analysis focused specifically on flutter, an unstable periodic movement due to the interaction between the flow and the structure at specific velocities. In order to make sure the aircraft or any component would not experience flutter during standard operations, the lowest natural frequency and corresponding flutter velocity of the wing, horizontal stabiliser and vertical stabiliser were computed. The vibration analysis is carried out in the following way. First, the natural frequency of the structure is assessed in Subsection 7.5.1. This is followed by the aeroelastic flutter analysis in Subsection 7.5.2. The verification of the method used is covered in Subsection 7.5.3. Finally, additional future tests are proposed in Subsection 7.5.4.

## 7.5.1. Natural Frequency

The natural frequency of the main wing was calculated using a modelling approach. In a meeting with Dr. Sergio Turteltaub, an expert in Aerospace Structures and Computational Mechanics at the TU Delft, a simple model able to predict the first flutter mode of the main wing and the empennage, was designed. Dr. Turteltaub expected that flutter would occur first by torsional excitation. Thus, the wing was simplified to a torsional model, existing of torsional shafts and a series of disks. These disks represented lumped masses which represented the engines and wing sections. Due to their relative magnitude, the structural weight of the wing and the fuel could not be assumed negligible and was divided in n disks, up to the user's desire and computational power. The size of the disks was approximated by generating a disk (cylinder) with the same volume as the section of the wing. The width of the cylinder was set as 0.1 times the length of the sectional cylinder. This width was chosen to have the disk be a relatively valid assumption [84]. With the width and volume of the cylinder fixed, the radius of gyration was computed. A sketch of the model can be seen in Figure 7.15. In this image, the green boxes represent the engines and the blue nodes a system where n has a value of four. For these nodes, the required properties were calculated halfway between two blue dots, the purple dots, as the wing root node would not move and the wing tip node would not have volume.

A unit rotation was applied on a single disk while keeping the previous disk at zero rotation. This process was repeated for each disk. This way, each disk plus the remaining system rotates with respect to the previous disk(s). From the corresponding n equations of motion a square (n by n) lumped mass matrix and (n by n) stiffness matrix were setup. The lumped mass matrix consisted of zeros apart from the diagonal values. The diagonal values were the polar moments of inertia of each disk. An example of the stiffness matrix for a three node system, the one that can be seen in Figure 7.16, had the form as shown in Equation 7.11. The mass-normalised stiffness matrix was then computed using Equation 7.12. The square root of the eigenvalues of this mass-normalised stiffness matrix were the circular natural frequencies of the system [84].

$$\begin{bmatrix} \kappa_1 + \kappa_2 & -\kappa_2 & 0 \\ -\kappa_2 & \kappa_2 + \kappa_3 & -\kappa_3 \\ 0 & -\kappa_3 & \kappa_3 \end{bmatrix} \tag{7.11}$$

$$\tilde{K} = M^{-\frac{1}{2}} \times K \times M^{-\frac{1}{2}} \tag{7.12}$$

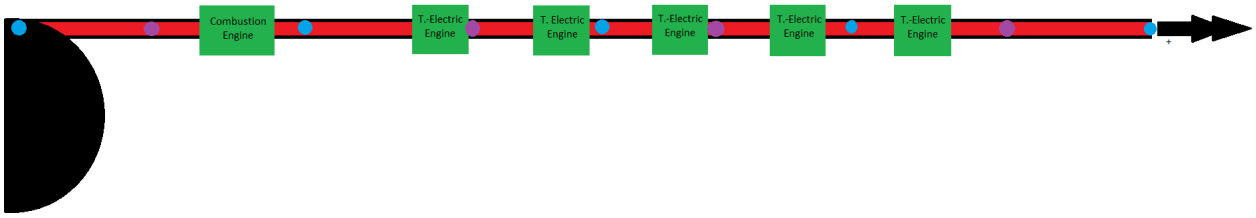


**Figure 7.15:** *Vibration model of the main wing. The green boxes represent the engines. The blue dots represent the system with four nodes. The purple dots represent the point were properties were calculated.*

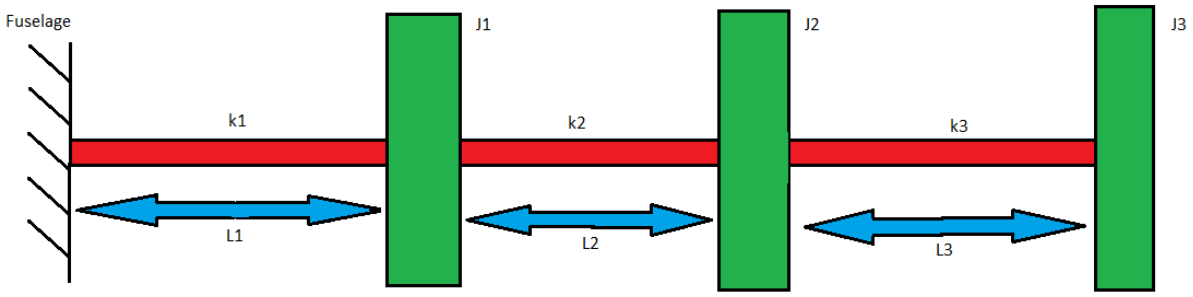


**Figure 7.16:** *Torsional model for a 3 node system.*

### 7.5.2. Aeroelastic Flutter

Aeroelastic flutter is an instability due to an interaction between aerodynamic, inertial and elastic forces. This instability occurs when a specific high flow velocity in combination with a specific density is obtained such that the natural frequencies of the structure are excited. Consequentially, aircraft components such as the wing or the horizontal or vertical stabiliser will resonate. This will, in turn, affect the oncoming flow which forced the vibration. In flutter, the oncoming airflow is affected such that it increases the amplitude of the structural vibration again such that the two systems amplify each other. In a usually short period of time, a catastrophic structural failure follows [85]. Therefore, the velocity at which flutter would occur was analysed.

From the lowest natural frequency of the wing and horizontal and vertical stabiliser, flutter velocities were calculated using the reduced frequency. The reduced frequency related the circular natural frequency to the free stream velocity as can be seen in Equation 7.13. In Equation 7.13, k is the reduced frequency, where a value of 0 signifies the border between stable and unstable behaviour. A value of k ≥0.05 signifies unstable aerodynamics [85]. Furthermore, $\omega_n$ is the circular natural frequency, $c_{half}$ is the semi-chord length, taken at the half-span, and $V_f$ is the flutter velocity. Thus, when the velocity for this value of k with the found natural frequency from Subsection 7.5.1 is obtained, flutter will occur. This velocity must thus be avoided for the reason mentioned in the previous paragraph. The calculated flutter velocities for the main wing, horizontal stabiliser and vertical stabiliser for n = 3000 nodes were tabulated in Table 7.6. For a larger number of nodes, the waiting time was considered too long for the increase in accuracy.

$$k = \omega_n \cdot \frac{c_{half}}{V_f} \tag{7.13}$$

From the results in Table 7.6 it was concluded that the first component that suffers from flutter due to torsion was the horizontal stabiliser. CS-23 regulations state that no flutter shall occur for a velocity of $1.2V_D$. Thus, no flutter should occur up to a speed of 318 kts. As the minimum flutter velocity in Table 7.6 is well above 318 kts, this requirement is complied with. However, it was thought the values for all surfaces were relatively high as the lowest flutter velocity of the surfaces is near Mach 1.44. An aeroelastic stability analysis performed by J.R. Banerjee et all. [86] calculated torsional circular natural frequencies in the range of 45 to 248 rad/s for aircraft wings varying from gliders to large airliner aircraft. As the obtained values are within from this range, it was assumed the model functioned correctly.

**Table 7.6:** *Lowest circular natural frequency ($\omega_n$), and corresponding natural frequency ($f_n$) and flutter speed ($V_f$) for the main wing with both the wing and engines, the wing only,the wing with only the engines, the horizontal stabiliser and the vertical stabiliser.*

| Condition | $\omega_n$ [rad/s] | $f_n$ [Hz] | $V_f$ [kts] |
|---|---|---|---|
| Main Wing (wing + engines) | 101.79 | 16.20 | 1019.00 |
| Main Wing (wing) | 189.20 | 30.11 | 1894.12 |
| Main Wing (engines) | 193.26 | 30.76 | 1934.82 |
| Horizontal Stabiliser | 280.89 | 44.70 | 961.70 |
| Vertical Stabiliser | 287.76 | 45.80 | 2237.59 |

### 7.5.3. Verification

The code was verified by manually checking every line of code for the correct unit and computation. A relatively large error was fixed which involved the calculation of the circular natural frequency. An error occurring in the calculation of the radius of gyration was corrected. Furthermore, an input error involving the thickness to chord ratio was solved. When these errors were removed no more flaw could be found for a system of up to 5 nodes. Following the mathematical verification process, the logic behind the code was also verified.

An initial investigation involved the simulation of components as disks: During the verification process it was found that when the engines were simulated as disks, they acted as standalone parts, interruptions even, in the wing. As the polar moments of inertia of these engines were small, this component would have a small eigenvalue. As the smallest eigenvalue represented the lowest natural frequency, a system including the engines would have a lower flutter speed. However, a wing system consisting of only the engines had both a low order of polar moment of inertia, and a low order of stiffness, and thus no flutter would occur at a low speed. Although it would make sense a large engine would interrupt the wing and would have a lower torsional resistance, it does not make sense if the engines are very small and the wing is, in real life, basically continuous. It was thought this was a mistake in the code logic, which could be fixed by making the code such that the complex internal geometry of the wing was taken into account.

A second investigation involved a literature study involving different modes of flutter: This model solely considered a simple torsional motion that would cause flutter. Literature indicated other modes of vibration could cause flutter at a lower velocity. For example, bending could have a lower natural frequency for specific configurations than torsion [86]–[88]. This meant that if the torsional model was accurate, flutter due to bending could still have a lower velocity. It would only have been proven torsional flutter would not be induced during standard operations. As a final note, it was, as proven, expected that one of the stabilisers would flutter before the main wing; as the polar moment of inertia of a cross-section of the main wing was larger than the polar moment of inertia of stabiliser.

The conclusion of the vibration analysis was that the model will for sure not suffer from a torsional motion as set up in this model. However, nothing could be said about other modes of failure. Future tests would have to prove what kind and at what velocity flutter behaviour occurs.

### 7.5.4. Future Tests

This model was thought to be sufficiently accurate as a first torsional flutter analysis of the main components of the aircraft. More complex models can be made in the next phase, where also additional flutter modes such as bending, which would also take into account the changing weight due to the fuel consumption, are incorporated. Additionally, inclusion of an aerodynamic model which models the aerodynamic forcing on the wing using the theory of Theodorsen [89] would make this model more accurate.

Using stress analysis software such as Nastran[61] even more accurate predictions of the natural frequency and flutter velocities of the aircraft components could be made. Furthermore, when the aircraft is built, Ground Vibration Tests (GVT) would be useful in order to find the natural frequency more accurately. GVT modal results would be compared to a structural FEM to then more accurately predict flutter behaviour.

The effect of the engine vibrations on the structure and how sensitive equipment is affected by this is also subject to future analyses. Due to the unfamiliar knowledge regarding propagation of vibrations in structures, no relevant conclusion could be made regarding this topic.

[61] Hexagon, MSC Nastran, https://www.mscsoftware.com/product/msc-nastran, date accessed = 14-06-2022

# 8

# Risk & Safety

As the JAPA-12 aircraft was generated in a limited timeframe, without testing a physical prototype, some risks were present during the development of the design. Therefore, a risk analysis was conducted, which is covered in this chapter. The risk analysis begins by considering risks of the actual design, this is covered in Section 8.1. This is followed by a RAMS analysis, which investigated the reliability, availability, maintainability and safety of the design. The RAMS analysis is treated in Section 8.2.

## 8.1. Risks

This section will introduce and describe the risks corresponding to the designed aircraft, described in previous chapters. This will be done by first describing the approach to discover risk and the different types of risks, discussed in Subsection 8.1.1, after which the most critical risks will be discussed and mitigated, in Subsection 8.1.2 and Subsection 8.1.3. These risks will also be displayed in a risk map, both pre and post-mitigation.

### 8.1.1. Risk Identification Method

To identify all relevant risks, different potential risks were categorised into the following categories: certification, financial, scheduling, technical, production and operational risks. These different categories are described in this subsection.

**Certification Risks**

Certification risks involved changes in the current certification requirements of the relevant class of aircraft, or limitations in the ability to certify the designed aircraft, due to the novel technology used.

**Financial Risks**

Costs have a significant importance in every project, and still project cost overruns are commonplace [90]. Therefore, financial risks were considered to be of high importance. The financial aspects that were evaluated included material, worker, fuel, and production costs.

**Scheduling Risks**

In order for a design project to be successful, a project plan is usually constructed, which is meant to keep the project within the time constraints, and thus ensure success [91]. However, sometimes there can be unforeseen setbacks in the project, either due to the design team or external parties. This can lead to delays which need to be prevented, and thus, risks concerning the project schedule were analysed.

**Production Risks**

During the production phase of the system, risk can arise from, for example, the improper assembly of the aircraft and faults in the materials or parts.

**Technical Risks**

In the operational phase of the aircraft, there is a risk that aircraft systems may fail. Most of these risks will lead to malfunctioning of the system itself, making it unable to complete its mission.

**Operational Risks**

As it is unavoidable that the operation of the designed aircraft is dependent on third parties, it was decided that risks regarding external parties during the operational phase of the aircraft had to be considered. External parties involved the maintenance staff, medical staff and relevant airfields.

### 8.1.2. Risk Identification

After the different categories of potential risks, as discussed in Subsection 8.1.1, were established and various risks falling under these categories were discovered, the relevant risks were classified. For this, it was decided that only the risks the design team could influence, and risks emerging from events that were not designed for, were deemed as relevant. Due to this, only risks under falling on the certification, financial, schedule and operational risk remained, and the list of relevant risks are shown in Table 8.1, in the column ”Explanation”. Every risk was designated a unique identifier and a score. The score was computed by multiplying the consequence of the event occurring with the probability of the event occurring, which resulted in a score between 1 up to and including 25, which can be found in the column ”Risk score” in Table 8.1. A risk with a risk score of 15 or higher was considered to be a high-level risk, and a risk with a

score between 5 and 15 was considered to be a medium-level risk. Both the high-level and medium-level risks required mitigation strategies to reduce their impact or probability, as described in Subsection 8.1.3.

**Table 8.1:** *Risk identification and mitigation.*

| Identifier | Explanation | Risk score | Strategy |
|---|---|---|---|
| | Certification risks | | |
| RSK-CER-01 | Certification is not updated to include hybrid-electric distributed propulsion. | 15 | Reduce |
| | Financial risks | | |
| RSK-FIN-01 | Lower number of sales. | 16 | Reduce |
| | Schedule risks | | |
| RSK-SCH-01 | Technology readiness level of a Commercial system is too low in 2030. | 15 | Reduce |
| RSK-SCH-02 | Unforeseen setbacks in certification and testing, due to invalid assumptions. | 16 | Reduce |
| | Production risks | | |
| RSK-PRD-01 | The TRL of the production process for synthetic kerosene is too low in 2030. | 5 | Accept |
| | Operational risks | | |
| RSK-OPS-01 | The amount of fuel available at the arrival airport is not sufficient for the return leg. | 5 | Accept |
| RSK-OPS-02 | Unexpected weather change while en route at a point where a return to departure airport is possible. | 4 | Accept |
| RSK-OPS-03 | Unexpected weather change while en route at a point where a return to departure airport is not possible. | 5 | Accept |
| RSK-OPS-04 | Aircraft heating equipment is not available when needed at Amundsen-Scott. | 10 | Transfer |
| RSK-OPS-05 | Insufficient de-icing performed on ground. | 10 | Transfer |
| RSK-OPS-06 | The aircraft is damaged and subsequently stuck at a remote airport. | 10 | Reduce |
| RSK-OPS-07 | An airfield used by the aircraft does not agree with the usage of synthetic kerosene. | 10 | Reduce |

### 8.1.3. Risk Mitigation

Four different strategies to mitigate the risks were considered [92]:

- Remove: The design will be changed such that the risk will be eliminated.
- Reduce: The impact and/or likelihood of the event causing the risk will be decreased.
- Accept: The risk will be accepted and monitored.
- Transfer: The risk will be shared or transferred to a third party.

The strategy that was chosen for each of the risks can be found in the column ”Strategy” in Table 8.1. For all the risks, the strategies are elaborated on below.

**RSK-CER-01** – *Reduce*: By staying in contact with the certification authorities the probability is reduced. This will ensure that the certification is updated and possibly also give insight into the requirements stemming from this certification. This results in the design needing to be altered less or not at all to be certifiable.

**RSK-FIN-01** – *Reduce*: The probability of this risk can be reduced, by making sure the market analysis is done correctly and realistically. A realistic number of sales will reduce the probability of miscalculating sales. In addition, making use of effective advertisement in the target market may result in more sales.

**RSK-SCH-01** – *Reduce*: The technology readiness levels of the technologies used will also be evaluated and if the TRL of a certain technology is too low, this technology will not be used and an alternative must be found. A TRL is too low when the technology is in the research phase (TRL of 1-3), which will be evaluated when a novel technology is first implemented.

**RSK-SCH-02** – *Reduce*: By making sure all assumptions made and all models used during the design process are verified and validated (as described in Chapter 11) the probability of unforeseen setbacks can be reduced.

**RSK-PRD-01** – *Accept*: This risk was accepted as the probability is low. This is because the TRL of each separate process in the production process is 9, which is the highest possible level. However, the TRL of the process as a whole is 7. This TRL is the lowest level in the deployment phase, which corresponds to the technology being demonstrated in the operational environment.

**RSK-OPS-01, RSK-OPS-02 & RSK-OPS-03** – *Accept*: As for these risks the probability was deemed rare and thus the corresponding risk score is low it was deemed that these risks were acceptable.

**RSK-OPS-04** – *Transfer*: The probability will be reduced, by partially transferring the responsibility to the Amundsen-Scott research station, as the heating equipment is already present at the base.

**RSK-OPS-05** – *Transfer*: Similarly to **RSK-OPS-04**, the risk will be reduced by reducing the probability, as the equipment used for deicing (as described in Section 5.2) is already present at Amundsen-Scott.

**RSK-OPS-06** – *Reduce*: This risk will be reduced by carrying some spare parts for critical system. From this mitigation strategy thus also stems a requirement, which is "**REQ-RSK-01**: *The system shall be able to carry 77 kg of spares in addition to the payload.*" This will not be a problem for the medevac mission as the payload required for this mission is less than the possible payload as discussed in Section 6.3. Meaning there is enough additional payload weight available for a fly-away kit. However, for the critical payload requirement (19 passengers for 150 NM), the fly-away kit might need to be reduced in weight, as the weight can be as much as 77 kg. This is because the aircraft can be operated by a single pilot on these short ranges, thus removing one pilot from the operating empty weight, making it possible to take the weight of this pilot (77 kg according to regulations [33]) in spare parts.

**RSK-OPS-07** – *Reduce*: The probability of this risk will be reduced, by making sure the airports are aware that no changes to the current infrastructure are required as described in Section 5.1 and the benefits of synthetic kerosene, such as the carbon-neutral nature of the fuel.

The risk maps showing the likelihood and consequence of the event corresponding to the risks are shown before and after mitigation in Table 8.2 and Table 8.3 respectively.

**Table 8.2:** *Risk map based on probability and consequence.*

| | | Probability | | | | |
|---|---|---|---|---|---|---|
| | | **Rare** | **Unlikely** | **Moderate** | **Likely** | **Almost Certain** |
| | | 1 | 2 | 3 | 4 | 5 |
| Consequence | **Catastrophic** 5 | RP-01<br>RO-01<br>RO-03 | RO-04<br>RO-05<br>RO-06<br>RO-07 | RC-01<br>RS-01 | | |
| | **Severe** 4 | RO-02 | | | RF-01<br>RS-02 | |
| | **Moderate** 3 | | | | | |
| | **Minor** 2 | | | | | |
| | **Negligible** 1 | | | | | |

**Table 8.3:** *Risk map based on probability and consequence after mitigation.*

| | | Probability | | | | |
|---|---|---|---|---|---|---|
| | | **Rare** | **Unlikely** | **Moderate** | **Likely** | **Almost Certain** |
| | | 1 | 2 | 3 | 4 | 5 |
| Consequence | **Catastrophic** 5 | RP-01<br>RO-01<br>RO-03<br>RO-04<br>RO-05<br>RO-06 | RC-01<br>RS-01 | | | |
| | **Severe** 4 | RO-02 | RS-02<br>RO-07 | RF-01 | | |
| | **Moderate** 3 | | | | | |
| | **Minor** 2 | | | | | |
| | **Negligible** 1 | | | | | |

## 8.2. RAMS

As the aircraft has to be operational in severe weather conditions, the design is pushing the limits of current technology and flight performance. Therefore, it was important to look into the design and determine the most critical systems, the redundancies within those systems, and the reliability and expected maintenance needs of the aircraft. This was done through a reliability, availability, maintainability and safety (RAMS) analysis, which is covered in this section. First, the reliability of the aircraft is assessed in Subsection 8.2.1. This is followed by the availability, presented in Subsection 8.2.2. Subsequently, the expected and unexpected maintenance needs of the aircraft are covered in Subsection 8.2.3. Finally, by combining the aforementioned risks, and the preliminary results from the RAMS analysis, the safety of the aircraft was assessed. The safety analysis is presented in Subsection 8.2.4.

### 8.2.1. Reliability

As the aircraft has to be operational under extreme weather conditions, the most critical systems stemmed from flight operations. The most critical systems that could fail were determined to be the combustion engines, the anti-icing system, the SVS system, the landing gear, the electrical buses, fuel system, and the hydraulics. These subsystems were selected as failure would very likely mean that the aircraft could not safely fulfill its mission.

The reliability of each subsystem is treated below. The reliability was scored on a scale of dangerous, unreliable, reliable, or safe. These scores are assigned qualitatively, as the subsystems are still far from being tested. The subsystems assigned a score of dangerous or unreliable will have to be further investigated in future stages of the design.

**Combustion Engines**

The combustion engines were assessed as they are the critical components of the propulsion system. During the design the engines were sized for one engine inoperative conditions. Therefore, the combustion engines were sized such that the subsystem still allows for nominal aircraft functionality when one half of the total propulsion system fails. However, as mentioned in Subsection 4.4.1, it is not clear from the manufacturer's manual whether the engines can operate below $-54$°C. As the operational region has temperatures down to $-76$°C, this poses problems during operations. A strategy to tackle this problem is to keep the engines running when such low temperatures are experienced, which will warm the engine. Yet, no additional measures were taken during this stage. Therefore, the uncertainty regarding operational temperature lead the engines to be labeled as dangerous. However, further analysis such as temperature testing of the engines will most likely change this classification.

**Anti-Icing**

As determined in Subsection 6.2.2, the aircraft will crash if the anti-icing system fails. Therefore, it was deemed vital that the anti-icing subsystem functions well during operation. For this reason, the anti-icing system was designed with redundancies. The redundancies within the design ensure that when the anti-icing subsystem fails, only a portion of the lifting surfaces are exposed to ice and thereby the aircraft remains operational. Because of these redundancies, the anti-icing was considered reliable.

**Synthetic Vision System**

To be able to land in the harsh weather conditions of Antarctica, a synthetic vision system (SVS) was implemented in the cockpit. Malfunctioning of the SVS could lead to an unsafe approach or take-off, where there is little room for error. Therefore, it was paramount to investigate this system. The SVS consists of various components like cameras, gyros and computers. As the SVS was mainly made for harsh weather conditions, it was expected to function as designed in these conditions. However, due to the complexity of the system, internal failure may occur. Again, as failure of such a system would result in inoperative aircraft, it was likely the third-party designers would have added redundancies inside the system. Therefore, the SVS system was labeled as reliable.

**Landing Gear**

As established in Section 2.3, one of the main reason for aircraft accidents on Antarctica is due to landing gear failure. Therefore, a reliability analysis of the landing gear was necessary to allow for safe landing and take-off. During the design of the landing gear, several safety factors were included to size the nose and main landing gear. Additionally, the selection of skis were such that the skis could handle higher landing loads than the loads that were calculated. Therefore, due to the inclusion of multiple safety factors and implementing full effort in preventing landing gear failure, the landing gear was scored as safe.

**Electronics**

Many subsystems on the aircraft depend on the power delivered by the combustion engines. The power is distributed via the electronics subsystem. Therefore, if the electronics subsystem fails, many subsystems become unusable. The electrical system was set up in such a way that if failure were to occur in one of the electric components, the main busses still receive power via a separate branch. Therefore, redundancy was added to the power grid. Due to the inclusion of redundancy, there is less chance of failure. Hence, the electronics subsystem was labeled as reliable.

**Fuel System**

As determined in Subsection 4.3.1, the fuel might freeze in close proximity to Amundsen-Scott. Frozen fuel would be catastrophic for the aircraft. To prevent the fuel from freezing, an anti-freeze system was implemented in the aircraft. However, no off-the-shelf device was found for this, and therefore the team had to come up with a solution themselves. Because of this, a solution was found, yet little was known about the functioning of this system. Therefore, the fuel system was considered unreliable.

**Hydraulics**
The final critical component was the hydraulics subsystem. The hydraulics were included as they allow for deployment of the landing gear and movement of the control surfaces. Thus, if the hydraulics fail, the aforementioned subsystems can not be used. The hydraulic fluid for this aircraft will freeze at $-45$°C. To operate at temperatures down to $-76$°C, the team added insulation and heating for the hydraulic fluid. However, as with the fuel system, this has not been worked out in detail yet. To take this into account, the team proposed frequent maintenance, mitigating some of the risk to failure. Combining these aspects, the hydraulic system was scored as unreliable.

### 8.2.2. Availability
Due to the weather conditions requirement defined by **REQ-STA-CUST-03**, the aircraft has to be operational 95% of the time within a time-frame of 7 days. Therefore, for the medical evacuation missions, it was expected that at least 95% of the time, the aircraft is available, provided that maintenance has already been carried out.

For the commercial flights with 19 passengers, the availability was estimated differently. First, because it was expected that the commercial flights would not be flown through the extreme Antarctic weather conditions, the expected operational time was higher than 95%, because the aircraft was over-designed with respect to conventional weather limitations. Additionally, due to the ease of passenger loading due to the rear door and various cargo holds, the mission payload loading can be done in a more rapid manner.

### 8.2.3. Maintenance
As the JAPA-12 aircraft can be used for two very different missions, namely commercial passenger transportation or medical evacuations, the maintenance schedule is dependent on the type of missions flown. Therefore, two separate maintenance schedules will be proposed due to the large difference between operational region and purpose.

General aircraft maintenance is split up in 5 categories, which indicate the 'severity' of the maintenance. These categories are[62]:

- Line maintenance: frequent, simple inspection by walk-around and checking basic components, such as fluid levels.
- Type A: Basic maintenance, done every 400-600 flight hours, general inspection by looking for, among others, corrosion and deformations.
- Type B: Extension on type A, done every 6-8 months, more thorough inspection including more in-detail checks on for example wheel alignment.
- Type C: Regarded as 'heavy maintenance', done roughly every 3000 flight hours, in-depth inspection of the majority of aircraft parts. Includes thorough inspections like the examination of primary load bearing structures.
- Type D: Maintenance round where most of the aircraft is stripped down, and components are replaced/upgraded. Happens every 6-10 years, is very expensive.

The type D maintenance was partially excluded in the maintenance strategy. This was done as the estimated costs of a type D maintenance can rise up to millions of dollars[63] for conventional aircraft. Now, as the JAPA-12 is a rather small aircraft, the costs for type D is expected to be less, but still relatively high. As the list price had to be below 7.5 million dollars it was expected that, type D maintenance was only carried out when the aircraft was worn out. Thus, when the JAPA-12 was used a lot. Therefore, the type D maintenance is excluded for the medical evacuations, as it was expected that medevac missions will not fly on a daily basis.

**Antarctic Medical Evacuation**
Due to the rough environmental conditions of Antarctica, the maintenance schedule was made more frequent. This was done due to the fact that many critical systems, as determined in Subsection 8.2.1, could fail during flight. The maintenance strategy is presented in Table 8.4. Note that the strategy was based on events rather than flight hours as it was expected that Antarctic medical evacuations do not happen on a regular basis. If one wanted to fly commercial flights as well, Table 8.5 may be used for flight hour indications.

**Commercial Flights**
The 19-passenger commercial flight maintenance schedule differs from the one for Antarctic evacuation missions. This is due to the fact that the commercial flights were expected to be in more gentle weather conditions. The proposed maintenance schedule does not differ from the general maintenance schedule used for other commercial flights. The maintenance schedule is presented in Table 8.5. Note that the type B inspection is done the second time the type

[62] Website covering various aircraft maintenance types, https://www.naa.edu/types-of-aviation-maintenance-checks/, date accessed = 12-06-2022
[63] Website covering various aircraft maintenance types, https://www.naa.edu/types-of-aviation-maintenance-checks/, date accessed = 12-06-2022

**Table 8.4:** *Proposed maintenance strategy for medical evacuation aircraft.*

| Event | Maintenance type |
|---|---|
| Before departure | Line maintenance |
| 15 hours before departure | Type A |
| After medevac mission | Type B |
| Start of Antarctic winter | Type C |

A inspection has to be carried out. Thus, the type A and B inspections alternate. This was chosen as type B is an extension on type A. Thus, when type B inspection is carried out, type A inspection is also done.

**Table 8.5:** *Proposed maintenance schedule for commercial flight aircraft.*

| Flight hours | Maintenance type |
|---|---|
| Before flight | Line maintenance |
| 400-600 | Type A |
| 2x 400-600 | Type B |
| 3000 | Type C |
| 20000 | Type D |

### 8.2.4. Safety

After the major aspects of reliability, availability and maintenance were determined, a concluding safety analysis of the aircraft was set up. From the reliability analysis, the most unreliable systems were found to be the combustion engines, fuel system, and the hydraulic system. As the fuel system and hydraulic system are dependent on the electricity generated by the combustion engines, the engines were considered the primary source of danger of the design. This was the case as it was unknown whether the engines could operate at the temperatures experienced at Amundsen-Scott. Therefore, to determine the feasibility of the engines or develop more heating devices, the engines have to be thoroughly assessed in the future. Additionally, due to the complexity of the hydraulics system and the fuel system, future development should investigate the mentioned subsystems on their reliability as well.

By implementing frequent maintenance, possible environmental impacts on the aircraft could be quickly identified. Therefore, if the aircraft experienced damage, quick action could be taken. This reduced the risk of flying with unknown failure, which could be catastrophic during harsh conditions. Therefore, by implementing frequent maintenance, the risk of subsystem failure was slightly mitigated.

Concluding, the current design of the aircraft was considered safe due to its strict maintenance strategy. However, to be proven airworthy, the combustion engines, fuel system, and hydraulics have to be assessed and further developed in future stages to ensure proper function at temperatures as low as $-76°$C. This will make the subsystems more reliable, and thereby the entire system more safe.

# 9 Financial Analysis

Now that the general aircraft design and performance was known, a more extensive financial analysis was executed. The analysis was mainly executed as it was desired for the customer to have a profitable aircraft. The analysis is covered in this chapter. First, the option of having a family of aircraft was looked into in Section 9.1. Next, the different markets of interest were determined and the expected market size was established in Section 9.2. Finally, the expected market share, economic strategy and break-even point is established in Section 9.3.

## 9.1. Family of Aircraft

As the desired aircraft by the customer was a rather mission specific design, due to medical evacuation in rough environmental conditions, the aircraft was not optimized for other mission types. To make the aircraft more attractive to potential customers, the team established future recommendations to create a family of aircraft. The family of aircraft is generally desired as this reduces the development costs of an aircraft type, mitigates high financial risks, and allows for different mission profile optimization, desired for customers [93]. The main advantage of the JAPA-12 is that it is operational in severe Antarctic weather conditions, which is generally nice. However, it does become more heavy and less efficient at regions where less extreme weather is present. Which makes it less attractive for these markets. The most obvious solution is to give the customer the choice whether to implement the SVS system or not. Due to its relative high system cost, and its advantages solely based on extreme weather conditions, it might be desired to exclude the SVS system from the design.

The first proposal is to limit the aircraft to non-snow runways. This immediately removes the skis from the aircraft, which also allows for removal of the fairings from the fuselage. Additionally, because of the avoidance of snow landing areas, one can also look in to the reduction of isolation material, which drastically reduces fuselage weight. By changing the design with these two aspects, the drag reduces, making the aircraft more efficient. This would be an even more suitable solution for flights to remote communities than the current JAPA-12 design.

The aircraft can be suited with less powerful combustion engines. Due to the strict STOL requirements of the design, very powerful combustion engines were included. Yet, for cruising conditions, the engines are very over-designed. If less powerful engines are accepted, and thereby less strict STOL requirements are set, the aircraft will become lighter and less expensive. Thereby, the aircraft would be more efficient due to the decrease in weight, and become less expensive to the customer. This adaptation can be desirable for e.g. search and rescue missions by the coast guard, as they can take-off from more conventional runways, while the aircraft still has excellent weather condition resistance.

The final proposed adaptation is by changing the design such that it is better operational at higher temperatures. The current design was mainly developed by keeping in mind lower temperatures, where smaller wings were required. Yet, when temperatures increase, more lift needs to be generated, and thereby the wings are expected to increase in size. The weight increase by the wing can be partially tackled by excluding skis, and reducing insulation and heating within the aircraft. By doing this, the aircraft can be used for medical missions in for example Africa or the Middle-East, where higher temperatures are present. This further extends possible markets of the JAPA-12.

## 9.2. Market Analysis

This section presents the market analysis performed. First, a SWOT analysis for the JAPA-12 was made which is presented in Subsection 9.2.1. After this, the different markets were determined, which is covered in Subsection 9.2.2. Finally, the competitors were identified together with their capabilities and the size of the market which JAPA-12 can serve was estimated, which is done in Subsection 9.2.3. The market analysis is adapted from the one performed in the baseline phase [6].

### 9.2.1. SWOT Analysis

The SWOT analysis aims at presenting the strengths, weaknesses, opportunities and threats of the design. This analysis focuses on comparing the JAPA-12 to other aircraft's, which will be discussed in the next subsections, that serve a similar market. With these pros and cons, a better market size estimation can be made. The analysis can be seen in Table 9.1.

**Table 9.1:** *SWOT for market analysis.*

| | Helpful | Harmful |
|---|---|---|
| **Internal** | **Strengths**<br>- CO2 neutral<br>- Operational in rough weather<br>- Rapid target entry<br>- Sustainable<br>- STOL | **Weaknesses**<br>- Maintenance |
| **External** | **Opportunities**<br>- Outdated alternatives<br>- Applicable to multiple sectors<br>- Growing sustainability concerns | **Threats**<br>- Multiple developers on sustainability<br>- Existing solutions<br>- Novel propulsion system<br>- Availability of proposed fuel |

Regarding the strengths and opportunities, the JAPA-12 has a propulsion system with net-zero carbon dioxide emissions in the operational phase and is sustainable, characteristics that are of interest to the market as sustainability concerns are growing[64]. This is an opportunity for the JAPA-12 that is associated with a threat since other companies are also developing aircraft that are sustainable. In addition, it can operate in rough weather conditions as it is designed to undergo the antarctic winter and it has a rapid target entry which is desirable for medical evacuations. Furthermore, it is applicable to multiple sectors with outdated alternatives making the design attractive to markets that are growing and investing in new aircraft.

Concerning the weaknesses and threats, the JAPA-12 is a complex aircraft due to its propulsion system and cabling so maintenance cost are expected to be higher compared to other aircraft because of the number of motors for example or propellers itself. Besides, different solutions already exist that serve the market of interest and, as mentioned before, multiple companies are developing sustainable aircraft. These combined will reduce the size of the market the aircraft can serve. Next, the propulsion system consists of a novel concept, namely distributed propulsion, which adds risks to the design process, posing a threat to the aircraft. Lastly, the availability of the fuel used might be limiting since it is a novel process of making fuel. The propulsion system can use standard kerosene but this would have an impact of sustainability. In that case the only action that would need to be taken would be cleaning thoroughly the fuel system as mixing different types of kerosene might have a negative impact on the system.

### 9.2.2. Market Determination

The different markets that might be interested in the JAPA-12 are listed below. These markets were chosen as they are expected to grow in the coming years. For the air ambulance market, this is excepted to grow from $4.89 billion in 2021 to $10.30 billion in 2029[65]. For the aircraft evacuation market, for which the market size exceeded $1 Billion in 2020, it is anticipated a growth from 2021 to 2027 that will reach a value of $1.53 billion[66]. For remote communities, countries are planning on investing money in this sector, such as Canada which wants to invest $250 million to support air access[67].

**Remote Communities**: A large number of remote communities throughout the world rely on aircraft for the supply of goods. Two examples of countries with a large number of remote communities are Australia and Canada. In Australia, 270 remote communities depend on weekly air transport services assured by the Remote Air Services Subsidy (RASS) scheme for the delivery of goods[68]. In Canada, there are 182 remote communities and the vast majority are isolated and therefore only accessible by air most or the entirety of the year.

**Air Ambulance**: The customer requires an aircraft which is able to perform a medical evacuation so the interior has the same configuration as an air ambulance. Serving this market is easy especially with the family of aircraft since missions can be performed under a variety of environmental conditions. There exist different air ambulance services which form

[64] Sustainability in aviation, https://cen.acs.org/environment/sustainability/Airlines-want-make-flight-sustainable/99/i32, date accessed = 12-06-2022

[65] Air ambulance market predicted growth , https://www.fortunebusinessinsights.com/air-ambulance-services-market-102577, date accessed = 13-06-2022

[66] Aircraft evacuation market predicted growth, https://www.gminsights.com/industry-analysis/aircraft-evacuation-market, date accessed = 13-06-2022

[67] Air access to remote communities in Canada, https://www.canada.ca/en/transport-canada/news/2020/08/new-measures-to-support-essential-air-access-to-remote-communities.html, date accessed = 12-06-2022

[68] Air services in Australia, https://www.infrastructure.gov.au/infrastructure-transport-vehicles/aviation/regional-remote-aviation/remote-air-services-subsidy, date accessed =12-06-2022

potential clients such as the South African Red Cross Air Mercy Service (AMS), Advanced Air Ambulance, the European Air Ambulance (EAA), among others.

**Victims of Natural Disasters:** In case of a natural disaster aircraft can play an important role especially in situations where the main infrastructures and access roads are destroyed or obstructed. The design can either have a medical evacuation configuration important in case of heavily injured victims or a 19 seater configuration which could both be used to evacuate victims to a safer place. Besides this, the different landing gear configurations and environmental resistance bring an additional advantage to the design and to the team.

### 9.2.3. Market Size Estimation

In order to estimate the size of the market the design can serve, first the competitors must be analysed. When looking at the different companies that serve the chosen markets, it can be seen that their fleet is composed by aircraft produced by five main manufacturers. These are Textron Aviation which incorporates Beechcraft and Cessna, Bombardier, de Havilland Canada, Pilatus Aircraft and Piper Aircraft. These manufacturers were all founded before 1943 and had time to make a name for themselves. The JAPA-12 still has to be presented to the market and the companies still need to be convinced that the aircraft being designed has advantages compared to the already operating aircraft. Subsection 9.2.1 presented the advantaged & disadvantages and opportunities & threats of the design compared to the previously mentioned competitors. Table 9.2 shows a list of aircraft models that are commonly used in the chosen markets together with the year of the first flight. From this list it can be seen that the different models used were developed longer than 27 years ago. This represents a great opportunity for the JAPA-12 since this is a new model and, if a company wants a new aircraft, then it is more likely they will invest in a relatively new aircraft.

**Table 9.2:** *List of aircraft models that represent competition for the JAPA-12.*

| Manufacturer | Aircraft | First flight |
|---|---|---|
| Textron Aviation | Cessna 208 caravan | 1982 |
| Textron Aviation | Cessna 210 | 1957 |
| Textron Aviation | Beechcraft king air | 1972 |
| Textron Aviation | Beechcraft | 1961 |
| Bombardier | Bombardier learjet 45 | 1995 |
| de Havilland Canada | DHC-8 | 1983 |
| de Havilland Canada | DHC-6 Twin Otter | 1965 |
| Pilatus Aircraft | Pilatus PC-12 | 1991 |
| Piper Aircraft | Piper PA-42 Cheyenne | 1979 |

The potential costumers are presented in Table 9.3 as well as their fleet size and the number of aircraft expected to be sold to them. The fleet size of each company presented below only includes the number of fixed-wing aircraft. This number was found by assuming that for every nine aircraft the company has, the team can sell them one. This was because it was assumed that the company would have at least one aircraft of each main competitor, and three other aircraft; either three from the main competitors again or from other manufacturers, before buying the JAPA-12 or a variant of the JAPA-12. The number of aircraft expected to sell was rounded to the nearest integer.

**Table 9.3:** *Market size estimation.*

| Company | Mission type | Fleet size | Number of aircraft expected to be sold |
|---|---|---|---|
| Aviair[69] | Remote communities (Australia) | 31 | 3 |
| Air Kimberley | Remote communities (Australia) | 9 | 1 |
| Skytrans[70] | Remote communities (Australia) | 9 | 1 |
| Katherine Aviation | Remote communities (Australia) | 24 | 3 |
| Chartair | Remote communities (Australia) | 45 | 5 |
| Air Iniut[71] | Remote communities (Canada) | 31 | 3 |

[69]Number aircraft Aviair, Air Kimberley, Katherine Aviation and Chartair, https://www.casa.gov.au/search-centre/aircraft-register, date accessed = 12-06-2022

[70]Number aircraft Skytrans, https://www.skytrans.com.au/flights/fleet/, date accessed = 13-06-2022

[71]Number aircraft Air Inuit, https://wwwapps.tc.gc.ca/Saf-Sec-Sur/2/CCARCS-RIACC/RchSimpRes.aspx?cn=%7C%7C&mn=%7C%7C&sn=%7C%7C&on=AIR+INUIT%7C&m=%7C%7C&print=y, date accessed = 13-06-2022

Continuation of Table 9.3

| Company | Mission type | Fleet size | Number of aircraft expected to be sold |
|---|---|---|---|
| Myflug Air[72] | Remote communities (Iceland) | 6 | 1 |
| Air Greenland[73] | Remote communities (Greenland) | 9 | 1 |
| MAF[74] | Remote communities (World) | 120 | 13 |
| AMS[75] | Air ambulance | 7 | 1 |
| Flying Doctors Nigeria[76] | Air ambulance | 20 | 2 |
| Ambulancevlucht Centrale[77] | Air ambulance | 28 | 3 |
| European Air Ambulance[78] | Air ambulance | 5 | 1 |
| Royal Flying Doctor Service[79] | Air ambulance | 79 | 9 |
| Flying Doctors of Malaysia[80] | Air ambulance | 18 | 2 |
| Flying Doctors Asia[81] | Air ambulance | 27 | 3 |
| Babcock Scandinavian Air Ambulance[82] | Air ambulance | 38 | 4 |
| Acadian Air Med[83] | Air ambulance | 5 | 1 |
| Air Ambulance 1[84] | Air ambulance | 100 | 11 |
| U.S. Coast Guard[85] | Rescue mission | 58 | 6 |
| Canadian Coast Guard[86] | Rescue mission | 8 | 1 |
| Surveillance Australia[87] | Rescue mission | 10 | 1 |
| Argentine Naval Prefecture[88] | Rescue mission | 8 | 1 |
| Her Majesty's Coast Guard[89] | Rescue mission | 7 | 1 |
| Japan Coast Guard[90] | Rescue mission | 27 | 3 |
| India Coast Guard[91] | Rescue mission | 36 | 4 |
| **Total** | | 765 | **85** |

In addition to looking at companies that could be interested in the design, an analysis of the expected growth in air ambulance service for Germany, U.K., France, Italy and Spain was looked into since little data was available for these countries. The air ambulance is expected to grow from $4.89 billion in 2021 to $10.30 billion in 2028. In 2021 75.5%

[72] Number aircraft Myflug Air, https://www.myflug.is/en/charter-flights, date accessed = 13-06-2022
[73] Number aircraft Air Greenland, https://www.airgreenland.com/charter/fleet, date accessed = 13-06-2022
[74] Number aircraft MAF, https://www.mafc.org/aircraft, date accessed = 13-06-2022
[75] Number aircraft AMS, https://ams.org.za/our-fleet/, date accessed = 13-06-2022
[76] Number aircraft Flying Doctors Nigeria, https://www.flyingdoctorsnigeria.com/facts-figures/, date accessed = 13-06-2022
[77] Number aircraft Ambulancevlucht Centrale, https://www.ambulancevlucht-centrale.nl/vliegtuigen.html, date accessed = 13-06-2022
[78] Number aircraft European Air Ambulance, https://www.air-ambulance.com/fleet, date accessed = 13-06-2022
[79] Number aircraft Royal Flying Doctor Service, https://www.flyingdoctor.org.au/about-the-rfds/our-fleet/, date accessed = 13-06-2022
[80] Number aircraft Flying Doctors of Malaysia, https://en.wikipedia.org/wiki/Flying_Doctors_of_Malaysia, date accessed = 13-06-2022
[81] Number aircraft Flying Doctors Asia, http://www.flyingdoctorsasia.com/airambulance.html, date accessed = 13-06-2022
[82] Number aircraft Babcock Scandinavian Air Ambulance, http://babcocknordics.com/, date accessed = 13-06-2022
[83] Number aircraft Acadian Air Med, https://acadianairmed.com/aircraft/, date accessed = 13-06-2022
[84] Number aircraft Air Ambulance 1, https://www.airambulance1.com/aircraft-fleet/, date accessed = 13-06-2022
[85] Number aircraft U.S. Coast Guard, https://en.wikipedia.org/wiki/List_of_equipment_of_the_United_States_Coast_Guard, date accessed = 13-06-2022
[86] Number aircraft Canadia Coast Guard, https://en.wikipedia.org/wiki/List_of_equipment_of_the_Canadian_Coast_Guard#Aircraft, date accessed = 13-06-2022
[87] Number aircraft Surveillance Australia, SurveillanceAustralia, date accessed = 13-06-2022
[88] Number aircraft Argentine Naval Prefecture, https://en.wikipedia.org/wiki/Argentine_Naval_Prefecture#Aircraft, date accessed = 13-06-2022
[89] Number aircraft Her Majesty's Coast Guard, https://en.wikipedia.org/wiki/Her_Majesty%27s_Coastguard, date accessed = 13-06-2022
[90] Number aircraft Japan Coast Guard, https://en.wikipedia.org/wiki/List_of_Japan_Coast_Guard_vessels_and_aircraft#Aircraft_inventory, date accessed = 13-06-2022
[91] Number aircraft Indian Coast Guard, https://en.wikipedia.org/wiki/Indian_Coast_Guard#Current_aircraft, date accessed = 13-06-2022

of the market consisted of rotary-wing aircraft and this share was predicted to decrease to approximately 66%[92]. It was assumed that the growth in this market would be linear for the excepted period and that the JAPA-12 could represent 14% of this market due to its advantages presented in the SWOT analysis compared to the already available models. Taking this into account and the list price of the aircraft, it was found that 35 JAPA-12 could be sold to this market.

From this market analysis, a minimum of 120 aircraft are expected to be sold. It is expected that the JAPA-12 can be sold to more companies as only a limited number of countries and companies were looked into since finding data on fleet size is not always possible. Besides, when looking at three different aircraft, the number of airframes sold was higher than 120. For the DHC-6 Twin Otter 400 up to and including 2020 146 airframes were sold and for the first three series 844 were produced, including prototypes[93]. For the Pilatus PC-12 by January 2019, 1640 aircraft were produced[94]. For the Cessna 337 Skymaster, together with the previous version, Cessna 336 Skymaster, a total of 1978 models had been built by January 1979[95].

## 9.3. Finances

A financial analysis of all phases regarding the design and manufacturing of the aircraft was performed. This analysis was performed in order to determine the output required for a positive return on investment. The total design costs were first determined in Subsection 9.3.1. Accordingly, the acquisition costs were estimated in Subsection 9.3.2. Finally the return on investment was determined, and is presented in Subsection 9.3.3.

### 9.3.1. Design Costs

The number of aircraft before a positive Return On Investment (ROI) is achieved is largely related to the design cost, as these costs are distributed over the total output. To estimate both the design costs and acquisition costs, methods from Roskam have been used [5]. Roskam uses historical data for design, manufacturing and tooling hourly rates. In order to relate these parameters to current times, a correction based on inflation was applied. The total inflation factor compared to reference year 1990 was found to equal 2.1 as a result of multiplication of inflation rates for the US, based on retrieved data[96]. This value was compared to data from various other online databases and was found to be similar and therefore validated. The inflation factor is mainly applied to determine salaries in the current market. On paper, this meant that for the cost estimation, a design dollar rate per hour of $55 in 1990 equals $115.5 in 2022. However, salary does historically not increase as much as inflation thus the total aircraft costs were computed as absolute maximum value[97].

The main inputs for estimating design costs were the aircraft cruise speed, inflation correction factor, difficulty factors depending on the cost category and the aeronautical manufacturers planning report weight. This weight was determined by subtracting weights of all purchased items from the aircraft empty weight. Purchased items were tyres, fuel tank, engines, starters, avionics and others based on class II weight estimation and data from manufacturers. The design phase was split up into four cost contributions, of which the first one was airframe engineering and designing. A breakdown of activities performed is itemised below.

- Planning
- Preliminary design and studies
- Establish testing methods and create models
- Create drawings and integrate design changes
- Further detailed development
- Analysis

These activities create costs that need to be distributed over the number of aircraft sold. It was determined that in case the aircraft were to be fully designed, experienced CAD engineers would be involved which thereby limit the required man hours. However, as the design was deemed to feature significant use of advanced technology a factor was applied

[92] Europena Air ambulance market predicted growth, https://www.grandviewresearch.com/industry-analysis/europe-air-ambulance-services-market-report#:~:text=The%20Europe%20air%20ambulance%20services%20market%20is%20expected%20to%20grow,USD%209.8%20billion%20by%202028, date accessed = 13-06-2022

[93] Development and production DHC-6 Twin Otter 400, https://customer.janes.com/Janes/Display/JAWAA417-JAWA, date accessed = 14-06-2022

[94] Development and production Pilatus PC-12, https://customer.janes.com/Janes/Display/JAWA0999-JAWA, date accessed = 14-06-2022

[95] Development and production Cessna 337 Skymaster, https://customer.janes.com/Janes/Display/JAU_1493-JAU_, date accessed = 14-06-2022

[96] Website for historical inflation US, https://www.usinflationcalculator.com/inflation/historical-inflation-rates/, date accessed = 14-06-2022

[97] Inflation comparison to salary increase, https://www.forbes.com/sites/johnbremen/2022/04/07/why-salary-increases-do-not-keep-pace-with-inflation/?sh=55ddbfae7533, date accessed = 14-04-2022

which increased the required man hours. Overall, it was estimated that about 183,000 man hours are required to complete the design process. For testing in the early phase, manufacturing and tooling are the main contributors to total costs. As the first aircraft are manufactured without the benefits of the learning curve, the number of man hours is estimated to be large. The total costs of the research, development, testing and evaluation phase is included in Table 9.4 below in euros with a current conversion rate of 0.95 (10-06-2022) from dollars.

**Table 9.4:** *Aircraft development cost breakdown.*

| Category | Costs [M€] |
|---|---|
| Engineering | 18.2 |
| Development | 1.7 |
| Test preparation | 98.8 |
| Test operations | 0.1 |
| Total costs | 118.7 |

### 9.3.2. Acquisition Costs

The aircraft acquisition costs are dependent on the number of aircraft designed. However, the costs per aircraft manufactured will slightly decrease as result of the learning curve. The learning curve occurs as a result of the manufacturing employees increased technical knowledge regarding the manufacturing of the aircraft. Doing the same task over and over again increases the effectiveness and decreases the time spent on performed tasks. A reduction in man hours per aircraft directly influences the cost for a specific aircraft number in the series. Manufacturing of all aircraft was assumed to not be outsourced, therefore no additional costs are introduced to the manufacturer profit.

Initially, an estimation of man hours was required in the manufacturing phase which was determined with the same parameters as the design phase. After that, costs for various subsystems and wages were determined. The cost of engines was obtained from the manufacturers of the combustion engine and electric motors. However, the cost of propellers had to be estimated by Roskam and corrected for inflation. Finally, in addition to various wages, the avionics costs had to be estimated. It was found that for the family of aircraft the avionics costs could be drastically reduced with respect to the Amundsen-Scott rescue mission. In Section 5.5 it was determined that the additional costs next to standard avionics for operation in the harsh Antarctic weather condition are k€500. As Roskam determined the cost of standard avionics to be about 10% of aircraft cost without avionics which also equals about k€500, this value was used to obtain more accurate estimation of total costs. The total cost breakdown in the manufacturing phase is included below in Table 9.5 for a minimum of 111 aircraft produced, as it was calculated that at this number the 15% profit margin was achieved for a M€7.5 list price.

**Table 9.5:** *Aircraft manufacturing cost breakdown.*

| Category | Costs [M€] |
|---|---|
| Engineering | 16.9 |
| Production | 549.3 |
| Test operations | 1.2 |
| Total costs | 567.4 |

### 9.3.3. Return on Investment

As stated in the previous section, the minimum number of aircraft produced equals 111. This includes 3 aircraft which are not sold as they are used for static tests and flight tests. It was found that 108 is the number of aircraft to be sold to achieve a list price below M€7.5 as required by the customer with 15% profit margin as established in [6]. In that case, the total cost per aircraft of M€6.35 is such that a ROI of 18% is achieved. It is expected that this number increases as the family of aircraft will costs much less than the mission specific JAPA-12 for Amundsen-Scott. This was already explained with respect to the avionics, however the team cost for engines, landing gear and cabin environmental control will also decrease as these subsystems will be less complex as covered in Section 9.1. If a larger number of aircraft were to be sold, as is likely to happen as established in the market analysis, both the profit margin and ROI will increase. This is expected as a result of the impact the avionics have on the design. By not including additional avionics which cost an additional k€500, about M€54.0 are already saved.

# 10 Sustainability Assessment

Due to climate change, it is generally desired to design a system which limits its impact on the environment. To determine how sustainable the design of the JAPA-12 is, a sustainability analysis was carried out, which is covered in this chapter. The sustainability analysis begins with a life cycle analysis in Section 10.1. After that, the noise characteristics of the aircraft are determined, which is done in Section 10.2. Finally, the sustainability assessment is carried out in Section 10.3, where the sustainability compliance is concluded.

## 10.1. Life Cycle Analysis

As introduced in Subsection 2.4.3 a life cycle analysis (LCA) was performed. To standardise the output of the LCA and make meaningful comparisons with other aircraft, the input was set as the passenger-kilometer (PKM). This unit refers to the actual number of transported passengers and their kilometers traveled [12]. For the case of the ArtEvac, the number of passengers was taken to be 19 and the range was taken to be 550 km as followed from Section 6.3. The output of the analysis was the environmental impact of all life cycle phases of the aircraft. The production, operation, and end-of-life phases are discussed in detail in this section. Discussion of the design and development life cycle phases has been left out as the results are inconsequential of the design choices made at this stage.

### 10.1.1. Production

Firstly, the environmental impact of the production process was analysed. The production phase consists of three driving factors, the use of facilities, the materials used, and the fuel production process. The effect of the facilities used is based on the number of aircraft that are to be produced. To analyse the effect of the materials used the composition of the aircraft was required. Based on the material selection performed in Section 7.2, the percentage by mass of each material of the OEW was found. The mass of the materials used and the percentage that they make up the OEW is shown in Table 10.1. The emissions per aircraft produced are based on the analysis performed by Böckmann & Schmitt [94]. Their analysis assesses the impact of the raw material extraction, resource consumption within manufacturing and assembly and a transport scenario of main components. The ecological impacts are derived from public databases compiled by the European Commission [95]. What is apparent from the emissions is that fully sustainable production is far from being achieved.

**Table 10.1:** *Percentage mass of materials and recyclability.*

| Material | Mass | % Recyclable |
|---|---|---|
| Aluminium | 2026.97 | 98[98] |
| Titanium | 341.86 | 100[99] |
| Steel | 987.02 | 100[100] |
| Composites | 318.97 | 0 |
| Misc | 1184.39 | 90 |

Different methods exist to produce synthetic kerosene, however all production methods require a source of carbon and hydrogen. The environmental impact depends on how the carbon and hydrogen is yielded. Viable carbon sources include biomass, industrial or power plant emissions, or direct air capture. **[REQ-STA-CUST-05.2]** stipulates that the propulsion system shall have net zero carbon dioxide emissions in the operational phase. Through the investigation conducted by the Ministerie van Infrastructuur en Waterstaat the best method is carbon capture from steel mills [96]. The required hydrogen is produced through electrolysis. If renewable energy is used to power this process there are no harmful emissions.

Carbon monoxide and dioxide are captured from the steel mill. Through Fisher-Tropsch synthesis, carbon monoxide is converted into jet fuel. Throughout this process carbon dioxide is sequestered. An analysis was done to quantify greenhouse gas emissions over the entire life cycle of the fuel. Compared to releasing the outputs of the steel mill

[98] Recycling of aluminium, https://www.alumeco.com/knowledge-technique/general/recycling-of-aluminium, date accessed = 13-06-2022

[99] Sustainability of titanium, https://titek.co.uk/how-can-titanium-help-your-business-to-be-more-environmentally-friendly-in-2020/, date accessed = 13-06-2022

[100] Sustainability of steel, https://www.steel.org/sustainability/, date accessed = 13-06-2022

straight to the atmosphere, conversion into jet fuel saves -5.992 kg $CO_2$ per kg of fuel [96]. Note, that this includes the green house gases that are emitted when the fuel is burned. Therefore **[REQ-STA-CUST-05.2]** is satisfied.

As of 2021 the TRL of the steel mill method is 7. However, all the components of the steel mill capture process have a TRL of 9 and are proven technology. Due to low demand for sustainable fuels no commercial size facilities have been set up. As the process is not commercial, the overall system TRL is low [96]. The aircraft shall enter service in 2030, therefore, this technology readiness level was deemed acceptable. This risk is further discussed in Section 8.1.

### 10.1.2. Operation

This sub-section analyses the emissions of the aircraft during operations. Based on statistical data from the European reference Life Cycle Database, the turbo-electric engines are assumed to have the emissions factors presented in Table 10.2. For each phase of the mission profile the emission factors differ, this is due to the different settings of the engines and atmospheric conditions. A few observations were made from the fuel fractions. Specifically the observation that the more power intensive the mission phase the greater the emission of $NO_x$ gas. On the contrary, the observation was made that the less power intensive the mission phase the greater the output of CO. Based on the fuel required for the medevac mission the total mass of the harmful gasses emitted during the medevac mission was found.

**Table 10.2:** *Emission factors of the turbo-electric motors.*

| **Unit** | **[kg/kg fuel]** | | | **[g/kg fuel]** | | | |
|---|---|---|---|---|---|---|---|
| Gas emitted | $CO_2$ | $O_2$ | $H_2O$ | $NO_x$ | HC | $SO_2$ | CO |
| Cruise | 3.15 | 3.40 | 1.23 | 16.50 | 0.07 | 0.84 | 1.72 |
| Approach | 3.15 | 3.40 | 1.23 | 8.94 | 0.45 | 0.84 | 2.80 |
| Idle | 3.15 | 3.40 | 1.23 | 4.29 | 1.53 | 0.84 | 18.50 |
| Take-off | 3.15 | 3.40 | 1.23 | 24.79 | 0.23 | 0.84 | 1.10 |
| Climb-out | 3.15 | 3.40 | 1.23 | 19.98 | 0.23 | 0.84 | 1.10 |

The airport operations were also considered. However, for this the methodology of the LCA had to be adjusted. The airport statistical data was altered to suit the market of the JAPA-12. The data from the Red Deer Regional airport situated in Canada was used[101]. The primary changes were in the emissions due to the number of passengers per year and the vehicles used.

### 10.1.3. End-of-life

Finally, the environmental impact of the end-of-life of the aircraft was analysed. The end-of-life analysis depends on the materials used and the recyclability of the used materials. Based on the material distribution given in Section 7.2, the total mass of each material was derived. The mass of each material and the percentage of it that may be recycled is compiled in Table 10.1. The composites group consists of CFRP and GFRP. The composites were conservatively estimated to not be recyclable. Mechanical grinding and high voltage fragmentation were considered for recycling, however the TRL and market appeal were considered infeasible [97]. In addition, for the miscellaneous materials a percentage recyclability of 90% was set. The majority of the miscellaneous materials stem from non-major sub-systems of the aircraft. These systems include the interior furnishing, avionics, and electronics. Most of these systems may be re-used or are recyclable, therefore justifying the percentage recyclability set. The total mass of the aircraft that is recyclable is 4381.26 kg. Therefore the percentage of the entire aircraft that is recyclable is 90.2%, and **[REQ-STA-CUST-05.1]** is met.

### 10.1.4. Interpretation

The result of the LCA was an overview of the environmental impact the aircraft inputs, output, and life cycle phases have on the environment. From the aircraft parameters input, values for the resources depleted and emissions are given in mass per passenger kilometer. With these values it is difficult to quantify the environmental impact. For example, the amount of $gCO_2$/PKM might be ten times as large as the $gNO_x$/PKM emitted, however $NO_x$ is 300 times as harmful per mass for the environment[102]. To make meaningful conclusions the parameters were scaled by weights that represented their environmental impact. These weights were derived from the ReCiPe model set by the RIVM and used throughout

[101] Red deer airport, https://www.flyreddeer.com, date accessed = 10-06-2022

[102] Nitrous oxide climate, https://www.cbc.ca/news/science/nitrous-oxide-climate-1.5753907, date accessed = 13-06-2022

the European Union for Life cycle assessments[103]. The scores were then standardised to highlight which inputs, outputs, and life cycle phases had the biggest environmental impact.

As is depicted in Figure 10.1 the $NO_X$ emissions are by far the belligerent factor of the JAPA-12 for the environment. A close second are the contrails formed by the aircraft. To mitigate their impact an option is to reduce the flight altitude [98]. However, the JAPA-12 already flies at a low flight altitude and decreasing it further would increase the flight time. Note that the environmental impact due to the $CO_2$ emissions left out the effects of fuel production. The reason for this is that this process has a beneficial environmental effect. Therefore the $CO_2$ environmental impact is relatively low and primarily due to the production process and cruise of the aircraft. The same applied to the $SO_2$ and particulate matter. Little may be done at this stage to circumvent their impact. The analysis of the environmental impact of the the different processes is presented in Figure 10.2. As expected cruise was found to be the most polluting process, followed by the landing and take-off cycle. All other processes were considered negligible.

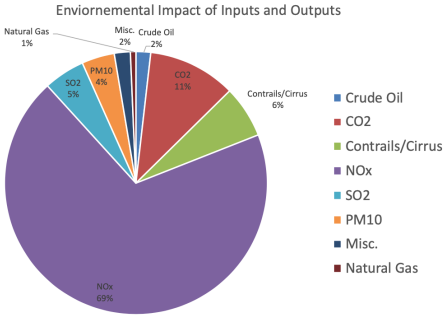


**Figure 10.1:** *Environmental impact of inputs and outputs.*

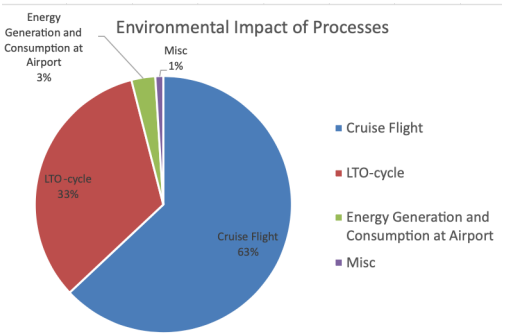


**Figure 10.2:** *Environmental impact of processes.*

To provide another perspective on the results a comparison of the emissions was done with those of the Twin Otter. The LCA software was run using the parameters of the Twin Otter provided by the manufacturer[104]. The harmful inputs and outputs are summarised in Figure 10.3. Due to the production of kerosene for the Twin Otter the performance is worse with regards to crude oil, natural gas, and carbon dioxide. The alternative method used to produce synthetic kerosene captures more carbon dioxide than is emitted throughout the entire life cycle of the JAPA-12. The JAPA-12 is heavier than the Twin Otter, as a result the fuel efficiency of the JAPA-12 is worse. Therefore, the JAPA-12 has slightly worse performance with regards to all emissions not related to the production of kerosene. This is reflected in the nitrogen oxide and carbon monoxide emissions. The nitrogen oxide emissions of the JAPA-12 are enhanced through the higher cruise altitude. Nevertheless, the savings due to mitigating the effects of kerosene production significantly outweighs the slightly increased emissions due to less fuel efficiency.

It must be noted that the LCA for the Twin Otter was performed for its conventional configuration. The conventional Twin Otter is not able to perform the medevac mission due to insufficient fuel tank storage. The adaptations made to the Twin Otter to perform the medevac mission added weight and decreased the fuel efficiency. These adaptations decrease the LCA performance. Unfortunately, sufficient data could not be found about the adaptations done to perform a completely fair comparison.

### 10.1.5. Verification

The LCA methodology considers the design from cradle to grave and is based on the statistics of commercial passenger aircraft [12]. To apply this software to the JAPA-12 certain adjustments and assumptions had to be made. The major inputs and statistical relations that had to be altered and are described and verified below.

Firstly, for the engine characteristics, a reference aircraft from the database built into the software had to be chosen. For the analysis performed the ATR 72–500 was chosen as a reference. This aircraft has two Pratt & Whitney PWC 127F turbo-prop engines that produce a maximum of 2509 kW of power. These engines are similar to the Pratt & Whitney PW118 used by the JAPA-12. In fact they are part of the same production series. The emissions of the engines are given per joule of fuel burned. Therefore for the purposes of the LCA the characteristics and emissions of the engines are similar.

[103] Life Cycle Assessment, https://www.rivm.nl/en/life-cycle-assessment-lca/downloads, date accessed = 13-06-2022

[104] Twin Otter technical brochure, https://www.vikingair.com/sites/default/files/twin_otter_technical_spec._brochure_06_2020v1_08-25-2021.pdf, date accessed = 13-06-2022

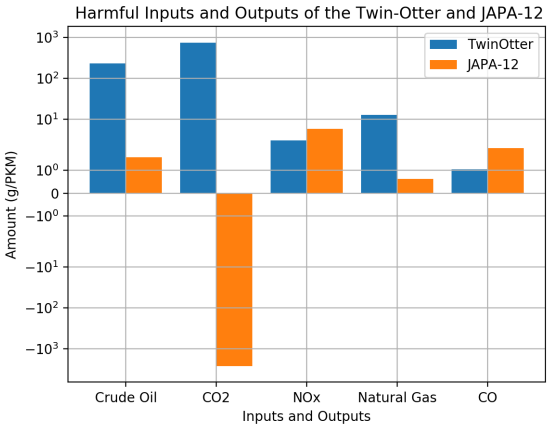


**Figure 10.3:** *Comparison of the harmful inputs and outputs of the Twin Otter and JAPA-12.*

Next, the material composition of the reference aircraft had to be adjusted. The LCA software has a built in database containing the material distribution of multiple aircraft. For the engine characteristics the ATR 72–500 was chosen as the reference aircraft, however the material composition of this aircraft is very different than the JAPA-12. The material composition summarised in Table 10.1 replaced the statistics of the ATR 72–500.

The recyclability and re-usability of each material had to be adjusted. The software used data from a reference published in 2007. As the source was outdated the percentages of recyclability and re-usability of certain materials was no longer accurate. The updated percentages of recyclability and sources are presented in Table 10.1.

While the software facilitates alternative fuel production methods, the emission data was not relevant to the production process that will be used for the JAPA-12. Based on the study conducted by Ministerie van Infrastructuur en Waterstaat [96], the emissions of the synthetic kerosene production process were input. As only the statistical data was adjusted, the rest of the software was not affected.

## 10.2. Noise

With the aim of creating a socially sustainable aircraft, noise levels generated by this aircraft were investigated. Although the noise levels might seem less relevant for the remote Antarctic mainland, it is relevant different markets. The International Civil Aviation Organisation (ICAO) has set regulations based on aircraft mass. How the noise level regulations affected the search for a suitable method was investigated in this section. First, the noise regulations are revised in Subsection 10.2.1. Then, the noise estimation methods are covered in Subsection 10.2.2. Finally, by carrying out the estimation methods, the total noise was estimated, and compared to the regulations. This is presented in Subsection 10.2.3.

### 10.2.1. ICAO Regulations

The maximum allowed take-off noise, defined by the ICAO, depends on the year of development of the aircraft and the maximum take-off weight. For an aircraft with a maximum mass under 8618 kg and the development year being later than 1988, the following noise requirement is set in ICAO Annex 16 Volume I. Chapter 10, section 10.4.a [99].

**ICAO Annex 16 Volume I, 10.4 a):** *For aeroplanes specified in 10.1.2 and 10.1.4, a 76 dBA constant limit up to an aeroplane mass of 600 kg varying linearly from that point with the logarithm of aeroplane mass until at 1400 kg the limit of 88 dBA is reached after which the limit is constant up to 8618 kg*

From the regulation, the maximum noise level is set to be 88 dBA for the aircraft, as its mass is higher than 1400 kg. The noise level is to be measured at the reference point, which is 2500 m from the start of the take-off roll, on the same line of the centre line of the runway, which can be seen in Figure 10.4. As the minimum climb gradient was known to be 4%, by **REQ-SYS-CON-1.06**, the absolute distance to the measurement equipment was obtained. This distance, which was found to be 100 m, or 328.08 ft, was used for calculations for the noise levels. The found Sound Pressure Levels (SPL) levels in dB, had to be A-weighted to reflect the sensitivity of the human ear.

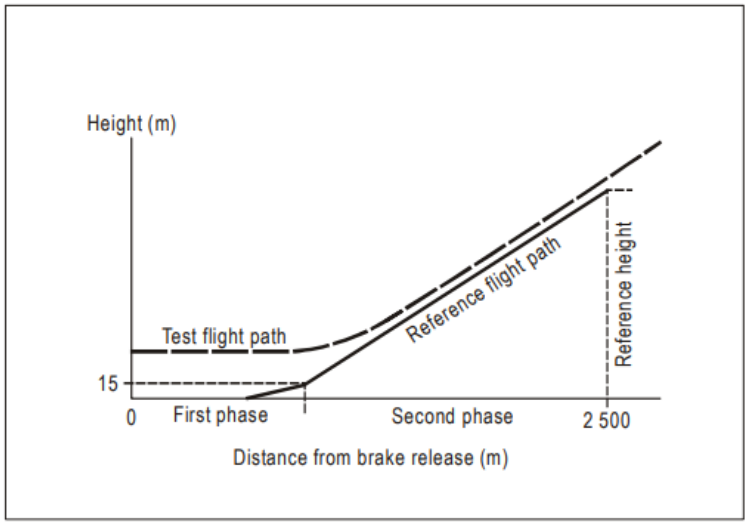


**Figure 10.4:** *Test set up for noise measurements [99].*

## 10.2.2. Noise Estimation Methods

The noise level investigation was done by initially separating the airframe and propulsion system noise. The propulsion system noise was divided into noise generated by the propellers, the noise generated during the combustion process and the noise generated by the electric motors, as generally done for noise estimations [100].

**Propeller Noise**

The far-field propeller noise estimation method from J.E Marte and D.W Kurtz [101] was used to estimate the propeller noise from both the combustion engine propellers and the propellers from the electric motors. This method uses the propeller diameter, shaft power, propeller speed, number of blades, the speed of sound, distance to far-field point of interest and the orientation to the reference point as inputs. The SPL in dB at the location of interest was obtained via this method. The procedure works as follows:

A reference level $L_1$ in dB, was obtained based on shaft horsepower from literature [101]. From this reference level, corrections were added for the number of blades and the propeller diameter. Two other corrections were then subtracted for the directional characteristics of sound propagation from a propeller and an attenuation correction due to the normal spherical spreading of sound. The summation of the aforementioned reference level and correction factors then resulted in a SPL for the point of interest. This SPL was then corrected for distortions by analysing the harmonic distribution levels. Using the reference values from literature [101] in combination with the true tip Mach number and the fundamental blade passage frequency, as calculated by Equation 10.1, the harmonic distribution levels were found. In Equation 10.1, B is the number of blades and n is the propeller rotation speed.

$$f = B \cdot n/60 \tag{10.1}$$

The harmonic distribution levels were then ordered into preferred octave passbands. These passbands presented frequency ranges within the human hearing range. By combining the harmonic levels based on the harmonics of blade passage frequency within the preferred octave bands, the octave band levels were obtained. Subsequently, A-weighting had to be applied to the octave band levels to get to the correct unit of dBA. A-weighting was applied using Equation 10.2 and Equation 10.3. Where f represented the frequency in both equations is the frequency of the octave band levels. Adding up the A-weighted octave band levels in the dB scale then results in an overall SPL. Finally, the overall A-weighted SPL for the smaller propellers with electric motors and for larger propellers with the combustion engines were found to be respectively 70.1 dBA and 64.9 dBA. These values could then be added up in the dB scale to a total noise emission value of 80.3 dBA.

$$R_A(f) = \frac{12194^2 \cdot f^4}{(f^2 + 20.6^2) \cdot \sqrt{(f^2 + 107.7^2) \cdot (f^2 + 737.9^2)} \cdot (f^2 + 12194^2)} \tag{10.2}$$

$$A(f) = 20 \cdot log(R_A(f)) + 0.17 \tag{10.3}$$

The accuracy of this propeller noise method is ±10 dB for a distance of 500 ft between the propeller center and the point of interest [101]. For points of interest further than the threshold value, local weather conditions could effect the accuracy

of the results noticeably. It is therefore advised to consider the results of the far-field propeller sound estimation method solely as first approximations under ideal conditions [101].

**Gas Turbine Noise**
The turboprop engine also contained a gas turbine, driving the propellers. This turbine also produces noise, as the air is taken through the inlet, combusted and subsequently exhausted. This leads to noise being emitted. The amount of noise being produced by the gas turbine was estimated from the method described in [102]. In this method, the noise emitted by a gas turbine is separated in three parts: the intake, the exhaust and the casing. The equations for the SPLs in A-weighted decibels are mentioned in Equation 10.4 - Equation 10.6 [102], and are dependent on the shaft power, $P_{shaft}$. The values, corrected for the right distance using the distance correction factor from [101], yielded SPL levels of 75.58, 76.34 and 64.09 dBA. For the two combustion engines, this resulted in a total noise of 82.1 dBA.

$$SPL_{intake} = 127 + 15 \cdot log(P_{shaft}) \tag{10.4}$$

$$SPL_{exhaust} = 129 + 10 \cdot log(P_{shaft}) \tag{10.5}$$

$$SPL_{casing} = 118 + 5 \cdot log(P_{shaft}) \tag{10.6}$$

**Electric Motor Noise**
To estimate the noise emitted by the electric motor, the method developed in [102], was used. This method gives a general formulation for the prediction of motor noise, which is dependent on shaft power $P_{shaft}$, shaft rotational speed $\Omega_{shaft}$, and the conformal surface area S. The equation for the sound pressure level of electric motors with a shaft power larger than 40 kW is stated in Equation 10.7 [102], and gives the SPL in A-weighted decibels at a measurement distance of 1 m. The found value was then corrected for the correct distance using the correcting factor as used in noise propeller calculations [101]. A final value of 26.6 dBA for one electric engine, and 33.6 dBA for all 10 engines was found.

$$SPL_{electricmotor} = 27 + 10 \cdot log(P_{shaft}) + 15 \cdot log(\Omega_{shaft}) + 10 \cdot log(S) \tag{10.7}$$

**Airframe Noise**
The airframe itself also produces noise. This noise is caused by convection of the wing and tail turbulent boundary layers past the trailing edges of those surfaces [103]. Other airframe components that contributed significantly to the total airframe sound emission during take-off and approach are the landing gear, and trailing and leading edge devices. A statistical formula was derived by NASA to make an initial estimation of the total airframe noise emission at approximately 450 m perpendicular to the ground track [104]. This value was also corrected for the right reference distance using the correction factor from the propeller noise calculations [101]. The formula derived by NASA is stated as Equation 10.8. With Equation 10.8, the clean airframe noise in dBA was calculated. This was based on a statistical regression of three jet aircraft. The paper also discussed an additional 7 dBA due to extended flaps and 5.5 dBA due to the landing gear, which were also added to account for the landing configuration of the aircraft. However, as the aircraft was significantly smaller, landed at a lower velocity and less big flap and landing gear systems were needed, it was chosen to subtract 3 dBA (half the value) as a first estimation of frame noise. A value of 84.57 dBA was found.

This most likely overestimated the noise level as the weight of the JAPA-12 was approximately half of the reference jet aircraft. It was also found surprising that the noise generated by the frame was found to be higher than the noise generated by the engines and propellers. It is expected that tests will prove the airframe noise to be more in the range of 81.5 dBA (half the emitted noise) following the logarithmic relation between weight and generated SPL levels. This would also be more in line with the expectations that the propulsion group generates more noise than the airframe. However, for a first noise estimate and keeping in mind that flaps and landing gear were fully extended, the 84.57 value was assumed to be sufficiently accurate.

$$SPL = 10 \cdot log(V^5) + 10 \cdot log(W) - 74 \tag{10.8}$$

As an initial noise estimation method, this solution was deemed sufficiently accurate. However, a more thorough airframe noise analysis should be performed in the next design phase by using more advanced noise estimation methods such as Computational Fluid Dynamics (CFD) and Finite Element Method (FEM) software.

### 10.2.3. Total Noise

When every contribution is added up via a logarithmic scale, a total noise value of 87.4 dBA was found. This value was the absolute maximum noise the aircraft would emit, as the thrust that was used was the maximum for all engines and flaps and landing gear were maximally extended. Most importantly, the by CS-23 regulations minimum required climb gradient of 4% was used. As the aircraft could climb with a steeper angle of up to 27%, if allowed by airport regulations,

the distance to the measurement point will in reality be larger, and the total A-weighted decibel level will be significantly lower: It was calculated that the total decibel level would decrease by approximately 20 dBA when the maximum climb angle was used. Furthermore, for the take-off power, a value of 1258 kW was calculated to be sufficient for take-off but a half maximum thrust value of 1975 kW was used for the noise calculations. This meant that in reality, by a logarithmic scale [101], the noise level generated by the engines and propellers would be approximately 6 dBA less. Combining this with aforementioned calculations and estimates, a more accurate noise emission at the reference point was found to be 82.2 dBA. A contingency factor of 3 dB (double the noise level) was added to account for unforeseen noise contributions or errors in the calculations. This resulted in a total A-weighted noise level of 85.2 dBA.

From the findings stated in the previous paragraph, it can safely be said it is not a problem if the propeller noise turns out to be 10 dB higher, as this can easily be compensated. For the other noise calculation sources, nothing was said regarding accuracy. However, with the contingency factor implemented, the uncertainty in their accuracy was considered accounted for. Finally, as the calculated maximum noise level with the safety factor has a smaller magnitude than the maximum certification level of 88 dBA, the noise requirements were considered to be met.

The aircraft that the JAPA-12 would be replacing, the DHC-6 Twin Otter, was rated with 84.3 dBA maximum during take-off[105]. This meant that without the estimated contingency factor the JAPA-12 would be less noisy than the Twin Otter. It is assumed the difference is due to the lower climb rate of the Twin Otter. Initially, it was expected that the JAPA-12 would produce more sound than the Twin Otter, as a slightly higher take-off power was required (1260 vs 1100 kW). However, due to the contingency factor, that could still happen and it would still not be an issue regarding regulations.

## 10.3. Sustainability Assessment

The sustainability of the design was evaluated based on the three fundamental dimensions: environmental, economic, and social. The criteria and methodology for scoring was presented in Subsection 2.4.3. Throughout the Twin Otter serves as a baseline for comparison. Where applicable the results of the analysis from Section 10.1 were applied.

### 10.3.1. Environmental

Firstly, the environmental dimension was evaluated. Similar to the LCA the assessment is limited to the production, operations, and end-of-life of the aircraft. Quantitative aspects from the LCA as well as qualitative factors were considered.

#### Production

The environmental impact of the production phase is primarily dictated through the fuel production process. As discussed in Subsection 10.1.1, the fuel production process for the JAPA-12 has a positive effect on the environment. As shown in Figure 10.3 the amount of carbon dioxide captured is so large during this process that the entire life cycle of the JAPA-12 actually has a net positive contribution to carbon dioxide emissions.

In addition, the production phase is highly dependent on the materials used by the aircraft. Based on the material distribution of the JAPA-12, an analysis was done of the three most used materials. For each material an estimate of the emissions per ton of material produced was created. The results are summarised in Table 10.3. While composites have excellent material properties, production is very harmful and energy intensive. The JAPA-12 uses little composites compared to modern jet-airliners [106]. Therefore the JAPA-12 has little environmental impact with respect to conventional aircraft. Due to the excellent performance, a score of 5 is assigned for the JAPA-12. For the Twin Otter there are no special considerations compared to a conventional aircraft, therefore a score of 3 is given.

**Table 10.3:** *Environmental considerations depending on material production processes.*

| Material produced | GHG [kg/ton] | Particulate [kg/ton] | Energy inputs [GJ/ton] |
|---|---|---|---|
| Aluminium | 2540 | 10.3 | 30.5 |
| Composite | 79000 | 418 | 920 |
| Steel | 1450 | 1.20 | 17.4 |

[105] EASA Pro *EASA Certification Noise Levels*, https://www.easa.europa.eu/domains/environment/easa-certification-noise-levels, date accessed = 09-06-2022

[106] Composites in the aircraft industry, https://www.appropedia.org/Composites_in_the_Aircraft_Industry, date accessed = 14-06-2022

#### Operations

Operations is the most significant life cycle phase for emissions. The cruise and LTO-cycle are the most impactful phases as shown in Figure 10.2. For the JAPA-12 a conventional turbo-prop engine is used. This engine has the same emissions as a conventional aircraft. Moreover, the maintenance strategy of the JAPA-12 used for commercial flights is very similar to a conventional aircraft. For this reason a score of 3 is assigned to the JAPA-12 and Twin Otter.

#### End-of-life

The end-of-life phase of the aircraft depends on the recyclability and re-usability of the aircraft. Recyclability has been discussed in Subsection 10.1.3. The JAPA-12 was calculated to be 90.2% recyclable. To add, no energy intensive recycling of composites is required to meet this percentage. The majority of the aircraft is made up of aluminium. Recycling aluminium uses less than 5% of the energy required to make the original product[107]. Similarly, for titanium and steel less than 25% of the original energy is required. As the majority of the aircraft is made from easily recyclable materials, the end-of-life phase has little environmental impact.

Re-using equipment is preferred as no additional energy is required to reshape the material for a new product. Apart from load bearing structures, almost everything of the JAPA-12 may be re-used. Load bearing structures may not be re-used as they will be prone to fatigue failure. Some parts might only be partially re-usable. An example of which is the interior of the aircraft which may have to be refurbished to meet modern comfort requirements. Parts for re-using may be sold to other manufactures or re-implemented in a new JAPA-12 aircraft.

The market of the JAPA-12 is limited and few aircraft will be produced. Therefore instead of creating customised parts, it might be worth while to re-use parts from other aircraft. This should be analysed for future development. The Twin Otter has a similar material composition to the JAPA-12. Both exhibit excellent end-of-life potential, however some waste will still go to the landfill or incineration plant. Therefore a value of 4 is assigned to both aircraft.

### 10.3.2. Economic

For the economic sustainability the production and direct operating costs were assessed. To evaluate these criteria the analysis performed in Chapter 9 was used.

#### Production Cost

The production cost of the JAPA-12 was estimated to be $5.1 million per unit. A reason why the production cost were found to be relatively low was due to the material distribution. Composite manufacturing is an expensive process, as the JAPA-12 uses very little composite material this greatly reduced the production costs. On the contrary aluminium, which composes the majority of the JAPA-12, is cheap to produce and work with [94]. The final list price was estimated to be $7.5 million. Therefore, a profit margin of 15% was obtained. Based on the statistics of Roskam, this is a good profit margin [25]. While no concrete data could be found about the production cost of the Twin Otter, the material distribution and list price is similar to the JAPA-12. Therefore a value of 4 is assigned to both aircraft.

#### Direct Operating Costs

The direct operating costs of the JAPA-12 and Twin Otter are expected to be similar. The only difference is the cost of the production of fuel. While using synthetic kerosene has a positive effect on the environment it comes at a steep price. Nevertheless, it has been predicted that in 2030 the price will be similar to that of fossil fuel kerosene[108]. Therefore a value of 3 is assigned to both the Twin Otter and the JAPA-12.

### 10.3.3. Social

The social sustainability dimension assesses the effect of the product on human health and society. To excel in this category the design must preserve or improve the quality of human life. Particulate emissions and noise were the evaluation criteria.

#### Particulate Emissions

Particulate emissions are dangerous for the human environment, causing a range of medical complications. The LCA considered the emission of $NO_x$ and inhalable particles with a diameter smaller than 10 microns. The JAPA-12 has an emission of 5.72 g/PKM of harmful particles. While this is a lot compared to popular aircraft such as the Airbus A320, the JAPA-12 flies at a significantly lower altitude. Flying at a lower altitude greatly reduces the impact of the particles emitted [105]. Therefore the emissions of the JAPA-12 are considered to have approximately the same impact as a conventional aircraft. The same applies to the Twin Otter and therefore a score of 3 is assigned to both aircraft.

[107] Environmental factoids, https://archive.epa.gov/epawaste/conserve/smm/wastewise/web/html/factoid.html, date accessed = 14-06-2022

[108] Synthetic fuels, https://www.bosch.com/stories/synthetic-fuels/, date accessed = 14-06-2022

**Noise**
The noise emitted by aircraft influences the quality of life of residential areas. Excessive exposure to noise may cause sleeping problems and stress. From the analysis conducted in Section 10.2 the average noise of the JAPA-12 found was 82.2 dBA. This is better than the Twin Otter which emits on average 84.3 dBA. Note that the difference of 2.1 dBA implies that the Twin Otter is almost twice as loud as the JAPA-12, this is a large difference. In addition, the maximum noise that may be emitted from the JAPA-12 is 87 dBA, this is still under the 88 dBA requirement. Therefore a score of 5 and 3 is assigned to the JAPA-12 and Twin Otter respectively.

### 10.3.4. Sustainability Overview
To provide a clear overview of the sustainability of the JAPA-12, the scores of the criteria are shown through a radar diagram. The diagram is presented in Figure 10.5. As a benchmark for comparison the performance of the Twin Otter was also plotted. Note, that EI stands for environmental impact.

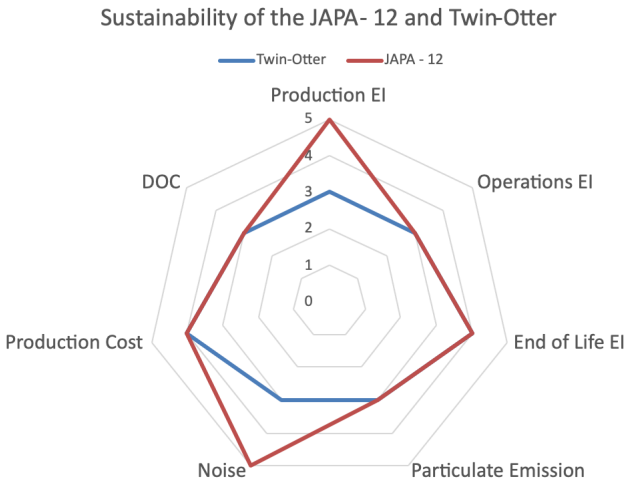


**Figure 10.5:** *Radar diagram presenting the sustainability scores of the Twin Otter and JAPA-12.*

# 11
# Final Design V&V

In order to have confidence in the design and demonstrate compliance with the requirements, the validation of the design was performed in this section. First, the final verification of the design is addressed in Section 11.1, Section 11.2 and Section 11.3. Next, the general validation approach is discussed in Section 11.4 which leads to Section 11.5 where the sizing model is validated by estimating errors and uncertainties. The sensitivity analysis is covered by Section 11.6 which is followed by Section 11.7 where design validation is briefly discussed. Finally, the chapter closes up with aircraft validation in Section 11.8.

## 11.1. Design Verification Approach

Design verification was carried out to ensure compliance of the final design with all the requirements established by the stakeholders and the team. The four aircraft verification methods which were or will be used are listed below.

- **[INS] Inspection** - simple requirements such as aircraft colour and dimensions can be verified by visual inspection.
- **[DEM] Demonstration** - for certification requirement such as: ”the aircraft shall be able to achieve 1.5% climb gradient” the demonstrations are performed for verification.
- **[TES] Tests** - for requirements such as the structure shall withstand n number of cycles the fatigue tests are performed as a form of verification.
- **[ANS] Analysis** - qualitative or quantitative analysis applicable for any kind of design requirement.

Due to the fact that upon completion of this paper JAPA-12 was still in the design development stage, verification methods such as test and demonstration could not be used. Most of the requirements, where applicable, were verified using mathematical analysis. Furthermore, the stakeholder requirements were grouped into 4 verification groups for which a specific verification method was used or is to be used in the future. These groups are indicated in the compliance matrix which is found in Table 11.1. In the following sections, the mathematical analysis was applied to verify the technical requirements.

## 11.2. Flight Performance Verification

Due to design iterations, all the performance parameters were changed at different stages of the design. The flight performance requirements were incorporated in Section 3.4 where the aircraft’s power and wing loading were chosen based on design space available after applying requirements. However, not all performance requirements were considered, and the design point changed in later design stages. In order to show that the final design values still comply with all the requirements, the flight performance verification was performed.

Due to the fact that the gas turbine was oversized to meet the one engine inoperative requirements as described in Section 4.4, the other performance requirements were set to be met with some margin. After applying safety factors where appropriate and padding factors for security, the final performance data was evaluated. The stall performance parameters are summarised below. Requirements Verified: **REQ-PER-01.1** - Fully, **REQ-STA-MAR-05**, **REQ-STA-CUST-03** and **REQ-STA-MAR-07** - Partially.

| | |
|---|---|
| Stall Speed (flaps down) : 32.4 m/s | Stall Speed (T = 40°C) : 30.0 m/s |
| Stall Speed ($\rho$ = 0.93 kg/m$^3$) : 32.4 m/s | Stall Speed (flaps up) : 37.7 m/s |

Take-off and landing distances or ground roll are limited by target airports and markets that the aircraft is to serve. The specific requirements **REQ-STA-TAP-01.1** and **REQ-STA-TAP-01.1** specify that aircraft shall take-off and land in 2216 and 692 m respectively. Landing distances were calculated using the same equation as for take-off by adapting braking and aerodynamic coefficients. The corresponding take-off and landing distances of JAPA-12 are summarised below. Requirements Verified: **REQ-PER-01.1**, **REQ-STA-MAR-06**, **REQ-PER-01.2**, **REQ-STA-MAR-05** and **REQ-STA-MAR-07** - Fully.

| | |
|---|---|
| T-O distance gravel (MSL): 255 m | T-O distance gravel ($\rho$ = 0.95 kg/m$^3$): 355 m |
| T-O distance snow (MSL): 410 m | T-O distance snow ($\rho$ = 0.95 kg/m$^3$): 580 m |
| LNG distance gravel (MSL): 225 m | LNG distance gravel ($\rho$ = 0.95 kg/m$^3$): 255 m |
| LNG distance snow (MSL): 360 m | LNG distance snow ($\rho$ = 0.95 kg/m$^3$): 410 m |

Cruise Performance was limited by minimum cruise speed specified in the CS-23 regulation and by average cruise speed of 103 m/s specified by **REQ-STA-CUST-09**. The following values for the average cruise were computed for JAPA-12. Requirements Verified: **REQ-STA-CUST-09** - Fully

Mean Cruise Speed (FL100): 107 m/s  Mean Cruise Speed (FL125): 106 m/s

Finally, the rate of climb and service ceiling, requirements **REQ-STA-CUST-06**, **REQ-PER-01.2** and **REQ-PER-01.3**, were evaluated for different conditions. Due to the fact that the engines were oversized, the maximum rate of climb values are rather high when compared to similar aircraft. Requirements Verified: **REQ-STA-CUST-06**, **REQ-PER-01.2** and **REQ-PER-01.3** - Fully

ROCmax (AEO MSL): 14.5 m/s  ROCmax (OEI MSL): 4.60 m/s
Service Ceiling(AEO) : 25000 ft  Service Ceiling (OEI): 13000 ft

## 11.3. Requirements Compliance Matrix

After the final design concept was created, the design was evaluated to ensure it satisfied the requirements. The results of this evaluation are presented in Table 11.1. In this table, the stakeholder and top-level subsystem requirements are included as well as a number of stand-alone requirements. These requirements were included as they either drive or define the design, or are important to the customer. All requirements, which are only partially compliant are discussed below Table 11.1.

**Table 11.1:** *Requirement compliance overview.*

| Identifier | Requirement | Compliance status | Compliance check method |
|---|---|---|---|
| Stakeholder | | | |
| **REQ-STA-CUST-01** | The system shall have a list price below 7.5 million euro, while making a profit. | Complied with | [ANS] |
| **REQ-STA-CUST-02** | The system shall be certifiable. | Partially complied with | [DEM], [TES], [ANS] |
| **REQ-STA-CUST-03** | The system shall perform within Antarctic weather conditions, being able to perform the mission, from notification up until landing back at Rothera, with a 95% probability in a given 7-day window. | Complied with | [ANS] |
| **REQ-STA-CUST-04** | The system shall be brought into service before 2030. | Complied with | [DEM] , [ANS] |
| **REQ-STA-CUST-05** | The system shall adhere to sustainability constraints. | Complied with | [TEST], [ANS] |
| **REQ-STA-CUST-05.1** | The system shall have a structure of which 90% of the mass is recyclable. | Complied with | [ANS] |
| **REQ-STA-CUST-05.3** | The system shall have a propulsion system with net zero carbon dioxide emissions in the operational phase. | Complied with | [TEST], [ANS] |
| **REQ-STA-CUST-06** | The system shall have a service ceiling of 25000 ft. | Complied with | [DEM], [ANS] |
| **REQ-STA-CUST-07** | The system shall have a range of 100 nm with a payload of 4000 lbs. | Complied with | [ANS] |
| **REQ-STA-CUST-08** | The system shall have a range of 400 nm with a payload of 3000 lbs. | Complied with | [ANS] |
| **REQ-STA-CUST-09** | The system shall have a cruise speed of 200 kts. | Complied with | [DEM], [ANS] |
| **REQ-STA-TAP-01.1** | The system shall land on a snow runway of 6000 ft. | Complied with | [ANS] |
| **REQ-STA-TAP-01.2** | The system shall land on a gravel runway 2500 ft. | Complied with | [ANS] |

Continuation of Table 11.1.

| Identifier | Requirement | Compliance status | Compliance check method |
|---|---|---|---|
| **REQ-STA-TAP-01.4** | The system shall endure a range of 1350 nm with one medevac payload. | Complied with | [ANS] |
| **REQ-STA-PAS-01** | The system shall allow for easy loading of a patient on stretcher. | Complied with | [DEM], [ANS] |
| **REQ-STA-MAR-01** | The structure shall withstand loading from landing with conventional landing gear and skis. | Complied with | [TES], [DEM], [ANS] |
| **REQ-STA-MAR-02** | The system shall accommodate for changing to a configuration which allows for the transport of 19 passengers over a range of 150 nm. | Complied with | [ANS] |
| **REQ-STA-MAR-03** | The system shall accommodate for changing to a configuration which allows for the transport of 3200 lbs of cargo over a range of 150 nm. | Complied with | [ANS] |
| **REQ-STA-MAR-04** | The system shall accommodate for changing to a configuration which allows for performing airdrops. | Complied with | [ANS] |
| **REQ-STA-MAR-05** | The aircraft shall be able to provide sufficient lift in all flight phases in environments with temperatures up to 40 degrees. | Complied with | [ANS] |
| **REQ-STA-MAR-06** | The aircraft shall be able to provide sufficient thrust to take off on a gravel runway of 2500ft in environments with temperatures up to 40 degrees. | Complied with | [ANS] |
| **REQ-STA-MAR-07** | The aircraft shall be able to take-off and land at an altitude of 2835 meters. | Complied with | [ANS] |
| Top-level subsystem requirements | | | |
| **REQ-SYS-FUNC-01** | The system shall provide power to all subsystems. | Complied with | [TEST], [ANS] |
| **REQ-SYS-FUNC-02** | The system shall provide communications. | Complied with | [TEST], [ANS] |
| **REQ-SYS-FUNC-03** | The system shall provide guidance and navigation. | Complied with | [TEST], [ANS] |
| **REQ-SYS-FUNC-04** | The system shall provide situational awareness in whiteout conditions. | Complied with | [ANS] |
| **REQ-SYS-FUNC-06** | The system shall provide structural integrity to withstand flight loads up to a maximum load factor of 9. | Complied with | [TEST], [ANS] |
| **REQ-SYS-FUNC-07** | The system shall provide environmental control. | Complied with | [TEST], [ANS] |
| **REQ-SYS-FUNC-08** | The system shall provide 6.9 kN of thrust to overcome drag. | Complied with | [TEST], [ANS] |
| **REQ-SYS-FUNC-10** | The system shall provide passenger and crew accommodation. | Complied with | [INS], [ANS] |
| **REQ-SYS-FUNC-11** | The system shall be manoeuvrable on the ground. | Complied with | [DEM], [ANS] |
| **REQ-SYS-FUNC-12** | The system shall take-off safely. | Complied with | [DEM], [ANS] |
| **REQ-SYS-FUNC-13** | The system shall perform ground operations. | Complied with | [ANS] |
| **REQ-SYS-FUNC-14** | The system shall produce sufficient braking power. | Complied with | [TES], [ANS] |
| Stand-alone requirements | | | |
| **REQ-RSK-01** | The system shall be able to carry 77 kg of spare parts in addition to payload. | Complied with | |

As can be noticed from the table only one requirement is partially complied with which is REQ-STA-CUST-02. The main certification requirements of the CS-23 certification class are met, but many subsystem requirements can not be

evaluated during this design phase at the level of detail required for certification. Compliance with these requirements can only be shown through in-flight testing. Besides, compliance with EASA Special Condition SC E-19 must be proven in addition to CS-23. This will certify that the electric propulsion system is safe to use in flight, which will require extensive flight testing [106]. In conclusion, the design complies with most of the main functional and stakeholder requirements, with the exception of certain certification requirement.

## 11.4. Validation Approach

In order to evaluate how close the design solution comes to reality and delivering desired safe and high performance, the validation of JAPA-12 was divided into three parts. First, the analytical validation of the entire aircraft sizing method was performed. Model validation mainly dived into the errors and uncertainties of design outputs in order to evaluate overall design accuracy. Since no physical validation could be performed within the framework of the design study, the validation procedures that will be performed at later stages were established. Following the model validation, the design of JAPA-12 will be validated in its entirety. Design validation was and will be a concurrent extension of the design verification process, performed to ensure that the final design meets the requirements and actually performs what it is meant to. The final part of validation will be the aircraft validation which will ensure that the final product is reliable. Furthermore, it will ensure high quality by supplementing analysis with test data and demonstrations. Part of the aircraft validation will be the certification of the aircraft within the CS-23 regulations and validating it for countries of operation outside of EASA member states. The flowchart for the validation process outlining the most important actions that will be taken is shown in Figure 11.1

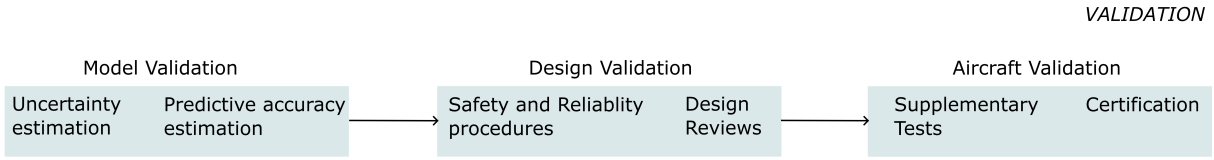


**Figure 11.1:** *Validation process flowchart.*

## 11.5. Model Validation

It is essential to analyse the degree to which models created in product design are accurate with respect to real-world data. In this section, the level of agreement between implemented models and the reference data from the real world is addressed.

### 11.5.1. Model Errors

Estimation of model errors is essential for the validation of the results obtained. Model errors arise from the use of simplified mathematical models to represent physical systems. The design of JAPA-12 made use of many different mathematical models in particular the ones described by Roskam, de Vries, Patterson and Gudmundsson. The model errors were estimated for the most important design steps in the preliminary sizing. Estimating model errors for every design step is a rather tedious task. However, since preliminary sizing outputs serve as inputs for the rest of the calculations, it was deemed sufficient to estimate errors in preliminary sizing outputs to give an overview of the general accuracy of the results.

Two of the most important outputs of the preliminary sizing are the design point and the MTOW. The first model that is examined is the point performance coupled with the aerodynamic model of the leading-edge distributed propulsion. The validation study which applies the point performance to a conventional aircraft, the Do-228, performed by de Vries shows that the model error in the design point is around 1% [16]. A separate study conducted by Matrone, using essentially the same approach to determine the design point of a hybrid-electric X-57 Mod-IV, determined a model error of 1.4% [24]. Following the power and wing loading analysis, the MTOW was estimated using mission analysis. The implementation of mission analysis differs from the method used by de Vries, to offset that difference a contingency of 15% was implemented in the verification study. After applying this correction, it was deemed appropriate to assume that the error in MTOW of JAPA-12 is comparable to that produced by the original model. According to a cross-validation study by de Vries, the model error attributed to the MTOW is within 4% [107]. Lastly, the equations used to determine the performance parameters are analysed. Using the data available the model errors were estimated as follows. For the stall equation, the aircraft used for verification was Cirrus SR22; by evaluating the stall speed and comparing it to the publicly available data from the Pilot Operating Handbook (POH), the error was estimated to be around 5.5% [20]. The same reference aircraft was used to estimate the error in take-off and landing distances which turned out to be around

3.8%. Equations for climb rate and ceiling carry an associated error of 5% and the cruise speed calculation method error was estimated to be 4%.

The overall degree of accuracy of the models used is sufficient for the Preliminary sizing as relative errors are mostly kept under 5%. Nevertheless, due to inconsistent implementation of these models, it is likely that the errors of the implemented models could stretch beyond that, possibly to 10 - 15% based on the mission analysis in Section 3.6. This number could be decreased to 3-5% by implementing a more rigorous verification on parts of the model.

## 11.5.2. Uncertainty Propagation

All of the design inputs at every iteration stage come with inherent measurement uncertainties. To assess the impact of uncertainty propagation through the calculations, a model which assesses such uncertainties in the outputs is created. These uncertainties are computed using uncertainty propagation rules. The method of choice, used in the analysis of uncertainty propagation, is the calculus approach. This approach utilises the linearisation of functions in order to determine the effect the input uncertainty has on the output $Z$. For a function of a single variable $f(x)$, uncertainty in output $Z$ is determined using Equation 11.1. For a multivariate function, this expression is modified into Equation 11.2 [108].

$$\alpha_z = \frac{\delta f}{\delta x}\alpha_x \tag{11.1}$$

$$\alpha_z = \sqrt{(\frac{\delta f}{\delta x_1}\alpha_{x_1})^2 + (\frac{\delta f}{\delta x_2}\alpha_{x_2})^2 + \ldots + (\frac{\delta f}{\delta x_n}\alpha_{x_n})^2} \tag{11.2}$$

Using the linear propagation theory, an uncertainty analysis was performed to determine the effect uncertainties in inputs have on the outputs. Based on the mission analysis verification study and estimation of iterative uncertainties, the overall uncertainty of the MTOW outputs was placed within a 5-15% margin with a very high probability. The final power values were determined by the selected engine and the wing surface area was mostly related to the sizing of high lift devices. As a consequence, the uncertainty in MTOW was assumed to be directly translatable to the $W/P$ and $W/S$ ratios. Similarly, the values of aerodynamic coefficients were assumed to lie within the same range of uncertainties as MTOW due to the changes observed in the iteration process. During the uncertainty analysis, specified uncertainties in the inputs, namely MTOW, W/P, W/S and aerodynamic coefficients, were translated into the uncertainties in the outputs such as L/D, rate of climb and range by using either explicit equation formulation or Ferrari's method for solving fourth-order polynomials. The summary of uncertainties found for 3 different cases is shown in Table 11.2.

The actual uncertainties in the final values most likely lay somewhere between scenario 1 and scenario 2 shown in Table 11.2. The uncertainties in the inputs have a significant propagation impact on the uncertainties in lift over drag ratio, range and rate of climb outputs. The calculated uncertainties reach up to 30% in the worst-case scenario and around 10% in the best-case scenario 1 which speaks to the need for further iterations to decrease input uncertainties. In conclusion, it was determined that the main source of epistemic uncertainties in the parameters calculated was the initial condition uncertainty. Due to a complex discrete modelling approach implemented in the design of JAPA-12, the time for iterations was limited which lead to iteration uncertainties having a large impact on the results.

**Table 11.2:** *Input and output uncertainties of the modelling approach.*

| | | Scenario 1 | Scenario 2 | Worst-case scenario |
|---|---|---|---|---|
| Inputs | MTOW | ± 5% | ± 10% | ± 15% |
| | W/P, W/S | ± 5% | ± 10% | ± 15% |
| | $C_D$, $C_L$, $C_{D_0}$ | ± 5% | ± 10% | ± 15% |
| Outputs | L/D | ± 6.9 % | ± 14.0 % | ± 21.3 % |
| | Range | ± 9.8 % | ± 19.6 % | ± 29.5 % |
| | $V_s$ | ± 3.9% | ± 6.8 % | ± 9.7% |
| | $s_{GR,TO}$ | ± 4.4 % | ± 8.4% | ± 12.8 % |
| | $s_{GR,LG}$ | ± 5.0% | ± 9.0 % | ± 13.0 % |
| | $ROC_{AEO}$ | ± 6.4% | ± 12.7 % | ± 19.0 % |
| | $ROC_{OEI}$ | ± 9.4 % | ± 18.9 % | ± 28.3 % |
| | $V_{c,\,max}$ | ± 2.6 % | ± 5.1 % | ± 7.7 % |
| | $V_{c,\,avg}$ | ± 1.4 % | ± 2.8 % | ± 3.7 % |
| | $h_{ceiling}$ | ± 0.0 % | ± 0.0 % | ± 0.0 % |

After determining possible uncertainties in the outputs, a sensitivity analysis was performed to allocate uncertainties

in the output to different sources of uncertainty in the input. The results of the analysis are displayed in Table 11.3. The columns are related to uncertainties in a specific output while the rows relate to the uncertainties in the inputs. For example, $\sigma$(L/D) relates to the relative uncertainty in the lift-to-drag ratio and $\sigma(C_D)$ is related to uncertainty in the drag coefficient used to calculate L/D. The cell (2,4) represents the percent decrease in the uncertainty of L/D when uncertainty in the input drag coefficient is set to zero. Hence, the bigger the decrease the more this input uncertainty affects the output. Notably, the overall pattern showed that the uncertainty in the power loading and hence the weight was largely driving the uncertainties in the outputs of take-off distance and rate of climb. With the rate of climb values having a significant uncertainty as seen in Table 11.2, it was now clear that these uncertainties were related to the power loading. By making the power loading values more precise it would be possible to significantly decrease the uncertainty in the rate of climb. On the other hand, other outputs such as maximum cruise speed and lift to drag ratio are significantly affected by more than one input meaning that it would be insufficient to refine one parameter to decrease output uncertainty to a great degree.

**Table 11.3:** *Sensitivity analysis for the general uncertainty of 10% in the inputs.*

| | $\sigma$ (L/D) | $\sigma$ (R) | $\sigma$ ($V_s$) | $\sigma$ ($s_{GR,\,TO}$) | $\sigma$ ($ROC_{AEO}$) | $\sigma$ ($ROC_{OEI}$) | $\sigma$ ($V_{c,\,max}$) | $\sigma$ ($V_{c,\,avg}$) |
|---|---|---|---|---|---|---|---|---|
| $\sigma$(W/S) = 0 | - | - | -21.1% | 0.0% | -3.3% | 0.0% | 0.0% | 0.0% |
| $\sigma$ (W/P) = 0 | - | - | - | -96.7% | -89.0% | -75.0% | -33.3% | -33.3% |
| $\sigma(C_D) = 0$ | -30.4% | -9.1% | - | 0.0 % | 0.0% | 0.0% | -33.3% | -26.7% |
| $\sigma(C_L) = 0$ | -30.4% | -9.1% | -31.6% | 0.0% | -33.3% | -26.7% | 0.0% | 0.0% |
| $\sigma(C_{D_0}) = 0$ | - | - | - | 0.0% | 0.0% | 0.0 % | -33.3% | -26.7% |
| $\sigma(W_{TO}) = 0$ | - | -18.2% | - | - | - | - | - | - |
| $\sigma(W_f) = 0$ | - | -18.2% | - | - | - | - | - | - |

## 11.6. Sensitivity Analysis of Performance Parameters

After performing uncertainty estimations and sensitivity analysis of the uncertainties, the robustness of the design was evaluated based on the sensitivity of the final performance parameters to their uncertainties. Only the most critical combinations of the uncertainties were evaluated as these lead to parameter changes that impact the design in the worst way. For this, the uncertainties in the inputs of the worst-case scenario presented in Table 11.3 were used which all have a value of 15%.

**Weight** - an increase of 15% in aircraft's weight, although undesirable, would still place JAPA-12 within the CS-23 commuter category. Most requirements could still be achieved even with this weight change while operating at the same power provided by the engines. Satisfying other requirements such as range and payload budgets in adverse conditions, namely OEI and headwind, may require revision of the powerplant choice. At the same time, the design could also accept the risk of OEI and not design aircraft to be able to achieve the same budgets if the engine breaks halfway. This would mean that JAPA-12 would still be able to meet all the requirements with a 15% increase in weight. Overall, this change was not deemed detrimental to the aircraft's performance.

**Range** - as stated in Section 6.3 JAPA-12 was over-designed for the calm weather conditions. With the worst-case uncertainty of 30% in the range, the aircraft could still meet all budget requirements. This is due to the fact that the maximum range calculated for specified payload values was in general over 40% greater than the required range. However, this did not consider the headwind and OEI conditions which would probably make design budgets unfeasible in the most critical case. This will be further investigated in the detailed design.

**Take-off and landing distances** - for these parameters the worst uncertainty estimated was 13%. The largest minimum take-off and landing distances were found at the air density of 0.95 kg/m$^3$. Given that the distances increase by 13%, JAPA-12 is still able to meet target airport constraints by a margin. The smallest difference between the calculated distance and the required was found to be 361 m which speaks to the STOL characteristics of the aircraft.

**Stall speed** - with the increase of 10% the stall speed at air density of 0.95 kg/m$^3$ increases to 34.8 m/s which is 2.4 m/s greater than the requirement. Since such low air density is not expected to be encountered very often this increase is not critical whatsoever. Furthermore, as the stall speed is more of a guide to the pilot it was concluded that this change has no implications for the final design.

**Rate of climb** - with the rate of climb values having the greatest uncertainty it was important to still meet the certification

requirements. On the other hand, due to the oversized engines, the final rate of climb value was found to be relatively high compared to similar aircraft. Including the 19.0% and 28.2% in the AEO and OEI ROC values results in the following rates of climb - 11.7 m/s and 3.3 m/s respectively. These values are still well above the certification requirements and even the technical requirements established for JAPA-12.

**Cruise speed** - in itself the cruise speed values have relatively small uncertainties. When decreasing the average cruise speed requirement by 7.7% the resulting value becomes 2 m/s smaller than the minimum speed required by the CS-23 requirements. However, since this cruise speed was calculated as an average of minimum and maximum cruise speed for 80% throttle it is possible to solve this issue by increasing the gas turbine throttle beyond 80% in cruise or decreasing flight altitude.

Overall, based on the sensitivity analysis, it was concluded that the design is very robust with respect to meeting the requirements even in the worst-case scenario. At the same time, this called into question whether JAPA-12 was too over-designed for its missions. At the end of this study, it was impossible to answer this question as possible uncertainties were still too high. Hence, investigation of the optimality of the design was left for the more detailed stages.

## 11.7. Design Validation

Design validation in the sense that it is defined in this design overlaps with both design verification and aircraft validation. Similarly to aircraft validation, the design validation process aims to ensure that the final product meets requirements and is designed in a way that achieves end-users expectations. The difference is that the design validation is a more user-focused process, ensuring passenger comfort and safety, while aircraft validation is a certification-focused process. Due to the fact that a novel propulsion system is being used in the design, there is a need for detailed procedures for handling and operating such a system. The design validation will commence with the following steps to ensure the safe operation of JAPA-12 under different conditions.

- Determination of detailed required maintenance procedures
- Determination of required flight crew procedures
- Training of the flight crew for extreme weather missions
- Training of maintenance staff
- Specify lists of required flight equipment per mission

Validation of the design must also integrate reviews of reports by a team or teams of experts in the field to ensure the best possible solution is offered to the customers. Such a team will review the outcomes of the steps described above, analyse the problem and report the feedback. An example of such a team is the Technical Advisory Board (TAB) which will evaluate design documentation.

## 11.8. Aircraft Validation

Validation of aircraft, although focused on certification, stretches beyond regulatory procedures. The aim upon the completion of validation is to have high confidence that JAPA-12 will deliver high and reliable performance that will meet the demands and expectations of potential customers. Validation and certification focus primarily on analytical proof of compliance supported by test evidence. The following categories for validation tests were outlined: Structures, aerodynamics and flight performance. Smaller tests will not be outlined at this stage of design development.

**Structural Testing** - is to be carried out using a traditional bottom-up approach. Testing will start at the determination of coupon and panel properties all the way up to the aircraft scale assessment which includes static and fatigue tests of all aircraft subsystems. The former should demonstrate the validity of calculated internal loads and design allowables. Static test will validate that deformations do not interfere with safe operations up to the design limit load, the structure does not permanently deform in a detrimental way at the limit load and that analytical prediction of internal stresses is correct. Moreover, fatigue tests will be carried out to validate the analytical analysis and if necessary make corrections to the design. The thermal strain compatibility tests will be of special importance to JAPA-12. Taking into account **[FAC.1]** - large temperature differences the aircraft must endure, interfaces between materials of different modulus of elasticity and CTE should demonstrate high compatibility. Along with the aforementioned tests, vibration, flutter, windshield and passenger window strength tests will be carried out.

**Aerodynamic Tests** - since aerodynamic interactions in distributed propulsion systems are non-trivial wind tunnel tests will be performed to validate data obtained from aerodynamic estimations and simulations. Firstly the data on the wing aerodynamic performance will be collected, this will include the data on the wing-propeller and propeller-wing interactions so that CFD simulations can be validated. Thereafter, a scaled model of the aircraft will be manufactured and tested in the wind tunnel to determine moment and force coefficients. Upon processing the results, it will be possible to identify areas of improvement in terms of both design and models. Aerodynamic tests will also be performed within the

design speed envelope to validate that the aircraft does not experience flutter.

**Flight Performance Tests** - flight tests up and until the dive speed will be performed to validate flight performance data. Things like manoeuvrability, stability, cruise, landing and take-off performance, structural integrity and limits will be validated. One engine inoperative conditions will be tested in flight tests to validate the high degree of safety and reliability of the aircraft. The noise levels of the aircraft will be measured to ensure compliance with the sustainability requirements. Moreover, subsystems such as avionics will be tested for proper functioning. On the structural side, flutter will be further evaluated by flying the aircraft to the maximum design speed and ensuring that it is flutter free. Most importantly, it will be evaluated by test flights whether the aircraft meets customers and mission needs.

**Extreme weather tests** - given that JAPA-12 was designed for operation in the Antarctic environment it is critical that the aircraft is tested and proven to be able to achieve safe operation under extreme conditions. This includes not only the extremely low temperatures but also temperatures up to 40 ° C as specified by stakeholder requirements. Static tests can be performed in specifically designed test facilities such as McKinley climatic laboratory in Florida where aircraft are subjected to controlled temperature changes in a special chamber. However, it could be more financially interesting to fly aircraft to test sites such as Iqaluit in Canada where it can be tested in authentic conditions both on the ground and in flight. In addition to extreme cold, the airplane should be tested in extremely hot and elevated sites too.

# 12
# Project Design & Development

In this chapter, the future actions that will be performed are presented. These actions will be shown in chronological order in a project design & development logic diagram and in a project Gantt chart. These actions are first presented in Section 12.1 and their logical order is shown in Section 12.2 as well as the Gantt chart that follows from this diagram.

## 12.1. Future Planning and Recommendations

The future of the project is divided into five main phases. These phases are the continuation of the detailed design, testing, production, operations and end-of-life. The steps that have to be taken for the continuation of the detailed design phase are presented below, together with recommendations on improving the work done so far.

- The preliminary sizing of the fuel should be done by calculating the energy required for each mission phase. This method should be implemented and verified.
- The ideal internal configuration should be determined. From this configuration, the dimensions of the fuselage for each aircraft configuration can be established when making a family of aircraft.
- The weight of the propulsion system should be calculated more accurately. This can be done by getting information about the different powertrain components.
- The propellers should be designed in more detail. The airfoil should be chosen, the twist angle should be calculated and the variable-pitch configuration should be designed.
- For the engines, the temperature range should be analysed in more detail. The possibility of downsizing them should be analysed as they are probably oversized even for the Antarctic evacuation mission.
- The values used for the sizing of the vertical tail should be obtained more accurately in order to get a more accurate estimation of the needed surface area.
- The possibility of integrating the landing gear into the fuselage should be investigated.
- The hydraulic subsystem should be designed in more detail.
- The electrical subsystem should be analysed in more detail and the components should be sized more accurately.
- The class II weight estimation should be performed until a difference of 1% is obtained between the MTOW calculated during preliminary sizing and the one acquired from class II. Different methods should be analysed to try to see if the distributed propulsion system can accurately be predicted. During the iterative process all the subsystems should be reevaluated.
- Class III and class IV weight estimations should be preformed.
- Anti-icing systems should be designed and a contingency added as this is of critical importance for the mission: In case the de-icing systems fail, the aircraft would most likely crash.
- A more detailed design of altitude determination system should be made.
- An initial autopilot software system should be designed.
- Actual aerodynamic models should be made to predict the actual lift and drag more accurately.
- The pitching moment should be estimated more accurately.
- The response of autopilot to inputs should be analysed with respect to stability and control. Design control system with desired control response for gentle flight.
- In terms of the structural analysis, a stress analysis should be performed for different materials and internal geometry. The loading cases also need to be revised, and the structure should be altered for different loading cases, such that the structure is most efficient for its weight. The strut should be designed and the integration of the strut with the model should be analysed. FEM model should be made in order to perform a detailed structural analysis.
- The fatigue life estimation of more parts of the aircraft structure should be performed. Furthermore, more accurate models for several different load cycles should be produced, such that fatigue life can be analysed in more detail.
- For the vibration analysis, the aerodynamic model should be incorporated in an expanded structural model for a more accurate flutter prediction.
- FEM models should be set up and used for an accurate noise calculation.
- TPM should be implemented in the following design phases as well. Furthermore, a decision should be made on a target value for the different parameters such as the MTOW which could be limited by CS-23 regulations.
- Errors of the different models should be estimated more accurately.
- The cost breakdown for families of aircraft should be re-evaluated more accurately with more detailed analyses regarding all technical areas.
- A detailed CAD model should be made for production.
- The use of SAF and the extra logistics associated to it should be evaluated in more detail.

Figure 12.1 presents the development cycle for a civil aircraft and was taken as a starting point to define the development cycle for the JAPA-12. The first two phases presented in the figure have already been performed by the team. The results from these phases were presented in the Baseline and Mid-term reports [1], [6]. At this moment the detailed design is still at the start. After completing the aforementioned actions, the last points of ”Detail Structural, Systems & Process Design” phase presented in Figure 12.1 will take place. This phase is followed by the testing & production phase which incorporates the ”Fabrication, Assembly & Testing” and the ”Flight Test” sub-phases. The testing phase and production phase will take place simultaneously: In order to test a part, this part has to be produced first. The testing phase will, however, end before the production phase. Once these have been concluded, the development cycle is finished and at that point, the JAPA-12 is ready for production and ready to enter the operational phase. The last phase consists of disassembling and recycling the different parts of the aircraft and dispose the non-recyclable parts. The detailed plan for the last two phases can be found in the Baseline report [6].

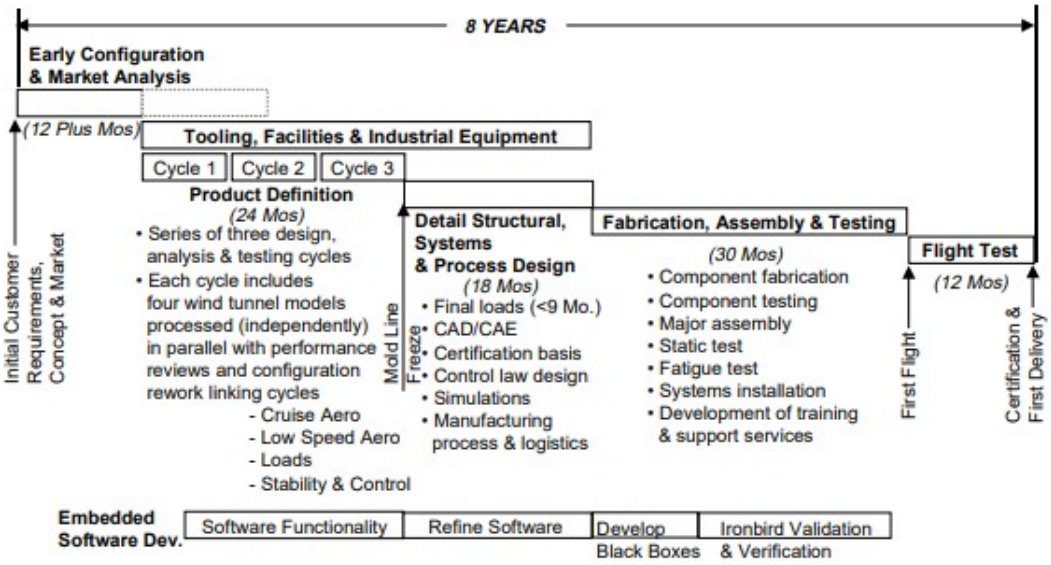


**Figure 12.1:** *Development cycle timeline [109].*

## 12.2. Project Logic Diagram and Gantt Chart

Figure 12.2 shows the logic diagram for the project design & development in detail until the first part of the ”Detail Structural, Systems & Process Design” phase. The tasks that already took place are not shown in the diagram. The implementation of TPM will happen during the entirety of the project and, therefore, it is presented in the first block and is not connected to any other block.

Figure 12.3 presents the different tasks that still need to happen together with the expected time duration. These were based on the values presented in Figure 12.1.

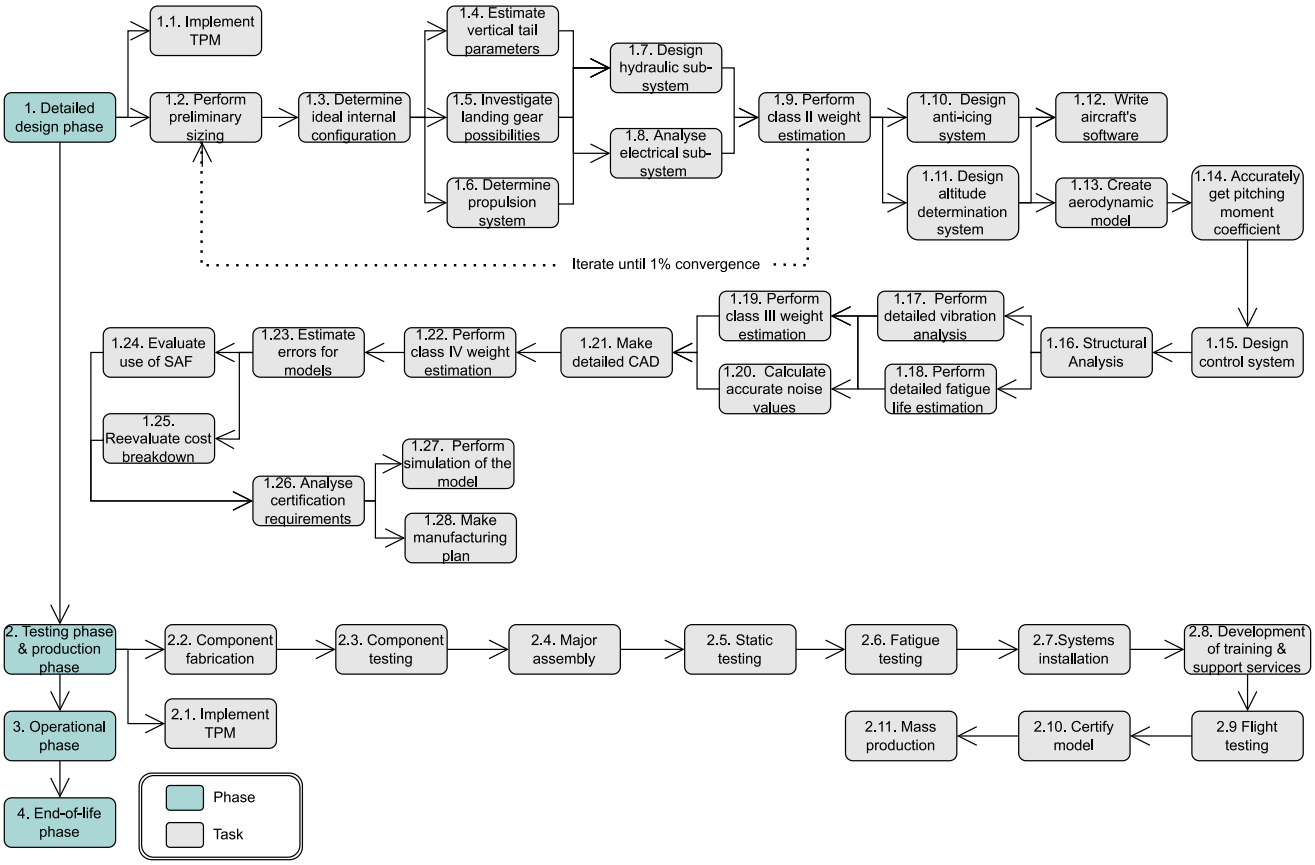


**Figure 12.2:** *Project design & development logic diagram.*

| ID | WBS | Task Name | Duration | Start | Finish |
|---|---|---|---|---|---|
| 0 | **0** | **JAPA-12 Development** | **363 wks** | **Mon 6/27/22** | **Fri 6/8/29** |
| 1 | **1** | **Detailed design phase** | **97 wks** | **Mon 6/27/22** | **Fri 5/3/24** |
| 2 | 1.1 | Implement TPM | 97 wks | Mon 6/27/22 | Fri 5/3/24 |
| 3 | 1.2 | Perform preliminary sizing | 4 wks | Mon 6/27/22 | Fri 7/22/22 |
| 4 | 1.3 | Determine ideal internal configuration | 2 wks | Mon 7/25/22 | Fri 8/5/22 |
| 5 | 1.4 | Estimate vertical tail parameters | 3 wks | Mon 8/8/22 | Fri 8/26/22 |
| 6 | 1.5 | Investigate landing gear possibilities | 3 wks | Mon 8/8/22 | Fri 8/26/22 |
| 7 | **1.6** | **Determine propulsion system** | **9 wks** | **Mon 8/8/22** | **Fri 10/7/22** |
| 8 | 1.6.1 | Size engines | 3 wks | Mon 8/8/22 | Fri 8/26/22 |
| 9 | 1.6.2 | Calculate propeller characteristics | 5 wks | Mon 8/8/22 | Fri 9/9/22 |
| 10 | 1.6.3 | Estimate accurately the weight of the propulsion system | 4 wks | Mon 9/12/22 | Fri 10/7/22 |
| 11 | 1.7 | Design hydraulic system | 3 wks | Mon 10/10/22 | Fri 10/28/22 |
| 12 | 1.8 | Analyse eletrical sub-system | 5 wks | Mon 10/10/22 | Fri 11/11/22 |
| 13 | 1.9 | Perform class II weight estimation | 3 wks | Mon 11/14/22 | Fri 12/2/22 |
| 14 | 1.10 | Design anti-icing system | 3 wks | Mon 12/5/22 | Fri 12/23/22 |
| 15 | 1.11 | Design altitude determination system | 5 wks | Mon 12/5/22 | Fri 1/6/23 |
| 16 | 1.12 | Write aircraft's software | 20 wks | Mon 1/9/23 | Fri 5/26/23 |
| 17 | 1.13 | Create aerodynamic model | 5 wks | Mon 1/9/23 | Fri 2/10/23 |
| 18 | 1.14 | Accurately get pitching moment coefficient | 3 wks | Mon 2/13/23 | Fri 3/3/23 |
| 19 | 1.15 | Design control system | 5 wks | Mon 3/6/23 | Fri 4/7/23 |
| 20 | **1.16** | **Structural anlysis** | **10 wks** | **Mon 4/10/23** | **Fri 6/16/23** |
| 21 | 1.16.1 | Perform stress analysis for other materials | 2 wks | Mon 4/10/23 | Fri 4/21/23 |
| 22 | 1.16.2 | Analyse different loading cases | 2 wks | Mon 4/10/23 | Fri 4/21/23 |
| 23 | 1.16.3 | Design strut | 3 wks | Mon 4/24/23 | Fri 5/12/23 |
| 24 | 1.16.4 | Create FEM and perform structural analysis | 5 wks | Mon 5/15/23 | Fri 6/16/23 |
| 25 | 1.17 | Perform detailed vibration analysis | 5 wks | Mon 6/19/23 | Fri 7/21/23 |
| 26 | 1.18 | Perform detailed fatigue life estimation | 3 wks | Mon 6/19/23 | Fri 7/7/23 |
| 27 | 1.19 | Perform class III weight estimation | 4 wks | Mon 7/24/23 | Fri 8/18/23 |
| 28 | 1.20 | Calculate accurate noise values | 3 wks | Mon 7/24/23 | Fri 8/11/23 |
| 29 | 1.21 | Make detailed CAD | 4 wks | Mon 8/21/23 | Fri 9/15/23 |
| 30 | 1.22 | Perform class IV weigth estimation | 5 wks | Mon 9/18/23 | Fri 10/20/23 |
| 31 | 1.23 | Estimate error for models | 6 wks | Mon 10/23/23 | Fri 12/1/23 |
| 32 | 1.24 | Evaluate use of SAF | 3 wks | Mon 12/4/23 | Fri 12/22/23 |
| 33 | 1.25 | Reevaluate cost breakdown | 4 wks | Mon 12/4/23 | Fri 12/29/23 |
| 34 | 1.26 | Analyse certification requirements | 12 wks | Mon 1/1/24 | Fri 3/22/24 |
| 35 | 1.27 | Perform simulation of the model | 4 wks | Mon 3/25/24 | Fri 4/19/24 |
| 36 | 1.28 | Make manufacturing plan | 6 wks | Mon 3/25/24 | Fri 5/3/24 |
| 37 | **2** | **Testing phase & production phase** | **266 wks** | **Mon 5/6/24** | **Fri 6/8/29** |
| 38 | 2.1 | Implement TPM | 264 wks | Mon 5/6/24 | Fri 5/25/29 |
| 39 | 2.2 | Component fabrication | 13 wks | Mon 5/6/24 | Fri 8/2/24 |
| 40 | 2.3 | Component testing | 13 wks | Mon 8/5/24 | Fri 11/1/24 |
| 41 | 2.4 | Major assembly | 24 wks | Mon 11/4/24 | Fri 4/18/25 |
| 42 | 2.5 | Static testing | 16 wks | Mon 4/21/25 | Fri 8/8/25 |
| 43 | 2.6 | Fatigue testing | 20 wks | Mon 8/11/25 | Fri 12/26/25 |
| 44 | 2.7 | Systems installation | 14 wks | Mon 12/29/25 | Fri 4/3/26 |
| 45 | 2.8 | Development of training & support services | 28 wks | Mon 4/21/25 | Fri 10/31/25 |
| 46 | 2.9 | Flight testing | 52 wks | Mon 11/3/25 | Fri 10/30/26 |
| 47 | 2.10 | Certify model | 232 wks | Mon 11/4/24 | Fri 4/13/29 |
| 48 | 2.11 | Mass production | 8 wks | Mon 4/16/29 | Fri 6/8/29 |

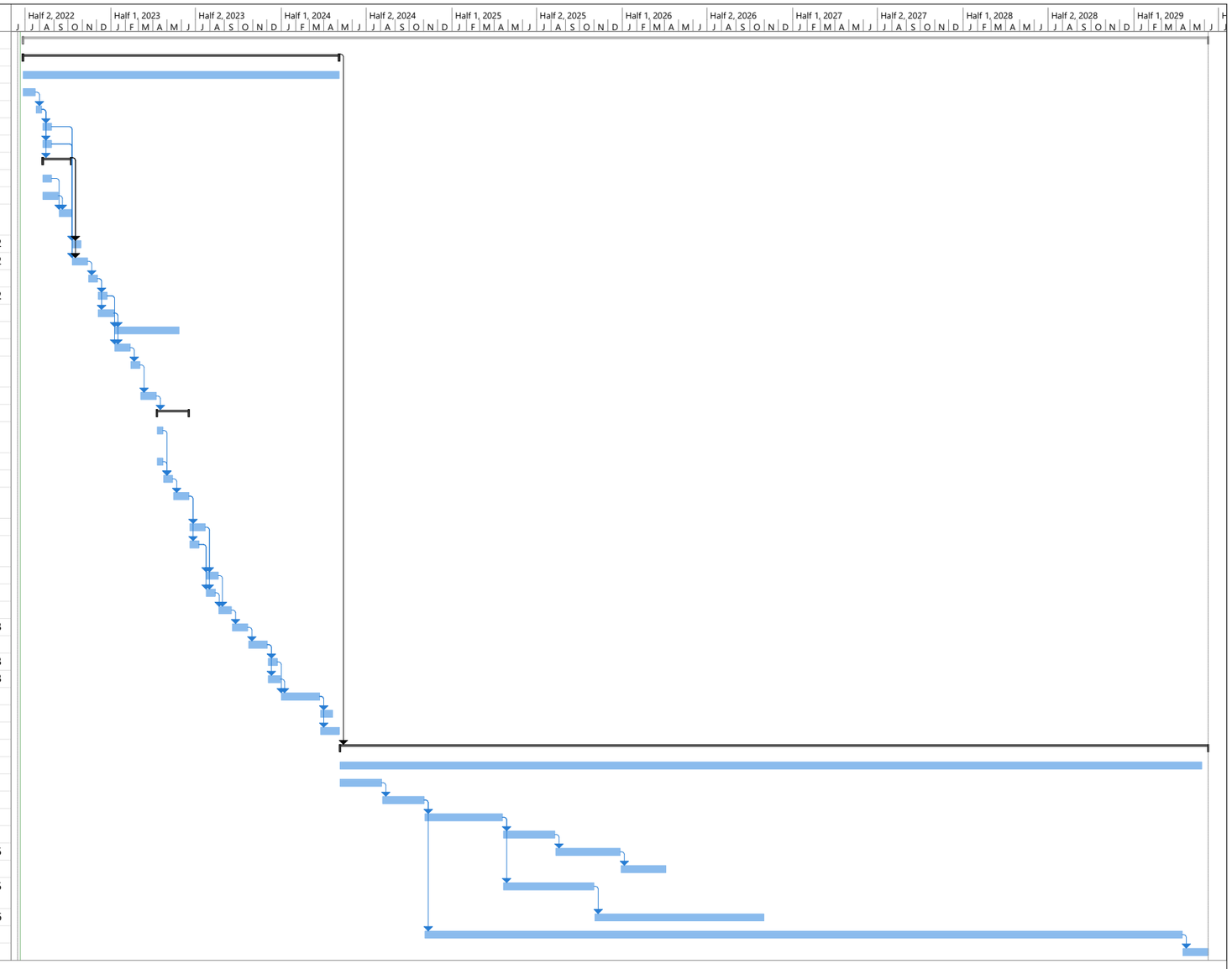


Project: JAPA-12 Development
Date: Tue 6/21/22

Task, Split, Milestone, Summary, Project Summary, Inactive Task, Inactive Milestone, Inactive Summary, Manual Task, Duration-only, Manual Summary Rollup, Manual Summary, Start-only, Finish-only, External Tasks, External Milestone, Deadline, Progress, Manual Progress

Page 1

**Figure 12.3:** *Gantt chart for future planning.*

# 13 Final Design

Now that the entire design has been covered, one may reflect on the entire design and major choices made. The JAPA-12 aircraft was designed to fulfil the desired medical evacuation mission on Antarctica. However, via a market analysis it was also determined that slight adaptations to the requirements make the aircraft enticing for different markets; like remote communities. This meant that the aircraft required excellent STOL and S&C characteristics, while being climate neutral and at least 90% recyclable by mass. The sizing of the aircraft was carried out via a wide set of safety margins and contingencies while simultaneously complying to the CS-23 regulations. On top of that, the team managed to make use of a distributed propulsion configuration, which improved the efficiency of the aircraft. Additionally, a rear door was included to facilitate easy payload loading. This resulted in the aircraft that can be seen in Figure 13.1. Additionally, the performance parameters of the aircraft are summarised in Table 13.1.

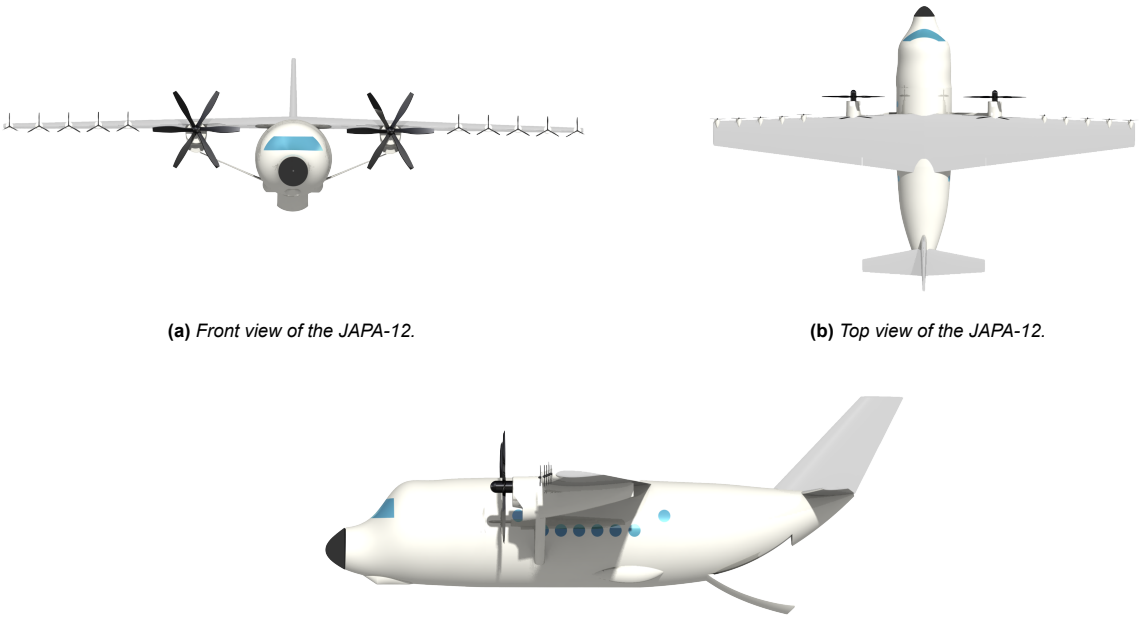

**(a)** *Front view of the JAPA-12.*

**(b)** *Top view of the JAPA-12.*

**(c)** *Side view of the JAPA-12.*

**Figure 13.1:** *3-view illustration of the JAPA-12 aircraft.*

**Table 13.1:** *Revised performance parameters of the JAPA-12 aircraft.*

| Parameter | Amount |
|---|---|
| Ferry range [km] | 6218 |
| Maximum mission payload [lbs] | 4000 |
| Maximum fuel capacity [lbs] | 3756 |
| Cruise velocity [kts] | 208 |
| Service ceiling [ft] | 25000 |
| Maximum passenger capacity | 19 |

Via a RAMS analysis, it was concluded that the design was able to safely operate within the operational boundaries set by the customer and the team. Yet, the critical subsystems of combustion engines, fuel tank, and hydraulics experienced

some uncertainties whether or not they could properly function at the low temperatures experienced. Therefore, in future stages of the design, these three subsystems have to be further looked into and be extensively tested. Additionally, to meet the harsh weather conditions experienced, an extensive maintenance strategy has been developed which largely mitigated the chance of operational failure. Therefore, by carrying out the mentioned steps, the design was expected to be safe for operations.

On top of that, a financial analysis was carried out. During this analysis, a list price of $7.5 million was set for the standard configuration established in this report. The production costs of a single aircraft were estimated to be $6.35 million. With this list price and production cost, 108 aircraft have to be sold to reach the break-even point. From the market analysis, it was estimated that customers would buy 120 JAPA-12 aircraft. Therefore, it was expected that further development of the JAPA-12 project would result in a profit. Now, to further extend possible markets for the JAPA-12 aircraft, a family of aircraft was established. By doing so, an even brighter future for the aircraft was generated as the family allowed for different markets, and better performance for the accompanied mission profiles. This was mainly done by deviating from the strict environmental requirements, after which the aircraft was more optimized for conventional conditions.

Due to the limited time available, the design was not developed into a physical entity, and tests were excluded from the development phase. On top of that, some subsystems need additional attention which was not feasible given the limited amount of time. Therefore, a future development plan was established. Further development of the design should first look into the most unreliable systems. Thus, the combustion engines, fuel system and hydraulic system have to be developed in further detail and thoroughly tested to make the subsystems more reliable. Then, from the requirement compliance, it was established that the maximum structural load factor of 9 was partially complied with. Due to the limited amount of time, a simplified structural analysis was carried out, which proved that a load factor of 9 could be resisted. Yet, this analysis was carried out on a far from optimal structure. Therefore, it was unknown whether the structure can cope with the loads when additional stress concentrations are introduced. Finally, from the future planning, it was determined that all subsystems of the aircraft have been touched upon. Yet, due to the limited time available, all subsystems have not been designed in the desired level of detail. To give an example, the propulsion group desired further designing of the propeller airfoils, and the stability and control group wanted further development of the pilot control inputs. Therefore, the design was far from complete. However, a solid foundation has been built. Note that, as the JAPA-12 was designed to comply with CS-23, the to-be-developed parts of the design still have to comply with the CS-23 regulations as stated in the compliance matrix. Therefore, when further designing the JAPA-12, the CS-23 regulations have to be taken into account at all times.

Looking back at the mission need statement: **Design an aircraft that can successfully conduct a medical evacuation under extreme Antarctic weather conditions at the Amundsen-Scott base and, possibly, serve other remote communities and roles**; it was concluded that the aircraft does comply with this statement as the JAPA-12 fully fulfilled this statement. Therefore, the team was convinced this design met the customer demands.

During the design process, the team gained a lot of additional knowledge on the full design cycle of an aircraft, where lots of ups and downs were experienced. It was a rather bumpy ride, but the project objective statement: **Obtain a better understanding of the full design cycle of a system and gain knowledge on designing an aircraft by producing a design that fulfills the mission need statement together with a group of 10 capable aspiring engineers in 10 weeks**, was achieved.

Concluding the final design, the JAPA-12 aircraft is considered a feasible aircraft to be used for the desired mission profiles set by the customer. By further improving the design by carrying out the aforementioned steps, the team is even more convinced that the design will fulfil its purpose. Furthermore, the aircraft can be used for both general transportation missions and medical evacuations at remote and extremely cold locations in the near future. Therefore, the team is convinced the JAPA-12 aircraft satisfies its customer.

# Bibliography


[1] E. Konopleva, N. vd Ploeg, S.-L. Lee, I. Oostmeijer, N. Grens, J. Baas, P. Hoogervorst, T. Tikkala, J. Kipping, and M. Broekers, "Mid-term report," TU Delft, Tech. Rep., 2022.

[2] R. de Vries, M. Brown, and R. Vos, "A preliminary sizing method for hybrid-electric aircraft including aeropropulsive interaction effects," Jun. 2018. DOI: 10.2514/6.2018-4228.

[3] M. Sadraey, "Aircraft design: A systems engineering approach," Sep. 2012. DOI: 10.1002/9781118352700.

[4] J. Roskam, *Airplane Design: Preliminary sizing of airplanes*, ser. Airplane Design. DARcorporation, 1985, ISBN: 9781884885426. [Online]. Available: https://books.google.nl/books?id=usXVaf8Qu0cC.

[5] ——, *Airplane Cost Estimation: Design, Development, Manufacturing and Operating*, ser. Airplane Design. DARcorporation, 2002, ISBN: 9781884885556.

[6] E. Konopleva, N. vd Ploeg, S.-L. Lee, I. Oostmeijer, N. Grens, J. Baas, P. Hoogervorst, T. Tikkala, J. Kipping, and M. Broekers, "Baseline report," TU Delft, Tech. Rep., 2022.

[7] M. A. Lazzara, L. M. Keller, T. Markle, and J. Gallagher, "Fifty-year amundsen–scott south pole station surface climatology," *Atmospheric Research*, vol. 118, pp. 240–259, 2012, ISSN: 0169-8095. DOI: https://doi.org/10.1016/j.atmosres.2012.06.027. [Online]. Available: https://www.sciencedirect.com/science/article/pii/S0169809512002256.

[8] A. Bolosov, *Russian Polar Aviation. 1946–2014 . Book 2*. Paulsen, 2022, ISBN: 9785457826984. [Online]. Available: https://books.google.nl/books?id=y5joCQAAQBAJ.

[9] H. V. Turner, M. A. C. Teixeira, J. Methven, and S. B. Vosper, "Sensitivity of the surface orographic gravity wave drag to vertical wind shear over antarctica," *Quarterly Journal of the Royal Meteorological Society*, vol. 145, no. 718, pp. 164–178, 2019. DOI: https://doi.org/10.1002/qj.3416.

[10] A. Sherratt, "Cradle to cradle," in *Encyclopedia of Corporate Social Responsibility*, S. O. Idowu, N. Capaldi, L. Zu, and A. D. Gupta, Eds. Berlin, Heidelberg: Springer Berlin Heidelberg, 2013, pp. 630–638, ISBN: 978-3-642-28036-8. DOI: 10.1007/978-3-642-28036-8_165.

[11] P. T. Anastas and J. B. Zimmerman, "Design through the 12 principles of green engineering," *IEEE Engineering Management Review*, vol. 35, no. 3, pp. 16–16, 2007. DOI: 10.1109/emr.2007.4296421.

[12] A. Johanning, *Life cycle assessment in conceptual aircraft design*, Mar. 2016. DOI: 10.13140/RG.2.1.1531.0485.

[13] J. Roskam, *Airplane Design: Component Weight Estimation*, ser. Airplane Design. DARcorporation, 1985, ISBN: 9781884885501. [Online]. Available: https://books.google.nl/books?id=mMU47Ld7yQkC&source=gbs_similarbooks.

[14] U.S. Department of Energy, "Cost estimating guide," 2018, pp. 15–16.

[15] R. J. Hamann, *Systems engineering & technical management techniques - part II*. TU Delft, 2006.

[16] R. de Vries, "Hybrid-electric aircraft with over-the-wing distributed propulsion: Aerodynamic performance and conceptual design," Ph.D. dissertation, Jan. 2022. DOI: 10.4233/uuid:ef87dc11-e7b2-4726-a41f-28588d64c58d.

[17] M. D. Patterson, "Conceptual design of high-lift propeller systems for small electric aircraft," Ph.D. dissertation, Georgia Institute of Technology, 2016.

[18] M. D. Patterson, M. J. Daskilewicz, and B. German, "Simplified aerodynamics models to predict the effects of upstream propellers on wing lift," in *53rd AIAA Aerospace Sciences Meeting*. DOI: 10.2514/6.2015-1673.

[19] R. de Vries, M. Brown, and R. Vos, "Preliminary sizing method for hybrid-electric distributed-propulsion aircraft," *Journal of Aircraft*, vol. 56, no. 6, pp. 2172–2188, 2019. DOI: 10.2514/1.C035388.

[20] S. Gudmundsson, "Chapter 3 - initial sizing," in *General Aviation Aircraft Design*, S. Gudmundsson, Ed., Boston: Butterworth-Heinemann, 2014, pp. 55–75, ISBN: 978-0-12-397308-5. DOI: https://doi.org/10.1016/B978-0-12-397308-5.00003-9.

[21] Civil Aviation Authority, *Safety sense leaflet 07: Aeroplane performance*, http://publicapps.caa.co.uk/modalapplication.aspx?appid=11&mode=list&type=sercat&id=21, accessed = 31-05-2022.

[22] Flight Safety Foundation, *Approach and landing accident reduction briefing notes 8.3 - landing distances*, https://flightsafety.org/toolkits-resources/past-safety-initiatives/approach-and-landing-accident-reduction-alar/alar-briefing-notes-in-english/, accessed = 31-05-2022.

[23] D. Raymer, *Aircraft Design: A Conceptual Approach, Sixth Edition*. Sep. 2018, ISBN: 978-1-62410-490-9. DOI: 10.2514/4.104909.

[24] A. Matrone, "Performance-based preliminary sizing of aircraft with distributed propulsion," M.S. thesis, Politecnico di Milano, Italy, 2020.

[25] J. Roskam, *Layout design of cockpit, fuselage, wing and empennage: Cutaways and inboard profiles*. DARcorporation, 2002.

[26] R. Vos and K. Schmidt, "Analytical weight estimation method for oval fuselages in conventional and novel aircraft," Jan. 2014. DOI: 10.2514/6.2014-0026.

[27] European Union Aviation Safety Agency, *Certification Specifications for Large Aeroplanes, CS-25 Amendment 3*, Sep. 2007.

[28] R. Budynas, A. M. Sadegh, and R. J. Roark, *Roark's formulas for stress and strain*, eighth. McGraw-Hill Professional, 2012.

[29] R. Alderliesten, *Selection of material & structure, fatigue & durability*, accessed = 10-06-2022.

[30] E. Torenbeek, *Advanced Aircraft Design - Conceptual Design, Analysis and Optimization of Subsonic Civil Airplanes*, English. United Kingdom: John Wiley & Sons, 2013, ISBN: 978-1-118-56811-8.

[31] R. Vos, J. Melkert, and B. T. C. Zandbergen, *A/C Preliminary Sizing (T/W-W/S diagram), Aerospace Design and Systems Engineering Elements I – AE1222-II*, accessed = 09-05-2022.

[32] A. Veld, *AE3212-I Aerospace flight dynamics and simulation, lateral stability and control derivatives*, accessed = 31-05-2022.

[33] European Union Aviation Safety Agency, *Certification Specifications and Acceptable Means of Compliance for Normal, Utility, Aerobatic, and Commuter Category Aeroplanes, CS-23 Amendment 4*, Jul. 2015.

[34] J. Viken, S. Viken, K. Deere, and M. Carter, "Design of the cruise and flap airfoil for the x-57 maxwell distributed electric propulsion aircraft," Jun. 2017. DOI: 10.2514/6.2017-3922.

[35] J. Melkert and R. Vos, *Aerospace design and systems engineering elements i, wing and propulsion system design*, accessed = 02-06-2022.

[36] F. Oliviero, *Ae3211-i systems engineering and aerospace design, requirement analysis and design principles for a/c stability & control (part 2)*, accessed = 31-05-2022.

[37] ——, *Ae3211-i systems engineering and aerospace design, aircraft balance*, accessed = 30-05-2022.

[38] FAA, *Advisory circular, aircraft weight and balance control*, accessed = 09-06-2022.

[39] A. Veld, *Ae3212-i aerospace flight dynamics and simulation, static stability*, accessed = 30-05-2022.

[40] J. Melkert, *Aerospace design and systems engineering elements i, landing gear and empennage sizing*, accessed = 02-06-2022.

[41] B. T. S. Garrett T. Klunk Jeffrey L. Freeman, "Vertical tail area reduction for aircraft with spanwise distributed electric propulsion," *AIAA Propulsion and Energy Forum*, 2018.

[42] I. G. Recant and A. R. Wallace, "Windtunnel investigation of the effect of vertical position of the wing on the side flow in the region of the vertical tail," NASA, Tech. Rep., Apr. 1941.

[43] Nicolosi, D. F. Ciliberti, P. Della Vecchia, S. Corcione, and V. Cusat, "A comprehensive review of vertical tail design," *Aircraft Engineering and Aerospace Technology*, vol. 89, pp. 547–557, 4 2017. DOI: 10.1108/AEAT-11-2016-0213.

[44] F. Oliviero, *Design for lateral-directional aspects & design for ground operations, Ae3211-i systems engineering and aerospace design*, accessed = 10-06-2022.

[45] R. de Vos and J. Melkert, "Aerospace design and systems engineering elements i, airplane design," 2020. [Online]. Available: https://brightspace.tudelft.nl/d2l/le/content/213451/Home?itemIdentifier=D2L.LE.Content.ContentObject.ModuleCO-1471999.

[46] J. Roskam, *Airplane Design: Layout Design of Landing Gear and Systems*, ser. Airplane Design. DARcorporation, 1985, ISBN: 9781884885532. [Online]. Available: https://books.google.nl/books/about/Airplane_Design.html?id=TfRcDpWw9i0C&redir_esc=y.

[47] M. Tooley and D. Wyatt, *Aircraft Electrical and Electronic Systems*. Butterworth-Heinemann, 2009.

[48] M. R. Lindeburg, *Mechanical engineering reference manual: For the PE exam*. Professional Publications, 1998.

[49] S. Saran, M. Gurjar, A. Baronia, V. Sivapurapu, P. S. Ghosh, G. M. Raju, and I. Maurya, "Heating, ventilation and air conditioning (hvac) in intensive care unit," *Critical Care*, vol. 24, no. 1, 2020. DOI: 10.1186/s13054-020-02907-5.

[50] ASHRAE, *Health care facilities, chapter 9*, accessed = 08-06-2022.

[51] S. Saran, *Heating, ventilation and air conditioning (hvac) in intensive care unit*, accessed = 08-06-2022. DOI: https://doi.org/10.1186/s13054-020-02907-5.

[52] F. Oliviero, *Weight estimation and iterations in a/c design, Aerospace Design and Systems Engineering Elements II AE2111-II aircraft part*, accessed = 11-05-2022.

[53] K. Volkov, *Flight Physics: Models, Techniques and Technologies*. IntechOpen, 2018, ISBN: 9789535138075. DOI: 10.5772/intechopen.68297.

[54] C. A. Moses, "Comparative evaluation of semi-synthetic jet fuels," Sep. 2008, CRC Project No. AV-2-04a.

[55] O. Meier and D. Scholz, "A handbook method for the estimation of power requirements for electrical de-icing systems," *DLRK, Hamburg*, vol. 31, 2010.

[56] P. Visser, "Data analysis: Space topic, ae2223-ii," *TU Delft*, 2021.

[57] P. S. Hausley, *Antarctica: Exploration, Perception and Metaphor*. Routledge, 1992.

[58] L. Prinzel, "Synthetic vision systems," *NASA*, 2009.

[59] Cheng et al., "A prototype of enhanced synthetic vision system using short-wave infrared," 2018. DOI: 10.1109/DASC.2018.8569799.

[60] National Science Foundation, *US Antarctic Program Interagency Air Operations Manual*, Oct. 2021.

[61] J. Roskam, *Airplane Design: Preliminary Calculation of Aerodynamic, Thrust and Power Characteristics*, ser. Airplane Design. DARcorporation, 1985, ISBN: 9781884885525. [Online]. Available: https://books.google.nl/books?id=0udGAQAAIAAJ&hl=nl&source=gbs_similarbooks.

[62] F. Oliviero, *Aerospace design and systems engineering elements ii, aircraft aerodynamic analysis lift & drag*, accessed = 02-06-2022.

[63] A. Veld, *Ae3212-i aerospace flight dynamics and simulation, dynamic stability analysis*, accessed = 05-06-2022.

[64] M. Naeije, *Ae3212-i aerospace flight dynamics and simulation, linearization*, accessed = 05-06-2022.

[65] D. Caughey, *Introduction to aircraft stability and control course notes for m&ae 5070*, accessed = 05-06-2022.

[66] A. Lampton, *Prediction of icing effects on the dynamic response of light airplanes*, accessed = 09-06-2022. DOI: 10.2514/1.25687.

[67] H. El Uamari, E. Adib, K. Burger, B. Jacobson, T. Duim, H. Aldrige, M. van der Toorn, M. Beyens, and P. Kováčik, "Bsc thesis: How far can we get?" Ph.D. dissertation, Jul. 2018.

[68] T. Megson, *An Introduction to Aircraft Structural Analysis*, fourth. Elsevier, 2007.

[69] R. Hibbeler, *Mechanics of Materials*, ser. Always learning. Pearson, 2016, ISBN: 9780134319650. [Online]. Available: https://books.google.nl/books?id=oMP5sgEACAAJ.

[70] W. Zhao, R. Kapania, J. Schetz, J. Coggin, T. Allen, and B. Sexton, "Nonlinear aeroelastic analysis of sugar truss-braced wing wind tunnel model under in-plane loads," Jan. 2015.

[71] J.-P. Immarigeon, R. Holt, A. Koul, L. Zhao, W. Wallace, and J. Beddoes, "Lightweight materials for aircraft applications," *Materials Characterization*, vol. 35, no. 1, pp. 41–67, Jul. 1995.

[72] A. B. F.J.L. Ales and A. Marques, "Metal and ceramic matrix composites in aerospace engineering," *Processing, Properties and Applications*, pp. 59–99, 2016.

[73] M. Ashby, *Materials Selection in Mechanical Design*, third. Butterworth-Heinemann, 2005.

[74] R. Nath and S. Nakvee, "Role of polymer as aircraft structural material," in *Idem*, Dec. 2016.

[75] R. Alderliesten, *Aircraft & spacecraft loads*, Live Lecture at the faculty of Aerospace Engineering, Dec. 2019.

[76] M. van Oosten, "Composite - metal connections," Ten Cate Advanced Composites BV, Tech. Rep. 1, 2015.

[77] P. Z. J. Dong X. Cui and D. Wang, "Summary of composite material-metal connection technology," *IOP Conference Series: Earth and Environmental Science*, vol. 632, Jan. 2021.

[78] R. Abbishek, B. R. Kumar, and H. S. Subramanian, "Fatigue analysis and design optimization of aircraft's central fuselage," *IOP Conference Series: Materials Science and Engineering*, vol. 225, p. 012 031, Aug. 2017. DOI: 10.1088/1757-899x/225/1/012031. [Online]. Available: https://doi.org/10.1088/1757-899x/225/1/012031.

[79] H. Mao and S. Mahadevan, "Fatigue damage modelling of composite materials," *Composite Structures*, vol. 58, no. 4, pp. 405–410, 2002, ISSN: 0263-8223. DOI: https://doi.org/10.1016/S0263-8223(02)00126-5. [Online]. Available: https://www.sciencedirect.com/science/article/pii/S0263822302001265.

[80] Q. Zhang, Y. Zhu, X. Gao, Y. Wu, and C. Hutchinson, "Training high-strength aluminum alloys to withstand fatigue," *Nature Communications*, vol. 11, p. 5198, Oct. 2020. DOI: 10.1038/s41467-020-19071-7.

[81] "20 - fatigue of aerospace materials," in *Introduction to Aerospace Materials*, A. P. Mouritz, Ed., Woodhead Publishing, 2012, pp. 469–497, ISBN: 978-1-85573-946-8. DOI: https://doi.org/10.1533/9780857095152.469. [Online]. Available: https://www.sciencedirect.com/science/article/pii/B9781855739468500200.

[82] K. Xu, "14 - hydrogen embrittlement of carbon steels and their welds," in *Gaseous Hydrogen Embrittlement of Materials in Energy Technologies*, ser. Woodhead Publishing Series in Metals and Surface Engineering, R. P. Gangloff and B. P. Somerday, Eds., vol. 2, Woodhead Publishing, 2012, pp. 526–561, ISBN: 978-1-84569-677-1. DOI: https://doi.org/10.1533/9780857093899.3.526. [Online]. Available: https://www.sciencedirect.com/science/article/pii/B9781845696771500144.

[83] H. Farhat, "Chapter 8 - lifetime extension: Assessment and considerations," in *Operation, Maintenance, and Repair of Land-Based Gas Turbines*, H. Farhat, Ed., Elsevier, 2021, pp. 175–196, ISBN: 978-0-12-821834-1. DOI: https://doi.org/10.1016/B978-0-12-821834-1.00003-4. [Online]. Available: https://www.sciencedirect.com/science/article/pii/B9780128218341000034.

[84] S. Turteltaub, *Modal analysis for free vibration of undamped multiple degree of freedom*, Live Lecture at the faculty of Aerospace Engineering at the TU Delft, Jan. 2021.

[85] J. Wright and J. Cooper, *Introduction to aircraft aeroelasticity and loads*, second. Wiley, 2015.

[86] X. L. J.R. Banerjee and H. Kassem, "Aeroelastic stability analysis of high aspect ratio aircraft wings," *Journal of Applied Nonlinear Dynamics*, vol. 3, pp. 413–422, Dec. 2014.

[87] A. Demirtas and M. bayraktar, "Free vibration analysis of an aircraft wing by considering as a cantilever beam," *Selcuk University Journal of Engineering Science and Technology*, vol. 7, pp. 12–21, Mar. 2019.

[88] P. D. P. Agrawal and P. Choudhary, "Comparative study on vibration characteristics of aircraft wings using finite element method," *Materials Today: proceedings*, vol. 46, pp. 176–183, May 2021.

[89] T. Theodorsen, "General theory of aerodynamic instability," NACA, Tech. Rep. 496, 1949.

[90] P. Smith, "Project cost management – global issues and challenges," *Procedia - Social and Behavioral Sciences*, vol. 119, pp. 485–494, Mar. 2014. DOI: 10.1016/j.sbspro.2014.03.054.

[91] S. Globerson and O. Zwikael, "The impact of the project manager on project management planning processes," *Project Management Journal*, vol. 33, pp. 58–64, Sep. 2002. DOI: 10.1177/875697280203300308.

[92] E. Gill, *Ae3211-i systems engineering and aerospace design, risk management & concurrent engineering*, accessed = 05-06-2022.

[93] J. Sinke, *Production of aerospace systems, costs & lean manufacturing*, accessed = 13-06-2022.

[94] M. G. Böckmann and R. Schmitt, "Methodology for ecological and economical aircraft life cycle analysis," in *Leveraging Technology for a Sustainable World*, D. A. Dornfeld and B. S. Linke, Eds., Berlin, Heidelberg: Springer Berlin Heidelberg, 2012, pp. 467–472, ISBN: 978-3-642-29069-5.

[95] European Commission, "European platform on life cycle assessment," 2013. [Online]. Available: https://eplca.jrc.ec.europa.eu/ELCD3/.

[96] E4tech (UK) Ltd. Ministerie van Infrastructuur en Waterstaat, 2021.

[97] A. van Oudheusden, *Recycling of composite materials*, pp. 42–44, 2019.

[98] G. Volker, M. Dameris, C. Frömming, and D. Lee, "Impact of aircraft nox emissions. part 2: Effects of lowering the flight altitude," *Meteorologische Zeitschrift*, vol. 11, pp. 197–206, May 2002. DOI: 10.1127/0941-2948/2002/0011-0197.

[99] Organisation de l'aviation civile internationale, *Environmental protection: Annex 16 to the Convention on international civil aviation*. Montréal : ICAO, 2011, vol. 1.

[100] I. Kroo and R. Shevel, *Aircraft Design: Synthesis and Analysis*. Desktop Aeronautics, Inc., Jan. 2001.

[101] J. Marte and D. Kurtz, "A review of aerodynamic noise from propellers, rofors, and liff fans," NASA, Tech. Rep., Jan. 1970.

[102] M. Crocker, *Handbook of Noise and Vibration Control*, ser. Wiley InterScience. Wiley, 2007, ISBN: 9780471395997. [Online]. Available: https://books.google.nl/books?id=46NvrvpHIxEC.

[103] M. Fink, "Airframe noise prediction method," U.S. Department of Transportation, Tech. Rep., Mar. 1977.

[104] P. Lasagna, K. Mackall, F. Burcham, and T. Putnam, "Landing approach airframe noise measurements and analysis," NASA, Tech. Rep. 1602, Jan. 1980.

[105] O. A. Søvde, S. Matthes, A. Skowron, D. Iachetti, L. Lim, B. Owen, Ø. Hodnebrog, G. Di Genova, G. Pitari, D. S. Lee, G. Myhre, and I. S. Isaksen, "Aircraft emission mitigation by changing route altitude: A multi-model estimate of aircraft nox emission impact on o3 photochemistry," *Atmospheric Environment*, vol. 95, pp. 468–479, 2014, ISSN: 1352-2310. DOI: https://doi.org/10.1016/j.atmosenv.2014.06.049. [Online]. Available: https://www.sciencedirect.com/science/article/pii/S1352231014004956.

[106] European Union Aviation Safety Agency, *Cri consultation paper, special condition, electric / hybrid propulsion system, SC E-19*, Apr. 7, 2021.

[107] D. Finger, R. de Vries, R. Vos, C. Braun, and C. Bil, "Cross-validation of hybrid-electric aircraft sizing methods," English, *Journal of Aircraft: devoted to aeronautical science and technology*, vol. 59, no. 3, pp. 742–760, 2022, ISSN: 0021-8669. DOI: 10.2514/1.C035907.

[108] C. Pols, *Applied physics tn2985-p: Introduction to experimentation manual*, 2021-2022.

[109] W. Spitz, F. Berardino, R. Golaszewski, and J. Johnson, "Development cycle time simulation for civil aircraft," NASA, Tech. Rep., Jan. 2001.

# Appendix A

**Table A.1:** *Medical equipment overview with their weights.*

| Medical equipment | Mass [kg] | Dimensions (l x w x h) [m] | Cost [$] | Power required |
|---|---|---|---|---|
| Ferno 35A stretcher | 33 | 2x0.6x1 | 3.400 | - |
| Oxygen mask | 0.05 | - | 10 | - |
| Nebulisers | 0.635 | 0.15x0.22x0.12 | 50 | 138 W |
| Self-inflating bag-valve-mask | 0.2 | - | 20 | - |
| Airways intubation equipment | 0.1 | - | 200 | - |
| Humidifcation and filter systems for patient | 1.1 | 0.16x0.16x0.13 | 300 | 90 W |
| Pleural drainage equipment | 0.25 | - | 17 | - |
| Aneroid sphygmomanometer | 0.4 | 0.8x0.7x0.1 | 100 | - |
| IV fluids, giving sets, pressure cuff | 1 | - | 40 | - |
| Needles, nasogastric tube | 0.1 | - | 20 | - |
| Urinary catheters and bags | 0.1 | - | 20 | - |
| Suturing instruments | 0.3 | 0.1x0.1x0.1 | 30 | - |
| Thermal insulation | 0.1 | - | 10 | - |
| Splints | 0.3 | - | 50 | - |
| Rigid cervical spine collars | 0.5 | 0.3x0.3x0.3 | 200 | - |
| Dressings and bandages | 0.3 | 0.1x0.1x0.1 | 50 | - |
| Maternity packs | 0.1 | - | 5 | - |
| Stethoscope | 0.18 | 0.2x0.2x0.2 | 250 | - |
| Fetal stethoscope | 0.1 | 0.1x0.1x0.05 | 10 | - |
| Temperature measuring device | 0.1 | - | 30 | - |
| ECG monitor-defibrillator | 5 | 0.33x0.32x0.14 | 3.000 | 250 W |
| Portable oxygen supply & regulator | 10 | 0.2x0.1x0.2 | 3.000 | 285 W |
| Portable mechanical ventilator | 2.7 | 0.4x0.6x0.25 | 1.000 | 295 W |
| Non-invasive blood pressure monitoring | 0.5 | 0.4x0.4x0.3 | 4.000 | 70W |
| Pulse oximeter | 0.1 | 0.15x0.1x0.1 | 1.000 | 1.6W |
| Portable spirometer | 0.14 | - | 1.000 | Not Found |
| Oxygen analyser | 10 | 0.1x0.1x0.1 | 350 | Battery powered |
| Restraints for uncooperative or violent patients | 0.3 | - | 15 | - |
| Volumetric infusion pump | 2 | 0.15x0.15x0.15 | 1.200 | 20 W |
| High pressure alarm | 0.32 | - | 10 | - |
| Syringe drivers | 2.1 | 0.2x0.2x0.1 | 3.000 | Battery powered |

Continuation of Table A.1.

| Medical equipment | Mass [kg] | Dimensions (l x w x h) [m] | Cost [$] | Power required [W]/input current [A] |
|---|---|---|---|---|
| Biochemical analyser | 6.85 | 0.3x0.3x0.1 | 1.200 | 70 W |
| Glucose, haemoglobin, renal function, coagulation | 0.5 | - | 60 | - |
| 12 lead ECG | 5 | 0.4x0.4x0.3 | 5.000 | Battery powered |
| Portable diagnostic ultrasound | 1.2 | 0.17x0.1x0.3 | 1.500 | 10 W |
| Limb splints | 2 | 0.12x0.8x0.2 | 500 | - |
| Pelvic splint | 0.27 | 0.1x0.1x0.1 | 100 | - |
| Paediatric restraint | 1.5 | - | 700 | - |
| Obese patient transport restraint | 2 | 0.1x0.1x0.1 | 100 | - |
| Standardized transport bags | 1 | 0.5x0.4x0.3 | 100 | - |
| Total | 94.8 | $1.87m^3$ | 31.648 | 1230 W |
| Total with margin | 125 | $2.5m^3$ | 50.000 | 1500 W |

**Table A.2:** *Required equipment list for the synthetic vision system [58]*

| Category | System |
|---|---|
| Synthetic vision sensors | Weather radar |
| | Radar altimeter |
| | Forward looking Infrared |
| | Millimeter wave radar |
| Synthetic vision displays | Primary flight display |
| | Navigation display |
| | Head-up display |
| Computers computational functions | Image object detection |
| | Computations and symbology generation |
| Additional aircraft systems | Differential GPS |
| | Inertial reference unit |
| | Air data computer |
| | Radio |
| | RADAR |
| | Traffic collision and avoidance system |
| | Data link aggregate |
| | Terrain awareness and warning system |
| | Laser altimeter |